

# IRE Transactions



## on Microwave Theory and Techniques

Volume MTT-8

**SEPTEMBER, 1960**

Number 5

### In This Issue

Noise Studies on Two-Cavity CW Klystrons

Optimum Quarter-Wave Transformers

The Quarter-Wave Transformer Prototype Circuit

Broad-Band Ridge Waveguide Ferrite Devices

Radiation Patterns of a Noise-Excited Thin Slot

Variational Principles and Mode Coupling in Periodic Structures

Determination of the Capacitance, Inductance, and Characteristic  
Impedance of Rectangular Lines

The Analysis of a Broad-Band Circular Polarizer Including  
Interface Reflections

Large Signal Analysis of a Parametric Harmonic Generator

A Waveguide Switch Employing the Offset Ring-Switch Junction

Some Limitations on Parametric Amplifier Noise Performance

TE Mode Excitation on Dielectric Loaded Parallel Plane and  
Trough Waveguides

A New Semiconductor Microwave Modulator

Theory and Measurement of Q in Resonant Ring Circuits

TK7800  
I23

**PUBLISHED BY THE**

**Professional Group on Microwave Theory and Techniques**



## IRE PROFESSIONAL GROUP ON MICROWAVE THEORY AND TECHNIQUES

The Professional Group on Microwave Theory and Techniques is an association of IRE members with professional interest in the field of Microwave Theory and Techniques. All IRE members are eligible for membership and will receive all Group publications upon payment of the prescribed annual fee of \$3.00. Members of the American Physical Society and the Institution of Electrical Engineers of Great Britain may become affiliated with PGMTT and receive all Group publications upon payment of the Affiliate fee of \$7.50 per year.

### Administrative Committee

#### Chairman

K. TOMIYASU

#### Vice Chairman

T. N. ANDERSON

#### Secretary-Treasurer

H. M. ALTSCHULER

R. E. BEAM

A. C. BECK

S. B. COHN

R. C. HANSEN

W. W. MUMFORD

A. A. OLINER

R. A. RIVERS

S. W. ROSENTHAL

T. S. SAAD

R. F. SCHWARTZ

G. SHAPIRO

G. SINCLAIR

P. D. STRUM

M. C. THOMPSON

R. D. WENGENROTH

#### *Ex-Officio*

W. L. PRITCHARD

#### *Honorary Life Members*

G. C. SOUTHWORTH

A. G. CLAVIER

#### Editor

DONALD D. KING

### PGMTT Chapters

Albuquerque-Los Alamos

Baltimore

Boston

Buffalo-Niagara

Chicago

Columbus

Denver-Boulder

Long Island

Los Angeles

New York

R. L. O'Nan

J. C. Wiltse

C. E. Faflick

E. S. Schlichter

Robert Janowiak

B. Querido

G. E. Schafer

B. Aaron

R. C. Hansen

Eugene Torgow

Northern N.J.

Omaha-Lincoln

Orange Belt

Philadelphia

San Diego

San Francisco

Schenectady

Syracuse

Tokyo, Japan

Washington, D.C.

R. M. Foley

C. O. Jett

D. Sabih

T. J. Vaughan

H. O. Dickstein

E. M. T. Jones

C. C. Allen

J. C. Williamson

Kiyoshi Morita

Benjamin Bernstein

### IRE TRANSACTIONS®

#### on Microwave Theory and Techniques

Published by the Institute of Radio Engineers, Inc., for the Professional Group on Microwave Theory and Techniques, at 1 East 79 Street, New York 21, N.Y. Responsibility for the contents rests upon the authors, and not upon the IRE, the Group, or its members. Annual subscription price: IRE members, \$8.50; colleges and public libraries, \$12.75; non-members, \$17.00. Individual copies of this issue and all available back issues may be purchased at the following prices: IRE members (one copy) \$2.25, libraries and colleges \$3.25, all others \$4.50.

Address all manuscripts to Donald D. King, PGMTT Editor, Electronic Communications, Inc., 1830 York Road, Timonium, Md. Submission of three copies of manuscripts, including figures, will expedite the review.

COPYRIGHT ©1960—THE INSTITUTE OF RADIO ENGINEERS, INC.

Printed in U.S.A.

All rights, including translations, are reserved by the IRE. Requests for republication privileges should be addressed to the Institute of Radio Engineers, 1 E. 79th St., New York 21, N.Y.



IRE Transactions

on

Microwave Theory and Techniques

EDITORIAL BOARD	Volume MTT-8	SEPTEMBER, 1960	Number 5
<i>Editor</i> Donald D. King			
<i>Advertising Editor</i> Robert A. Rivers			
	TABLE OF CONTENTS		
	CONTRIBUTIONS		
D. J. Angelakos	Noise Studies on Two-Cavity CW Klystrons.....	George A. Espersen	474
F. R. Arams	Optimum Quarter-Wave Transformers.....	Leo Young	478
W. P. Ayres	The Quarter-Wave Transformer Prototype Circuit.....	Leo Young	483
R. W. Beatty	Broad-Band Ridge Waveguide Ferrite Devices.....	E. S. Grimes, Jr., D. D. Bartholomew, D. C. Scott, and S. C. Sloan	489
A. D. Berk	Radiation Patterns of a Noise-Excited Thin Slot.....	Nicholas George	493
A. D. Bresler	Variational Principles and Mode Coupling in Periodic Structures.....	T. J. Goblick, Jr. and R. M. Bevensee	500
J. C. Cacheris	Determination of the Capacitance, Inductance, and Characteristic Impedance of Rectangular Lines.....	Tsung-Shan Chen	510
S. B. Cohn	The Analysis of a Broad-Band Circular Polarizer Including Interface Reflections.....	S. Adachi and E. M. Kennaugh	520
R. E. Collin	Large Signal Analysis of a Parametric Harmonic Generator.....	Kenneth M. Johnson	525
M. P. Forrer	A Waveguide Switch Employing the Offset Ring-Switch Junction.....	R. C. Johnson, A. L. Holliman, and J. S. Hollis	532
I. Goldstein	Some Limitations on Parametric Amplifier Noise Performance.....	R. D. Weglein	538
R. C. Hansen	TE Mode Excitation on Dielectric Loaded Parallel Plane and Trough Waveguides.....	M. Cohn, E. S. Cassedy, and M. A. Kott	545
H. Heffner	A New Semiconductor Microwave Modulator.....	H. Jacobs, F. A. Brand, M. Benanti, R. Benjamin, and J. Meindl	553
E. T. Jaynes	Theory and Measurement of Q in Resonant Ring Circuits.....	Hellmut Golde	560
E. M. T. Jones	CORRESPONDENCE		
R. W. Klopfenstein	Ferrite Shape Considerations for UHF High-Power Isolators.....	Ernest Stern	565
P. A. Loth	Measurement Technique for Narrow Line Width Ferromagnets.....	J. I. Masters, B. R. Capone, and P. D. Gianino	565
R. V. Lowman	Multidiode Switches.....	Janis Galejs	566
T. Moreno	Technique for Polishing Single Crystal Yttrium-Iron-Garnet Spheres.....	P. D. Gianino, B. R. Capone, E. Kelly, and J. I. Masters	569
S. P. Morgan	Tunable Two-Mode Cavity with Capacitative Loading.....	J. D. McGee	569
K. S. Packard, Jr.	Unloaded Q of Single Crystal Yttrium-Iron-Garnet Resonator as a Function of Frequency.....	P. S. Carter, Jr., and C. Flammer	570
M. C. Pease	A Note on the Derivation of the Fields in a Radial Line.....	J. F. Dienst	571
J. Reed	Surface Waves on Symmetrical Three-Layer Sandwiches.....	J. H. Richmond	572
J. M. Richardson	Higher-Order Evaluation of Dipole Moments of a Small Circular Disk.....	Wilhelm H. Eggimann	573
P. A. Rizzi	Properties of Symmetric Hybrid Waveguide Junctions.....	R. Levy	573
S. D. Robertson	Contributors.....		574
N. G. Sakiotis			
R. F. Schwartz			
W. Sichak			
D. C. Stinson			
E. Strumwasser			
L. Swern			
P. H. Vartanian, Jr.			
M. T. Weiss			
G. J. Wheeler			
R. F. Whitmer			
J. C. Wiltse			
L. Young			
F. J. Zucker			



# Noise Studies on Two-Cavity CW Klystrons\*

GEORGE A. ESPERSEN†, FELLOW, IRE

**Summary**—The noise properties of a two-cavity CW 3-cm klystron oscillator are discussed with the purpose of studying the noise contribution located close to the center frequency in the audio-frequency range. A system permitting measurements to be made of the mean square frequency deviation is described. Comparisons are made indicating the noise performance of the klystron oscillator when operated under air-cooled and water-cooled conditions.

## INTRODUCTION

THIS PAPER is concerned with the study of noise as it applies to a two-cavity CW 3-cm klystron oscillator intended for use in MTI or Doppler radar systems, where large amounts of nearly monochromatic power are required. The designers of such systems are concerned largely with noise located close to the center frequency in the audio-frequency range from 0 to 20 kc which is of interest in helicopter landing systems having a low Doppler shift.

In considering the sources of noise which are present in the measurement of microwave oscillators, we will consider only the noise produced by frequency modulation and will neglect the small order amplitude modulation effects which are cancelled out by making the measurement system (which will be described later) insensitive to amplitude modulation. Factors which contribute to the noise signal resulting in possible causes of frequency instability are:

- 1) Noise due to fluctuations of the power supply.
- 2) Noise due to the fluctuations of the admittance of the load connected to the klystron oscillator.
- 3) Noise due to variable thermal expansions and contractions of the dimensions of the klystron.
- 4) Shot noise excitation of the resonant cavities.
- 5) Noise mechanisms involving fluctuations in beam parameters, such as those due to changes in current density of the cathode, flicker effect, beam velocity, and beam current fluctuations.

It is believed that the fundamental mechanism contributing to frequency fluctuations in klystron oscillators depends upon the essential design parameters; namely, the applied voltages, the admittance of the load connected to the klystron and the time scale of the

fluctuations being considered. Shimoda<sup>1</sup> presented a theory of the electronic limitation to frequency stability, which yielded a root-mean-square frequency deviation that agreed with measurement. However, Bernstein<sup>2</sup> criticized Shimoda's result and suggested that the agreement with experiment was produced by chance since the theory given considered only electronic noise; while the experiment allowed measurement of frequency fluctuations produced by nonelectronic noises. Few attempts were made to correlate observed klystron frequency fluctuations with theory, especially comparisons of audio rate fluctuation in high powered klystron oscillators. Some attempt will be made in this report to present data which will help to bring about a better understanding of klystron oscillator noise.

## THE PKX-4 KLYSTRON OSCILLATOR

The PKX-4 klystron oscillator was used exclusively in all measurements made and described in this report. This klystron has been described previously<sup>3</sup> and consists essentially of a two-cavity resonator construction employing no diaphragms and tuners, with a fixed feedback coupling. These precautions are taken in the design of this tube to reduce to a minimum the effects of microphonism. The modulating cavity is dimensioned to yield the desired resonant frequency and the output cavity is adjusted mechanically to produce oscillations by applying a force to the collector, which is sufficient to strain the cavity wall beyond the elastic limit of the cavity wall material. Fig. 1 shows a cross-sectional view of the resonator system.

In addition to ruggedizing the resonator system, the design of the gun structure<sup>4</sup> was also improved upon to increase its rigidity, so that little if any microphonism was noted through a frequency range from 20 cycles to 20 kc. The Philips impregnated cathode operating at an emission density of approximately 2 a/cm<sup>2</sup> (having a perveance of  $0.25 \times 10^{-6}$  a/v<sup>3/2</sup>) was used as a source of thermionic emission.

The PKX-4 klystron oscillator is liquid cooled and a maximum rate of flow required for water cooling is about  $\frac{1}{2}$  gallon per minute. This tube bolts directly to standard RG-52/U waveguide fittings.

<sup>1</sup> K. Shimoda, "Length of coherent microwaves generated by an electronic oscillator," *J. Phys. Soc. Japan*, vol. 8, p. 131; 1953.

<sup>2</sup> I. L. Bernstein, "Fluctuations of klystron oscillation," *C. R. Acad. Science URSS*, vol. 106, pp. 453-456; 1956.

<sup>3</sup> R. A. La Plante, "Development of a low-noise X-band CW klystron power oscillator," *IRE TRANS. ON ELECTRON DEVICES*, vol. ED-1, pp. 99-106; December, 1954.

<sup>4</sup> G. A. Espersen, "A low noise high power klystron oscillator of great reliability," *Le Vide*, pp. 270-280; September-October, 1956.

\* Received by the PGMTT, February 29, 1960; revised manuscript received, April 28, 1960.

† Philips Labs., Irvington-on-Hudson, N. Y.



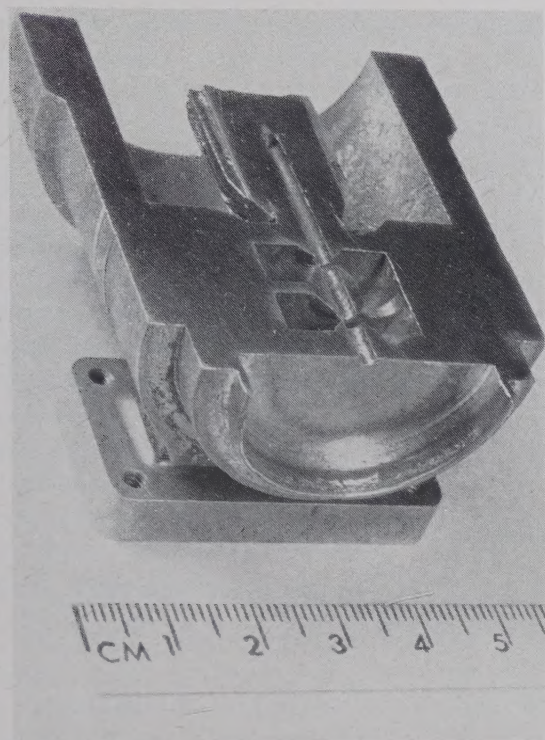


Fig. 1—Opened X-band oscillator of the PKX-4 type.

### THE NOISE-MEASURING SYSTEM

Early klystrons which were not completely corrected for microphonic defects were measured with a system<sup>5</sup> which proved to be inadequate for studying improved models of the klystron. Atkinson developed a system<sup>6</sup> of measurement which permitted measurements to be made of the mean square frequency deviation that would result from various types of electronic fluctuations being converted into frequency fluctuations. A block diagram of an improved version of this system is shown in Fig. 2. The improved system differs from the earlier measuring system in the following ways:

- 1) Crystal currents of 0.001 ampere (formerly 0.0005 ampere) and 300-ohm dc loads were used to increase the tube to crystal noise ratio to a value greater than could be achieved with quadratic operation of the crystal detectors and 10,000-ohm dc loads. The crystal in the FM arm is not operated in the quadratic range, hence it is necessary to use the indicated calibrated adjustable attenuator to set the discriminator to the inflection point of its transmission curve.
- 2) Type 1N415C and 1N415E crystals were substituted for the relatively noisy 1N23B crystals. The polarity reversibility of these crystals made

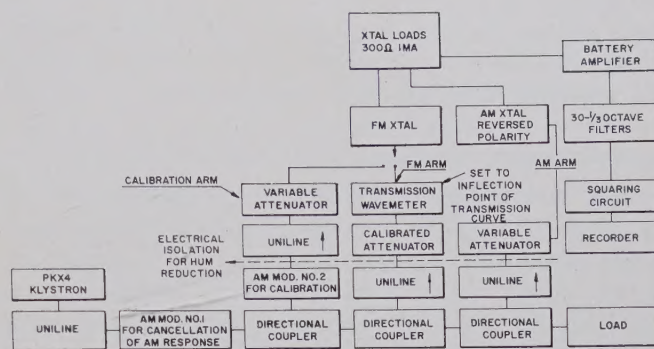


Fig. 2—Principal system for measurement of random frequency deviations.

possible AM cancellation without using a mixing transformer (formerly used on initial measurement system).

- 3) An air-driven resistive-card amplitude modulator no. 1 was placed in the main line to allow the power absorbed by the AM bucking crystal to be adjusted so as to render the system insensitive to AM, thus eliminating the need for matched crystals.
- 4) A calibrated air-driven resistive-card amplitude modulator no. 2 is included in the calibration arm to produce a known amount of modulation, which is used to determine the sensitivity of the crystal used in the FM arm. This modulator makes possible calibration of the crystal-load-amplifier, filter squaring circuit and indicator chain. The AM bucking crystal acts as a shunt for the FM crystal and the loading effect of the AM crystal is varied with the proper amount of excitation required for AM cancellation. During calibration of the chain, the FM crystal and its holder are moved to the calibration arm and an output reading is taken.
- 5) A 30-member set of third octave filters is used to form a selective amplifier in place of the previously used narrow band heterodyne arrangement. This method insured the advantages of increased bandwidth over most of the audio range.
- 6) The output of the selective amplifier is fed to a series of diodes to form a squaring circuit, the output of which is recorded on a chart recorder to obtain the mean square voltage from the selective amplifier.
- 7) The background noise of the amplifiers and crystals is found by connecting the crystal holder (normally connected to the FM branch) to the frequency insensitive calibration arm.

With these changes and using a loaded discriminator cavity having a  $Q$  of 8500, one is able to detect rms frequency deviations as small as 2 cps over a third octave band in the audio spectrum above 500 cps, with a reproducibility amounting to a rms deviation from the mean value of measured quantity of 0.7 cps. At

<sup>5</sup> G. A. Espersen and R. A. La Plante, "Studies and Investigations of a 100 Watt CW X-Band Klystron," AFRCRC, Contract No. AF19(604)-454; March, 1954.

<sup>6</sup> W. R. Atkinson, "Research on Noise in High Powered Klystrons," ARDC, Contract No. AF18(603)-33 Supp. 1 (57-345); May 31, 1958.



lower ranges of the audio spectrum where the rms frequency deviations were 70 cps over a third octave, relative reproducibility was five times better.

#### MEASUREMENT OF RANDOM FREQUENCY DEVIATIONS

Most measurements were made on klystrons which operated in the mode corresponding to a transit angle of  $9/4$  cycles and delivering a power output of approximately 20 CW watts. A number of measurements were also taken in the mode corresponding to transit angles of  $11/4$  and  $15/4$  cycles respectively. All measurements taken used the circuitry shown in Fig. 2.

A plot of rms frequency deviation against central filter frequency for a number of different klystrons, shown in Fig. 3, indicates that the frequency deviation is greatest at values of central filter frequency below 400 cps.

Fig. 4 shows how the rms frequency deviation varies when plotted against central filter frequency for various transit angles.

Fig. 5 indicates how the frequency deviation varies with respect to central filter frequency for a given klystron, comparing water cooling with air cooling.

Some measurements taken at a central filter frequency of 40 cps indicate that increasing the water flow rate from 0.08 to 0.30 gallon per minute increased the frequency deviation from 45 to 65 cps. Other measurements at a filter frequency of 40 cps show that increasing the beam voltage from 3.5 to 4.5 kv increased the frequency deviation from 38 to 75 cps.

#### DISCUSSION

It is significant to point out that all measurements were taken at frequencies other than the line frequency and its harmonics. The amount of power supply ripple

noise at the measured frequencies was in the order of 1 cps, while the beam modulation sensitivity of the PKX-4 klystron oscillator was approximately 7.5 kc/v.

The low frequency beam current fluctuations, as observed by connecting a 1000-ohm resistor in series with the klystron and the fluctuating voltage, indicated that the mean square current fluctuations were at least twenty times less than the full shot noise throughout the entire audio spectrum for a given klystron.

Figs. 2, 3, 4 and 5 all indicate that the rms frequency deviation increases rapidly with decreased filter frequency at values below 400 cps. This phenomenon is

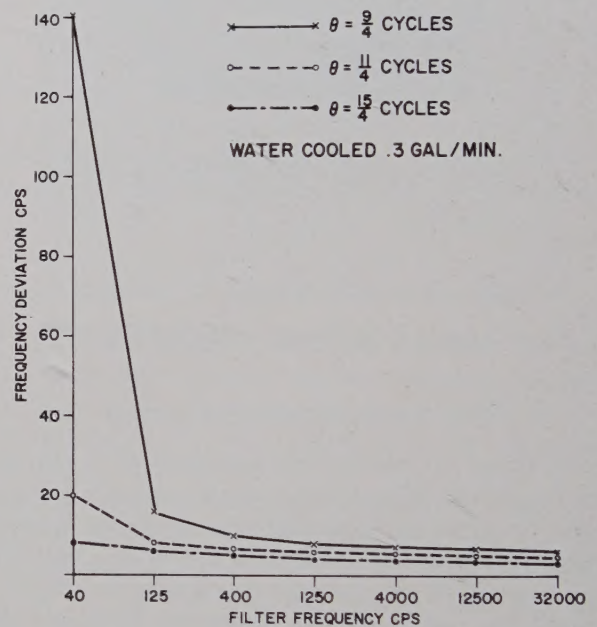


Fig. 4—RMS frequency deviation vs central filter frequency for various transit angles.

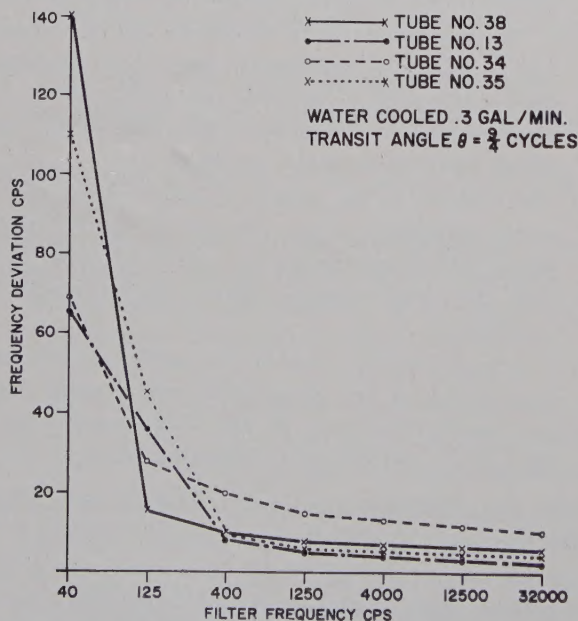


Fig. 3—RMS frequency deviation vs central filter frequency for a number of PKX-4 klystrons.

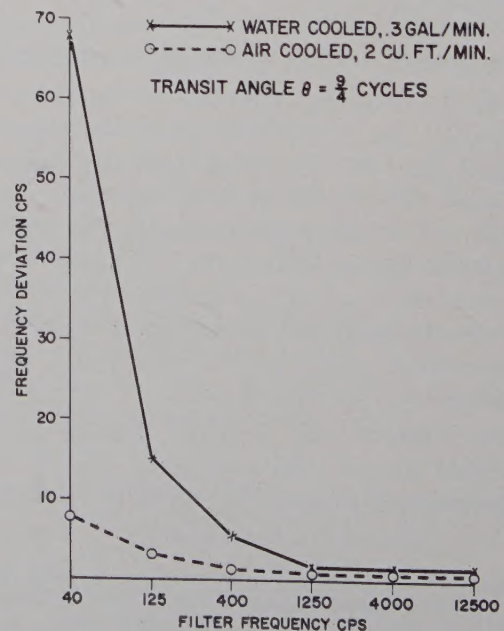


Fig. 5—RMS frequency deviation vs central filter frequency, PKX-4 klystron no. 9.



similar to that displayed by klystrons having tuning diaphragms which definitely do possess microphonism in the same frequency range. However, these klystrons are of a massive construction, and since they are supported by a shock mounted table it is felt that the main source of the microphonic excitation is probably due to the flow of the coolant both in the water-cooled and air-cooled klystrons. This is confirmed by the fact that changing the water flow rate from 0.08 to 0.30 gallon per minute increases the frequency deviation from 45 to 65 cps for a central filter frequency of 40 cps. Furthermore, Fig. 5 shows that the frequency deviation of an air-cooled klystron is only 8 cps, as compared to 68 cps in a water-cooled klystron, even though the body temperature of the air-cooled klystron is 90° greater than the water-cooled klystron, which operated at a body temperature of 30°C.

The reason for the improved performance using air cooling is not fully understood. It has been shown experimentally that when the coolant becomes hot enough to simmer audibly, the spectrum of the cathode current fluctuations indicates sharp peaks of several thousand cycles. This behavior shows that the microphonic variation of the cathode to anode spacing or the microphonic variation of the ion current flowing back to the cathode does accompany the increased simmering condition of the coolant. It is possible that the current fluctuations which accompany the simmering are responsible for the frequency fluctuations present. Since only total cathode current was measured, no data were available regarding the fluctuations of the transmitted current.

The resonant cavities of the klystrons have frequency fluctuations which contribute to the noise picture since these cavities are sensitive to gap spacings. The sensitivities range in value from  $5.7 \times 10^{12}$  cps/m for small gap spacings (0.020 inch) to  $0.73 \times 10^{12}$  cps/m for large gap spacings (0.040 inch). The frequency variation of the buncher and catcher cavities shows mode to mode alterations in which case the klystron oscillates in either the buncher or catcher mode, which can be identified by the transit angle. As the beam voltage increases, the klystron oscillates alternately in the two types of modes and in some cases it will skip a mode. The increase in the rms deviation at low frequencies that accompanies increased power input (smaller transit angle) is shown in Fig. 4.

It was believed that the addition of cooling fins to the anode collector (shown in Fig. 1) would decrease the frequency deviation. Measurements taken after cleaning the collector (no cooling fins attached) on a number of klystrons indicated that the rms deviation at 40 cps doubled in value. With cooling fins attached to the collector and with normal water flow rate and power input, no bubbling of water was observed, but without cooling fins bubbles formed on the collector. When the surface

was cleaned, large bubbles would appear, but when the surface was painted, small bubbles would appear and remain attached to the collector for long periods of time. It has not been possible to determine whether the bubble phenomenon is significant with the degree of frequency fluctuation or whether some other phenomenon is responsible for both the frequency fluctuations and the bubbles. No audible simmering was noted in the observations mentioned above and the temperature of the center point of the collector was 50°C for the tests involving both the cleaned and painted collectors.

It was felt that the second catcher cone would expand to a considerable extent if the beam would momentarily strike it, thus causing frequency fluctuations of several hundred cycles per second. Attempts to measure the cone temperature fluctuations have not been successful to date. An experimental PKX-4 klystron was made in which the bore diameter of the second catcher cone was increased from 0.085 inch to 0.095 inch. Using air cooling one obtained a frequency deviation as low as 4 cps. The best result for frequency deviation of an air-cooled PKX-4 klystron having a constant bore diameter of 0.085 inch, as indicated in Fig. 5, was 8 cps at a filter frequency of 40 cps.

#### CONCLUSIONS

A summary of the essential results indicates that lower frequency deviation can be achieved if air cooling is used in place of water cooling, and if changes are made in the cavity configuration of the catcher cavity to reduce thermal effects from the electron beam. A frequency deviation of 4 cps at a filter frequency of 40 cps has been achieved, and with further refinement in the tube design it should be possible to attain a value of frequency deviation which is near or even less than unity. For measurements of these klystrons, it is suggested that the more elaborate system proposed by Whitwell and Williams,<sup>7</sup> which is capable of a resolution of a few tens of cycles, may be used to advantage.

#### ACKNOWLEDGMENT

The author would like to acknowledge the work of W. R. Atkinson, chief investigator of this project, who contributed many of the ideas expressed in this paper.

Appreciation is extended to the Air Force Cambridge Research Center and the Air Force Office of Scientific Research for providing some of the funds required for this noise study under Contracts AF19(604)-454, AF19(604)-1080, and AF18(603)-33.

<sup>7</sup> A. L. Whitwell and N. Williams, "A new microwave technique for determining noise spectra at frequencies close to the carrier," *Microwave J.*, vol. 2, pp. 27-32; November, 1959.



# Optimum Quarter-Wave Transformers\*

LEO YOUNG†, SENIOR MEMBER, IRE

**Summary**—The design of uniformly dispersive quarter-wave transformers is a well explored subject. Common examples are rectangular waveguide E-plane transformers, in which the  $a$  dimension is kept constant.

In this paper, it is shown that the performance of conventional quarter-wave transformers of a single section can always be improved by making the middle section less dispersive than the input and output waveguides, and a formula for the optimum  $a$  dimension is given.

The theory was verified experimentally. In this instance, the improved transformer measured 50 per cent more bandwidth than did the conventional one, and was 25 per cent shorter besides.

## INTRODUCTION

IN the design of quarter-wave transformers, it has hitherto always been assumed that the guide wavelength is independent of position along the line. This is so, for instance, for TEM modes, or for  $TE_{0n}$  modes in rectangular waveguide where the wide or  $a$  dimension is kept constant. Such transformers, having guide wavelength independent of position, are called *homogeneous* transformers.<sup>1</sup> When the guide wavelength varies along the length of the transformer, it is called *inhomogeneous*. The first exact design formulas for ideal homogeneous quarter-wave transformers<sup>2</sup> were given by Collin,<sup>3</sup> who considered up to four sections. The first complete synthesis procedure was given by Riblet.<sup>4</sup> The author later computed extensive numerical tables,<sup>5</sup> which have been checked out experimentally on numerous occasions.

This paper is concerned only with single-section quarter-wave transformers. In particular, it will be shown that the performance of the conventional homogeneous waveguide transformer of a single section can always be improved by making the transformer section

less dispersive than the input and output waveguides, and that an optimum inhomogeneous transformer exists in general. Transformers with two or more sections<sup>6</sup> are not considered in this paper.

## THE INSERTION LOSS FUNCTION, $P_L$

Consider a single-section rectangular waveguide transformer operating in the  $TE_{01}$  mode. Let  $a$  denote the wide dimension, and  $b$  the height, of waveguide. The input guide has dimensions  $a_0 \times b_0$ , the output guide  $a_2 \times b_2$ , and the quarter-wave section  $a_1 \times b_1$ , as shown in Fig. 1.

The transformer is shown schematically in Fig. 2. The characteristic impedances are  $Z_0$ ,  $Z_1$  and  $Z_2$ . The reflection and transmission coefficients<sup>6,7</sup> at the two transformer steps, are  $\Gamma_1$ ,  $\Gamma_2$  and  $T_1$ ,  $T_2$  given by

$$\Gamma_1 = \frac{Z_1 - Z_0}{Z_1 + Z_0}, \quad \Gamma_2 = \frac{Z_2 - Z_1}{Z_2 + Z_1} \quad (1)$$

and

$$T_1 = \frac{2(Z_1 Z_0)^{1/2}}{Z_1 + Z_0}, \quad T_2 = \frac{2(Z_2 Z_1)^{1/2}}{Z_2 + Z_1} \quad (2)$$

The over-all transfer or wave matrix<sup>6,7</sup> of the transformer can then be written

$$T = \frac{1}{T_1 T_2} \begin{pmatrix} 1 & \Gamma_1 \\ \Gamma_1 & 1 \end{pmatrix} \begin{pmatrix} e^{j\theta} & 0 \\ 0 & e^{-j\theta} \end{pmatrix} \begin{pmatrix} 1 & \Gamma_2 \\ \Gamma_2 & 1 \end{pmatrix} \quad (3)$$

where  $\theta$  is the electrical length of the transformer section at any frequency. If we write  $T = (T_{ij})$ ,  $i, j = 1, 2$ , the insertion loss function  $P_L$  is

$$P_L = |T_{11}|^2 = \frac{1}{T_1^2 T_2^2} |e^{j\theta} + \Gamma_1 \Gamma_2 e^{-j\theta}|^2, \quad (4)$$

which after manipulation reduces to

$$P_L = 1 + \frac{1}{T_1^2 T_2^2} [(\Gamma_2 - \Gamma_1)^2 + 4\Gamma_1 \Gamma_2 \cos^2 \theta]. \quad (5)$$

\* Received by the PGMTT, March 2, 1960; revised manuscript received, April 28, 1960. This paper is based on part of a Dr. Engrg. dissertation, Johns Hopkins University, Baltimore, Md.

† Stanford Res. Inst., Menlo Park, Calif. Formerly with Electronics Div., Westinghouse Electric Corp., Baltimore, Md.

<sup>1</sup> L. Young, "Concerning Riblet's theorems," IRE TRANS. ON MICROWAVE THEORY AND TECHNIQUES, vol. MTT-7, pp. 477-478; October, 1959.

<sup>2</sup> The junction of the two transmission lines when junction discontinuities are neglected is called an "ideal transformer." (This is analogous to two perfectly-coupled coils of turns ratio  $(Z_2/Z_1)^{1/2}$  and having infinite inductance.)

<sup>3</sup> R. E. Collin, "Theory and design of wide-band multisection quarter-wave transformers," PROC. IRE, vol. 43, pp. 179-185; February, 1955.

<sup>4</sup> H. J. Riblet, "General synthesis of quarter-wave impedance transformers," IRE TRANS. ON MICROWAVE THEORY AND TECHNIQUES, vol. 5, pp. 36-43; January, 1957.

<sup>5</sup> L. Young, "Tables for cascaded homogeneous quarter-wave transformers," IRE TRANS. ON MICROWAVE THEORY AND TECHNIQUES, vol. MTT-7, pp. 233-237; April, 1959.

<sup>6</sup> L. Young, "Design of Microwave Stepped Transformers with Applications to Filters," Ph.D. dissertation, the Johns Hopkins University, Baltimore, Md.; April, 1959.

<sup>7</sup> G. L. Ragan, "Microwave Transmission Circuits," M.I.T. Rad. Lab. Ser., McGraw-Hill Book Co., Inc., New York, N. Y., vol. 9; 1951.



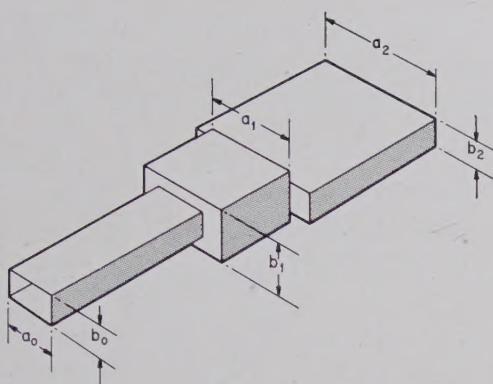


Fig. 1—Quarter-wave transformer (showing notation).

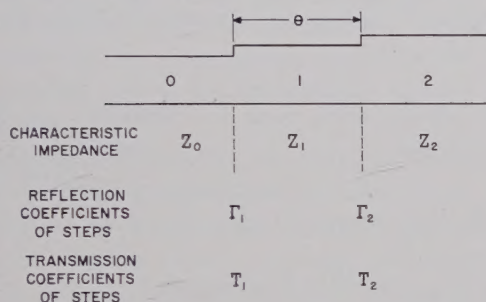


Fig. 2—Quarter-wave transformer parameters.

For a quarter-wave transformer, a match is required at  $\theta = \pi/2$ , so

$$\Gamma_2 = \Gamma_1 \quad \text{at} \quad \theta = \frac{\pi}{2}. \quad (6)$$

#### SOME FORMULAS FOR WAVEGUIDES

Denote the free space (or medium) wavelength by  $\lambda$  and define the differential operator

$$D = \lambda \frac{d}{d\lambda} = \frac{d}{d(\ln C\lambda)} \quad (7)$$

where  $C$  is any constant. Define the dimensionless ratios

$$s = \frac{\lambda_g}{\lambda_c} \quad (8)$$

$$t = \frac{\lambda_g}{\lambda} \quad (9)$$

$$u = \frac{\lambda}{\lambda_c} \quad (10)$$

where  $\lambda_g$  is the guide wavelength and  $\lambda_c$  is the cutoff wavelength of the waveguide, for the mode of propagation.

Since

$$\frac{1}{\lambda_g^2} = \frac{1}{\lambda^2} - \frac{1}{\lambda_c^2}, \quad (11)$$

then

$$t^2 - s^2 = 1. \quad (12)$$

Also

$$ut = s. \quad (13)$$

Their derivatives are

$$Dt = s^2 t \quad (14)$$

$$Ds = st^2 \quad (15)$$

$$Du = u. \quad (16)$$

The derivative of the electrical length  $\theta$  is given by

$$D\theta = -t_1^2 \theta. \quad (17)$$

For TE modes,

$$Z_{(TE \text{ mode})} \propto \frac{b}{a} \cdot \frac{\lambda_g}{\lambda}, \quad (18)$$

and remembering that  $a$  and  $b$  are constants for the differential operator  $D = \lambda(d/d\lambda)$ , it can be shown<sup>6</sup> that

$$\begin{aligned} D\Gamma_1 &= \frac{1}{2}(1 - \Gamma_1^2)(t_1^2 - t_0^2) \\ D\Gamma_2 &= \frac{1}{2}(1 - \Gamma_2^2)(t_2^2 - t_1^2). \end{aligned} \quad (19)$$

#### THE OPTIMUM TRANSFORMER

For a quarter-wave single-section transformer, (6) ensures a perfect match at one frequency, the "center frequency." This equation does not, however, completely determine the transformer if dispersive, since the rates of change of  $\Gamma_1$ ,  $\Gamma_2$  and  $\theta$  may still be adjusted by one remaining parameter, the cutoff wavelength of the intermediate section. For optimum performance set

$$D^2 P_L = 0 \quad \text{at} \quad \theta = \frac{\pi}{2}. \quad (20)$$

From (5), this becomes

$$D(\Gamma_2 - \Gamma_1)^2 + 4\Gamma^2(D\theta)^2 = 0 \quad (21)$$

where use has been made of (6) after differentiation. Referring to (17) and (19) one finally obtains

$$t_1^2 = \frac{1}{2} \left[ \frac{t_0^2 + t_2^2}{1 + \left( \frac{\pi\Gamma}{1 - \Gamma^2} \right)^2} \right] \quad (22)$$

as the required condition, where  $\Gamma_1 = \Gamma_2 = \Gamma$  by (6). This can also be expressed

$$\lambda_{g1}^2 = \frac{1}{2} \left[ \frac{\lambda_{g0}^2 + \lambda_{g2}^2}{1 + \left( \frac{\pi}{4} \right)^2 \frac{(Z_2 - Z_0)^2}{Z_2 Z_0}} \right]. \quad (23)$$

Note that

$$\lambda_{g1}^2 \leq \frac{1}{2}(\lambda_{g0}^2 + \lambda_{g2}^2) \quad (24)$$



(equal only if  $\Gamma = 0$ ); and if furthermore  $a_0 = a_2$ , then

$$a_{1 \text{ optimum}} > a_0 = a_2 \quad (25)$$

in all cases, *i.e.*, in this case the matching section should always be less dispersive than the input and output waveguides (as might have been expected). Thus, a homogeneous transformer is never an optimum transformer (except in the trivial case  $\Gamma = 0$ ). A flatter frequency response can be obtained, at least for small bandwidths, by making the transformer inhomogeneous.

In general, if  $\Gamma$  is large enough, or  $t_0$  and  $t_2$  small enough, or both, (22) may yield a value for  $t_1$  less than unity, and a true optimum transformer then does not exist. In that case,  $t_1 = 1$  gives the best transformer.

### NUMERICAL RESULTS

To test the theory and to assess the sharpness of the optimum, we analyzed numerically several transformers. In all cases, the optimum transformer was correctly predicted by (22).

The numerical work shows that the improvement obtained in going from a homogeneous to an inhomogeneous transformer of one section is significant only for fairly large transformer ratios and more-than-average dispersive lines. One such example is reproduced below.

It is required to transform from 0.900 inch  $\times$  0.050 inch to 0.900 inch  $\times$  0.400 inch waveguide at a design wavelength of  $\lambda_0 = 1.638$  inches. The intermediate section dimensions will be denoted by  $a_1 \times b_1$ . The VSWR against wavelength response of the homogeneous ( $a_1 = 0.900$  inch) and optimum ( $a_1 = 1.90$  inches) transformers are plotted in Fig. 3. The slope at the center of the optimum transformer curve is less than half (about 45 per cent) of the corresponding slope for the homogeneous transformer. Again, further computations show that the response curve changes slowly near the optimum, and most of the improvement occurs as one pulls away from the homogeneous case. Thus, more than half the improvement is realized in changing  $a_1$  from 0.900 to 0.990 inch, an increase in width of only ten per cent. This response is also plotted in Fig. 3. Eq. (22) has also been verified numerically where the input and output waveguide wide dimensions ("a-dimensions") are different, and therefore a homogeneous transformer is not possible at all.

### PRACTICAL CONSIDERATIONS FOR COAXIAL LINE AND $TE_{01}$ MODE RECTANGULAR WAVEGUIDE TRANSFORMERS

All exact synthesis procedures assume the existence of ideal transformers. These produce only a change in characteristic impedance, which occurs in the plane of the transformer.

The departure from ideal conditions can be explained in more than one way. Thus, any obstacle can be represented as a transformer at one frequency by choosing

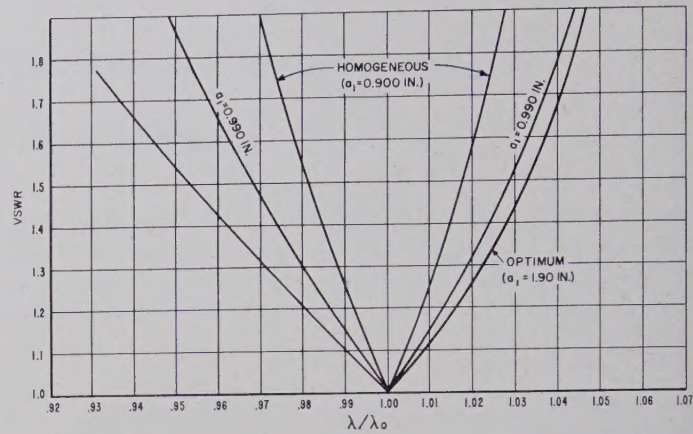


Fig. 3—VSWR against wavelength of homogeneous and optimum inhomogeneous transformers, as well as one intermediate transformer.

reference planes with real  $\Gamma$ . However, as the frequency changes,

- 1) the magnitude of the junction VSWR changes differently from the impedance ratio of the two waveguides,
- 2) the left reference plane moves,
- 3) the right reference plane moves.

Thus, the frequency behavior of *three parameters* must be given to describe completely a lossless two-port.

### Coaxial Line and Waveguide E-Plane Steps

Coaxial line junctions and rectangular waveguides with E-plane steps can be represented by an ideal transformer plus a shunt susceptance at the discontinuity.<sup>8,9</sup> Formulas and graphs are given by Marcuvitz.<sup>10</sup> For this type of junction, the transformer ratio is also independent of frequency, and equal to the impedance ratio. The susceptance value is positive, *i.e.* capacitive, but its frequency dependence is different from that of a capacity. Since the discontinuity susceptance is usually small, its effect on the amplitude of the (real) reflection coefficient is second-order, and the only first-order manifestation is a phase-shift through the transformer. It can, therefore, be compensated quite accurately by changes in length, usually a decrease from the quarter-wave spacings between the steps.<sup>11</sup>

### Waveguide H-Plane Steps

When a change in the wide or  $a$  dimension occurs in rectangular waveguide propagating in the  $TE_{01}$  mode, the discontinuity may be represented<sup>8,9</sup> by an ideal transformer modified by a shunt susceptance which is negative (inductive). However, this alone is not suf-

<sup>8</sup> N. Marcuvitz, "Waveguide Handbook," M.I.T. Rad. Lab. Ser., McGraw-Hill Book Co., Inc., New York, N. Y., vol. 10; 1951.

<sup>9</sup> L. Lewin, "Advanced Theory of Waveguides," Iliffe and Sons, Ltd., London, Eng.; 1951.

<sup>10</sup> Marcuvitz, *op. cit.*, pp. 307-312.

<sup>11</sup> S. B. Cohn, "Optimum design of stepped transmission-line transformers," IRE TRANS. ON MICROWAVE THEORY AND TECHNIQUES, vol. MTT-3, pp. 16-21; April, 1955.



ficient. Unlike for the E-plane step, the maximum number of three parameters must be specified. In Marcuvitz,<sup>12</sup> the three parameters chosen and graphed are

- 1) a shunt inductance;
- 2) the transformer impedance ratio;
- 3) the position of one reference plane; the position of the other reference plane is defined to be in the plane of the junction.

The transformer impedance ratio of an H-plane step is no longer simply the ratio of the characteristic impedances of the two waveguides, as is the case for E-plane steps, but is greater. Thus, even after the inductances are compensated for by a change in the spacings (as for the capacitances at E-plane steps), there remains an increase in the transformer ratio of the H-plane step over and above the impedance ratio of the two waveguides.

The practical effects on the design of H-plane transformers are usually as follows:

- 1) The effect of the shunt inductance can be corrected for by Cohn's method.<sup>11</sup>
- 2) The increase in transformer ratios has the effect of increasing the effective value of the output-to-input impedance ratio  $R$ . The effective  $R$  is the product of all the transformer ratios. One also has to compensate the individual section characteristic impedances, which can be done by simply adjusting the waveguide heights.
- 3) The distance of the reference plane from the junction increases from zero approximately as the square of  $(a_1 - a_2)$ , where  $a_1$  and  $a_2$  are the two guide widths ("a-dimensions"). This distance can become considerably larger than a quarter-wave length for H-plane steps in excess of 10 or 20 per cent of the guide-widths. In practice, a first-order correction might therefore be expected to hold only for steps smaller than this. In general, as cutoff is approached, the ratio  $(\lambda_g/a)$  becomes large, and the correction will become a smaller fraction of  $\frac{1}{4}\lambda_g$ , and so proportionately larger steps might then be corrected for.

#### Compound Steps in Waveguide

For compound steps in both the E-plane and the H-plane simultaneously (changes in both  $a$  and  $b$  dimensions at one junction of two guides), no formulas or numerical information are available. If the necessary corrections are small enough, it should be possible to treat the E-plane capacity correction, and the two H-plane corrections for inductance and reference plane position, separately. Then add the three corrections to each section length as if they were independent.

Finally, symmetrical steps generally require less compensation than asymmetrical steps, and are for this reason to be preferred.

#### EXPERIMENTAL VERIFICATION

Two of the transformers described in the numerical example, the homogeneous (conventional) transformer with  $a_1 = 0.900$  inch and the inhomogeneous (improved) transformer with  $a_1 = 0.990$  inch, were built and tested. (The optimum transformer, with  $a_1 = 1.90$  inches would have introduced higher-order modes, besides performing theoretically little better than the transformer with  $a_1 = 0.990$  inch; and was therefore not constructed. Compare Fig. 3.) The free space wavelength of 1.638 inches corresponds to a frequency of 7211 mc per second. The output waveguide size of 0.900 inch  $\times$  0.400 inch is Retma waveguide type No. WR90 and could conveniently be connected directly to a standard X-band slotted line. For the output waveguide of cross section 0.900 inch  $\times$  0.050 inch, a special sliding load was constructed which had a VSWR of better than 1.02 over most of the frequency band covered in the tests. The inside dimensions of the two transformers, including the intermediate sections after correction for the junction susceptances and reference plane positions<sup>8,10</sup> are shown in Fig. 4. All steps were symmetrical.

The VSWR against wavelength response of these two transformers (Fig. 4), treated as ideal transformers, corresponds to the upper two curves in Fig. 3. The inhomogeneous response curve (middle curve in Fig. 3) has to be modified to allow for the junctions not being ideal, which increases the effective transformer ratio,  $R$ , of the inhomogeneous transformer by some factor. This factor is determined from a figure in Marcuvitz' work,<sup>13</sup> for the symmetrical step, and in this case turns out to be about 1.095 per step; hence, the effective  $R$  equals  $(1.095)^2 = 1.20$  times 8, or 9.6.

Thus, after making the appropriate length corrections, the electrical performance of this transformer [Fig. 4(b)] should correspond to the following ideal transformer:

Input waveguide: 0.900 inch  $\times$  0.050 inch  
 Middle section: 0.990 inch  $\times$  0.231 inch  
 Output waveguide: 0.900 inch  $\times$  0.480 inch

at a frequency of 7211 Mc.

The VSWR against wavelength response of this ideal transformer is shown as curve (c) in Fig. 5. This, therefore, becomes the expected performance of the improved transformer [Fig. 4(b)], whose ideal response corresponds to the middle curve in Fig. 3, or curve (b) in Fig. 5. Finally, curve (a) in Fig. 5 is both the ideal and the expected performance of the *homogeneous* transformer [Fig. 4(a)].

The measured points for the two transformers shown in Fig. 4 are plotted in Fig. 6, together with their expected (computed) curves. It is seen that the experimental points for both the conventional (homogeneous) and improved (inhomogeneous) transformers lie close

<sup>12</sup> Marcuvitz, *op. cit.*, pp. 292-304.

<sup>13</sup> Marcuvitz, *op. cit.*, p. 299, Fig. 5.24-2.



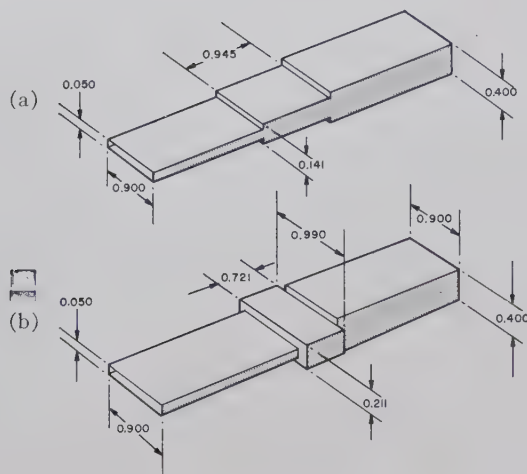


Fig. 4—One-section transformers: (a) control transformer (homogeneous); (b) improved transformer (inhomogeneous).

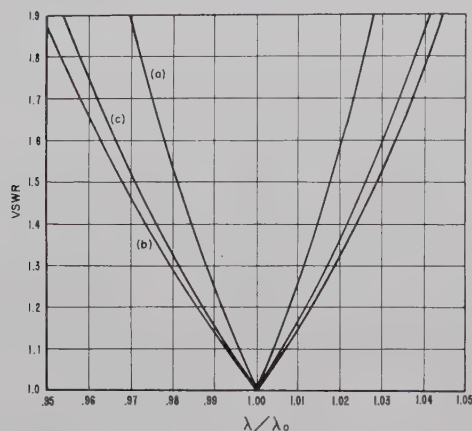


Fig. 5—VSWR against wavelength of three transformers of one section: (a) homogeneous transformer; (b) inhomogeneous transformer without allowing for transformer ratio increase; (c) same inhomogeneous transformer assuming increase of transformer ratio as determined from Marcuvitz.<sup>8</sup>

to the computed curves, and bear out the theory to within experimental accuracy. (The spread in the measured points is thought to be due mainly to the presence of harmonic frequencies from the signal generator.)

### CONCLUSION

We conclude, therefore, that the ideal transformer theory applies to inhomogeneous as well as homo-

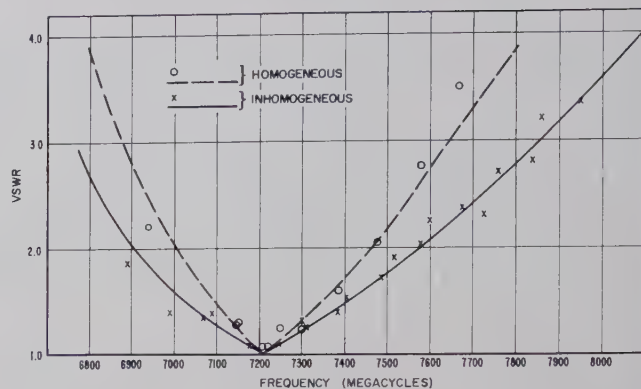


Fig. 6—Experimental points and theoretical curves for the two transformers tested.

geneous transformers in rectangular waveguide after computable corrections<sup>8,10</sup> have been applied. In particular, a single-section inhomogeneous transformer is capable of bettering the performance of the homogeneous one, and this improvement is obtained with a shorter transformer.

It is interesting to note that Solymar<sup>14</sup> and Riblet<sup>15</sup> have recently compared quarter-wave transformers to other impedance transformers and demonstrated their superiority under certain conditions. Both, however, considered only conventional transformers, which (for dispersive waveguides) can further be improved, as demonstrated in this paper.

### ACKNOWLEDGMENT

The author owes much to the teaching and encouragement of Dr. W. H. Huggins of the Johns Hopkins University. The help of Dr. Ferdinand Hamburger, Jr. and Dr. C. F. Miller, also of the Johns Hopkins University, is gratefully acknowledged.

W. M. Etchison and A. C. Robertson helped with most of the computations.

This work was made possible by the financial support of the Westinghouse Electric Corporation's B. G. Lamme Graduate Scholarship for 1958–1959.

<sup>14</sup> L. Solymar, "Some notes on the optimum design of stepped transmission-line transformers," *IRE TRANS. ON MICROWAVE THEORY AND TECHNIQUES*, vol. MTT-6, pp. 374–378; October, 1958.

<sup>15</sup> H. J. Riblet, "A general theorem on an optimum stepped impedance transformer," *IRE TRANS. ON MICROWAVE THEORY AND TECHNIQUES*, vol. MTT-8, pp. 169–170; March, 1960.



# The Quarter-Wave Transformer Prototype Circuit\*

LEO YOUNG†, SENIOR MEMBER, IRE

**Summary**—A quarter-wave transformer not only changes impedance levels, but will also behave as a band-pass filter. In practice, however, band-pass filters are usually required to terminate in equal input and output impedances. They often consist of several direct-coupled cavities, which are similar to transformers whose impedance steps have been replaced by reactive obstacles.

It is demonstrated how one can synthesize a quarter-wave transformer, and then "distort" it to obtain a direct coupled cavity filter with a predictable performance. This is illustrated and confirmed by numerical examples.

The method is particularly convenient to use in reverse. The quarter-wave transformer prototype is easily derived for a direct-coupled cavity filter which has already been designed by another approximate method, and thus gives an independent evaluation of its performance. If necessary, the filter can then be redesigned, as illustrated in this paper.

## INTRODUCTION

THIS PAPER is concerned with a novel method of design of direct-coupled cavity filters. Previous methods have relied on lumped constant equivalent or prototype circuits, or at least have made use of the concept of  $Q$  as it occurs in those circuits. A survey of these methods has recently been given by Riblet.<sup>1</sup>

Instead of starting with an  $L$ - $C$  circuit, another transmission line circuit is here taken as the prototype. This is a quarter-wave transformer, or a half-wave filter, which can be synthesized exactly.<sup>2</sup> It might be expected that by taking one transmission line circuit as a model or prototype for another transmission line circuit, it should be possible to relate their performances more accurately than when the final transmission line filter is based on a lumped-constant equivalent circuit. That this can indeed be so will be demonstrated by numerical examples in this paper.

## THE HOMOGENEOUS QUARTER-WAVE TRANSFORMER

The homogeneous ideal quarter-wave transformer is described by an impedance function  $Z(p)$ , where<sup>2</sup>

$$p = -j \cot \theta, \quad (1)$$

$\theta$  being the electrical length of each section of the multi-section cascaded transformer (Fig. 1).

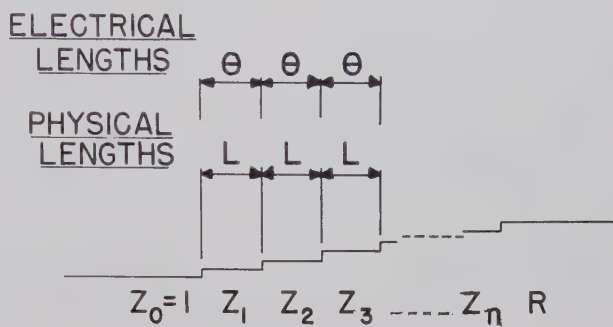


Fig. 1—Quarter-wave transformer ( $\theta = \pi/2$  and  $L = \frac{1}{4} \lambda_g$  at center frequency).

The insertion loss polynomial,  $P_L$ , is given by

$$P_L = 1 + P_n(\mu^2), \quad (2)$$

where  $P_n$  must be positive for real values of  $\mu = \cos \theta$ . If all roots of  $P_n$  are to occur at real frequencies, they must all be double roots for  $P_n$  to stay positive. Hence  $P_L$  is of the form

$$P_L = 1 + Q_n^2(\mu), \quad (3)$$

where  $Q_n$  is even or odd in  $\mu$ . Riblet showed further that, given an insertion loss polynomial of the form (3), one can always synthesize a quarter-wave transformer having this same  $P_L$ . Following Collin,  $Q_n(\mu)$  may be set equal to  $kT_n(\mu/\mu_0)$  for Tchebycheff performance,<sup>3</sup> or  $k\mu^n$  for maximally flat (Butterworth) performance.

The author<sup>4</sup> has tabulated the values of the characteristic impedance ratios  $Z_1, Z_2, Z_3, \dots$ , (Fig. 1) for the homogeneous quarter-wave transformer, to give an equal ripple (Tchebycheff) response. The length  $L$  of each section (Fig. 1) is a quarter guide wavelength at "center frequency" and is defined by

$$L = \frac{\lambda_{g1}\lambda_{g2}}{2(\lambda_{g1} + \lambda_{g2})}, \quad (4)$$

where  $\lambda_{g1}$  is the greatest and  $\lambda_{g2}$  is the smallest guide wavelength in the pass band.

\* Received by the PGM-TT, March 2, 1960; revised manuscript received, May 4, 1960. This paper is based on part of a dissertation for the Dr. of Engrg. degree at the Johns Hopkins University, Baltimore, Md., 1959.

† Stanford Res. Inst., Menlo Park, Calif. Formerly with Electronics Div., Westinghouse Electric Corp., Baltimore, Md.

<sup>1</sup> H. J. Riblet, "A unified discussion of high- $Q$  waveguide filter design theory," IRE TRANS. ON MICROWAVE THEORY AND TECHNIQUES, vol. MTT-6, pp. 359-368; October, 1958.

<sup>2</sup> H. J. Riblet "General synthesis of quarter-wave transformers," IRE TRANS. ON MICROWAVE THEORY AND TECHNIQUES, vol. MTT-5, pp. 36-43; January, 1957. The half-wave filter is an extension of the quarter-wave transformer concept, which will be described in this paper.

<sup>3</sup> R. E. Collin, "Theory and design of wide-band multisection quarter-wave transformers," PROC. IRE, vol. 43, pp. 179-185; February, 1955. Our scale factor  $\mu_0$  is Collin's  $p$  and Riblet's  $s$ .  $T_n$  is the Tchebycheff polynomial of degree  $n$ , and  $k^2$  is a constant, called the pass-band tolerance.

<sup>4</sup> L. Young, "Tables for cascaded homogeneous quarter-wave transformers," IRE TRANS. ON MICROWAVE THEORY AND TECHNIQUES, vol. MTT-7, pp. 233-237, April, 1959; and vol. MTT-8, pp. 243-244, March, 1960.



The bandwidth  $W$  is defined by

$$W = 2 \left( \frac{\lambda_{\theta 1} - \lambda_{\theta 2}}{\lambda_{\theta 1} + \lambda_{\theta 2}} \right). \quad (5)$$

Given the output-to-input impedance ratio  $R$  (taken greater than unity) and the bandwidth  $W$ , the relative characteristic impedances are tabulated in Young's article<sup>4</sup> for values of  $R$  from 1 to 100, and  $W$  from 0 (maximally flat) to 120 per cent.

Since the quarter-wave transformer converts between two impedance levels with the minimum reflection inside a specified pass band, it behaves as a bandpass filter. From the filter point of view, it is unfortunate that the input and output impedances are different. The next section shows how a band-pass filter with equal, or nearly equal, input and output impedances can be achieved.

#### DIRECT SYNTHESIS OF THE HOMOGENEOUS HALF-WAVE FILTER

To avoid the monotone increase in impedance levels of the "Tchebycheff" quarter-wave transformer, the theory may be extended to a cascade of lines in which each section is 180 electrical degrees long at center frequency. Instead of a quarter-wave transformer, there results a half-wave filter, which is a direct-coupled cavity-resonator type of filter,<sup>5</sup> with the resonant cavities defined by the characteristic impedance discontinuities (Fig. 2). The synthesis may be carried out directly, or may be based on the design of a quarter-wave transformer prototype. The latter approach is sketched in below.

#### SYNTHESIS BASED ON THE QUARTER-WAVE TRANSFORMER

##### Synthesis by Quarter-Wave Transformer Tables<sup>4</sup>

To find the appropriate conversions, regard every other step in the half-wave filter as an equivalent circuit consisting of one  $90^\circ$  and one  $(-90^\circ)$  line length, with a step in between, as illustrated in Fig. 3. They are equivalent in the sense that they provide identical normalized impedances with respect to the respective characteristic impedances. This follows from the identity

$$\frac{1}{T} \begin{pmatrix} 1 & \Gamma \\ \Gamma & 1 \end{pmatrix} \equiv \begin{pmatrix} \pm j & 0 \\ 0 & \mp j \end{pmatrix} \frac{1}{T} \begin{pmatrix} 1 & -\Gamma \\ -\Gamma & 1 \end{pmatrix} \begin{pmatrix} \mp j & 0 \\ 0 & \pm j \end{pmatrix}. \quad (5a)$$

Note particularly that the  $90^\circ$  lines in the equivalent circuit are perfectly frequency independent. When this substitution is made for every other step in the half-wave filter (Fig. 2), it contracts into a quarter-wave transformer with one difference, that each line section

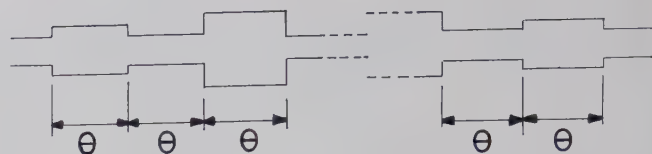


Fig. 2—Half-wave filter.  $\theta$  = electrical length ( $\theta = \pi$  at center frequency).

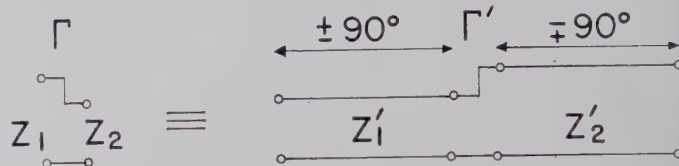


Fig. 3—Equivalent circuit of an impedance step. Impedance ratio:  $Z_2'/Z_1' = Z_1/Z_2$ . Reflection coefficient:  $\Gamma' = -\Gamma$ .

is now twice as frequency sensitive as a quarter-wave section of line. To use the tables<sup>4</sup> for designing a half-wave filter, the procedure in a typical case might be as follows:

- 1) The maximum permissible VSWR in the given pass band and the number of sections (cavities) is specified.
- 2) From the "Maximum VSWR" tables, find the parameter  $R$  by looking under the column for *twice* the bandwidth actually specified.
- 3) With  $R$  so determined, and still using twice the bandwidth specified, find from the tables the impedance ratios  $Z_1, Z_2, Z_3, \dots$ .
- 4) Invert every other impedance step, making successive line impedances either

$$Z_1, \frac{Z_1^2}{Z_2}, \frac{Z_1^2 Z_3}{Z_2^2}, \frac{Z_1^2 Z_3^2}{Z_2^2 Z_4}, \frac{Z_1^2 Z_3^2 Z_5}{Z_2^2 Z_4^2}, \quad (6)$$

or

$$\frac{1}{Z_1}, \frac{Z_2}{Z_1^2}, \frac{Z_2^2}{Z_1^2 Z_3}, \frac{Z_2^2 Z_4}{Z_1^2 Z_3^2}, \frac{Z_2^2 Z_4^2}{Z_1^2 Z_3^2 Z_5}, \quad (7)$$

instead of  $Z_1, Z_2, Z_3, Z_4, Z_5$  (if  $n=4$ ,  $Z_5=R$ ; if  $n=3$ ,  $Z_4=R$ ; etc.).

#### General Synthesis Procedure Based on the Quarter-Wave Transformer

For  $n > 4$ , or  $R > 100$ , or half-wave filter bandwidths in excess of 60 per cent, no tables are as yet available. In this case,  $\mu_0$  is first determined from the half-wave filter bandwidth  $W$  by

$$2W = 2 \left( \frac{\text{maximum frequency} - \text{minimum frequency}}{\text{arithmetic mean frequency}} \right) = \frac{4}{\pi} \sin^{-1} \mu_0. \quad (8)$$

Note that  $2W$ , not  $W$ , has to be used for the half-wave filter. (For dispersive guides, replace frequency by reciprocal guide wavelength.)

<sup>5</sup> S. B. Cohn, "Direct-coupled-resonator filters," PROC. IRE, vol. 45, pp. 187-196; February, 1957.



In place of step 2),  $R$  is determined from the formula<sup>3</sup>

$$\frac{(R+1)^2}{4R} = 1 + k^2 T_n^2 \left( \frac{1}{\mu_0} \right), \quad (9)$$

where

$$\begin{aligned} k^2 &= P_m - 1 \\ &= \frac{|\Gamma_m|^2}{1 - |\Gamma_m|^2} \\ &= \frac{(V_m - 1)^2}{4V_m}, \end{aligned} \quad (10)$$

$P_m$ ,  $|\Gamma_m|$ , and  $V_m$  being the maximum values of the insertion loss function, the reflection coefficient, and the VSWR, respectively.

Instead of referring to the tables,<sup>4</sup> Riblet's method is now used, with  $\mu_0$  from (8) and  $R$  from (9), *i.e.*, as if a quarter-wave transformer of twice the desired bandwidth were being designed.

Finally every other impedance step is again inverted.

#### Condition for Equal Input and Output Impedances

We observe from (6) or (7) that if  $n=1$  or 3, the input and output impedances are the same, since<sup>2,3</sup>  $Z_i Z_{n+i-1} = R$ ; whereas for  $n=2$  or 4, they are not equal. This result can be generalized for odd and even  $n$ , respectively.

**Lemma:** The output-to-input impedance ratio of the half-wave filter is equal to the VSWR of the filter at center frequency.

**Corollary:** The input and output impedances of a half-wave filter are equal if and only if the filter is matched at center frequency.

**Proof of Lemma:** At center frequency, each line length is  $180^\circ$  by definition of the half-wave filter. Now input impedances are unchanged when adding or subtracting  $180^\circ$  line sections. Therefore, at center frequency, all intermediate line sections may be removed, leaving the input and output lines directly connected. This proves both the lemma and its corollary.

It is clear from the lemma that all Tchebycheff half-wave filters consisting of an odd number of sections will have equal input and output impedances, since  $T_n(0) = 0$  if  $n$  is odd. Similarly, all Tchebycheff half-wave filters consisting of an even number of sections cannot have equal input and output impedances, since  $T_n(0) \neq 0$  if  $n$  is even, except in the limiting case when Tchebycheff becomes maximally flat performance.

#### Numerical Results

To obtain numerical confirmation of these results, a nondispersive two-section quarter-wave transformer was designed and analyzed, and the half-wave filter derived from it was also analyzed. The two response curves so obtained are shown superposed in Fig. 4.

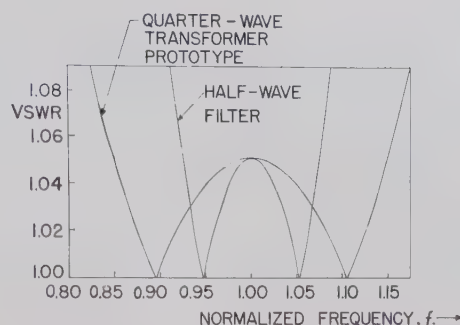


Fig. 4—VSWR against frequency of half-wave filter and its quarter-wave transformer prototype.

The prototype quarter-wave transformer chosen has  $n=2$ ,  $R=5$  and a bandwidth of 30 per cent. From the tables,

$$\begin{aligned} Z_0 &= 1, \\ Z_1 &= 1.5142, \\ Z_2 &= 3.30208, \\ Z_3 &= R = 5. \end{aligned} \quad (11)$$

The normalized frequency response plotted in Fig. 4 confirms the bandwidth of 30 per cent and gives a maximum VSWR of 1.051 as predicted in Table I of Young.<sup>4</sup>

For the half-wave filter, (6) yields:

$$\begin{aligned} Z_0 &= 1, \\ Z_1 &= 1.5142, \\ Z_2 &= 0.6944, \\ Z_3 &= 1.05125. \end{aligned} \quad (12)$$

This is also plotted in Fig. 4 and, as expected, gives a 15 per cent bandwidth (just half that of the quarter-wave transformer), but the same maximum VSWR of 1.051, which is also the output-to-input impedance ratio of the half-wave filter.

#### DIRECT COUPLED CAVITY FILTERS

The homogeneous quarter-wave transformer and half-wave filter perform like a transmission line loaded at equal intervals by obstacles of real and constant reflection coefficients. They resemble the direct-coupled cavity resonator filter,<sup>5</sup> in which each cavity is a section of uniform transmission line bounded by reactive obstacles.

The existence of an exact synthesis procedure for the ideal quarter-wave transformer and half-wave filter suggests using these circuits as "prototypes" for the approximate design of direct-coupled cavity filters.<sup>6</sup> This is analogous to the use of lumped constant "equivalent"

<sup>5</sup> The derivation of the half-wave filter from the quarter-wave transformer was itself a similar (but exact) procedure. The present application calls not merely for the inversion of impedance steps (having real  $\Gamma$ ), but their replacement by reactive obstacles (complex  $\Gamma$ ).



circuits, for which synthesis procedures and formulas have been worked out by Darlington<sup>7</sup> and others. Cohn,<sup>5</sup> for instance, has thus worked out some very useful formulas. The author can attest to the accuracy of Cohn's formulas for most cases of practical interest. Nevertheless, there are times when they must be expected to, and do, break down. This happens, for instance, when the cavity length is no longer close to 180 electrical degrees, as is stipulated in Fig. 14 of Cohn's article.<sup>5</sup>

#### THE QUARTER-WAVE TRANSFORMER PROTOTYPE

Any transmission line loaded at intervals (Fig. 5) can be represented by a transformer circuit consisting of line lengths  $\theta_1, \theta_2, \theta_3$ , etc., separated by impedance step transformers (Fig. 6). The reflection-coefficient of the first step,  $\Gamma_1$ , should be equal to the reflection coefficient of the first obstacle, and so on for  $\Gamma_2, \Gamma_3$ , etc. Each  $\Gamma$  is real but is no longer constant, varying in amplitude with frequency. Similarly the  $\theta$ 's of the prototype transformer (Fig. 6) are no longer equal to each other, or even commensurable, and may all vary differently with frequency.

Each obstacle in Fig. 5 has two symmetrically located reference planes giving it a real reflection coefficient. At center frequency, each reference plane is separated from the next one by an electrical length of 90 degrees.<sup>8</sup> The separations between obstacles at center frequency are  $\phi_1, \phi_2, \dots$  electrical degrees, as shown. It follows that this filter is represented by a half-wave filter equivalent as shown in Fig. 6, with  $\theta_1 = \theta_2 = \dots = 90^\circ$  at center frequency. It would have a frequency behavior like that of a quarter-wave transformer if the  $\Gamma$ 's remained constant, and the  $\theta$ 's remained equal to each other.

Now, if the  $\Gamma$ 's increased or decreased slowly together with frequency, then a performance still not very different from a quarter-wave transformer's might be expected. Also, the  $\theta$ 's increase or decrease together at about the same rate for similar obstacles (e.g., shunt inductances). We shall therefore average their rate of change, compare it to that of an originally  $90^\circ$  long line, and use it to predict the filter bandwidth.

The reference planes, which in Fig. 5 are shown  $90^\circ$  apart at center frequency, shift with frequency and determine the changes in the  $\theta$ 's. Their movement can be traced to two main causes:

- 1) Treating the transfer matrix of each obstacle as constant, the electrical separation between adjacent reference planes at any frequency is equal to the change in the initial electrical separation  $\phi$  between the corresponding obstacles.
- 2) Any frequency dependence of the obstacle parameters may cause the reference planes to move.

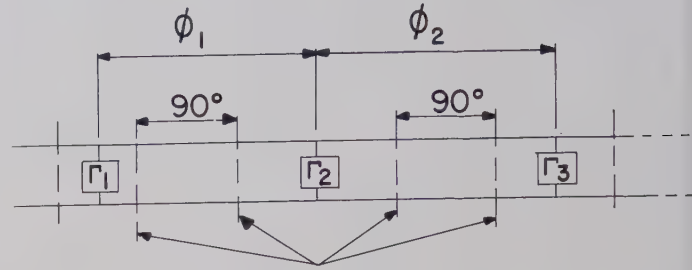


Fig. 5—Direct-coupled cavity filter (synchronously tuned). Reference planes with real  $\Gamma$  are  $90^\circ$  apart at center frequency. All parameter values ( $\Gamma_1, \Gamma_2, \dots, \phi_1, \phi_2, \dots$ ) pertain to center frequency.

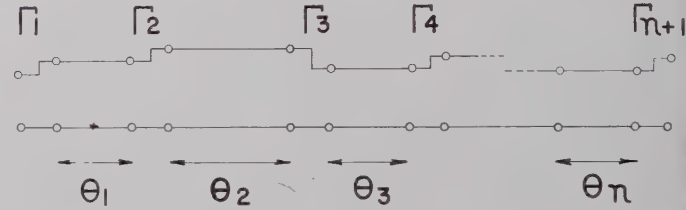


Fig. 6—Equivalent circuit of cascade of two ports.

Thus, if each obstacle is a shunt inductance, its susceptance is inversely proportional to frequency, and the reference plane positions are functions of the susceptance values.

Consider, for instance, the three-cavity symmetrical filter shown in Fig. 7, which uses shunt susceptances  $b_1, b_2, b_2, b_1$ . At center frequency, the spacings are

$$\begin{aligned}\phi_1 &= 90^\circ + \frac{1}{2} \{ \arctan(b_1/2) + \arctan(b_2/2) \} \\ \phi_2 &= 90^\circ + \arctan(b_2/2),\end{aligned}\quad (13)$$

in order to satisfy the synchronous tuning condition which requires that adjacent reference planes with real  $\Gamma$  be  $90^\circ$  apart at center frequency. If the  $b$ 's were constant, the incremental separations of the reference planes over a bandwidth  $W$  due to "Cause 1)" would be

$$\phi_1 W; \phi_2 W; \text{ and } \phi_1 W. \quad (14)$$

The change in magnitude of each  $b$  causes additional separations over the band  $W$  due to "Cause 2)" of

$$\begin{aligned}& \frac{1}{2} \left\{ \arctan\left(\frac{b_1}{2-W}\right) - \arctan\left(\frac{b_1}{2+W}\right) \right. \\ & \quad \left. + \arctan\left(\frac{b_2}{2-W}\right) - \arctan\left(\frac{b_2}{2+W}\right) \right\}, \\ & \arctan\left(\frac{b_2}{2-W}\right) - \arctan\left(\frac{b_2}{2+W}\right), \text{ and} \\ & \frac{1}{2} \left\{ \arctan\left(\frac{b_2}{2-W}\right) - \arctan\left(\frac{b_2}{2+W}\right) \right. \\ & \quad \left. + \arctan\left(\frac{b_1}{2-W}\right) - \arctan\left(\frac{b_1}{2+W}\right) \right\},\end{aligned}\quad (15)$$

respectively.

<sup>7</sup> S. Darlington, "Synthesis of reactance four-poles which produce prescribed insertion loss characteristics," *J. Math. and Phys.*, vol. 18, pp. 257-353; September, 1939.

<sup>8</sup> I.e., the filter is "synchronously tuned."



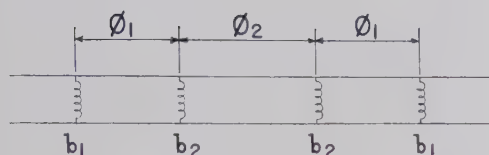


Fig. 7—Direct-coupled cavity filter using shunt inductances.  $\phi_1$ ,  $\phi_2$  are spacings at center frequency;  $b_1$ ,  $b_2$  are susceptances at center frequency.

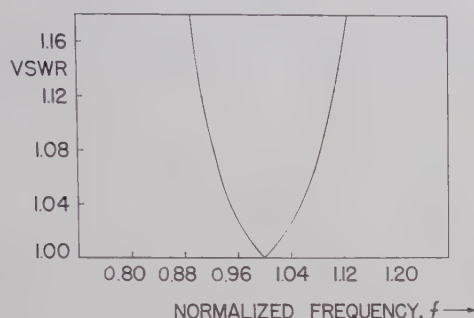


Fig. 8—VSWR against frequency of direct-coupled three-cavity filter designed by  $L$ - $C$  equivalent circuit (example 1).

Together, (14) and (15) give the total movement over the band  $W$ . When they are averaged and divided into  $(90W)^\circ$ , they also show how much the original quarter-wave transformer bandwidth has contracted. This may be used to predict the filter bandwidth.

This procedure can be applied to any number of sections or cavities, and to couplings other than shunt inductive elements, provided their frequency behavior is known.

Numerical examples will illustrate the working of this method. Excellent agreement was obtained between predicted and subsequently analyzed performance. The method of solution is essentially a trial-and-error procedure, in which a quarter-wave transformer has to be found which, after "distortion," meets the filter requirements.

## NUMERICAL EXAMPLES

### Specification and Description

A symmetrical direct-coupled cavity filter using inductive coupling posts is to be synthesized in coaxial line, to the following specifications:

number of cavities ( $n$ ) . . . . . 3,  
maximum VSWR . . . . . 1.1 approximately,  
bandwidth ( $W$ ) . . . . . 0.3 (= 30 per cent).

The filter structure is shown schematically in Fig. 7. At center frequency, the shunt susceptances are  $b_1$  and  $b_2$ , their reflection coefficients are  $\Gamma_1$  and  $\Gamma_2$ , and the spacings are  $\phi_1$  and  $\phi_2$ , as shown.

Two design methods are now presented, one by a lumped constant equivalent circuit, and one using the quarter-wave transformer prototype.

### Design by $L$ - $C$ Equivalent Circuit

Example 1: Cohn's design formulas<sup>5</sup> for  $n=3$ ,  $W=30$  per cent, and maximum VSWR = 1.143, yield

$$b_1 = 0.42849, \quad b_2 = 1.29085. \quad (16)$$

This corresponds to

$$\Gamma_1 = \frac{b_1}{\sqrt{4 + b_1^2}} = 0.20949, \quad \Gamma_2 = \frac{b_2}{\sqrt{4 + b_2^2}} = 0.54229, \quad (17)$$

and makes, by (13),

$$\phi_1 = 112.465^\circ, \quad \phi_2 = 122.837^\circ, \quad (18)$$

which is appreciably less than the near  $180^\circ$  spacings demanded by the approximation.<sup>5</sup> When this filter was analyzed, the frequency response curve shown in Fig. 8 was obtained. Instead of a Tchebycheff response with three zeros and two "hoops," there is only one zero and no hoop. To understand this failure of the  $L$ - $C$  equivalent circuit method, consider the quarter-wave transformer prototype corresponding to (17). Taking  $Z_0=1$ , this transformer has

$$\begin{aligned} Z_1 &= \frac{1 + \Gamma_1}{1 - \Gamma_1} = 1.4981, \\ Z_2 &= Z_1 \left( \frac{1 + \Gamma_2}{1 - \Gamma_2} \right) = 5.1657, \\ Z_3 &= R/Z_1 = 17.8120, \\ R &= Z_2^2 = 26.6844. \end{aligned} \quad (19)$$

From the tables,<sup>4</sup> we see that no transformer with  $R=26.6844$  has a  $Z_1$  less than 1.5295, which value occurs only for the maximally flat transformer. Therefore, we would indeed expect a frequency response like that obtained in Fig. 8.

### Design by Quarter-Wave Transformer Prototype

Example 2: For our first trial solution, we select a prototype transformer with  $R=25$  and (transformer) bandwidth of 45 per cent, for which the maximum VSWR is 1.06. From the tables<sup>4</sup> (with  $Z_0=1$ ), one obtains by interpolation

$$\begin{aligned} Z_1 &= 1.5955, \\ Z_2 &= 5.0000, \\ Z_3 &= 15.670, \\ R &= 25.000, \end{aligned} \quad (20)$$

yielding

$$\Gamma_1 = \frac{Z_1 - 1}{Z_1 + 1} = 0.22943, \quad \Gamma_2 = \frac{Z_2 - Z_1}{Z_2 + Z_1} = 0.51619, \quad (21)$$

and hence

$$\begin{aligned} b_1 &= \frac{2\Gamma_1}{\sqrt{1 - \Gamma_1^2}} = 0.47143, \\ b_2 &= \frac{2\Gamma_2}{\sqrt{1 - \Gamma_2^2}} = 1.2054. \end{aligned} \quad (22)$$



Also

$$\arctan(b_1/2) = 13.263^\circ, \quad \arctan(b_2/2) = 31.077^\circ, \quad (23)$$

and therefore

$$\phi_1 = 112.170^\circ, \quad \phi_2 = 121.077^\circ. \quad (24)$$

We now wish to predict the filter bandwidth  $W$ . The average  $\phi$  is

$$\frac{\phi_1 + \phi_2 + \phi_1}{3} = 115.139^\circ. \quad (25)$$

If the susceptances did not change with frequency and remained equal to their initial values  $b_1$ ,  $b_2$ , then the bandwidth would be reduced to  $(90/115.139) \times 45$  per cent = 35.2 per cent. The effect of the variation of the susceptances over the band is given by (15) and reduces this further. To calculate the quantities in (15), we must guess a value for  $W$ . Taking this as 0.3, (15) becomes

$$\frac{1}{2}\{15.500^\circ - 11.583^\circ + 35.355^\circ - 27.658^\circ\} = 5.807^\circ, \\ 35.355^\circ - 27.658^\circ = 7.697^\circ, \quad (26)$$

and again

$$5.807^\circ,$$

which have an average value of  $6.437^\circ$ . Since this is the incremental separation due to the change in the susceptances in a 30 per cent change in frequency about the center, the  $6.437^\circ$  increase is equivalent to an increase in the average line length of

$$6.437^\circ \div 0.3 = 21.46^\circ. \quad (27)$$

Moreover, it is clear that, although (27) was derived by assuming a 30 per cent bandwidth, it is a measure of the average rate of movement of the reference planes, and this average will not be rapidly affected by the exact length of the frequency interval used for averaging. Hence, the exact guessed value of  $W$  to obtain (27) is not critical.

We therefore anticipate, by (25) and (27), a reduction in bandwidth from the 45 per cent of the quarter-wave transformer to

$$\frac{90}{115.14 + 21.46} \times 45 \text{ per cent} = 29.7 \text{ per cent}. \quad (28)$$

The filter given by (22) and (23) was analyzed and its frequency response is given in Fig. 9. Its maximum VSWR is 1.03, and its bandwidth (for 1.03 VSWR) is 24 per cent, instead of 1.06 and 29.7 per cent, respectively, predicted from the quarter-wave transformer prototype of (20).

*Example 3:* It is seen from Fig. 9 that the bandwidth is still too small. To increase the bandwidth, one sees

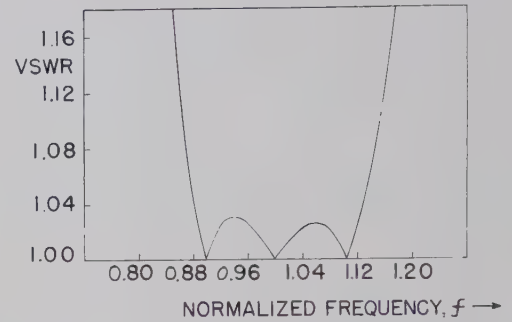


Fig. 9—VSWR against frequency of direct-coupled three-cavity filter designed from quarter-wave transformer prototype (example 2).

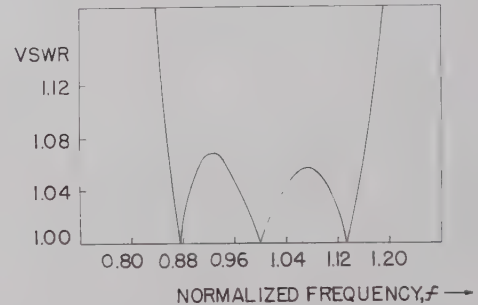


Fig. 10—VSWR against frequency of direct-coupled three-cavity filter designed from quarter-wave transformer prototype (example 3).

that from the transformer tables<sup>4</sup>  $b_1$  should be increased and  $b_2$  decreased. We try

$$b_1 = 0.50000, \quad b_2 = 1.2000. \quad (29)$$

This gives

$$\phi_1 = 112.500^\circ, \quad \phi_2 = 120.964^\circ, \quad (30)$$

and

$$\Gamma_1 = 0.24254, \quad \Gamma_2 = 0.51449, \quad (31)$$

so that the transformer prototype (with  $Z_0 = 1$ ) is

$$\begin{aligned} Z_1 &= 1.6404, \\ Z_2 &= 5.1159, \\ Z_3 &= 15.955, \\ R &= 26.172, \end{aligned} \quad (32)$$

which the tables show has a maximum VSWR of 1.10 and a (transformer) bandwidth of 52.8 per cent. The filter bandwidth  $W$  is again predicted as in the last example, and is expected to be 34.6 per cent. This filter was also analyzed and its frequency response is shown in Fig. 10. It is seen that the maximum VSWR is 1.07 instead of 1.10 as predicted; the bandwidth (for 1.07 VSWR) is 30.6 per cent instead of 34.6 per cent, as predicted (for 1.10 VSWR).

#### CONCLUDING REMARKS

It has been demonstrated that one can start with a quarter-wave transformer, which is a microwave circuit that can be synthesized to a given specification, and



"distort" it to obtain a direct coupled cavity filter with a predictable performance. Some examples were analyzed numerically, and the predicted performance was closely confirmed.

This method is usually tedious to synthesize a filter *ab initio*, but it is quite easy to use in reverse, *i.e.* to derive the quarter-wave transformer prototype from a direct coupled cavity filter which has already been designed by another method. This was found to lead to a quick and accurate evaluation of its performance. If this predicted performance turns out to be inadequate, the filter can then be redesigned as illustrated in this paper.

#### ACKNOWLEDGMENT

The author is very grateful for the help, always freely given, of Dr. W. H. Huggins, Dr. F. Hamburger, Jr., and Dr. C. F. Miller, of the Johns Hopkins University. Much of the numerical work was done by A. C. Robertson under the guidance of W. M. Etchison.

Most of the ideas for this paper originated during design work done at Westinghouse, and this investigation was made possible by the financial assistance of the Westinghouse Electric Corp.'s B. G. Lamme graduate scholarship during the academic year 1958-1959.

## Broad-Band Ridge Waveguide Ferrite Devices\*

E. S. GRIMES, JR.<sup>†</sup>, MEMBER, IRE, D. D. BARTHOLOMEW<sup>†</sup>, D. C. SCOTT<sup>†</sup>, MEMBER, IRE, AND  
S. C. SLOAN<sup>†</sup>, MEMBER, IRE

**Summary**—The design and development of a medium CW power level, 1.57:1 bandwidth, quadruply-ridged circular waveguide Faraday rotator and two high CW power, 2:1 bandwidth, double ridge rectangular waveguide isolators are discussed.

The rotator is designed in quadruply-ridged circular waveguide with a ferrite configuration somewhat different from that proposed by other investigators. It can be made to exhibit broadband rotation and large rotation per unit length of ferrite section, and may be used in most medium CW power level applications. Forty-five degree rotation is achieved over the 7.0-kMc to 11.0-kMc band.

The isolators operate from 2.0 kMc to 4.0 kMc in DR-37 waveguide and from 3.8 kMc to 7.6 kMc in D-34 waveguide respectively. The reverse to forward wave attenuation ratio exceeds 10.0 db to 1.0 db for both isolators.

#### INTRODUCTION

THE development of microwave components with operating bandwidths in excess of previously established maximums has been necessitated by the requirements of modern microwave systems. Perhaps the most widely used method for maintaining good performance characteristics of a microwave component over a large operating bandwidth is to reduce the variation of guide wavelength with frequency. The guide wavelength for any air-filled microwave transmission line is determined from the formula

$$\lambda_g = \frac{\lambda}{\sqrt{1 - (\lambda/\lambda_c)^2}},$$

where

$\lambda$  = operating wavelength

$\lambda_g$  = guide wavelength

$\lambda_c$  = cutoff wavelength.

Thus, for operating frequencies far above the cutoff frequency the variation in guide wavelength with frequency is greatly reduced. This condition can be brought about in circular and rectangular waveguides by using ridges protruding into the guide, thus lowering the dominant mode cutoff frequency without appreciably affecting the next higher mode cutoff frequency.<sup>1,2</sup> There, the resultant increase in bandwidth of the transmission line allows operation far above cutoff.

It is the purpose of this paper to present design information on a quadruply-ridged circular waveguide Faraday rotator and two double-ridge rectangular waveguide isolators.

#### FARADAY ROTATOR

A number of techniques have been proposed for maintaining rotation constant with frequency. In terms of maximum bandwidth the most successful ones known to the authors have utilized quadruply-ridged wave-

\* Received by the IRE, November 4, 1959; revised manuscript received, May 10, 1960. This paper was presented at the PGMTT National Symposium, Cambridge Mass., June 1-3, 1959. The work was supported by the U. S. Air Force Wright Air Dev. Center under Contract No. AF30(600)35477.

<sup>†</sup> Sperry Microwave Electronics Co., Div. of Sperry Rand Co., Clearwater, Fla.

<sup>1</sup> S. B. Cohn, "Properties of ridge waveguide," PROC. IRE, vol. 35, pp. 783-788; August, 1947.

<sup>2</sup> S. A. Schelkunoff, "Electromagnetic Waves," D. Van Nostrand Co., Inc., New York, N. Y., pp. 392-395; 1943.



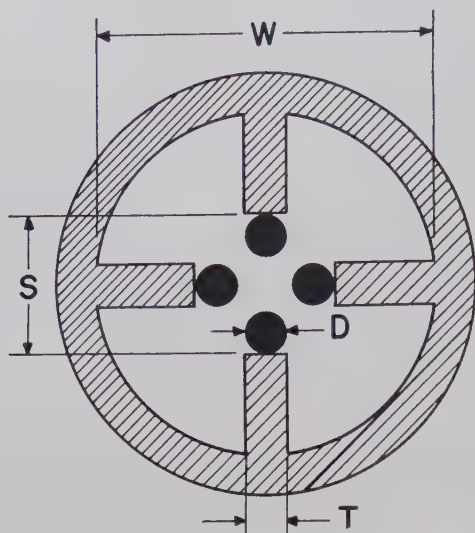


Fig. 1—General quadruply-ridged rotator structure.  $W$ =circular guide inside diameter,  $S$ =ridge separation,  $T$ =ridge thickness,  $D$ =ferrite diameter.

guide.<sup>3-5</sup> The general quadruply-ridged rotator described in this paper is shown in Fig. 1. It has a ferrite configuration somewhat different from that proposed by other investigators, in that the usual axially located ferrite rod is replaced by four ferrite rods (or slabs) mounted on the ridge edges. A rotation of forty-five degrees is attained over the 7.0-kMc to 11.0-kMc band without the use of "stagger-tuned" sections.

The variation of rotation with frequency due to changes in ridge separation ( $S$ ) and ferrite diameter ( $D$ ) has been measured. During the measurement, the ferrite type and length ( $L$ ), ridge thickness ( $T$ ), circular waveguide diameter ( $W$ ), and axially applied magnetic field ( $H_a$ ) remained constant. The measurement apparatus was similar to that used by Rizzi.<sup>6</sup> Linear ridge tapers were used with a taper length of 1.50 inches.

The usual considerations were made in establishing the ferrite material. For maximum rotation the highest saturation magnetization possible was chosen subject to the requirement of minimum low field loss. Low dielectric loss tangent and reasonably high Curie temperature were also desired. This suggested the choice of a magnesium manganese ferrite with a saturation magnetization of about 2000 gauss. The rotator configurations to be discussed can operate down to zero field with a low insertion loss. However, the data to be presented were taken with the ferrite in a magnetically saturated condition. To design a fixed low loss rotator, the saturation magnetization could exceed 2000 gauss since operation at zero field would not be required. This

would, of course, result in more rotation per unit length than in the configurations presented in this paper.

The effects of ridge separation and ferrite rod diameter on rotation as a function of frequency are shown in the curves of Fig. 2. The insertion loss for all configurations was less than 1.0 db for applied magnetic fields from 0 to 120 gauss. The small fluctuations in rotation are probably caused by mismatches in the rotator structure. Utilizing these basic design curves, it was found empirically that by increasing the ridge taper length to improve the impedance match, and optimizing the ferrite length and diameter, the desired rotation was obtained. The resultant performance, after modifying the structure as outlined, is shown in Fig. 3.

Since the ferrite is located on a metallic ridge, the heat generated due to CW power is dissipated more easily than in most other rotator structures. Furthermore, it has been found that the ferrite rods can be replaced by slabs of equivalent cross-sectional area. Thus, the ferrite can make good thermal contact on the ridge edge.

Although the use of dielectrics was not explored in conjunction with the configuration of Fig. 3, it is believed that broadband forty-five degree rotation over bandwidths in excess of 1.57:1 might be achieved by using them.

The configuration just described may be incorporated in most medium CW power level microwave components using the Faraday rotation principle.

#### DOUBLE-RIDGE ISOLATORS

In the design of high CW power isolators it is desirable to place the ferrite against a guide wall so as to assure efficient heat conduction. Such a location also provides a simple means of fixing the ferrite in place. Unfortunately, in air-filled double-ridge waveguide propagating the dominant mode, measurements indicate that the clearly defined regions of circularly polarized magnetic fields required for maximum nonreciprocity do not exist adjacent to a guide wall. Rather, there appears to be a curvature of the circular polarization surfaces and a weak component of the microwave magnetic field at the points where these planes intersect the waveguide walls.

A technique is described herein that allows the ferrite to be positioned on the waveguide ridges where the important advantages of high microwave field intensity, smaller biasing magnet gap (with the attendant reduction in magnet size and weight), efficient heat conduction, and ease of assembly are realized. The general double-ridge waveguide isolator structure is shown in Fig. 4. As indicated, the technique involves positioning a low loss dielectric slab in the area between the ridges extending from one ridge surface to the other. It is then possible to attach the ferrite to the flat areas of the ridges adjacent to the dielectric-air interface and achieve good nonreciprocal attenuation characteristics. This technique, originally proposed by Ahrens at Sperry and subsequently investigated by Swern and

<sup>3</sup> M. L. Kales, "Propagation of Fields Through Ferrite Loaded Guides," *Proc. Symp. Modern Advances of Microwave Techniques*, Poly. Inst. of Brooklyn, Brooklyn, N. Y., pp. 215-228; 1955.

<sup>4</sup> P. H. Vartanian, J. L. Melchor and W. P. Ayers, "Broadbanding Ferrite Microwave Isolators," 1956 IRE CONVENTION RECORD, vol. 4, pt. 5, pp. 79-83.

<sup>5</sup> H. N. Chait and N. G. Sakiotis, "Broad-band ferrite rotators using quadruply-ridged circular waveguide," IRE TRANS. ON MICROWAVE THEORY AND TECHNIQUES, vol. MTT-7, pp. 38-41; January, 1959.

<sup>6</sup> P. A. Rizzi, "High-power ferrite circulators," IRE TRANS. ON MICROWAVE THEORY AND TECHNIQUES, vol. MTT-5, pp. 230-237; October, 1957.



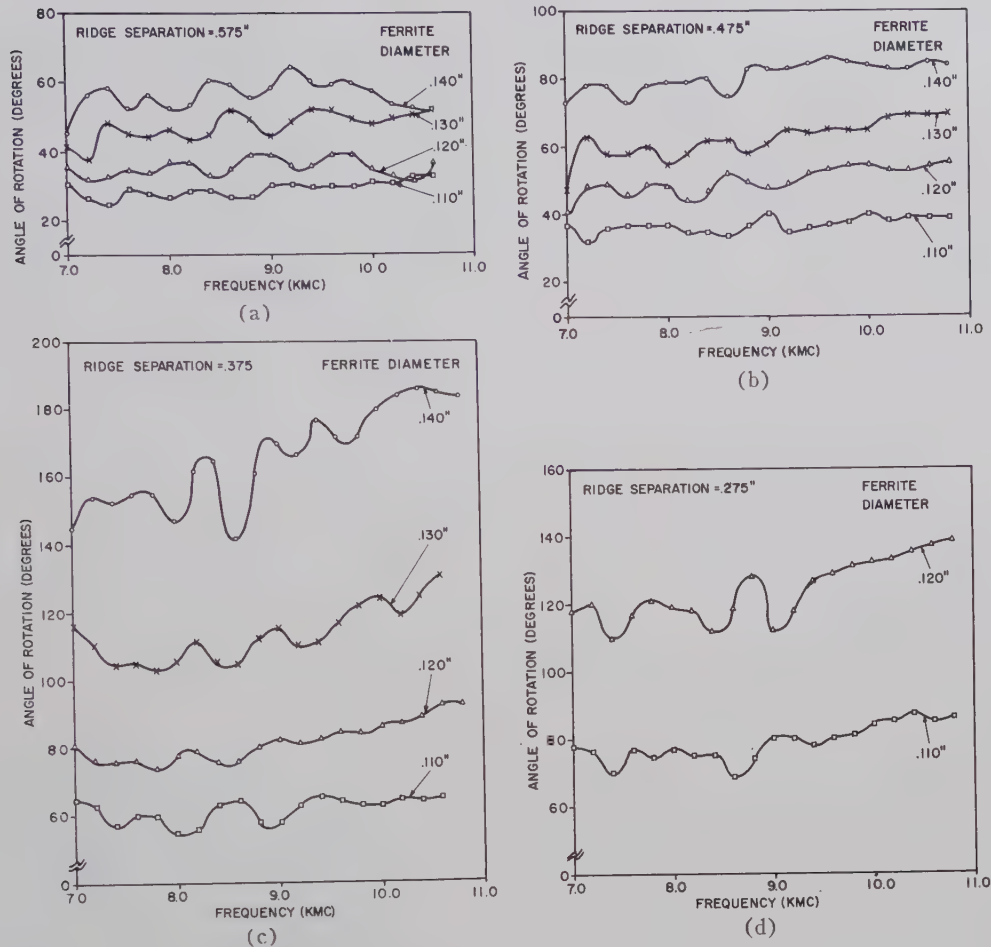


Fig. 2—Angle of rotation vs frequency. Magnesium manganese ferrite,  $4\pi M_s = 2175$  gauss,  $L = 3.00$  inches,  $H_a = 120$  gauss,  $W = 1.125$  inches,  $T = 0.125$  inch. (a)  $S = 0.575$  inch. (b)  $S = 0.475$  inch. (c)  $S = 0.375$  inch. (d)  $S = 0.275$  inch.

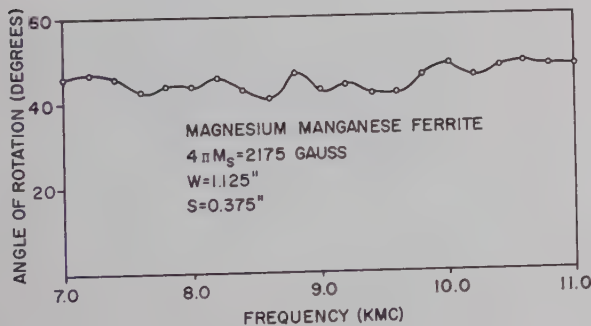


Fig. 3—Angle of rotation vs frequency for final rod configuration.

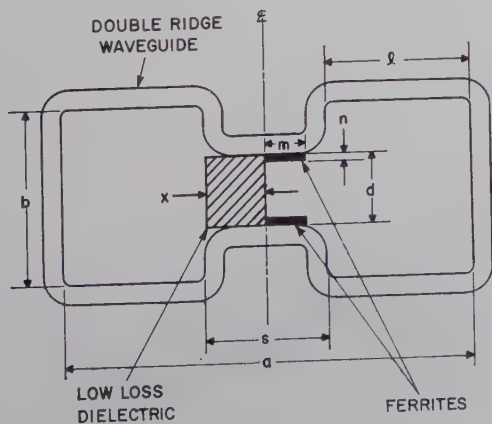


Fig. 4—General double-ridge waveguide isolator structure.

Fleri,<sup>7</sup> is applied in this paper to the design of two high power, 2:1 bandwidth double ridge waveguide isolators in S-band and C-band. Dielectric loading techniques<sup>8-10</sup> in other transmission lines have been applied successfully in increasing the bandwidth of various devices.

The effects of dielectric constant and dielectric slab width on attenuation ratio were investigated during development. For best results a dielectric constant of about ten (alumina ceramic) and a width of approximately  $s/2$  were established. The variation in guide wavelength with frequency is reduced due to the presence of the dielectric.<sup>11</sup> However, the variation in wavelength encountered at the lower operating frequencies is more pronounced in DR-37 and D-34 waveguide due to closer proximity to cutoff.

<sup>7</sup> L. Swern and D. Fleri, "Final Engineering Report Broadband Ferrite Devices Study Program," research sponsored by Air Force Cambridge Res. Center, Air Res. and Dev. Command, Cambridge, Mass., contract no. AF19(604)2248, Sperry rept. no. 7210-13027, May, 1958. AFCRC-TR-58-138 ASTIA document no. AD-152392.

<sup>8</sup> E. A. Ohm, "A broad-band microwave circulator," IRE TRANS. ON MICROWAVE THEORY AND TECHNIQUES, vol. MTT-4, pp. 210-217; October, 1956.

<sup>9</sup> B. J. Duncan, L. Swern, K. Tomiyasu and J. Hannwacker, "Design considerations for broad-band ferrite coaxial line isolators," Proc. IRE, vol. 45, pp. 483-490; April, 1957.

<sup>10</sup> P. H. Vartanian, W. P. Ayres, and A. L. Helgesson, "Propagation in dielectric slab loaded rectangular waveguide," IRE TRANS. ON MICROWAVE THEORY AND TECHNIQUES, vol. MTT-6, pp. 215-222; April, 1958.

<sup>11</sup> D. J. Sullivan and D. A. Parkes, "Stepped transformers for partially filled transmission lines," IRE TRANS. ON MICROWAVE THEORY AND TECHNIQUES, vol. MTT-8, pp. 212-217; March, 1960.

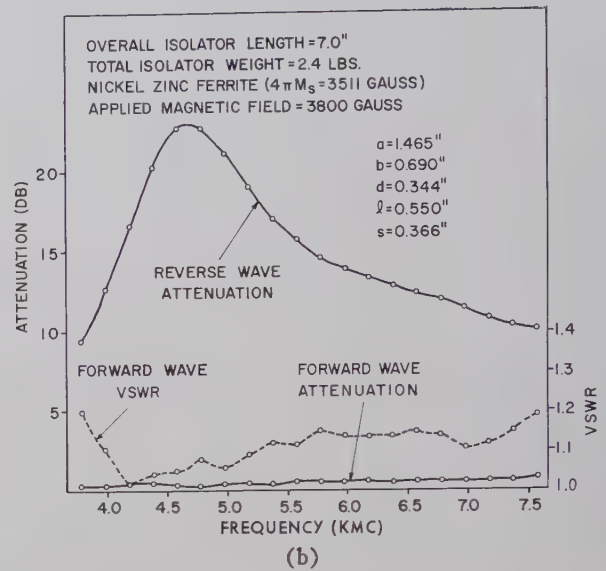
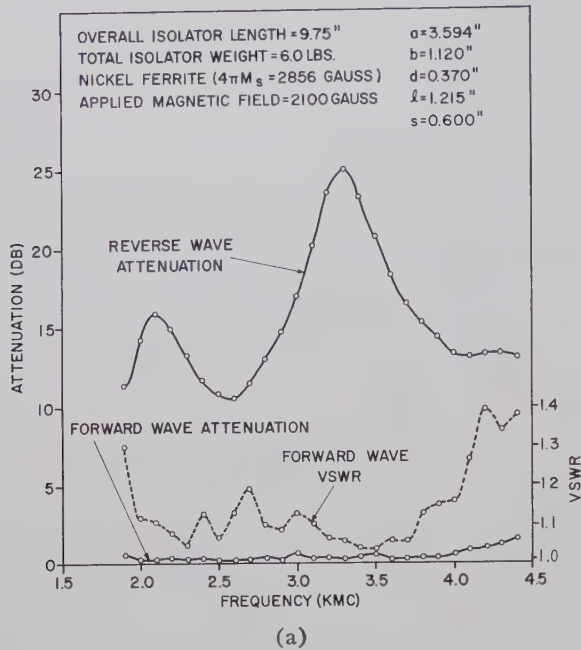


Fig. 5—Performance curves of isolators in (a) DR-37 and (b) D-34 waveguide.

The ferrite types were chosen to have a high  $4\pi M_s$  for maximum activity, consistent with low field loss considerations, high Curie temperature and operation over the required bandwidth. The ferrite aspect ratio ( $m/n$ ) was chosen to be as large as possible for maximum heat dissipation area consistent with minimum forward wave attenuation.

The performance characteristics for the DR-37 and D-34 isolators at room temperature and low power are shown in Figs. 5(a) and 5(b) respectively. An increase in VSWR is indicated for both units at the lower operating frequencies due to proximity to cutoff and the dielectric transition mismatch. It is fully anticipated that, with additional development, the operating bandwidth of the DR-37 isolator can be made to cover the 2.0-kMc to 5.0-kMc frequency range. High CW power measurements on both isolators at room temperature and atmospheric pressure indicate satisfactory operation up to 200 watts. At low power, both units maintain good performance characteristics over the ambient temperature range from  $-55^\circ\text{C}$  to  $+125^\circ\text{C}$ . Photographs of the operative liquid cooled isolators are shown in Figs. 6(a) and 6(b).

The nonreciprocal structure described here may also be applied to other ferrite devices designed in double ridge waveguide.

#### CONCLUSIONS

It has been shown that a medium CW power level Faraday rotator with ferrite rods or slabs on the ridge edges can be made to exhibit forty-five degree rotation over a 1.57:1 bandwidth. Also the design of 2:1 bandwidth, high CW power large attenuation ratio isolators in DR-37 and D-34 double ridge waveguide has been

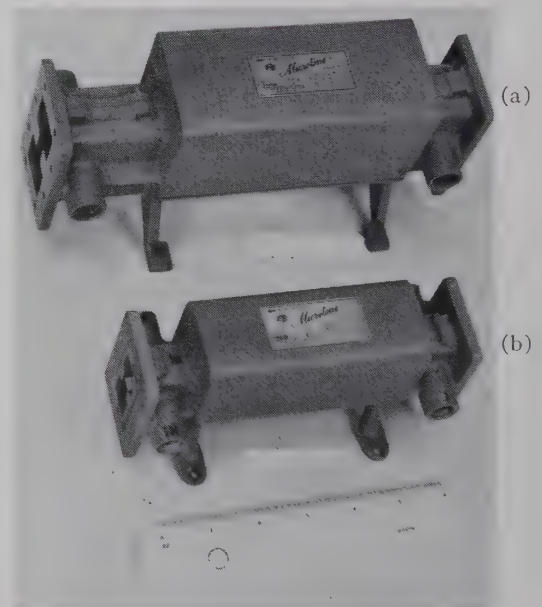


Fig. 6—Typical isolator in (a) DR-37 and (b) D-34 waveguide.

proven feasible by the judicious use of dielectric loading. The inherent simplicity of these rotator and isolator structures lend themselves to straight-forward assembly procedures and are rugged enough to withstand reasonable shock and vibration while providing excellent heat transfer properties.

#### ACKNOWLEDGMENT

The authors are grateful to B. J. Duncan for his suggestions during the course of this work and to Dr. J. E. Pippin for his advice during the preparation of this paper.



# Radiation Patterns of a Noise-Excited Thin Slot\*

NICHOLAS GEORGE†, MEMBER, IRE

**Summary**—Theoretical and experimental radiation patterns are given in spectral form for the thermal radiation from a cylindrical discharge column which is adjacent to a long thin slot in a metallic plane. A spatial distribution is predicted which exhibits interference minima and maxima when the length of the slot and the wavelength of the emission are the same order of magnitude. The analysis is based on Maxwell's equations and the Leontovich-Rytov distributed source generalization of Nyquist's noise formula.

Fraunhofer pattern measurements are presented in which an argon source is used to excite slots of  $7.3\pi$  and  $9.5\pi$  radians in length. Data are also presented to show the effects of variations in the pressure and the dc current of the discharge. The pattern measuring apparatus is a Dicke radiometer, having the following characteristics: frequency 9200 Mc, bandwidth to the detector 16 mc, modulation frequency 1000 cps, and residual noise level 0.3 rms°K.

An interference phenomenon is predicted by the theory and demonstrated by an experiment, even though the source excitation is spatially distributed and essentially uncorrelated in time and in space. The patterns are not even approximately Lambertian, *e.g.*, a thin slot of  $9.5\pi$  radians exhibits a pattern having nine relative maxima in  $180^\circ$ , with the maximum emission at  $63^\circ$  from the normal.

## I. INTRODUCTION

THE chaotic motion of the electrons in a plasma or in a metal gives rise to electromagnetic radiation over a wide spectrum which includes the microwave frequencies. The terminal characteristics of such noise sources have been studied both theoretically [1], [2] and experimentally [3], [4]. On the other hand, while the distributed nature of the noise arising from such sources has been recognized from the time of the earliest work in the theory of fluctuations, it had received comparatively little attention until the derivation by Leontovich and Rytov [5] of the formula for the correlation function of the noise electric field in a lossy medium, (1) below. In this paper, attention is directed to a related problem, an analysis and an experiment, in which the distributed nature of the noise plays a dominant role. Specifically, the problem is to determine the far-zone radiation pattern for a long thin slot which is excited by a distributed noise source.

In the analysis which follows it is necessary to use the distributed source description derived by Leontovich and Rytov. Their formula for the correlation function of the  $x$  component of the effective noise electric field in a conductive medium is given by

$$\langle E_x(\mathbf{r}, t) E_x^*(\mathbf{r} - \mathbf{r}_0, t - t_0) \rangle = \frac{2\bar{\epsilon}}{\sigma} \delta(\mathbf{r}_0) \delta(t_0). \quad (1)$$

If a generalized Ohm's law holds for the medium, *i.e.*,

if  $j(\mathbf{r}) = \sigma \mathbf{E}(\mathbf{r})$ , then an equivalent expression for the correlation function of the  $x$  component of the current density is given by

$$\langle j_x(\mathbf{r}, t) j_x^*(\mathbf{r} - \mathbf{r}_0, t - t_0) \rangle = 2\bar{\epsilon} \sigma \delta(\mathbf{r}_0) \delta(t_0). \quad (2)$$

$E_x(\mathbf{r}, t)$  and  $j_x(\mathbf{r}, t)$  are the  $x$  components of the source electric field and the current density, respectively;  $\delta(\mathbf{r})$  is Dirac's delta function;  $\sigma$  is the conductivity; and  $\bar{\epsilon}$  is the mean energy per degree of freedom given by Planck as

$$\bar{\epsilon} = \frac{hf}{e^{hf/kT} - 1}, \quad (3)$$

where  $f$  is the frequency,  $T$  is the absolute temperature,  $h$  is Planck's constant, and  $k$  is the Boltzmann constant.

The angular parentheses,  $\langle \rangle$ , are used throughout this paper to denote an ensemble average. A second notational convenience, adopted herein, is that time dependence is always indicated explicitly while frequency dependence is not. Therefore,  $E(x, y)$  may mean  $E(x, y, \omega)$ , but it will never mean  $E(x, y, t)$ .

An important result in spectral analysis is quoted for later use. Let  $f(x, t)$  be a sample function of a stationary random process. It can be shown that the two-dimensional correlation function, and the mixed spectral density and correlation function, satisfy the following Fourier transform relationship.

$$\begin{aligned} \int_{-\infty}^{\infty} \langle f(x_1, t) f^*(x_2, t - t_0) \rangle e^{-i\omega t_0} dt_0 \\ = \lim_{2T \rightarrow \infty} \left\langle \frac{F(x_1, \omega) F^*(x_2, \omega)}{2T} \right\rangle \end{aligned} \quad (4)$$

in which

$$F(x, \omega) = \int_{-T}^T f(x, t) e^{-i\omega t} dt.$$

## II. THEORETICAL RADIATION PATTERNS

Consider a metallic plate in the  $y=0$  plane with a long thin  $z$ -oriented aperture of dimensions  $(a, b)$  where  $a \gg b$  (Fig. 1). The aperture is illuminated or excited by a distributed noise source that generates electromagnetic energy which is incoherent spatially and timewise, *e.g.*, a closely-spaced hot wire or a plasma column (Section III). An approximate analysis for the resultant aperture distribution is made in the following section. The effects of radiation losses are neglected; and furthermore, aside from the generation of the noise, the influence of the noise medium of contrasting dielectric constant and

\* Received by the PGM-TT, January 28, 1960; revised manuscript received, May 16, 1960.

† Calif. Inst. Tech., Pasadena, Calif. Formerly with Engrg. Div., Hughes Aircraft Co., Culver City, Calif.

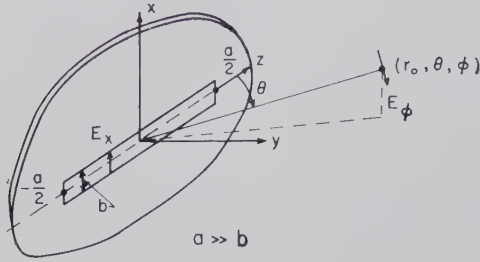


Fig. 1—Coordinates for the thin slot.

conductivity is assumed calculable, by allowing for a perturbation in the propagation constant for the region surrounding the slot.

#### A. Approximate Aperture Illumination for the Thin Slot

A simple transmission line model is used below in order to obtain an approximate expression for the resultant electric field, which is induced in the aperture by the distributed noise source. For this transmission line model, it is convenient to express the noise excitation in terms of a distributed source current that is induced in the metallic plane by the rapidly moving plasma electrons (Fig. 2). An approximate value for this current is obtained in the following manner. Let the noise source, rapidly moving plasma electrons, fill the half-space for which  $y < 0$ , and suppose that the plate at  $y = 0$  is not slotted. The moving electrons induce eddy currents; but over the range of frequencies for which the plasma is opaque, only those electrons close to the plate are effective in inducing these currents. It is assumed that the characteristic depth is the absorption skin depth of the plasma,  $\delta$ . Let  $I_s(x, z, \omega)$  be the  $x$  component of the induced eddy current measured in units of current per unit frequency interval per unit length in the  $z$  direction and let  $I_s(z, \omega)$  be the  $x$  component of this surface current averaged over a length  $b$  which corresponds to the narrow dimension of the slot, i.e.,

$$I_s(z, \omega) = \frac{1}{b} \int_{-b/2}^{b/2} I_s(x, z, \omega) dx.$$

This surface current can be expressed in terms of the  $x$  component of the noise current density,  $j_x(x, y, z, \omega)$ , by

$$I_s(z, \omega) \approx \frac{1}{b} \int_{-\delta}^0 \int_{-b/2}^{b/2} j_x(x, y, z, \omega) dx dy, \quad (5)$$

where  $j_x$  is measured in units of current per unit frequency interval per unit area in the  $y$ - $z$  plane. The integrations are required in order to take account of the spatial incoherence of the noise currents. Eqs. (2), (4), (5) are combined to give the following mixed spectral density and correlation function for the  $x$  component of the source current in the metal plate.

$$\lim_{2T \rightarrow \infty} \left\langle \frac{I_s(z_1, \omega) I_s^*(z_2, \omega)}{2T} \right\rangle = \frac{2\epsilon\sigma\delta}{b} \delta(z_1 - z_2). \quad (6)$$

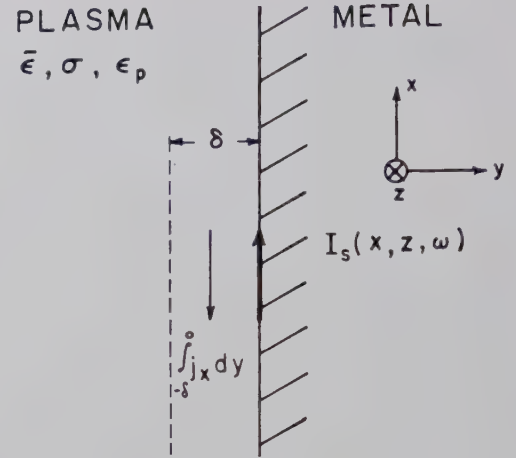


Fig. 2—Induced current approximation.

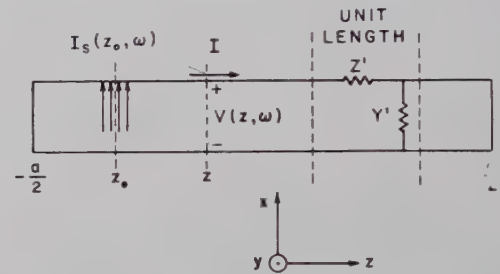


Fig. 3—Transmission-line model for the aperture distribution of the electric field.

Now with a slotted plane, the influence of the source current,  $I_s$ , in the region from  $z$  to  $z + dz$  is felt everywhere along the gap. Consider the principal mode analysis in which the slot is viewed as a transmission line with the source field propagating mainly along the gap and with a standing wave being established by the reflections at  $z = \pm a/2$  (Fig. 3). The voltage per unit frequency interval,  $V$ , and the current per unit frequency interval,  $I$ , are related in the following manner by the transmission line equations:

$$\frac{\partial V}{\partial z} = -Z'I \quad (7)$$

and

$$\frac{\partial I}{\partial z} = -Y'V + I_s(z, \omega), \quad (8)$$

where the series impedance per unit length,  $Z'$ , and the shunt admittance per unit length,  $Y'$ , are related to the complex propagation factor,  $\beta_c = \beta - i\alpha$ , by

$$\beta_c^2 = -Y'Z' \quad (9)$$

and where the potential,  $V$ , is defined by

$$V = \int_{-b/2}^{b/2} E_x(x, 0, z, \omega) dx.$$



Taking  $\partial/\partial z$  of (7) and substituting from (8), (9) give the wave equation for  $V$ ,

$$\frac{\partial^2 V}{\partial z^2} + \beta_c^2 V = -Z' I_s(z, \omega). \quad (10)$$

The general solution of (10), subject to the boundary condition that  $V(\pm a/2, \omega) = 0$ , is readily obtained by standard methods; and the result is given by

$$V(z, \omega) = \int_{-a/2}^{+a/2} Z' I_s(z_0, \omega) \frac{1}{2\beta_c} \left[ \frac{\cos \beta_c(z + z_0) - \cos \beta_c(a - |z - z_0|)}{\sin \beta_c a} \right] dz_0 \quad (11)$$

where an alternative special form must be written for the cases in which  $\beta_c a = \pi, 2\pi, 3\pi, \dots$

In the final result, an expression containing  $Z'$  is not convenient. This series impedance per unit length can be eliminated in favor of a more fundamental impedance parameter by means of an approximate relation developed in (14) below. Using the form of Babinet's principle as generalized for vector fields by Booker [6], [7], one can readily establish the following relationship between  $Z'$ ,  $Y'$  for a slot and the corresponding  $Z''$ ,  $Y''$  for the complementary electric dipole, *i.e.*, a thin metallic strip of cross section  $a$  by  $b$ .

$$\frac{Z'}{Y''} = \frac{\eta^2}{2} \quad \text{and} \quad \frac{Y'}{Z''} = \frac{2}{\eta^2} \quad (12)$$

where  $\eta$  is the characteristic impedance of the medium which surrounds the antenna. Then, using the transmission line model for the *metallic* dipole and expressing the input impedance of a center-driven antenna in terms of an open-circuited line of length  $a/2$ , one obtains

$$Y'' = \frac{\beta_c \cot \frac{\beta_c a}{2}}{z_{in}}, \quad (13)$$

in which  $z_{in}$  is the input impedance of the center-driven *metallic* dipole of length  $a$ . Strictly, the admittance per unit length varies along the length of the antenna; hence, (13) should be regarded as a defining equation for an averaged admittance to be used with the transmission line model.<sup>1</sup> Combining (12) and (13), one obtains the final expression for the  $Z'$  of the slot, *i.e.*,

$$Z' = \frac{\eta^2 \beta_c \cot \frac{\beta_c a}{2}}{2z_{in}} \quad (14)$$

<sup>1</sup> The result in (13) can also be deduced in another, perhaps more fundamental, way from (19), (24), (25) of Weber [8].

Elimination of  $Z'$  in (11) by (14) gives the following result for the aperture illumination:

$$V(z, \omega) = \frac{\eta^2}{4z_{in}} \int_{-a/2}^{a/2} I_s(z_0, \omega) \left[ \frac{\cos \beta_c(z + z_0) - \cos \beta_c(a - |z - z_0|)}{1 - \cos \beta_c a} \right] dz_0. \quad (15)$$

### B. Radiation in the Fraunhofer Region

The approximate tangential electric field over the  $y=0$  plane is now determined. The specification of the tangential electric field over this plane together with the radiation condition for the field as  $r_0 \rightarrow \infty$  are sufficient to uniquely determine the radiation field. The radiation field is conveniently expressed in terms of the Fourier integral analog of (1-14.19) of Smythe [9]. This formula gives the exact diffracted vector potential,  $\mathbf{A}$ , in terms of the aperture distribution for an arbitrary aperture. Differentiating, since  $\mathbf{E} = -\partial \mathbf{A} / \partial t$ , suppressing the  $e^{i\omega t}$  factor, dropping the near-zone term, and making the usual far-zone approximation in the phase term, *i.e.*,  $r \approx r_0 - z_1 \cos \theta$ , one can reduce (1-14.19) to the following form:

$$E_\phi(r_0, \theta, \phi, \omega) = \frac{-i\beta_0 \sin \theta e^{-i\beta_0 r_0}}{2\pi r_0} \int_{-a/2}^{a/2} V(z, \omega) e^{i\beta_0 z \cos \theta} dz, \quad (16)$$

in which the coordinates  $(r_0, \theta, \phi)$  are the radius, the polar angle, and the azimuthal angle measured in the  $x$ - $y$  plane from the  $x$  axis. (See Fig. 1.)

In the far-zone, the power radiated through a solid angle  $d\Omega$  is given by Poynting's theorem as the product  $[r_0 E_\phi(r_0, \theta, \phi, t)]^2 d\Omega / \eta$ . From this, it follows that in spectral form, the average power radiated through a solid angle  $d\Omega$  in the frequency interval  $df$  is given by

$$P_{f\Omega} df d\Omega = \lim_{2T \rightarrow \infty} \frac{2r_0^2}{\eta} \left\langle \frac{E_\phi(r_0, \theta, \phi, \omega) E_\phi^*(r_0, \theta, \phi, \omega)}{2T} \right\rangle df d\Omega. \quad (17)$$

Arbitrarily, the power through a unit solid angle per unit frequency interval,  $P_{f\Omega}$ , is defined above on the basis of a one-sided frequency interval, *i.e.*, the total average power per solid angle is given by  $\int_0^\infty P_{f\Omega} df$ . Substitution of (15), (16) into (17) gives the following integral form for the radiation pattern of the slot:

$$P_{f\Omega} = \frac{\eta}{8\pi^2} \left[ \frac{\eta |\beta_c| \sin \theta}{|z_{in}| \beta_0} \right]^2 \int_{-a/2}^{a/2} \int_{-a/2}^{a/2} \int_{-a/2}^{a/2} \int_{-a/2}^{a/2} I_s(z_0, \omega) I_s^*(z_1, \omega) \times \lim_{T \rightarrow \infty} \left\langle \frac{1}{2T} \right\rangle \times \left[ \frac{\cos \beta_c(z_2 + z_0) - \cos \beta_c(a - |z_2 - z_0|)}{2\beta_c(1 - \cos \beta_c a)} \right] \times \left[ \frac{\cos \beta_c(z_3 + z_1) - \cos \beta_c(a - |z_3 - z_1|)}{2\beta_c(1 - \cos \beta_c a)} \right]^* \times e^{i\beta_0(z_2 - z_3) \cos \theta} \beta_0^4 dz_0 dz_1 dz_2 dz_3. \quad (18)$$

### C. Radiation Pattern for the Delta-Correlated Source

Eq. (18) is integrated directly with respect to the variables  $z_2$  and  $z_3$ . Then, (6) is substituted for the source function, and the expression is integrated with respect to  $z_0$  and  $z_1$ . These integrations lead in a tedious but straightforward way to the intermediate form given below.

$$P_{f\Omega} = \frac{\eta \bar{\epsilon} \sigma \delta}{4\pi^2 b} \left[ \frac{\eta |\beta_c|}{|z_{in}| \beta_0} \right]^2 \frac{4\beta_0^4 \sin^2 \theta}{|1 - \cos \beta_c a|^2 |\beta_c^2 - (\beta_0 \cos \theta)^2|^2} K_1, \quad (19)$$

in which

$$K_1 = a \left| \sin \beta_c \frac{a}{2} \cos \beta_c \frac{a}{2} \right|^2 + \frac{\sinh \alpha a}{2\alpha} \left[ \left| \sin \beta_c \frac{a}{2} \right|^2 \cos^2 \left( \beta_0 \frac{a}{2} \cos \theta \right) + \left| \cos \beta_c \frac{a}{2} \right|^2 \sin^2 \left( \beta_0 \frac{a}{2} \cos \theta \right) \right] + \frac{\sin \beta a}{2\beta} \left[ \left| \sin \beta_c \frac{a}{2} \right|^2 \cos^2 \left( \beta_0 \frac{a}{2} \cos \theta \right) - \left| \cos \beta_c \frac{a}{2} \right|^2 \sin^2 \left( \beta_0 \frac{a}{2} \cos \theta \right) \right] + \operatorname{Re} \frac{\beta_c^* \sin \beta_c a}{\beta_c^{*2} - (\beta_0 \cos \theta)^2} [\cos \beta_c^* a - \cos (\beta_0 a \cos \theta)].$$

Eq. (19) is not in a convenient form for computation. A more convenient form is obtained by introducing a  $(4\beta_0)$  portion of the coefficient into the central bracket, replacing  $\beta_0/\eta$  by  $\omega\epsilon_0$ , and eliminating  $\beta_c$  in favor of  $\alpha, \beta$ . Finally, after considerable manipulation, the following expression is obtained for the one-sided spectral intensity of the power which is radiated per unit frequency per unit solid angle:

$$P_{f\Omega} = \frac{\sigma \delta \bar{\epsilon} \eta^2 (\rho^2 + \gamma^2) (\sin \theta)^2 K_2}{4\pi^2 \omega \epsilon_0 b |z_{in}|^2 [\cosh \alpha a - \cos \beta a]^2 [(\gamma^2 - \rho^2 - \cos^2 \theta)^2 + 4(\gamma \rho)^2]} \quad (20)$$

in which

$$K_2 = \beta_0 a \left\{ \frac{\sinh \alpha a}{\alpha a} [\cosh \alpha a - \cos (\beta_0 a \cos \theta) \cos \beta a] + \frac{1}{2} \cosh 2\alpha a - \frac{1}{2} \cos 2\beta a \right\} + \frac{\beta_0 \sin \beta a}{\beta} [-\cos \beta a + \cos (\beta_0 a \cos \theta) \cosh \alpha a] + \frac{4}{(\gamma^2 - \rho^2 - \cos^2 \theta)^2 + 4(\gamma \rho)^2} \{ \gamma [\gamma^2 + \rho^2 - \cos^2 \theta] \times \sin \beta a [\cos \beta a - \cos (\beta_0 a \cos \theta) \cosh \alpha a] - \rho [\gamma^2 + \rho^2 + \cos^2 \theta] \sinh \alpha a \times [\cosh \alpha a - \cos (\beta_0 a \cos \theta) \cos \beta a] \}$$

and where

$$\begin{aligned} a &= \text{length of the slot (Fig. 1),} \\ b &= \text{width of the slot, } b \ll \lambda, \\ \sigma \delta &= \text{conductivity, skin-depth product for the plasma,} \\ i\beta_c &= i\beta + \alpha, \\ \gamma &= \beta/\beta_0, \\ \rho &= \alpha/\beta_0, \\ z_{in} &= \text{input impedance of center-driven complementary metallic dipole [7],} \\ \eta &= (\mu_0/\epsilon_0)^{1/2} \cong 377 \text{ ohms,} \\ \omega &= 2\pi f. \end{aligned}$$

The above equation represents a first order approximation to the radiation pattern for a thin slot which is excited incoherently both spatially and timewise. This analysis is similar to that of Levin and Rytov [10] for the thermal radiation pattern of a thin linear antenna. However, even allowing for the complementary aspect, there are two differences. First, the solution (20) appears to apply for a greater range of lengths due to the incorporation of  $z_{in}$  [11]. Secondly, a complex wave number is assumed for the propagation along the slot in order to account for loss and phase retardation due to the noise source. Setting  $\alpha=0$  and  $\beta=\beta_0$  in (20), one finds that the *spatial variation* agrees with that obtained by Levin and Rytov.

### D. Selected Cases

Radiation patterns are plotted for several different slot lengths when there is no loss and when the wave numbers are equal (Fig. 4). The graphs are of  $P_{f\Omega}$  (from (20) with  $\alpha=0, \beta=\beta_0$ ) normalized to  $\sigma \delta \bar{\epsilon} \eta^2 / (4\pi^2 \omega \epsilon_0 b |z_{in}|^2)$  and plotted vs the angle from the normal,  $\pi/2 - \theta$ , for values of the length  $\beta a/\pi = 2.5, 4.5, 6.5$ , and  $8.5$ .

Radiation patterns are also plotted for a variable loss factor but with a fixed length and with no phase retardation (Fig. 5). The graphs are of  $P_{f\Omega}$  (from (20) with

$\beta=\beta_0, \beta_0 a=9.5\pi$ ) normalized to  $\sigma \delta \bar{\epsilon} \eta^2 / (4\pi^2 \omega \epsilon_0 b |z_{in}|^2)$  and with the attenuation parameter,  $\alpha$ , selected to give 0, 1, 3, 5, and 20 db of attenuation per wavelength.

### III. EXPERIMENTAL RADIATION PATTERNS

There are two radiation experiments which would be very interesting to perform in the course of verifying the theory. One of these is the measurement of the thermal radiation from a hot wire of moderately high conductivity. In order to make this measurement in the far zone at microwave frequencies, it has been estimated that receiver sensitivities of  $2 \times 10^{-30}$  K and  $0.1^\circ$  K are required using sources of tungsten and silicon carbide, respectively [11]. Restricting the receiver bandwidth to approximately 100 mc in order to prevent excessive smoothing of the pattern, one concludes that



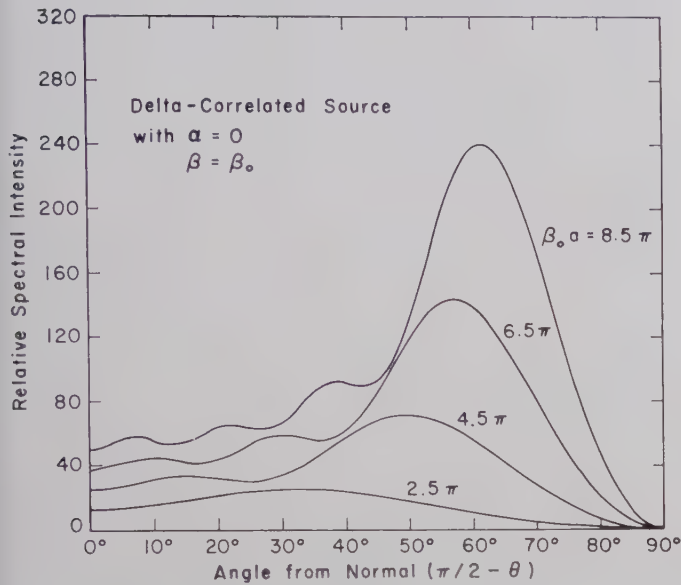


Fig. 4—Thermal radiation patterns for thin slots of various lengths.

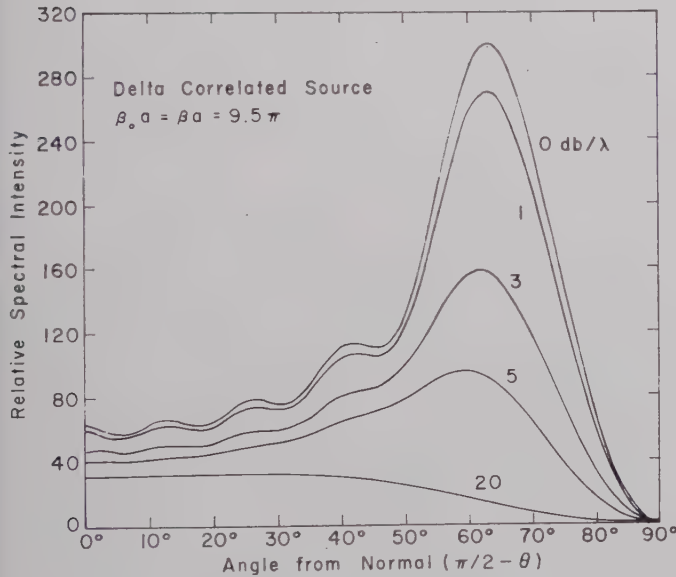


Fig. 5—Thermal radiation patterns with lossy propagation along the slot.

with the best present-day receiver this measurement is practical using silicon carbide or a similar material, but not using tungsten. However, near-zone measurements of the microwave radiation from incandescent tungsten are practical; and in fact, such a measurement has been described by Westberg [12]. A theoretical analysis of the near-zone case has not appeared in the literature.

The other experiment of interest is the measurement of the thermal radiation from a noise-excited thin slot. For this latter experiment, using a gaseous discharge as a source, one finds, as detailed below, that a receiver sensitivity of 1°K or 2°K is sufficient to permit pattern measurements in the far-zone. This sensitivity is considerably less than is quoted above for the experiments using a hot-wire source. This is due both to the much higher radiation temperature and to the higher emissivity of the gaseous discharge source.

### A. Description of the Measurement

From a conceptual point of view, the measurement of a radiation pattern is quite simple. Briefly, a receiver and a transmitter are positioned at some fixed separation. For either antenna, the radiation pattern is simply the received signal as a function of the angular position as the antenna being measured is rotated about its center.

In these experiments, the transmitting antenna is typically a 4.75 by 0.122 wavelength slot in a 28 by 19 wavelength metallic ground plane. The source of the thermal radiation is an argon glow discharge tube<sup>2</sup> clamped to the ground plane and running along the length of the slot. This entire ground plane assembly is mounted on a wooden turntable with provisions for measuring the angle of rotation.

The receiving aperture is a microwave horn which is positioned at a 1.500-meter range with the electric-field polarization perpendicular to the long edge of the radiating slot, *i.e.*, placed at  $(1.500, \theta, \pi/2)$  to read  $E_\phi(\theta)$  in Fig. 1. The *E*- and *H*-plane dimensions of this aperture are 8.04 cm and 11.10 cm, respectively; and at 9200 Mc the measured absolute gain is 72 (vs a theoretical value of 70). Hence, the effective solid angle, computed from  $\Omega = G\lambda^2/(4\pi r_0^2)$ , is  $2.70 \times 10^{-3}$  sterad. Approximate criteria for the Fraunhofer region require that  $r_0 > 2al/\lambda$  and  $r_0 > a^2/\lambda$ , in which  $l$  is the *H*-plane dimension of the receiving aperture [11], [14]. For  $\beta_0 a = 9.5\pi$  and a frequency of 9200 Mc, these give  $r_0 > 1.05$  meters and 0.74 meter, respectively. Therefore, one concludes that with a slot length of  $9.5\pi$  radians, a range of 1.500 meters places the receiving aperture in the far-zone region.

The problem of detecting the thermal radiation from either a heated wire or a noise-excited thin slot is similar to a detection problem which is encountered in radio astronomy. In these two applications both the signal and the internal receiver noise have essentially the same wide spectral density. Dicke devised a practical method for detecting such signals, even though they are less than 1/1000th of the level of the receiver noise [15]. A receiver of this basic type was designed for the experiments which are described in this paper. The characteristics of this receiver are briefly summarized as follows: a total fluctuation, drift, and reflection error of 0.3 rms°K; an amplification bandwidth of 16 Mc centered at 9200 Mc (9166 to 9174 Mc and 9226 to 9234 Mc); a noise ratio for the mixer and the IF amplifier of 5 (7 db); a modulation frequency of 1000 cps; and an integration time of 30 seconds. This receiver is calibrated by using an argon noise source and a variable

<sup>2</sup> The dimensions of the tube are 0.765-cm ID, 0.953 cm OD, and 21.2-cm long. The tube is filled with pure argon; and for these experiments, unless otherwise specified, a pressure of  $30.0 \pm 0.3$ -mm Hg and an operating point of 200 ma and 71 v are used. For these values, the kinetic temperature of the plasma electrons is computed from (8.36) of von Engel [13], and the result is a temperature

$$T = 11,300^\circ \text{K}.$$

The measured value of the microwave noise temperature is, as expected [2], [4], essentially the same, *i.e.*,

$$T = 10,072 \pm 200^\circ \text{K}.$$

attenuator as a secondary standard. Although these measurements are reproducible to better than 3 per cent their absolute accuracy is probably no better than 20 per cent.

### B. Measurements

Experimental thermal radiation patterns are shown for slot lengths of  $\beta_0 a = 7.30\pi$  and  $9.50\pi$ , and for a common slot width of  $\beta_0 b = 0.244\pi$  (Figs. 6, 7). The radiation received from the noise-excited thin slot is expressed in terms of an effective received temperature and this is plotted vs the angle from the normal,  $\pi/2 - \theta$ . In the notation of Section II, the received temperature is given by solving  $kT_a df = P_{f\Omega} d\Omega$  for  $T_a$ , i.e.,  $T_a = P_{f\Omega} \Omega / k$ . Only one quadrant of the pattern is plotted due to the symmetry about the plane  $\theta = \pi/2$ . It should be noted that the effective received temperature, as defined above, represents only the thermal radiation from the aperture system, while the thermal radiations which are received from the other surroundings have been eliminated in the course of the data reduction.

In addition, the thermal radiation is measured for several argon-filled tubes at different pressures (Fig. 8). In this measurement there is no ground plane; but the receiver, the range, and the tube envelope are unchanged. Only the received temperature which is due to the  $\phi$  component of the noise electric field is shown. However, in the absence of the ground plane, there is also a  $\theta$  component of the electric field with a Poynting vector at  $\theta = \pi/2$  of approximately one-half the value of that shown. In the presence of the ground plane, this component is no longer detected in the radiation field, due to the inefficient excitation of  $E_z(x, y, z, \omega)$  when the slot is thin, i.e., when  $b \ll \lambda$ .

In order to permit a comparison of the classical radiation pattern to those above, an experimental curve is also shown for the radiation pattern of the thin slot at optical frequencies (Fig. 9). Essentially the same experimental arrangement is preserved, except that now a sensitive photocell receiver is used to measure the intensity. The thin slot is of the order of  $10^6$  wavelengths long at the peak of the spectral response of the photocell.

### C. Comparison of Measurement with Theory

First, it is seen that the optical radiation pattern is approximately Lambertian, while the microwave pattern is not. Furthermore, the general features of the microwave pattern measurements agree quite well with the theory which is presented in this paper.

In making a quantitative comparison, it is noted from a computation of (20) for the  $\beta = \beta_0$  case, that there are 7 and 9 relative maxima predicted for slots of  $7.3\pi$  and  $9.5\pi$  radians in length, respectively. However, from the experimental curves, it is seen that there are 8 and 10 relative maxima observed in these respective cases.

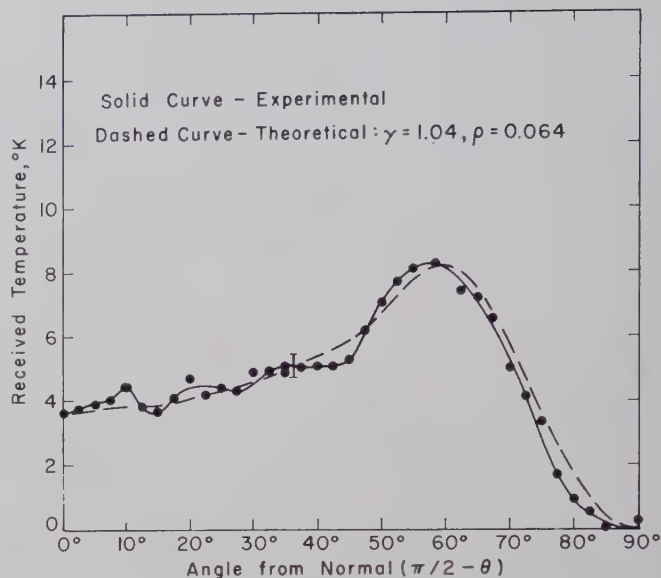


Fig. 6—Thermal radiation pattern for a thin slot of  $7.3\pi$  radians in length. Data are taken for  $r_0 = 1.500$  meters,  $f = 9200$  Mc, and  $\Omega = 2.7 \times 10^{-3}$  sterad.

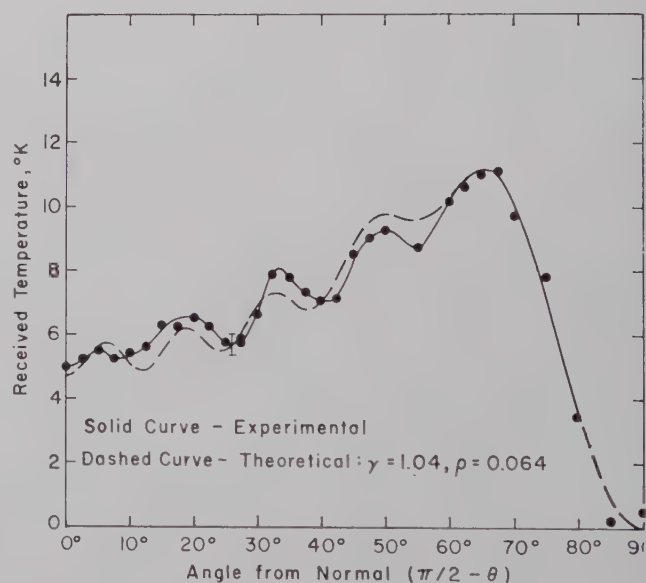


Fig. 7—Thermal radiation pattern for a thin slot of  $9.5\pi$  radians in length. Data are taken for  $r_0 = 1.500$  meters,  $f = 9200$  Mc, and  $\Omega = 2.7 \times 10^{-3}$  sterad.

Although the geometry makes an exact solution difficult, it is known that the effect of the glass walls of the discharge tube is to decrease the phase velocity along the slot, while that of the plasma column itself is to increase this velocity. Apparently, their combined effect is to slightly decrease the value of the phase velocity from that in free space. Using a phase factor of  $\gamma = 1.04$  and an attenuation constant of  $\rho = 0.064$  (3.5 db/ $\lambda$ ) in (20), one finds fair agreement between the experiment and the theory as is seen by comparing the solid to the dashed curve in Figs. 6 and 7. The values for  $\gamma$  and  $\rho$  have



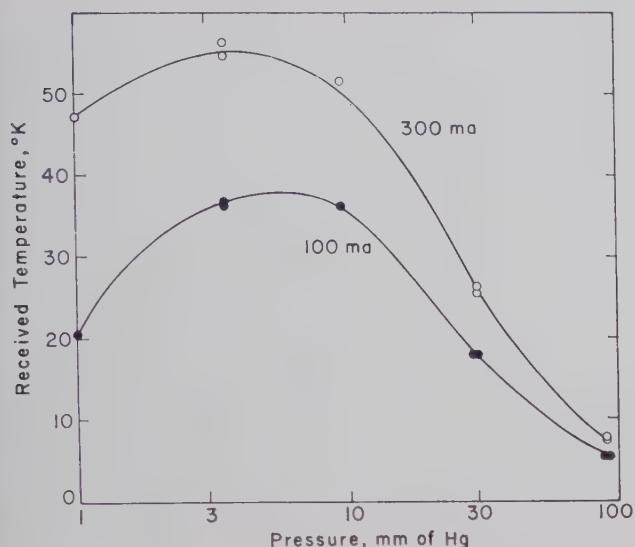


Fig. 8—Radiation level as a function of pressure for argon. Data are taken for  $r_0=1.500$  meters,  $f=9200$  Mc,  $\theta=\pi/2$ ,  $\Omega=2.7\times 10^{-3}$  sterad and no slotted metallic plane.

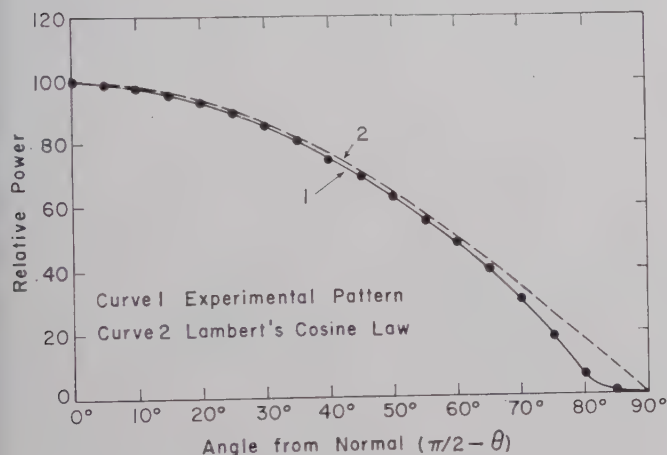


Fig. 9—Radiation pattern at optical frequencies with the same slot as in Fig. 7.

been selected to give a compromise fit for both of the slot lengths. The main discrepancy appears in the  $\beta_0 a = 7.3\pi$  case, where the observed ripple exceeds the theoretical value. This could be due to the compromise method of selecting  $\gamma$ ,  $\rho$  or to some more fundamental cause, e.g., a slight degree of coherence in the slot excitation.<sup>3</sup> The angles at which the relative maxima occur are tabulated (see Table I). In compiling this table, a lower attenuation constant is used for the  $\beta_0 a = 7.3\pi$  case in order to enhance the ripple and thereby to permit the determination of the tabulated angles.

<sup>3</sup> The radiation patterns for an exponentially-correlated source show the same general features as those given by (20), but the relative ripple is higher even for a correlation length which is less than  $\lambda$  [11].

TABLE I  
COMPARISON OF EXPERIMENT TO THEORY FOR THE THIN SLOT

Radian Length	Angle of Rel. Max.	$z_{in}$	$T_a$ at $\theta=\pi/2$
$(\beta_0 a)$	$ \pi/2-\theta $	(ohms)	(°K)
7.3π	Expt. 10, 21, 36, 58 Theory 8, 26, 44, 62	332.	3.6 $1.89 \times 10^4 \sigma \delta$
9.5π	Expt. 5, 19, 33, 50, 65 Theory 6, 19, 33, 51, 65	343.	5.0 $2.74 \times 10^4 \sigma \delta$

The theoretical curves in Figs. 6 and 7 are drawn with an arbitrary normalization of the amplitude. Although the precise value of  $\sigma \delta$  is not known, it is worth while to compare the ratio of the received temperature for the two slots at some convenient angle. Substituting the values  $\beta_0 a = 7.3\pi$  or  $9.5\pi$ ,  $f = 9.2 \times 10^9$  cps,  $b = 3.97 \times 10^{-3}$  meters,  $\gamma = 1.04$ ,  $\rho = 0.0641$ , and  $\theta = \pi/2$ , one finds from (20) that  $K_2 = 42.92$  or  $66.55$  and from formulas in Schelkunoff [7] that  $|z_{in}| = 332$  or  $343$  ohm. Then, since  $T = 10.1 \times 10^3$ °K and  $\Omega = 2.7 \times 10^{-3}$  sterad, the received temperatures can be computed as  $T_a = 1.89 \times 10^4 \sigma \delta$  and  $2.74 \times 10^4 \sigma \delta$  for the  $7.3\pi$  and the  $9.5\pi$  radian lengths, respectively. Their ratio of 0.69 agrees fairly well with the observed ratio of 0.72. From these data, an average value of  $\sigma \delta$  is computed, i.e.,  $\sigma \delta \approx 1.87 \times 10^{-4}$  mho.

#### IV. CONCLUSIONS

An investigation has been made of the spatial distribution of the radiant energy emitted by a body for wavelengths at which the body dimensions and the wavelength are of the same order of magnitude. It is shown both theoretically and experimentally that in such cases the radiation pattern has the following characteristics:

- 1) It exhibits pronounced minima and maxima.
- 2) It is sensitive to the radian dimensions of the body.
- 3) It can have a well-defined polarization.
- 4) It is not, in general, a maximum in the direction for which the radiator subtends the maximum solid angle.

Although the source excitation is uncorrelated in time and in space, the resultant distribution of the electric field in the aperture is partially correlated, as may be shown by combining (6) and (11). It is this correlation which gives rise to the interference phenomenon in the radiated field. Furthermore, it is clear from the theory that an analogous interference effect will occur in the case of the radiation from a small hole

of arbitrary shape in an otherwise isothermal cavity. In more general terms, these effects will occur in the radiation from a blackbody surface at wavelengths which are of the order of the body dimensions.

Finally, it is worth while to recall that simply by invoking the thermodynamic principle of the detailed balancing of radiation one can compute the spectral absorptivity of a body from its spectral thermal radiation pattern or vice versa. Thus, it follows that the spectral absorptivity of a body also exhibits the above-itemized characteristics at wavelengths which are of the order of the body dimensions.

#### V. ACKNOWLEDGMENT

The author wishes to acknowledge the many helpful discussions with C. H. Papas throughout the course of this work. Valuable consultation was also given by G. J. Stanley on radiometer principles and practices during the design of the equipment for the experiments.

The author wishes to express his appreciation to R. L. Roderick and G. F. Smith who encouraged this work. This research was supported in part by a fellowship grant from the Hughes Aircraft Company, Culver City, Calif.

#### REFERENCES

- [1] H. Nyquist, "Thermal agitation of electric charge in conductors," *Phys. Rev.*, vol. 32, pp. 110-113; July, 1928.
- [2] P. Parzen and L. Goldstein, "Current fluctuations in dc gas discharge plasma," *Phys. Rev.*, vol. 79, pp. 190-191; July, 1950.
- [3] J. B. Johnson, "Thermal agitation of electricity in conductors," *Phys. Rev.*, vol. 32, pp. 97-109; July, 1928.
- [4] W. W. Mumford, "A broad-band microwave noise source," *Bell Syst. Tech. J.*, vol. 28, pp. 608-618; October, 1949.
- [5] M. A. Leontovich and S. M. Rytov, *Zh. Eksp. Teor. Fiz.*, vol. 23, pp. 246-252; 1952.
- [6] H. G. Booker, "Slot aerials and their relation to complementary wire aerials," *J. IEE*, vol. 93, pp. 620-626; 1946.
- [7] S. A. Schelkunoff and H. T. Friss, "Antennas, Theory and Practice," John Wiley and Sons, Inc., New York, N. Y.; 1952.
- [8] J. Weber, "Scattering of electromagnetic waves by wires and plates," *Proc. IRE*, vol. 43, pp. 82-89; January, 1955.
- [9] W. R. Smythe, "Static and Dynamic Electricity," McGraw-Hill Book Co., Inc., New York, N. Y.; 1950.
- [10] M. L. Levin and S. M. Rytov, "Thermal radiation from a thin rectilinear antenna," *J. Tech. Phys.*, vol. 25, pp. 323-332; 1955.
- [11] N. George, "Spatial distribution of thermal radiation at microwave frequencies," Antenna Lab., Calif. Inst. Tech., Pasadena, Calif., rept. no. 18, 1959.
- [12] V. Westberg, "Measurements of noise radiation at 10 cm from glow lamps," *Chalmers Tek. Högskol. Handl.*, nr. 180, pp. 1-14; 1956.
- [13] A. von Engel, "Ionized Gases," Oxford Univ. Press, London, Eng.; 1955.
- [14] S. Silver, "Microwave Antenna Theory and Design," McGraw-Hill Book Co., Inc., New York, N. Y.; 1949.
- [15] R. H. Dicke, "Measurement of thermal radiation at microwave frequencies," *Rev. Sci. Instr.*, vol. 17, pp. 268-275; July, 1946.

## Variational Principles and Mode Coupling in Periodic Structures\*

T. J. GOBLICK, JR.† AND R. M. BEVENSEE‡, MEMBER, IRE

**Summary**—Variational techniques are used in analyzing periodic "cold" microwave structures for the angular frequency,  $\omega$ , as a function of assumed phase shift per periodic cell. Two variational expressions are given: one for  $\omega$  in terms of the  $E$ - and  $H$ -fields, and one for  $k^2 = \omega^2 \mu \epsilon$  in terms of the  $E$ -field. For structures with relatively light coupling between cells, the trial fields to be used with the variational expressions are composed of closed cavity modes, phase shifted by  $\phi$  radians from cell to cell. Both variational expressions yield determinantal equations for  $k^2(\phi)$  which agree with equations previously derived from a mode coupling point of view. One form of an equivalent lumped circuit is given to represent the structure within one of its pass bands.

Curves compare the variational-mode coupling expression for  $k^2(\phi)$  of a periodically lumped loaded transmission line with exact expressions.

#### I. INTRODUCTION

PERIODIC structures have received extensive theoretical and experimental treatment in the past in regard to applications in traveling wave tubes. The advent of high power traveling wave tubes proved it was still not a simple matter to design slow wave structures which could dissipate large amounts of power while still operating over a relatively large band of frequencies [1].

To analyze a simple periodic structure, such as an iris-loaded waveguide, is a formidable task. The method of analysis used here is that of mode coupling. For the case of a very heavily shunt-loaded waveguide, the coupling holes in the irises are small compared to the total iris area. The structure resembles a chain of loosely-coupled resonant cavities and so the electric and magnetic fields of the structure resemble normal cavity modes of a section of the structure. The weaker the coupling between sections is made, the closer is the resemblance of the fields to those of the actual cavities.

\* Received by the PGMTT, November 9, 1959; revised manuscript received, May 23, 1960. This work was supported in part by the U. S. Army Signal Corps, the U. S. Air Force Office of Scientific Res., Air Res. and Dev. Command, and the U. S. Navy Office of Naval Research.

† Dept. of Electrical Engrg., Res. Lab. of Electronics, Mass. Inst. Tech., Cambridge, Mass.

‡ Res. Div., Varian Associates, Palo Alto, Calif. Formerly with Dept. of Electrical Engrg. and Res. Lab. of Electronics, Mass. Inst. Tech., Cambridge, Mass.



In this mode-coupling analysis, the fields of the periodic structure are approximated by the normal cavity modes of oscillation of a section of the structure. These cavity modes are phase shifted from section to section by a phase angle  $\phi$  to simulate a propagating wave. By use of these approximations, a relation between  $\omega^2$  ( $\omega$ =frequency) and phase shift per section,  $\phi$ , may be derived. In this way, the propagation characteristics of the heavily loaded structure are obtained in terms of resonant modes of a cavity section of the structure for any assumed phase shift  $\phi$ . The coupling coefficients between adjacent sections are expressed in an intuitively appealing form in this mode coupling approach.

In solving for the physical parameters of a very complicated system, we often find it advantageous to use variational techniques to arrive systematically at good approximate answers. Such techniques have been used to find cutoff frequencies and propagation constants of waveguides as well as resonant frequencies for cavities. In all of these applications, variational principles allowing the use of trial fields which are not exactly correct in detail can give quite accurate results.

The periodically loaded waveguide, viewed either as a waveguide with slight periodic perturbations of its walls or as a chain of coupled cavities, can be treated using a variational principle. The variational principle used here allows  $\omega^2$  to be computed for assumed trial fields and phase shift per section  $\phi$ . For the case of heavy shunt loading of the guide, trial fields which are actually resonant modes of a cavity section of the structure are used together with an assumed  $\phi$ . The relation between  $\omega^2$  and  $\phi$  that is found is identical to the coupling equations derived purely from a mode coupling approach [2], [3].

The variational technique is appealing because it yields a sort of optimum value of  $\omega^2$  for the given set of trial functions, namely that  $\omega^2$  which is minimized for these trial functions. But this implies that the error in  $\omega^2$  is of second order compared to the actual error in the trial functions, and this is the advantage of this technique. The trial fields are not just used as approximate fields to get answers; they may be adjusted according to a definite procedure to obtain the most accurate approximation to the correct  $\omega^2$  for the assumed form of the trial fields.

The fact that the same coupling equations are found from mode coupling and from the variational principle signifies that the mode-coupling formalism has a formal mathematical basis in variational techniques. Mode coupling, then, is not simply an intuitively convenient approximation to use in some problems.

The results obtained here for the heavily-loaded periodic structure are useful in studying the effects of more complicated schemes of coupling between adjacent cavity sections. The mode-coupling equations for a capacitively lumped-loaded transmission line were derived, and for this simple periodic structure it is easy

to obtain curves to show how well very simple trial fields may be used to obtain accurate answers.

## II. THE VARIATIONAL PRINCIPLE

In a lossless periodic structure such as the iris-loaded waveguide shown in Fig. 1, we know that the electric and magnetic fields satisfy Maxwell's equations

$$\nabla \times \mathbf{E} + j\omega\mu\mathbf{H} = 0, \quad (1)$$

$$\nabla \times \mathbf{H} - j\omega\epsilon\mathbf{E} = 0, \quad (2)$$

when the medium filling the structure is isotropic, homogeneous, and nonconducting (a time-dependence of  $e^{j\omega t}$  has been assumed). The boundary condition that the electric field satisfies is stated as

$$\mathbf{n} \times \mathbf{E} = 0 \quad \text{on } S, \quad (3)$$

where  $\mathbf{n}$  is the unit vector which is normal to the perfectly conducting surface  $S$  which makes up the periodic structure, (see Fig. 2). Another important property of the fields in a periodic structure is expressed in a theorem by Floquet [4]. From this theorem, we may write in functional notation

$$\mathbf{E}(u_1, u_2, z) = \hat{\mathbf{E}}(u_1, u_2, z)e^{-\gamma z}, \quad (4)$$

where now  $\hat{\mathbf{E}}(u_1, u_2, z)$  is a periodic function of  $z$  having the same period  $L$  as the structure. ( $u_1$  and  $u_2$  are generalized transverse coordinates.)

$$\hat{\mathbf{E}}(u_1, u_2, z) = \hat{\mathbf{E}}(u_1, u_2, z + L). \quad (5)$$

The magnetic field naturally has this same property.

Using these known properties of the fields of the periodic structure, one may derive a variational expression for  $j\omega$ . Consider the  $\mathbf{E}$ - and  $\mathbf{H}$ -fields of (1) and (2) to pertain to a wave traveling in the positive  $z$ -direction

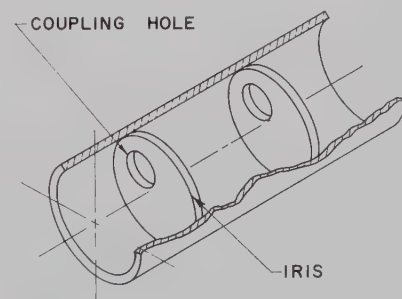


Fig. 1—An iris-loaded waveguide.

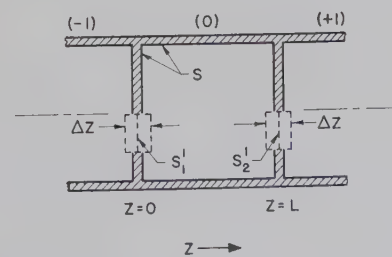


Fig. 2—A section of the periodic structure showing notation used.

of the structure. Calling these fields  $\mathbf{E}_+$  and  $\mathbf{H}_+$ , we may now dot-multiply (1) by  $\mathbf{H}_-^*$  (\*stands for complex conjugate), the magnetic field of another wave solution called the adjoint solution, and integrate throughout the volume  $V$  of one cell or section of the structure. Correspondingly, multiply (2) by  $\mathbf{E}_-^*$ , the electric field of the adjoint solution, and integrate. Subtracting the two resulting equations and solving for  $j\omega$ , which is not a function of the variables of integration, gives

$$j\omega = \frac{\int_V \mathbf{E}_-^* \cdot \nabla \times \mathbf{H}_+ dV - \int_V \mathbf{H}_-^* \cdot \nabla \times \mathbf{E}_+ dV}{\mu \int_V \mathbf{H}_+ \cdot \mathbf{H}_-^* dV + \epsilon \int_V \mathbf{E}_+ \cdot \mathbf{E}_-^* dV} \quad (6)$$

The proof that (6) is actually a variational principle for  $\omega$  is given in Appendix I. It is found in this proof that for arbitrary first-order variation of  $\omega$  equal to zero, the adjoint solution satisfies the equations

$$\nabla \times \mathbf{E}_-^* - j\omega\mu\mathbf{H}_-^* = 0 \quad (7)$$

$$\nabla \times \mathbf{H}_-^* + j\omega\epsilon\mathbf{E}_-^* = 0, \quad (8)$$

provided the adjoint trial field satisfies boundary condition (3) and the conditions  $\mathbf{E}_-(L) = \mathbf{E}_-(0)e^{-\gamma L}$ ,  $\mathbf{H}(L) = \mathbf{H}_-(0)e^{-\gamma L}$ . Since the latter conditions imply Floquet's theorem, we can demand

$$\mathbf{E}_-(u_1, u_2, z) = \mathbf{E}_-(u_1, u_2, z)e^{-\gamma z}, \quad (9)$$

where this is the same value of  $\gamma$  as in (4), which indicates that the adjoint wave also propagates in the positive  $z$ -direction.

The variational principle may be used together with suitable trial fields for  $\mathbf{E}_+$ ,  $\mathbf{H}_+$ ,  $\mathbf{E}_-$ , and  $\mathbf{H}_-$  to obtain approximations to  $\omega$  which are in error to second order compared to the errors in the trial fields themselves. Consider first an iris-loaded waveguide in which the coupling holes in the irises are very small. The coupling between adjacent cells is now very weak and the periodic structure actually appears to be a chain of weakly-coupled cavities. The fields in a particular cavity section of the periodic structure should resemble to a fair degree the fields of an undriven cavity. For this case then, the pass bands are very narrow compared to the stop bands; and since we are interested in the propagation characteristics in a pass band only, we are concerned with a narrow frequency range. It seems reasonable, then, to approximate each field by several terms of a normal mode expansion of a cavity section. This is what we will do to construct trial fields. The simplest approximation would be to use only one term of a mode expansion as a trial field.

However there are two different normal mode expansions which can be defined for a cavity section. The short-circuit mode expansion is derived for the boundary condition that the tangential electric field disappears over the entire surface of the cavity including the sur-

faces  $S_1'$ ,  $S_2'$  (see Fig. 2) in the plane of the holes. The open-circuit mode expansion is found for the boundary condition of (3) on  $S$  (but the tangential magnetic field must be zero on  $S_1'$ ,  $S_2'$ ). These two mode expansions are closely related to the behavior of the periodic structure. For every short-circuit resonant mode, there is a corresponding open-circuit mode which has fields very similar to the short-circuit mode except in the immediate vicinity of the coupling holes. The resonant frequencies of this pair of modes are not very different when the holes are small. The frequency range between them corresponds to a pass band of the periodic structure [4]. To obtain an approximation to the propagation characteristics in a particular pass band, we would choose the short-circuit mode corresponding to that pass band as the  $\mathbf{E}_+$  and  $\mathbf{H}_+$  trial fields and the open-circuit mode as the  $\mathbf{E}_-$  and  $\mathbf{H}_-$  trial fields.

Let us summarize the properties of these two mode expansions. First, the fields of the  $n$ th short-circuit mode can conveniently be defined by the equations [5]:

$$\nabla \times \mathbf{E}_n = P_n \mathbf{H}_n, \quad (10a)$$

$$\nabla \times \mathbf{H}_n = P_n \mathbf{E}_n, \quad (10b)$$

$$P_n^2 = \omega_{sn}^2 \mu \epsilon, \quad (11)$$

$$\mathbf{n}_0 \times \mathbf{E}_n = 0 \quad \text{on } S, S_1', S_2', \quad (12)$$

where  $\mathbf{n}_0$  is the outward unit vector normal to the boundary surface of a cavity section.  $\omega_{sn}$  is the resonant frequency of this  $n$ th short-circuit mode. For the  $m$ th open circuit mode the resonant frequency is  $\omega_{om}$  and the corresponding equations are:

$$\nabla \times \mathbf{e}_m = p_m \mathbf{h}_m, \quad (13a)$$

$$\nabla \times \mathbf{h}_m = p_m \mathbf{e}_m, \quad (13b)$$

$$p_m^2 = \omega_{om}^2 \mu \epsilon, \quad (14)$$

$$\mathbf{n}_0 \times \mathbf{e}_m = 0 \quad \text{on } S, \quad (15a)$$

$$\mathbf{n}_0 \times \mathbf{h}_m = 0 \quad \text{on } S_1', S_2'. \quad (15b)$$

We have seen from Appendix I that the trial fields must also satisfy Floquet's theorem, so the  $\mathbf{E}_+$  trial field is constructed as follows. Remember that we are trying to approximate the fields of the periodic structure for frequencies in the  $n$ th pass band for a propagating wave having a phase shift per section of  $\phi$  radians. The electric field in the (0) cavity section of Fig. 2 is approximated by the cavity short-circuit mode  $\mathbf{E}_n$ . The field in the preceding  $(-1)$  cavity section is assumed to be the same as in the (0) section, but phase shifted by an angle  $\phi$  to simulate propagation in the positive  $z$ -direction,

$$\mathbf{E}_+^{(0)} = V_n \mathbf{E}_n; \quad \mathbf{E}_+^{(-1)} = V_n \mathbf{E}_n e^{j\phi}. \quad (16a)$$

The  $\mathbf{H}_+$  trial field is similarly constructed from  $\mathbf{H}_n$ .

$$\mathbf{H}_+^{(0)} = I_n \mathbf{H}_n; \quad \mathbf{H}_+^{(-1)} = I_n \mathbf{H}_n e^{j\phi}. \quad (16b)$$



$V_n$  and  $I_n$  are merely adjustable amplitude factors in the trial fields which will be adjusted in an optimum way using the variational principle.

For the adjoint trial fields, propagation in the positive  $z$ -direction is also simulated, and we use the open-circuit mode corresponding to this  $n$ th pass band in which we are interested.

$$\mathbf{E}_-^{(0)} = v_n \mathbf{e}_n; \quad \mathbf{E}_-^{(-1)} = v_n \mathbf{e}_n e^{i\phi} \quad (17a)$$

$$\mathbf{H}_-^{(0)} = i_n \mathbf{h}_n; \quad \mathbf{H}_-^{(-1)} = i_n \mathbf{h}_n e^{i\phi}. \quad (17b)$$

These trial fields are now substituted into (6) and a relation for  $j\omega$  is found in terms of  $\phi$ , the phase shift per section. An important point to notice is the fact that the trial fields are discontinuous in the plane of the holes because each cavity mode is actually a standing oscillation. The discontinuity is due to a phase shift and possibly to the behavior of the mode patterns (see Figs. 3 and 4). If the surfaces  $S_1'$  and  $S_2'$  are considered as pillbox volumes only  $\Delta z$  thick in which the discontinuities appear, we must choose the volume,  $V$ , of one section so that it includes part of the pillbox at  $S_1'$  and part of the pillbox at  $S_2'$  so the total volume integral throughout a section contains the volume of one whole pillbox (see Fig. 2).

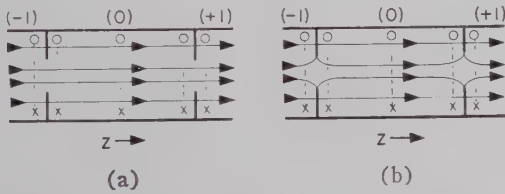


Fig. 3—Examples of (a) an even short-circuit mode and (b) an even open-circuit mode. Solid lines represent electric field lines; dashed lines represent magnetic field lines.

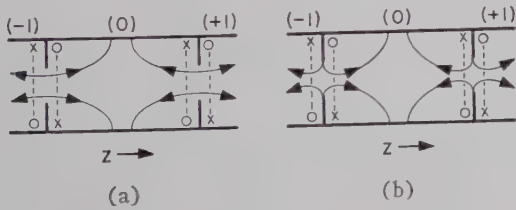


Fig. 4—Examples of (a) an odd short-circuit mode and (b) an odd open-circuit mode.

In (6), the integral

$$\int_V \mathbf{E}_-^* \cdot \nabla \times \mathbf{H}_+ dV$$

may be broken up into the integral over the volume of a section plus an integral over a pillbox. The pillbox volume is important in this term since there is a differentiation of field discontinuities in  $\nabla \times \mathbf{H}_+$ . Since  $\Delta z$  is considered to be very small and the trial field to be substituted for  $\mathbf{E}_-^*$  is tangential at  $S_1'$  and  $S_2'$ , we may replace  $\nabla \times \mathbf{H}_+$  by  $\mathbf{a}_z \times \partial \mathbf{H}_+ / \partial z$ , which is the only term

producing components tangential to  $S_1'$  and  $S_2'$ . The pillbox integral may be written as

$$\begin{aligned} & \int_{S_1'} \left[ \int_{Z=0^-}^{Z=0^+} \mathbf{e}_n^* \cdot \nabla \times \mathbf{H}_n dz \right] da \\ &= \int_{S_1'} \left[ \int_{Z=0^-}^{Z=0^+} \mathbf{e}_n^* \cdot \mathbf{a}_z \times \frac{\partial}{\partial z} \mathbf{H}_n dz \right] da \\ &= \frac{1}{2} \int_{S_1'} [\mathbf{e}_n^*(0^-) + \mathbf{e}_n^*(0^+)] \\ & \quad \cdot [\mathbf{a}_z \times \mathbf{H}_n(0^+) - \mathbf{a}_z \times \mathbf{H}_n(0^-)] da. \end{aligned} \quad (18)$$

The final result in (18) is obtained by our assuming any smooth functional variation of the fields  $\mathbf{e}_n^*$  and  $\mathbf{H}_n$  within the pillbox, so long as each of these fields has the same functional variation. The final result, then, does not depend on the specific functional variation, and the form in (18) emerges.

The cavity modes of a section of the periodic structure are either symmetric or antisymmetric with respect to the  $z$ -axis in a section. Let us define an "even" mode as one which has an even number of reversals of its electric field along the  $z$ -axis of a section. From Fig. 3, we can see that for even modes,

$$\mathbf{H}_n^{(0)}(0^-) = \mathbf{H}_n^{(-1)}(L) = \mathbf{H}_n^{(-1)}(0) = \mathbf{H}_n^{(0)}(0) e^{i\phi}, \quad (19a)$$

$$\mathbf{e}_n^{(0)}(0^-) = \mathbf{e}_n^{(-1)}(L) = -\mathbf{e}_n^{(-1)}(0) = -\mathbf{e}_n^{(0)}(0) e^{i\phi}. \quad (19b)$$

Let us solve for  $\omega(\phi)$  between  $P_2$  and  $p_2$  by employing the  $\mathbf{E}_2 - \mathbf{H}_2$  and  $\mathbf{e}_2 - \mathbf{h}_2$  modes in (6). With the aid of (16), (17), and (18), the expression for  $\omega$  is found to be

$$j\omega = \frac{v_2^* I_2 P_2 T_2 - v_2^* I_2 M_2 (1 - \cos \phi) - i_2^* V_2 P_2 U_2}{\mu I_2 i_2^* U_2 + \epsilon V_2 v_2^* T_2}. \quad (20)$$

We have defined

$$T_2 = \int_V \mathbf{e}_2^* \cdot \mathbf{E}_2 dV$$

$$U_2 = \int_V \mathbf{h}_2^* \cdot \mathbf{H}_2 dV$$

$$M_2 = \int_{S_1'} \mathbf{a}_z \times \mathbf{e}_2^*(0^+) \cdot \mathbf{H}_2(0^+) da,$$

where  $\mathbf{a}_z$  is the unit vector in the  $z$ -direction. To optimize the coefficients for the best approximation to  $\omega$  we must minimize (20) with respect to each amplitude coefficient. Setting the partial derivatives of (20) with respect to  $i_2^*$  and  $v_2^*$  equal to zero gives the coupling equations

$$P_2 V_2 = -j\omega \mu I_2, \quad (21)$$

$$P_2 I_2 T_2 = j\omega \epsilon V_2 T_2 + I_2 M_2 (1 - \cos \phi). \quad (22)$$

Eliminating  $V_2$  from these two expressions results in one equation

$$(P_2^2 - k^2) T_2 = P_2 M_2 (1 - \cos \phi), \quad (23)$$

where  $k^2 = \omega^2 \mu \epsilon$ . Eq. (23) also results from our varying (20) with respect to  $I_2$  and  $V_2$ .

When the phase shift per section is  $\pi$  radians, we are at a cutoff of the pass band and also at a resonance of a cavity section. For even modes,  $\phi = \pi$  radians corresponds to the open circuit resonance where then  $k^2 = p^2$ . Use of this information in (23) leads to<sup>1</sup>

$$\frac{P_2 M_2}{T_2} = \frac{1}{2} (P_2^2 - p_2^2). \quad (24)$$

Then (23) may be simplified to,

$$k^2 = \frac{p_2^2 + P_2^2}{2} - \frac{p_2^2 - P_2^2}{2} \cos \phi. \quad (25)$$

We define "odd" modes as those normal modes of a cavity section in which the electric field reverses an odd number of times along the  $z$ -axis. From Fig. 4, we can see that for odd modes (19a) and (19b) take the new form

$$H_n^0(0^-) = H_n^{(-1)}(L) = -H_n^{(-1)}(0) = -H_n^{(0)}(0)e^{j\phi}, \quad (26a)$$

$$e_n^0(0^-) = e_n^{(-1)}(L) = e_n^{(-1)}(0) = e_n^{(0)}(0)e^{j\phi}. \quad (26b)$$

Use of these expressions would give as a final result

$$k^2 = \frac{p_1^2 + P_1^2}{2} + \frac{p_1^2 - P_1^2}{2} \cos \phi, \quad (27)$$

where we use the odd subscript 1 to show that (27) applies for an odd mode pair.

If more cavity modes are included in the trial fields, one obtains a matrix equation whose determinant set equal to zero replaces the (23) for  $k^2$ . This determinant checks that previously derived from a mode-coupling approach [2]. It will also agree with the determinant later to be derived from a variational expression for  $k^2$  in terms of the  $\mathbf{E}$ -field alone.

An equivalent circuit interpretation of (20) follows for both even and odd modes. Combining (19a) and (19b) with (26a) and (26b) results in a compact way to express the mode properties:

$$H_n(L) = (-1)^n H_n(0) = H_n(0^-) e^{-j\phi} \quad (28a)$$

$$e_m(L) = (-1)^{m+1} e_m(0) = e_m(0^-) e^{-j\phi}, \quad (28b)$$

where the subscripts  $n$  will be even to refer to even modes and odd when odd modes are used. If we use (28a) and (28b) in (6) and obtain a more general form of (20) valid for even or odd mode pairs we may vary this expression with respect to  $V_n$ ,  $I_n$ ,  $v_n^*$ , and  $i_n^*$  in a man-

ner analogous to our operations with (20). We obtain a set of equations which leads to an equivalent circuit representation of the two-mode-coupling approximation (even or odd modes) for a periodic cavity structure. Now define

$$V_n = -j\omega L_n I_n$$

$$L_n = \frac{\mu}{P_n}; \quad C_n = \frac{\epsilon}{P_n}. \quad (29)$$

We have now

$$V_n + \frac{I_n}{i\omega C_n \frac{T_n}{M_n}} - \frac{I_n}{j\omega C_n} - \frac{I_n e^{j\phi}}{2j\omega C_n \frac{T_n}{M_n}} (-1)^n$$

$$- \frac{I_n e^{-j\phi}}{2j\omega C_n \frac{T_n}{M_n}} (-1)^n = 0. \quad (30)$$

Fig. 5 shows a lumped circuit which leads to the same (30) and is then one form of an equivalent circuit for the periodic structure. This equivalent circuit stems directly from the mode-coupling approach. For even modes, the quantity  $T_n/M_n$  is negative. For odd modes,  $T_n/M_n$  is positive and there is a negative capacitive coupling between cavity sections.

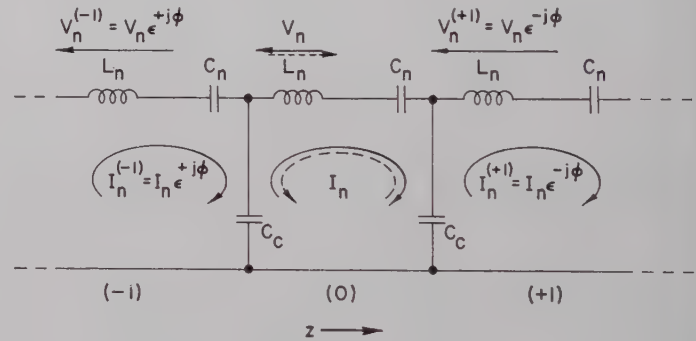


Fig. 5—A lumped equivalent circuit for the periodic structure from the single mode pair analysis. The dotted lines correspond to odd modes, solid lines to even modes. ( $C_e = -2C_n T_n/M_n$ ).

In the variational principle derived here, both electric and magnetic fields appear, and this means both trial fields must be chosen, but according to certain constraints. There is another variational principle for periodic structures in which only a single field appears. The electric field of a periodic structure obeys the vector wave equation

$$\nabla \times \nabla \times \mathbf{E} - k^2 \mathbf{E} = 0. \quad (31)$$

We may consider the  $\mathbf{E}$ -field of (31) to pertain to a wave traveling in the positive  $z$ -direction and call it the  $\mathbf{E}_+$  field. Then dot-multiply (31) by  $\mathbf{E}_-^*$ , the adjoint wave electric field, and integrate throughout the volume of one section of the structure. Solving for  $k^2$ , we get

<sup>1</sup> It is to be understood that this relation (24) is valid for a cavity section if the fields used for  $\mathbf{E}_-^*$  and  $\mathbf{E}_+$  in the integrals  $M_2$  and  $T_2$  are valid representations of the exact fields at its open- and short-circuit resonances, respectively. In this case of a lossless structure, only a single mode is used to represent the fields at each of these resonances, and (24) is exact. If complete open- and short-circuit normal mode expansions for the cavity section were used in  $M_2$  and  $T_2$ , in general, (24) would be exactly true.



$$k^2 = \frac{\int_V \mathbf{E}_-^* \cdot \nabla \times \nabla \times \mathbf{E}_+ dV}{\int_V \mathbf{E}_-^* \cdot \mathbf{E}_+ dV} \quad (32)$$

The actual proof that (32) is a variational principle for  $k^2$  involving only electric fields is shown in Appendix II. It is found in this proof that setting  $\delta[k^2] = 0$  forces the adjoint solution to satisfy the equation

$$\nabla \times \nabla \times \mathbf{E}_-^* - k^2 \mathbf{E}_-^* = 0, \quad (33)$$

provided  $\mathbf{E}_-(L) = \mathbf{E}_-(0)e^{-\gamma L}$ . Since the latter condition implies (9), we see that the adjoint is a wave propagating in the positive  $z$ -direction. Now we need only to construct trial fields for  $\mathbf{E}_+$  and  $\mathbf{E}_-$  for (32).

This time, let us construct more general trial fields for more accuracy in finding  $k^2$ . If the modes of either

same) and set the equations equal to zero. For the  $u$ th ( $a_u$ ) coefficient, we would get

$$\sum_m \left[ (P_u^2 - k^2) T_{um} - P_u M_{um} \left\{ \frac{1}{2} + \frac{1}{2} (-1)^{m+u} - \frac{e^{i\phi}}{2} (-1)^u - \frac{e^{-i\phi}}{2} (-1)^m \right\} \right] b_m^* = 0. \quad (35)$$

The following definitions have been introduced:

$$T_{um} = \int_V \mathbf{E}_u \cdot \mathbf{e}_m^* dV$$

$$M_{um} = \int_{S_1'} \mathbf{a}_z \times \mathbf{e}_m^*(0^+) \cdot \mathbf{H}_u(0^+) da.$$

We could cast this set of equations into matrix form, which would yield the determinantal equation for  $k^2$  in terms of  $\phi$ .

$$\begin{bmatrix} [(P_1^2 - k^2)T_{11} - P_1 M_{11}(1 + \cos \phi)] & [-P_1 M_{12}(j \sin \phi)] & \cdots \\ [-P_2 M_{21}(-j \sin \phi)] & [(P_2^2 - k^2)T_{22} - P_2 M_{22}(1 - \cos \phi)] & \cdots \\ \vdots & \vdots & \ddots \end{bmatrix} \begin{bmatrix} b_1^* \\ b_2^* \\ \vdots \end{bmatrix} = 0 \quad (36)$$

expansion were arranged in order of increasing resonant frequencies, one would find even and odd modes alternating. We could attach even or odd subscripts to correspond to even and odd modes, and then the mode properties could be written as in (28a) and (28b). The simple single mode-pair approximation using only a single term for each trial field gives good results when the coupling between cavities is weak. As the coupling holes are made larger, the actual fields do not resemble very closely a single resonant mode of a section. The next step in trial fields would be to make them more accurate by including several more terms of each expansion for trial fields. The extra terms should, of course, be chosen as those having resonant frequencies closest to the pass band of interest. The trial fields in the (0) cavity may be expressed as

$$\begin{aligned} \mathbf{E}_+^{(0)} &= a_1 \mathbf{E}_1 + a_2 \mathbf{E}_2 + \cdots + a_n \mathbf{E}_n + \cdots \\ &= \sum_n a_n \mathbf{E}_n, \end{aligned} \quad (34a)$$

the lowest-order mode being even, as depicted in Fig. 3.

$$\begin{aligned} \mathbf{E}_-^{(0)} &= b_1 \mathbf{e}_1 + b_2 \mathbf{e}_2 + \cdots + b_m \mathbf{e}_m + \cdots \\ &= \sum_m b_m \mathbf{e}_m. \end{aligned} \quad (34b)$$

Putting these trial fields [(34a) and (34b)] into (32) would give a coupling equation containing the coefficients  $a_n$  and  $b_m$ . To optimize these coefficients for the values of  $k^2$  corresponding to the perturbed  $P_n$  and  $P_m$ , we would take partial derivatives with respect to each  $a_n$  (or  $b_m$ ; the final determinantal equation is the

The determinantal equation arising from (36) agrees exactly with that found by Bevensee [2], solving the problem without the use of the variational principle but merely using a straightforward mode-coupling approach. It can also be seen that (36) simplifies to (25) (with the "2" subscript changed to "0") or (27), if only  $M_{11}$  or  $M_{22}$  is assumed to be nonzero. This reduces the trial fields to the single mode-pair case again.

If we used the complete normal mode expansions in (34a) and (34b), we could represent the fields in a cavity section exactly at any frequency, and these trial fields, together with (32), would yield an exact determinantal equation for  $k^2$ . In this paper, we are studying the problems of approximating this determinantal equation for  $k^2$  by using approximate but simple trial fields in (32).

### III. THE PERIODICALLY LUMPED-LOADED TRANSMISSION LINE

For illustration of the accuracy inherent in this mode-coupling approach to periodic structures, numerical results were worked out for a simple model of a periodic structure. The model chosen was a transmission line shunted periodically by lumped capacitance. Since the exact propagation characteristics for this model can easily be found, a comparison could be made between the exact behavior and that predicted by the mode-coupling equations [6], [7].

The periodically-loaded lossless transmission-line model that was found very convenient to handle using variational techniques was that of a nonuniform line in

which the inductance and capacitance were allowed to vary (periodically) with distance along the line. Analogous to the Maxwell equations used for the periodic cavity structure, we now have the nonuniform transmission-line equations

$$\frac{d}{dz} V(z) = -j\omega L(z)I(z) \quad (37)$$

$$\frac{d}{dz} I(z) = -j\omega C(z)V(z), \quad (38)$$

where the time dependence  $e^{j\omega t}$  is assumed again, and  $z$  is the distance along the line. It can be verified in a manner completely analogous to the above presentation that a variational principle for this periodic structure is

$$\omega^2 = - \frac{\int_0^L V_-^* \frac{d}{dz} \left[ \frac{1}{L(z)} \frac{d}{dz} V_+ \right] dz}{\int_0^L C(z) V_+ V_-^* dz}, \quad (39)$$

where  $L$  is the length of one periodic section of the structure.

Up to this point these expressions are perfectly general for a lossless, periodic, transmission-line structure. For simulation of periodic shunt loading by lumped capacitor elements,  $L(z)$  is treated as a constant,  $L_0$ , and  $C(z)$  takes the form of a constant,  $C_0$ , plus impulse functions (area  $2C_s$ ) which appear periodically with separation  $L$ . This completes the one-dimensional formulation of this structure. Fig. 6 shows

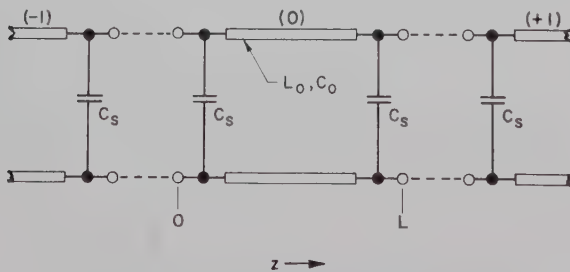


Fig. 6—The periodically-loaded transmission line broken into sections.

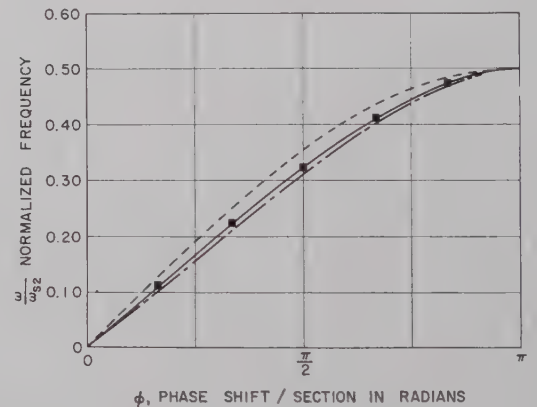
the structure that is analyzed when it is broken into convenient periodic sections. The open-circuit and short-circuit modes of a section of this structure are easily found, and these modes are used to approximate voltage and current distributions on the section. The open-circuit modes are substituted in (39) for  $V_-$  and the short-circuit modes for  $V_+$ .

Curves for the structure shown in Fig. 6 are shown only for two pass bands occurring at the lowest frequencies. When the trial fields consist of only single

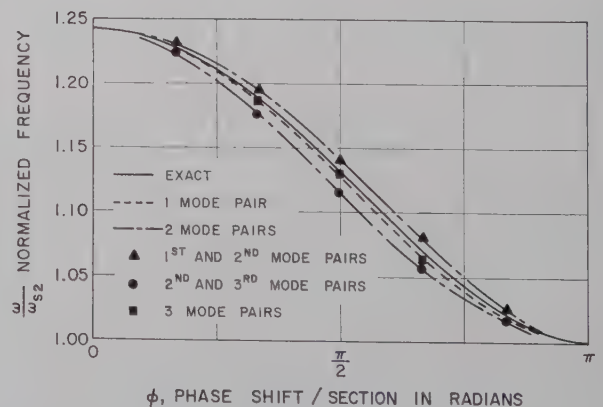
terms of the mode expansions discussed above, the curves are marked "single mode-pair case"; for trial fields of two terms from each expansion, the terminology "two mode-pair case" is used, etc.

The loading factor is defined as the ratio of the susceptance of one of the shunt capacitors to the characteristic admittance of the unloaded line at a normalized frequency of 1. Fig. 7 shows the  $\omega$  vs  $\phi$  characteristics for the first two pass bands for the various trial fields. Fig. 8 shows the  $\omega$  vs  $\phi$  curves for various loading factors (various amounts of shunt loading) for the first two pass bands.

Notice that in Fig. 7(b) the two mode-pair approximations give poorer results than does the single mode-pair case. When two modes are used for a trial field, one mode would be the one corresponding to the second pass band and the other would correspond to either the first or third pass band. But the corrections in  $\omega$  resulting from the resonant modes corresponding to the first and third pass bands are of equal magnitude. Inclusion of the first and not the third pass band contribution causes more of an error than if both extra terms were not used.



(a)



(b)

Fig. 7—(a) The  $\omega$  vs  $\phi$  characteristics for the periodically loaded transmission line for the first pass band. (b) The  $\omega$  vs  $\phi$  characteristics for the periodically loaded transmission line for the second pass band.



Notice that the three mode-pair case using resonant modes corresponding to all three pass bands is more accurate.

Fig. 8 indicates that as the shunt loading is increased, the mode-coupling equations give better results. This is due to the fact that coupling between adjacent sections of the structure is weaker and each section behaves more like an independent cavity. The trial fields then resemble the actual fields more closely and hence we get better results.

#### IV. CONCLUSIONS

It has been shown that a mode-coupling approach to the solution of a heavily-loaded periodic structure leads to simple and appealing equations. Moreover, the mode-coupling approach is shown to have as its formal mathematical basis the variational principle which allows the use of approximations in field configurations. Indeed, the use of a variational principle guarantees that the approximations resulting from the chosen trial field configurations are made in a systematic way

so as to give the optimum value of  $\omega$  or  $k^2$  for a given phase shift per section,  $\phi$ . It is legitimate to make the small errors in choosing trial fields as long as one knows that these errors lead to errors of lower order in the final results, the values of  $\omega$  or  $k^2$ .

Also, the mode-coupling or variational technique did lead to an acceptable and simple equivalent lumped circuit for a periodic structure with heavy shunt loading. This form of equivalent circuit has been assumed many times without the mathematical verification for its validity.

The single mode-pair coupling coefficient between sections of the periodic structure has the form

$$\frac{\int_{S_1'} \mathbf{a}_z \times \mathbf{e}_m^*(0^+) \cdot \mathbf{H}_n(0^+) da}{\int_V \mathbf{e}_m^* \cdot \mathbf{E}_n dV},$$

which gives a clear indication as to the mechanism involved in this coupling. What one must do to increase or decrease or change the sign of this coupling is also clear. Very complicated coupling schemes have been studied from the point of view of mode coupling and it is easy to predict qualitative behavior of these complicated structures [6].

One must realize that mode coupling as used here, is an intuitive concept, in that it allows the intuition to help in getting an approximate solution to a complicated problem. Mode coupling provides the trial fields which are then used with a variational principle to arrive at mathematically-sound expressions for approximate answers.

#### APPENDIX I

It is to be understood that (6) is a variational principle for  $\omega$  if it can be shown that for first-order variations of the trial fields from the exact fields, the first-order variation in  $\omega$  vanishes. There remain only second- and higher-order variations in  $\omega$ . Consider  $\mathbf{E}_+$  to be the exact field existing in the periodic structure. We do not know the details of this exact field solution, but we can make reasonable guesses from experience as to what the field should look like. As a trial field, we then do not use  $\mathbf{E}_+$  because we don't know it, but we use a trial field which may be expressed as the exact field plus a small functional variation,

$$\mathbf{E}_+^T = \mathbf{E}_+ + \delta \mathbf{E}_+. \quad (40)$$

We wish to see how the variations of all the fields appearing in (6) affect the value of  $\omega$ . Notice that the variational notation  $\delta$  used as an operator is commutative with respect to differentiation, so we can perform

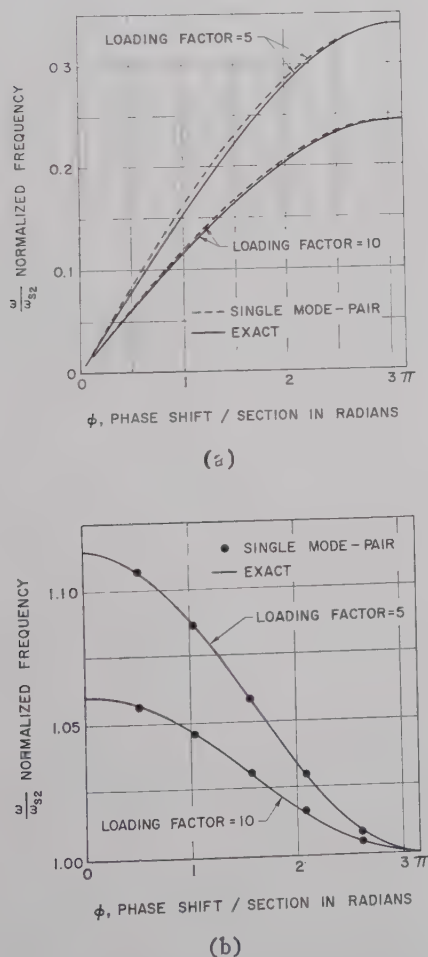


Fig. 8—(a) The  $\omega$  vs  $\phi$  characteristics for two loading factors for the first pass band. (b) The  $\omega$  vs  $\phi$  characteristics for two loading factors for the second pass band.

the following type of transformation,

$$\begin{aligned} \int_V \mathbf{E}_-^* \cdot \nabla \times \delta \mathbf{H}_+ dV &= \int_V \delta \mathbf{H}_+ \cdot \nabla \times \mathbf{E}_-^* dV \\ &+ \oint \mathbf{n}_0 \times \delta \mathbf{H}_+ \cdot \mathbf{E}_-^* da. \end{aligned} \quad (41)$$

We can then find the first-order variation of  $\delta[\omega]$  to be

$$\begin{aligned} j\delta[\omega] &\left[ \mu \int_V \mathbf{H}_+ \cdot \mathbf{H}_-^* dV + \epsilon \int_V \mathbf{E}_+ \cdot \mathbf{E}_-^* dV \right] \\ &= \int_V \delta \mathbf{E}_-^* \cdot (\nabla \times \mathbf{H}_+ - j\omega\epsilon \mathbf{E}_+) dV \\ &- \int_V \delta \mathbf{H}_-^* \cdot (\nabla \times \mathbf{E}_+ + j\omega\mu \mathbf{H}_+) dV \\ &- \int_V \delta \mathbf{E}_+ \cdot (\nabla \times \mathbf{H}_-^* + j\omega\epsilon \mathbf{E}_-^*) dV \\ &+ \int_V \delta \mathbf{H}_+ \cdot (\nabla \times \mathbf{E}_-^* - j\omega\mu \mathbf{H}_-^*) dV \\ &- \oint \mathbf{n}_0 \times \mathbf{E}_-^* \cdot \delta \mathbf{H}_+ da - \oint \mathbf{n}_0 \times \delta \mathbf{E}_+ \cdot \mathbf{H}_-^* da. \end{aligned} \quad (42)$$

Since we know that the  $\mathbf{E}_+$  and  $\mathbf{H}_+$  (exact) fields satisfy Maxwell's equations, the first two terms on the right-hand side of (42) vanish. Also, we see that the adjoint solution is the wave solution that must satisfy

$$\nabla \times \mathbf{E}_-^* - j\omega\mu \mathbf{H}_-^* = 0 \quad (43)$$

$$\nabla \times \mathbf{H}_-^* + j\omega\epsilon \mathbf{E}_-^* = 0, \quad (44)$$

if the third and fourth terms on the right-hand side of (42) are to vanish. We are further constrained to have as a boundary condition on the adjoint solution

$$\mathbf{n}_0 \times \mathbf{E}_-^* = 0 \quad \text{on } S, \quad (45)$$

and we must also be careful in choosing trial fields so that

$$\mathbf{n}_0 \times \delta \mathbf{E}_+ = 0 \quad \text{on } S. \quad (46)$$

In order to show that  $\delta\omega$ , the first-order variation of  $\omega$ , vanishes for arbitrary variations of the fields, we must deal with the surface integrals over the plane of the coupling holes  $S_1'$  and  $S_2'$ .

One way to make these surface integrals vanish is to have the integrals over  $S_1'$  cancel those over  $S_2'$ . If we choose trial fields which satisfy Floquet's theorem, then we see that if the adjoint solution satisfies Floquet's theorem we have for one of the integrals,

$$\begin{aligned} &\int_{S_1'} \mathbf{n}_0 \times \mathbf{E}_-^*(0) \cdot \delta \mathbf{H}_+(0) da \\ &+ \int_{S_2'} \mathbf{n}_0 \times \mathbf{E}_-^*(L) \cdot \delta \mathbf{H}_+(L) da. \end{aligned} \quad (47)$$

But  $\mathbf{n}_0$  on  $S_2'$  is the unit vector  $\mathbf{a}_z$  and  $\mathbf{n}_0$  on  $S_1'$  is  $-\mathbf{a}_z$ . Also, we choose trial fields so that

$$\delta \mathbf{H}_+(L) = \delta \mathbf{H}_+(0) e^{-\gamma L}. \quad (48)$$

Then, if we have

$$\mathbf{E}_-(L) = \mathbf{E}_-(0) e^{-\gamma L}, \quad (49)$$

it is seen the surface integral  $S_1'$  cancels the one over  $S_2'$  for  $\gamma$  imaginary. Also, we are forced to have

$$\begin{aligned} \delta \mathbf{E}_+(L) &= \delta \mathbf{E}_+(0) e^{-\gamma L} \\ \mathbf{H}_-(L) &= \mathbf{H}_-(0) e^{-\gamma L}, \end{aligned} \quad (50)$$

in order that the last integral in (42) be zero. This means that the adjoint fields satisfy Floquet's theorem and so satisfy all the constraints that the original fields  $\mathbf{E}_+$  and  $\mathbf{H}_+$  do. But it is important to notice that the trial fields must be chosen so that the variations in the  $\mathbf{E}_+$  and  $\mathbf{H}_+$  fields satisfy Floquet's theorem and this will be fulfilled if the trial fields themselves satisfy Floquet's theorem. Under all these constraints, (6) is a variational principle for  $\omega$ .

Notice the important point in this mathematical development that although the adjoint solution satisfies the same constraints that the original fields do, we are not constrained to make the adjoint the same as the original solution. This degree of freedom in choosing the adjoint solution is the key to the treatment of the periodic cavity structure.

## APPENDIX II

To show that (32) is actually a variational principle for  $k^2$ , we find the first-order variation in  $k^2$  using the usual variational operational notation. Notice that the double transformation of the integral below leads to two surface integrals.

$$\begin{aligned} \int_V \mathbf{E}_-^* \cdot \nabla \times \nabla \times \delta \mathbf{E}_+ dV &= \int_V \nabla \times \delta \mathbf{E}_+ \cdot \nabla \times \mathbf{E}_-^* dV \\ &+ \oint \mathbf{n}_0 \times (\nabla \times \delta \mathbf{E}_+) \cdot \mathbf{E}_-^* da \\ &= \int_V \delta \mathbf{E}_+ \cdot \nabla \times \nabla \times \mathbf{E}_-^* dV \\ &+ \oint \mathbf{n}_0 \times \delta \mathbf{E}_- \cdot (\nabla \times \mathbf{E}_-^*) da \\ &+ \oint \mathbf{n}_0 \times (\nabla \times \delta \mathbf{E}_+) \cdot \mathbf{E}_-^* da. \end{aligned} \quad (51)$$

By use of (51) a variation of (32), yields

$$\begin{aligned} &\left[ \int_V \mathbf{E}_+ \cdot \mathbf{E}_-^* dV \right] \delta[k^2] \\ &= \int_V \delta \mathbf{E}_-^* \cdot [\nabla \times \nabla \times \mathbf{E}_+ - k^2 \mathbf{E}_+] dV. \end{aligned}$$



$$\begin{aligned}
& + \int_V \delta \mathbf{E}_+ \cdot [\nabla \times \nabla \times \mathbf{E}_+^* - k^2 \mathbf{E}_+^*] dV \\
& + \oint \mathbf{n}_0 \times (\nabla \times \delta \mathbf{E}_+) \cdot \mathbf{E}_+^* da \\
& + \oint \mathbf{n}_0 \times \delta \mathbf{E}_+ \cdot (\nabla \times \mathbf{E}_+^*) da. \quad (52)
\end{aligned}$$

If we substitute into (52) the exact solution for the periodic structure,  $\delta \mathbf{E}_+ = 0$  everywhere and we see that

$$\delta[k^2] = 0. \quad (53)$$

Then, (32) is a variational principle for  $k^2$  but it remains for us to find the constraints on the  $\mathbf{E}_-$  field. Clearly, if  $\delta \mathbf{E}_+$  is not zero, we must have

$$\nabla \times \nabla \times \mathbf{E}_-^* - k^2 \mathbf{E}_-^* = 0 \quad (54)$$

to make the right-hand side of (52) zero. A boundary condition that

$$\mathbf{n}_0 \times \mathbf{E}_-^* = 0 \quad \text{on } S \quad (55)$$

is also required, as well as the constraint of (5). We are constrained to choose the trial field so that

$$\mathbf{n}_0 \times \delta \mathbf{E}_+ = 0 \quad \text{on } S, \quad (56)$$

in addition to the properties for  $\mathbf{E}_-$  found in Appendix I. Also, if the trial field  $\mathbf{E}_+^T$  is constructed so as to satisfy Floquet's theorem, we see that the surface integrals vanish again and (32) is a variational principle for  $k^2$ .

#### ACKNOWLEDGMENT

The authors wish to express their thanks to Prof. H. Haus, who initiated this research program and who also contributed so generously to its successful conclusion. Thanks also go to Prof. L. Smullin and the members of the Microwave Tube Laboratory of the Research Laboratory of Electronics, M.I.T., for their deep interest in our work.

#### BIBLIOGRAPHY

- [1] M. Chodorow and R. A. Craig, "Some new circuits for high-power traveling-wave tubes," *Proc. IRE*, vol. 45, pp. 1106-1118; August, 1957.
- [2] R. M. Bevensee, "Coupling-of-Modes Theory of Periodic Lossless, Electromagnetic Cavity Chains," E.E. thesis, Dept. of Electrical Engrg., Mass. Inst. Tech., Cambridge, Mass.; December, 1957. See also "Periodic Electromagnetic and Quantum Systems," to appear in the *Annals of Physics*.
- [3] ———, "Mode Coupling in Periodic Cavity Chains," Res. Lab. of Electronics, Mass. Inst. Tech., Cambridge, Quart. Prog. Rept., p. 25; October 15, 1957.
- [4] L. Brillouin, "Wave Propagation in Periodic Structures," McGraw-Hill Book Co., Inc., New York, N. Y.; 1946.
- [5] J. C. Slater, "Microwave Electronics," D. Van Nostrand Co., Inc., Princeton, N. J.; 1954.
- [6] T. J. Goblick, "A Study of Mode Coupling in Periodic Structures," M.S. thesis, Dept. of Electrical Engrg., Mass. Inst. Tech., Cambridge; 1958.
- [7] ———, "Mode Coupling in a Periodically Loaded Transmission Line," Res. Lab. of Electronics, Mass. Inst. Tech., Cambridge, Quart. Prog. Rept., p. 50; January 15, 1958.
- [8] H. A. Haus, "Electron beam waves in microwave tubes," *Proc. Symp. on Electronic Waveguides*, Polytechnic Inst. of Brooklyn, Brooklyn, N. Y., p. 89; April, 1958.
- [9] P. M. Morse and H. Feshbach, "Methods of Theoretical Physics, II," McGraw-Hill Book Co., Inc., New York, N. Y.; 1953.
- [10] F. B. Hildebrand, "Methods of Applied Mathematics," Prentice Hall, Inc., New York, N. Y.; 1952.

# Determination of the Capacitance, Inductance, and Characteristic Impedance of Rectangular Lines\*

TSUNG-SHAN CHEN†, MEMBER, IRE

**Summary**—This paper determines the capacitance, inductance, and characteristic impedance of rectangular lines by the method of conformal transformation. In practical applications, such lines may be used as transmission links of RF energy, as impedance-transforming sections, or as components in electron tubes.

Formulas are given for the calculation of the parameters of rectangular lines having the following characteristics: 1) The inner conductor may have varying thickness compared with the depth of the outer conductor. 2) The axes of the conductors may coincide or may be displaced with respect to each other. 3) The edges of the inner conductor may be rounded to lessen the electrical stress occurring at sharp corners.

Excellent agreement has been obtained between the calculated results and those found by use of the relaxation method, by direct measurement of models, and by electrolytic tank measurement.

## I. INTRODUCTION

THE rectangular line consists of a rectangular inner conductor located symmetrically or asymmetrically inside a rectangular hollow outer conductor in a manner similar to a coaxial line. When the depth of each conductor is equal to its width, the line becomes a square line. The electric and magnetic fields in such a geometry bear a close resemblance to those in a coaxial line, especially for the case of a small inner conductor. If the ratio of width to depth in both conductors is large and the inner conductor forms a flat strip, the field patterns in the rectangular line approach those existing in a shielded strip line.<sup>1</sup> Thus, the rectangular line, besides being used to transmit RF energy, may serve as an impedance transformer interposed between coaxial and strip transmission lines.

This article concerns the determination of the capacitance, inductance and characteristic impedance of rectangular lines where the inner conductor may be thick or thin in comparison with the depth of the outer conductor. If the spacings between the conductors are small relative to their width and depth, the line parameters can be determined analytically even when the inner conductor is placed asymmetrically with respect to the outer one. For the purpose of reducing the electrical stress in the annular region between conductors, the edges of the inner conductor are rounded, and the effect of rounding the corners on the line parameters is evaluated.

The parameters of rectangular lines calculated by means of the formulas derived here agree very closely with the results obtained by the relaxation method, by direct measurement of full-sized models and by electrolytic tank measurement.

## II. RELATION BETWEEN THE INTER-CONDUCTOR CAPACITANCE AND THE CHARACTERISTIC IMPEDANCE

The rectangular line is essentially a two-wire transmission system along which TEM waves are propagating. The velocity of propagation, when dissipation is neglected, equals the velocity of light, and is given by

$$v = 1/(\mu\epsilon)^{1/2} = 1/(LC)^{1/2}. \quad (1)$$

The characteristic impedance of such a lossless line is given by

$$Z = (L/C)^{1/2} = 1/(vC). \quad (2)$$

In MKS units, the quantities used in (1) and (2) are as follows:

- $Z$  = characteristic impedance of the line in ohms
- $L$  = inductance of the line in henries per meter
- $C$  = capacitance of the line in farads per meter
- $v$  = velocity of propagation in free space in meters per second
- $= 2.998 \times 10^8$  meters per second
- $\mu$  = permeability of free space
- $= 4\pi \times 10^{-7} = 1.257 \times 10^{-6}$  henry per meter
- $\epsilon$  = permittivity of free space
- $= 1/(36\pi) \times 10^{-9} = 8.854 \times 10^{-12}$  farad per meter.

Eq. (2) shows that the evaluation of the characteristic impedance of rectangular lines reduces to the determination of the interconductor capacitance by experimental or analytical means. The experimental determination of the capacitance between the conductors can be accomplished by direct measurement of a full-scale model or by mapping the equipotentials and flux lines existing between appropriate electrode shapes placed in an electrolytic tank.

The analytical process of obtaining the capacitance is based upon the solution of Laplace's equation for a static field in two dimensions subjected to proper boundary conditions. The solution involves the determination of the potential functions, the flux lines, and the charge distribution on the electrodes. A numerical result can be found for a specific problem by use of the

\* Received by the PGMTT, April 11, 1960; revised manuscript received, May 31, 1960.

† Electron Tube Div., Radio Corp. of America, Harrison, N. J.

<sup>1</sup> R. M. Barrett, "Microwave printed circuits—a historical survey," IRE TRANS. ON MICROWAVE THEORY AND TECHNIQUES, vol. MTT-3, pp. 1-9; March, 1955.



relaxation method,<sup>2</sup> or analytical expressions may be obtained from formal mathematics.

If the conductor geometries are simple, such as concentric spheres or parallel cylinders, Laplace's equation can be integrated formally, and boundary conditions are applied to get explicit solutions. In other cases, the two-dimensional differential equation can be solved by means of conjugate functions, the real or imaginary parts of which represent the potential or flux functions. When the conductor boundary assumes a polygon, the determination of the proper conjugated function can be effected by means of the Schwarz-Christoffel transformation.

### III. RECTANGULAR LINE WITH SMALL SPACINGS BETWEEN CONDUCTORS

Fig. 1 illustrates the configuration of a symmetrical rectangular line. The exact determination of the capacitance by the method of conformal transformation involves hypergeometric functions and four variable parameters; the process of obtaining numerical results would be so laborious that it has not been attempted. If the sides of the conductors are large compared with their spacings, the distorted fields at the two ends along the same side of the inner conductor do not interact, and only one quarter of the cross section needs to be transformed. The interconductor capacitance can then be calculated as a combination of parallel-plate condensers formed by the walls of the conductors, plus excess capacitance caused by the disturbances of flux lines close to the corners. In fact, this method is valid whenever the short side of the inner conductor exceeds the spacing distances, as evidenced by the negligible amount of flux distortion at points not far away from the bend shown in Fig. 2.

#### A. Line Capacitance

One corner of the line cross section assumes the shape of a right-angle bend; two successive transformations are necessary in this case as discussed in Appendix I.<sup>3,4</sup> The first process transforms the  $z$ -plane polygon into the real axis of the  $t$  plane, and another transformation from the  $w$  plane to the  $t$  plane relates the potentials of the two conductors to values of  $t$ . The capacitance between the conductors is evaluated by letting  $z$  as well as  $t$  take critical values which depend on the particular problem.

In the L-shaped bend, the excess or fringing capacitance caused by the disturbance of flux lines eman-

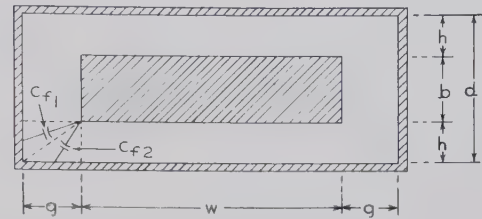


Fig. 1—The symmetrical rectangular line.

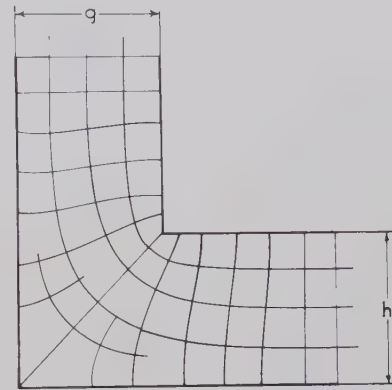


Fig. 2—Distortion of electric field at one corner of the rectangular line.

ating at the vertical side is expressed by

$$C_{f1} = \frac{\epsilon}{\pi} \left[ \log \frac{g^2 + h^2}{4h^2} + 2 \left( \frac{h}{g} \right) \arctan \frac{g}{h} \right] \quad \text{farads per meter, (3)}$$

where  $g$  is the lateral spacing and  $h$  the vertical spacing. Similarly, the equation for fringing capacitance produced by flux disturbance along half of the horizontal side is

$$C_{f2} = \frac{\epsilon}{\pi} \left[ \log \frac{g^2 + h^2}{4g^2} + 2 \left( \frac{g}{h} \right) \arctan \frac{h}{g} \right] \quad \text{farads per meter. (4)}$$

On the supposition that the conductor sides are large, the fringing capacitance depends only on the spacings and not on the conductor dimensions. The ratios  $C_{f1}/\epsilon$  and  $C_{f2}/\epsilon$  are plotted in Fig. 3 as a function of  $h/g$  or of  $g/h$ . The total capacitance between the conductors is

$$C = 2\epsilon \left( \frac{w}{h} + \frac{b}{g} \right) + \frac{4\epsilon}{\pi} \left[ \log \frac{g^2 + h^2}{4h^2} + 2 \left( \frac{h}{g} \right) \arctan \frac{g}{h} \right] + \frac{4\epsilon}{\pi} \left[ \log \frac{g^2 + h^2}{4g^2} + 2 \left( \frac{g}{h} \right) \arctan \frac{h}{g} \right] \quad \text{farads per meter, (5)}$$

<sup>2</sup> R. V. Southwell, "Relaxation Methods in Engineering Science," Oxford University Press, Oxford, Eng.; 1940. "Relaxation Methods in Theoretical Physics," Oxford University Press, Oxford, Eng., vol. I, 1946; vol. II, 1956.

<sup>3</sup> J. J. Thomson, "Recent Researches in Electricity and Magnetism," Oxford University Press, Oxford, Eng.; 1893.

<sup>4</sup> J. H. Jeans, "The Mathematical Theory of Electricity and Magnetism," Cambridge University Press, Cambridge, Eng., 5th ed.; 1925.

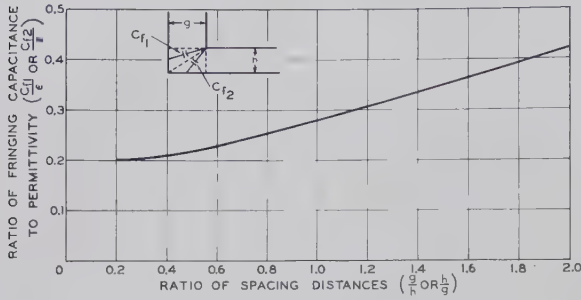


Fig. 3—Ratio of fringing capacitance to permittivity ( $C_{f1}/\epsilon$ , or  $C_{f2}/\epsilon$ ) as a function of the spacing ratio ( $g/h$  or  $h/g$ ).

where  $w$  and  $b$  are, respectively, the width and thickness of the inner conductor. If  $g=h$ , both (3) and (4) reduce to

$$C_f = \frac{\epsilon}{\pi} \left[ \frac{\pi}{2} - \log 2 \right] = 0.279\epsilon, \quad (6)$$

and the line capacitance is expressed by

$$C = \frac{2\epsilon(w+b)}{g} + 2.232\epsilon. \quad (7)$$

### B. Line Inductance

The method of conformal transformation demonstrates that the fringing effect caused by charge concentration close to the edges of the inner conductor may be accounted for by the addition of correction lengths to the conductor sides. In Fig. 2, half of the vertical side of inner conductor should be increased by the amount

$$X_1 = \frac{1}{\pi} \left[ g \log \frac{g^2 + h^2}{4h^2} + 2h \arctan \frac{g}{h} \right] = g \frac{C_{f1}}{\epsilon}. \quad (8)$$

The extension in half of the horizontal side,  $X_2 = hC_{f2}/\epsilon$ , can be obtained from (8) by interchanging  $g$  and  $h$ . When the effective lengths of the sides are used in the formula for calculating the inductance of parallel-plate transmission lines, the inductance of the rectangular line  $L$  is given by

$$L = \frac{L_v L_H}{L_v + L_H} \text{ henries per meter.} \quad (9)$$

In this expression,  $L_v$  and  $L_H$  are the inductances corresponding to the vertical and horizontal parallel-plate systems and are, respectively, given by

$$L_v = \frac{1}{2} \frac{\mu g}{b + \frac{2}{\pi} \left[ g \log \frac{g^2 + h^2}{4h^2} + 2h \arctan \frac{g}{h} \right]}, \quad (10)$$

and

$$L_H = \frac{1}{2} \frac{\mu h}{w + \frac{2}{\pi} \left[ h \log \frac{g^2 + h^2}{4g^2} + 2g \arctan \frac{h}{g} \right]}. \quad (11)$$

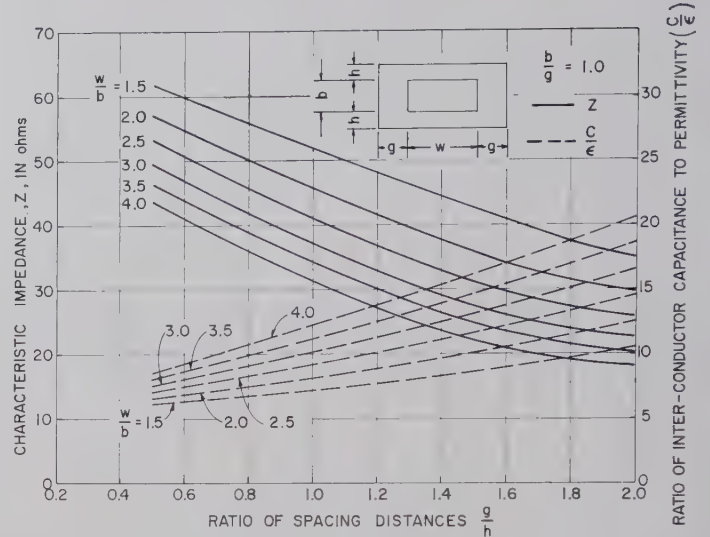


Fig. 4—Characteristic impedance and interconductor capacitance of symmetrical rectangular lines ( $b/g = 1$ ).

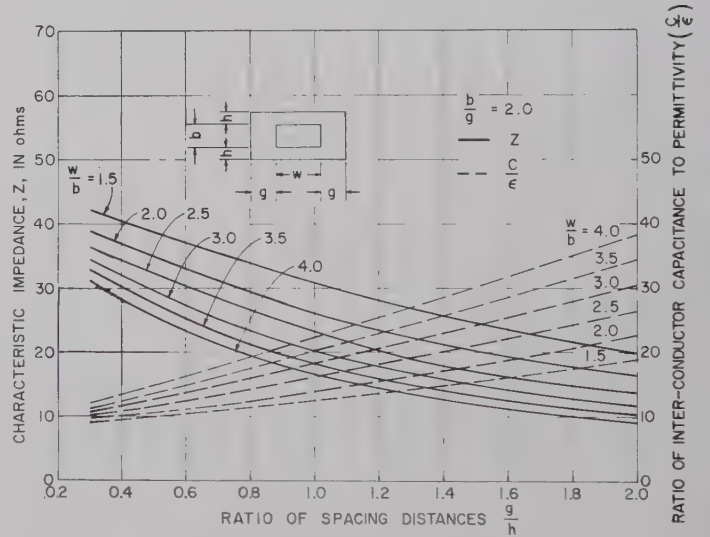


Fig. 5—Characteristic impedance and interconductor capacitance of symmetrical rectangular lines ( $b/g = 2$ ).

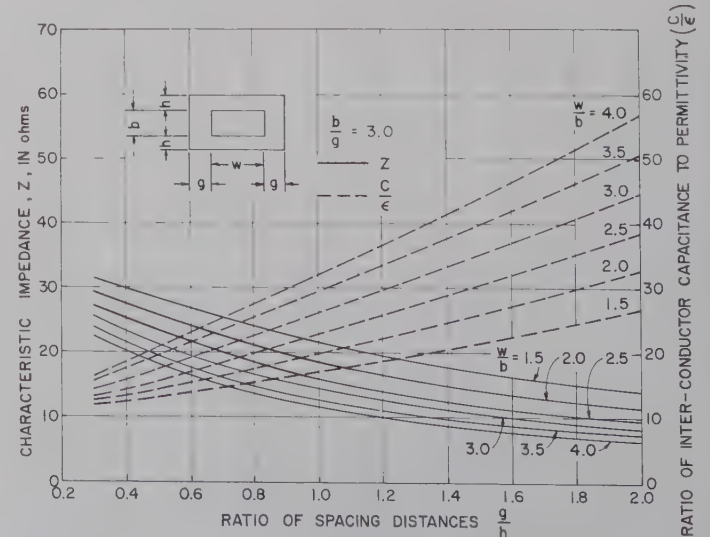


Fig. 6—Characteristic impedance and interconductor capacitance of symmetrical rectangular lines ( $b/g = 3$ ).



### C. Characteristic Impedance of a Rectangular Line

When the line is concentric as shown in Fig. 1, the characteristic impedance can be obtained by use of (2), in which the capacitance given by (5) has been employed. Then

$$Z = \frac{376.62}{2\left(\frac{b}{g} + \frac{w}{h}\right) + \left(\frac{C_{f1}}{\epsilon} + \frac{C_{f2}}{\epsilon}\right)} \text{ ohms.} \quad (12)$$

The rectangular line in which  $g=h$  has the characteristic impedance is

$$Z = \frac{376.62}{2\left(\frac{b+w}{g}\right) + 2.232} \text{ ohms.} \quad (13)$$

For a line having the dimensions,  $w=0.218$ ,  $b=0.050$ , and  $g=h=0.050$  inch, the line capacitance as determined from (7) is  $C = (10.72 + 2.232)\epsilon = 12.952\epsilon = 114.677 \times 10^{-12}$  farad per meter. The inductance of the line is equivalent to that of a parallel-plate system which has a separation of 0.050 inch and an effective width of

$$2(0.218 + 0.050) + 8\left(\frac{1}{\pi}\right)\left(\frac{\pi}{2} - \log 2\right)(0.05) = 0.6438 \text{ inch.}$$

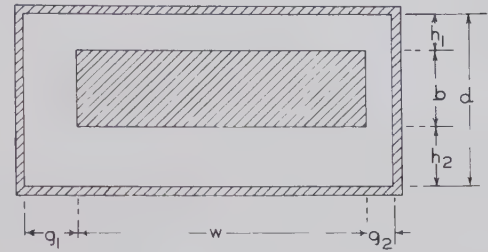


Fig. 7—Doubly eccentric rectangular line.

### D. Doubly Eccentric Rectangular Line

The inner conductor may be displaced both horizontally and vertically with respect to the outer conductor so that the line becomes doubly eccentric, as shown in Fig. 7. The capacitance between the conductors becomes

$$C = \epsilon \left( \frac{b}{g_1} + \frac{b}{g_2} + \frac{w}{h_1} + \frac{w}{h_2} \right) + \sum_{m=1,2}^{n=1,2} \frac{\epsilon}{\pi} \left[ \log \frac{g_n^2 + h_m^2}{4h_m^2} + 2\left(\frac{h_m}{g_n}\right) \arctan \frac{g_n}{h_m} \right] + \sum_{m=1,2}^{n=1,2} \frac{\epsilon}{\pi} \left[ \log \frac{g_n^2 + h_m^2}{4g_n^2} + 2\left(\frac{g_n}{h_m}\right) \arctan \frac{h_m}{g_n} \right]. \quad (14)$$

Eight different terms of fringing capacitance are involved in the last expression. There are also eight different correction lengths for the determination of the line inductance. The characteristic impedance can be written as

$$Z = \frac{376.62}{\sum_{n=1,2} \frac{b}{g_n} + \sum_{m=1,2} \frac{w}{h_m} + \frac{1}{\epsilon} \left[ \sum_{m=1,2}^{n=1,2} C_{f1}(g_n, h_m) + \sum_{m=1,2}^{n=1,2} C_{f2}(g_n, h_m) \right]}. \quad (15)$$

The value of this inductance is as follows:

$$L = \frac{\mu(0.05)}{0.6438} = \frac{\mu}{12.876} = 9.755 \times 10^{-8} \text{ henry per meter.}$$

The velocity of wave propagation is  $v=1/(LC)^{1/2} = 2.992 \times 10^8$  meters per second, which is very close to the accepted value of  $2.998 \times 10^8$ . The characteristic impedance of the line is found to be 29.12 ohms.

By using relaxation calculation, W. N. Parker, of the RCA Electron Tube Division, Lancaster, Pa., has found the characteristic impedance of the same structure to be 27.8 ohms, while the result of electrolytic tank measurement conducted under his direction is slightly less than 27 ohms. The characteristic impedance and inter-conductor capacitance of rectangular lines have been calculated by means of (5) and (12) for a variety of dimensions; the results are plotted in Figs. 4-6.

The capacitance of a singly eccentric line having the dimensions  $w=0.120$ ,  $b=0.041$ ,  $g=0.027$ ,  $h_1=0.019$  and  $h_2=0.0462$  inch as calculated from (14) is

$$C = [6.312 + 2.603 + 3.034 + 2(0.244 + 0.342 + 0.224 + 0.382)]\epsilon = 14.336\epsilon = 126.931 \times 10^{-12} \text{ farad per meter.}$$

After the computation of the correction lengths from equations similar to (8), the component inductances pertaining to the upper, lower, right and left parallel-plate guides are

$$L_{\text{upper}} = \frac{\mu(0.019)}{0.120 + 2(0.0046)} = 0.1466\mu,$$

$$L_{\text{lower}} = \frac{\mu(0.0462)}{0.120 + 2(0.0176)} = 0.2975\mu,$$

$$L_{\text{right}} = L_{\text{left}} = \frac{\mu(0.027)}{0.041 + 0.0092 + 0.0061} = 0.479\mu.$$

The sum of the reciprocals of the component inductances equals the reciprocal of the line inductance. This relation yields the value

$$L = \mu/14.357 = 8.756 \times 10^{-8} \text{ henry per meter.}$$

The velocity of propagation as obtained from  $v=1/(LC)^{1/2}$  is  $3 \times 10^{-8}$  meters per second, and the characteristic impedance from  $Z=1/vC$  is 26.2 ohms. The capacitance of a full-sized model of such a line was measured by R. Schumacher of RCA Electron Tube Division, Lancaster, Pa., and found to be  $128.9 \times 10^{-12}$  farad per meter. This value of capacitance gives an impedance of 25.9 ohms.

The preceding formulas for calculation of the parameters of rectangular lines give accurate results when  $g$  and  $h$  are, respectively, less than  $w$  and  $b$ . This conclusion is substantiated by the flux mapping of the L-shaped bend and by comparison of the result so calculated with the exact solution. The flux distribution becomes almost uniform at a distance from the corner equal to half the spacing. If the thickness of the inner conductor is too small, the distorted fields at the two ends of the short side interfere, and the formulas so far derived do not provide sufficient accuracy.

#### IV. RECTANGULAR LINES WITH THIN INNER CONDUCTORS

Rectangular lines often occur where one side of the inner conductor is smaller than the spacing between the two conductors. The line capacitance in such cases has been treated by J. D. Cockcroft<sup>5</sup> as discussed in Appendix II, in which the Schwarz-Christoffel transformation is applied to one half of the conductor cross section. The exact solution involves elliptic functions and theta functions, and the determination of the variables to give required conductor dimensions becomes very complex. For a certain range of conductor spacings and sizes, the expressions take comparatively simple form. The fictitious increase in the conductor side resulting from charge concentration at one complete corner is given by

$$X = \frac{1}{2k} \log \frac{2(k)^{1/2}}{q^{1/2}(1-k)} - \left( K - \frac{K'}{2} \right) \left( \frac{1+k}{2k} - \frac{\pi}{2kK} \right), \quad (16)$$

where  $q = \exp(-\pi K'/K)$ ,  $K$  is the complete elliptic integral to modulus  $k$ , and  $K'$  is the complementary integral. The dimensions of the conductors are given by

$$b/2 = K \left[ \frac{1+k}{2k} - \frac{\pi}{2kK} \right],$$

<sup>5</sup> J. D. Cockcroft, "The effect of curved boundaries on the distribution of electrical stress round conductors," *J. IEE*, vol. 66, pp. 385-409; April, 1928.

$$g = K' \left[ \frac{1+k}{2k} \right]; \quad h = \frac{\pi}{2k}.$$

The correction length for one corner is the essential factor that enters into the determination of both the capacitance and inductance of the line. Fig. 8 gives the values of  $C_f(g, b)/\epsilon = X/g$  as a function of  $b/g$  for the case  $g=h$ . It is to be noted that when the two sides of the inner conductor are short, the fringing capacitance for one corner is dependent on the short side  $b$  as well as on the spacings  $g$  and  $h$ . The case that  $b/g$  tends to infinity corresponds to a very thick inner conductor; then the fringing capacitance for one corner becomes twice that given in (6), and the correction length in (16) simplifies to

$$X = g \left[ 1 - \frac{2}{\pi} \log 2 \right]. \quad (17)$$

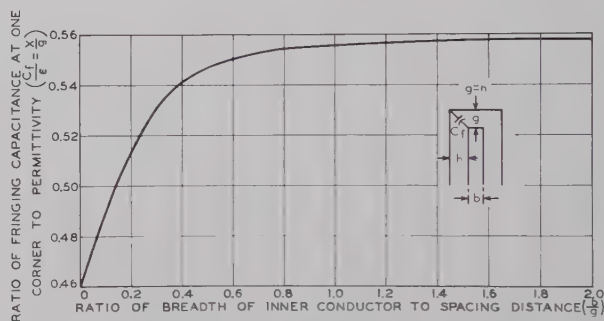


Fig. 8—Ratio of fringing capacitance to permittivity ( $C_f/\epsilon$ ) as a function of the ratio of breadth of inner conductor to spacing distance ( $b/g$ ).

The capacitance between the two conductors per unit length of line is

$$C = 2\epsilon \left( \frac{w+b}{g} \right) + 4C_f(g, b), \quad (18)$$

and the inductance of the line is determined from the equation

$$L = \frac{\mu g}{2(b+w) + 4X}, \quad (19)$$

in which  $X$  is found from (16) or from Fig. 8. The characteristic impedance of the line is as follows:

$$Z = \frac{376.62}{2 \left( \frac{w+b}{g} \right) + \frac{4C_f(g, h)}{\epsilon}} \text{ ohms.} \quad (20)$$

For the line having the dimensions  $w=0.218$ ,  $b=0.050$ , and  $g=h=0.050$  inch, the fringing capacitance found from Fig. 8 is  $4C_f(g, h)=4(0.5537\epsilon)=2.215\epsilon$ . The result calculated previously from the thick conductor formula is  $2.232\epsilon$ , which is very close to the above exact value.



### V. APPROXIMATE FORMULAS FOR THIN INNER CONDUCTORS

The expressions for the determination of the capacitance of the rectangular lines having thin inner conductors and unequal spacings contain complex combinations of elliptic functions, and are very difficult to evaluate in applications. It becomes necessary to derive approximate formulas yielding capacitance and inductance values of an accuracy comparable to those obtained from Cockcroft's exact solutions.

#### A. Inner Conductor of Zero Thickness

The capacitance between the conductors in Fig. 9(a) can be divided into three parts: 1) capacitance of parallel-plate capacitors formed by the horizontal walls of the conductors, 2) capacitance due to fringing flux lines from each end of the inner conductor to the opposite horizontal walls of the outer one, and 3) fringing capacitance caused by the presence of the lateral walls of the outer conductor.

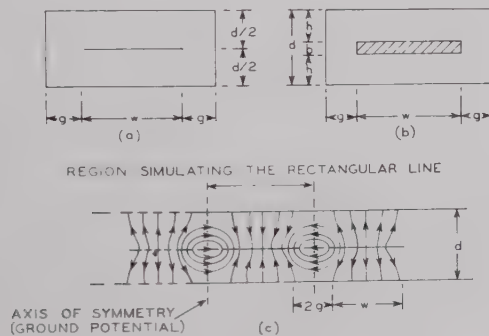


Fig. 9—(a) Rectangular line with inner conductor of zero thickness, (b) rectangular line with inner conductor of finite thickness, and (c) approximate field distribution in a shielded coupled-strip line operating in the odd mode.

The first capacitance can be readily determined. Inspection of Fig. 9(c) indicates that the disturbance of flux lines close to the ends of the inner conductor is not pronounced; consequently, the second item of capacitance can be neglected. The effect of sidewalls present in the outer conductor is the same as that obtained on the addition of a series of plates similar to the inner conductor spaced at  $2g$  between their ends, as shown in Fig. 9(c). The dotted lines are at the same potential as the two infinite plates and can be taken to represent the sidewalls of the rectangular line. From the character of the flux distribution, it can be seen that because of the sidewalls, the fringing capacitance equals that between two coupled, odd-mode strips located midway between two infinite parallel plates. Cohn<sup>6</sup> gives the capacitance

as follows:

$$C_{f0}\left(0, \frac{2g}{d}\right) = \frac{2\epsilon}{\pi} \log \left(1 + \coth \frac{\pi g}{d}\right), \quad (21)$$

where  $d$  is the spacing between the infinite plates. The line capacitance is given by

$$C = \frac{4\epsilon w}{d} + 4\epsilon \left[ \frac{2}{\pi} \log \left(1 + \coth \frac{\pi g}{d}\right) \right], \quad (22)$$

and the characteristic impedance of the line is

$$Z = \frac{376.62}{4 \left[ \frac{w}{d} + \frac{2}{\pi} \log \left(1 + \coth \frac{\pi g}{d}\right) \right]} \text{ ohms.} \quad (23)$$

If the dimensions of a rectangular line are  $w=0.300$ ,  $d=0.200$ ,  $b=0$ , and  $g=h=0.100$  inch, the capacitance as found from Fig. 8 becomes  $6\epsilon + 4(0.46)\epsilon = 7.84\epsilon$ , whereas (22) gives  $C = 6\epsilon + 1.88\epsilon = 7.88\epsilon$ .

#### B. Inner Conductor of Finite Thickness

When the thickness of the inner conductor is appreciable, but is less than  $d/3$ , the line capacitance can be determined by the method adopted for the case of the infinitely thin inner conductor. However, the fringing capacitance caused by the sidewalls should be corrected for the finite thickness of the inner conductor in Fig. 9(b).

Consider a semi-infinite plate of thickness  $b$  located in the middle of two infinite parallel plates which are separated at a distance  $d$ , as shown by Fig. 15(a) in Appendix III. The semi-infinite plate is charged to a potential  $V$ , and the two infinite plates are at ground potential. The fringing capacitance for one corner of the semi-infinite plate as obtained by Thomson is<sup>3</sup>

$$C_f = \left(\frac{b}{d}\right) = \frac{\epsilon}{\pi} \left[ \frac{d}{d-b} \log \frac{2d-b}{b} + \log \frac{b(2d-b)}{(d-b)^2} \right]. \quad (24)$$

If the thickness of the middle plate is reduced to zero, the fringing capacitance at one corner is then expressed by

$$C_f(0) = \frac{2\epsilon}{\pi} \log 2 = 0.4407\epsilon. \quad (25)$$

When applied to the rectangular line, the fringing capacitance for each corner of the inner conductor can be approximated by

$$C_f\left(\frac{b}{d}, \frac{2g}{d}\right) = C_{f0}\left(0, \frac{2g}{d}\right) \frac{C_f(b/d)}{C_f(0)}. \quad (26)$$

<sup>6</sup> S. B. Cohn, "Shielded coupled-strip transmission line," IRE TRANS. ON MICROWAVE THEORY AND TECHNIQUES, vol. MTT-3, pp. 29-38; October, 1955.

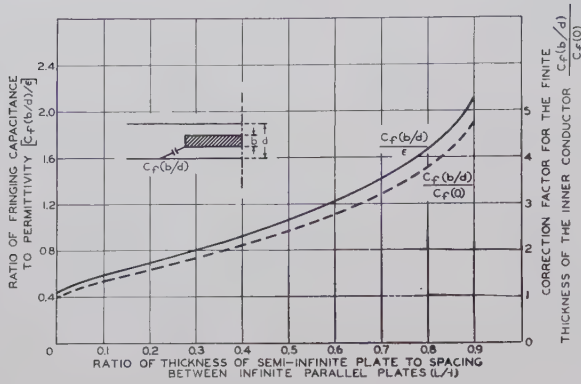


Fig. 10—Fringing capacitance at one corner for shielded semi-infinite plate and the correction factor for the thickness of the semi-infinite plate.

The term  $C_f(b/d)/\epsilon$  along with the ratio  $C_f(b/d)/C_f(0)$  is plotted in Fig. 10 as a function of  $b/d$ . The complete expressions for the line capacitance and characteristic impedance are, respectively

$$C = \frac{4\epsilon w}{d-b} + 4 \frac{\epsilon}{\pi} \left[ \frac{d}{d-b} \log \frac{2d-b}{b} + \log \frac{b(2d-b)}{(d-b)^2} \right] \frac{\log \left( 1 + \coth \frac{\pi g}{d} \right)}{\log 2}, \quad (27)$$

$$Z = \frac{1}{4\epsilon \left\{ \frac{w}{d-b} + \frac{1}{\pi} \left[ \frac{d}{d-b} \log \frac{2d-b}{b} + \log \frac{b(2d-b)}{(d-b)^2} \right] \right\} v} \text{ ohms.} \quad (30)$$

and

$$Z = \frac{376.62}{4 \left[ \frac{w}{d-b} + \frac{1}{\epsilon} C_{f0} \left( 0, \frac{2g}{d} \right) \frac{C_f(b/d)}{C_f(0)} \right]} \text{ ohms.} \quad (28)$$

A rectangular line has the description,  $w=0.218$ ,  $b=0.050$ ,  $d=0.150$ , and  $g=h=0.050$  inch. Eqs. (21), (24)–(26) yield, respectively,  $C_{f0}(0, 2g/d)=0.526\epsilon$ ,  $C_f(b/d)=0.839\epsilon$ ,  $C_f(0)=0.4407\epsilon$ , and  $C_f(b/d, 2g/d)=1.002\epsilon$ . The total capacitance of the line is  $C=8.72\epsilon + 4(1.002\epsilon)=12.728\epsilon$ , compared with the previously obtained results of  $12.952\epsilon$  and  $12.935\epsilon$  farads per meter.

A second line has the dimensions  $w=0.180$ ,  $b=0.030$ ,  $g=h=0.060$  inch. The use of Fig. 8 gives the result:

$$C = 2(0.180 + 0.030)\epsilon/0.060 + 4(0.548)\epsilon = 9.192\epsilon.$$

The preceding formulas give  $C_{f0}(0, 2g/d)=0.4954\epsilon$ ,  $C_f(b/d)=0.694\epsilon$ ,  $C_f(0)=0.4407\epsilon$ , and  $C_f(b/d, 2g/d)=0.781\epsilon$ . These values give a total capacitance:

$$C = 2\epsilon(0.180)/0.06 + 4(0.781)\epsilon = 9.124\epsilon.$$

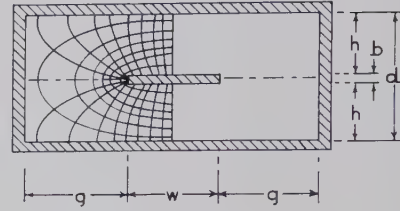


Fig. 11—Electric and magnetic fields in a rectangular line with narrow inner conductor.

## VI. RECTANGULAR LINES WITH NARROW INNER CONDUCTORS

When the flat inner conductor is not more than one-quarter as wide as the outer conductor, the effect of the presence of sidewalls may be ignored.<sup>7</sup> Thus, in Fig. 11, the fringing field at each end of the inner conductor has the same character as that occurring in a semi-infinite plate situated between two infinite parallel plates. If the rectangular line has a narrow inner conductor of negligible thickness, the expression for characteristic impedance, when (25) is used, should be the following:

$$Z = \frac{1}{4\epsilon \left( \frac{w}{d} + \frac{2}{\pi} \log 2 \right) v} \text{ ohms.} \quad (29)$$

When the inner conductor of the line has finite thickness, then by using (24),

The capacitance and inductance of such lines can be readily evaluated.

## VII. INNER CONDUCTOR WITH ROUNDED CORNERS

In applications involving high voltages, the annular space between the conductors may be subjected to high electrical stress. The stress at the sharp corners of the inner conductor can reach as much as six times the mean value.<sup>5</sup> To alleviate this stress concentration, the edges of the inner conductor are rounded. Cockcroft has treated the case when the spacings  $g$  and  $h$  are equal and are small compared with conductor sides, and has found that the electrical stress is considerably reduced by rounding the edges, but the change in capacitance is insignificant. The fringing capacitance at one corner is plotted in Fig. 12 in the form  $C_f/\epsilon$ , which is equivalent to  $X/g$ . The fringing effect decreases with the increase in the ratio of the radius of curvature  $R$  to the spacing  $g$ . The process of conformal representation for this case is given in Appendix IV.

<sup>7</sup> R. H. T. Bates, "The characteristic impedance of the shielded slab line," IRE TRANS. ON MICROWAVE THEORY AND TECHNIQUES, vol. MTT-4, pp. 28–33; January, 1956.



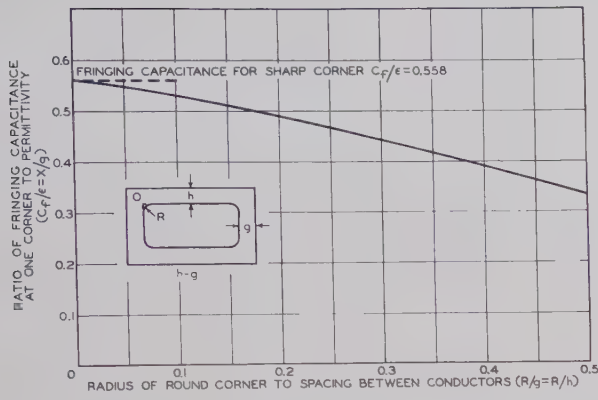


Fig. 12—Fringing capacitance for one round corner to permittivity as a function of the ratio of the corner radius to conductor spacing.

The fictitious increase in length of the sides may be utilized to calculate the capacitance and inductance of the line as follows:

$$C = 2\epsilon(w + b + 2X)/g, \quad (31)$$

and

$$L = \mu g / (2w + 2b + 4X). \quad (32)$$

The characteristic impedance can next be calculated from (2).

#### APPENDIX I L-SHAPED BEND

When the sides of the conductors are large compared with the spacings between them, one quarter of the cross section is to be considered. This portion of the cross section then constitutes a right-angled bend as shown in Fig. 13(a) and forms the polygon in the  $z$ -plane bounded by the lines  $ABC$  and  $DEF$ , which are maintained at potential  $V$  and zero, respectively. It can be assumed that  $t = -\infty$  at a distant point on  $AB$ ,  $t = -a$  at  $B$ ,  $t = 0$  at a distant point on  $BC$ , and  $t = 1$  at  $E$ . The internal angles of the polygon are  $\pi/2$  at  $B$ , zero at  $C$ , and  $3\pi/2$  at  $E$ . The quantity  $a$  has to be determined from the geometry of the system. The Schwarz-Christoffel transformation which turns the boundary of the polygon into the real axis in the  $t$  plane, shown in Fig. 13(b), is

$$\frac{dz}{dt} = A_1(t-1)^{1/2}(t-0)^{-1}(t-a)^{-1/2}. \quad (33)$$

The diagram in the  $w$  plane, shown in Fig. 13(c), consists of the real axis and a line parallel to it. The internal angle of the polygon is at  $t = 0$ , and is equal to zero. The transformation which turns this diagram into the real axis of the  $t$  plane is

$$\frac{dw}{dt} = B_1(t-1)^0(t-0)^{-1}(t-a)^0, \quad (34)$$

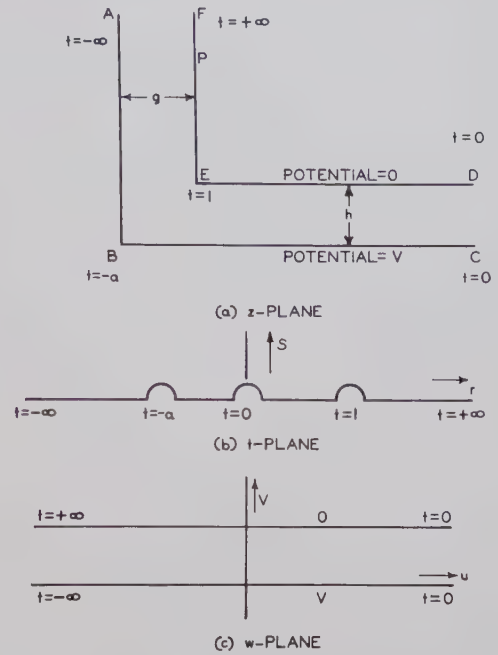


Fig. 13—Conformal transformation of the L-shaped bend.

which, upon integration and use of the boundary conditions, becomes

$$w = u + iv = \frac{V}{\pi} \log t. \quad (35)$$

To integrate (33), let

$$X = (t-1)^{1/2}(t-a)^{-1/2}, \quad (36)$$

and obtain

$$z = -2A_1(1/a)^{1/2} \arctan(a^{1/2}X) + A_1 \log \frac{1+X}{1-X}, \quad (37)$$

in which point  $E$  is chosen as the origin in the  $z$  plane. Consideration of the values of  $t$  and  $X$  at point  $B$  leads to the relations

$$g = A_1\pi, \quad h = A_1\pi(1/a)^{1/2}, \quad (h/g)^2 = 1/a. \quad (38)$$

Let  $P$  be a remote point on the line  $EF$ . The total charge on the strip  $EP$  per unit length in the direction normal to the plane of the paper is given by<sup>3,4</sup>

$$Q_{EP} = \left(\frac{V}{\pi}\right)\epsilon \left[ \log(a+1) + 2(1/a)^{1/2} \arctan a^{1/2} - 2 \log 2 + \frac{\overline{EP}}{A_1} \right].$$

If the flux lines were not disturbed, the charge on the strip  $EP$  would be  $(\overline{EP})\epsilon V/g$ , which is the last term in the preceding expression. The first three terms represent the excess charge caused by the flux disturbances. When the excess charge is divided by  $V$  and the relations in (38) are used, the fringing capacitance  $C_{f1}$  is obtained as

$$C_{f1} = \frac{\epsilon}{\pi} \left[ \log \frac{g^2 + h^2}{4h^2} + 2 \left( \frac{h}{g} \right) \arctan \frac{g}{h} \right]. \quad (39)$$

Similarly, the fringing capacitance associated with the horizontal side  $C_{f2}$  may be obtained from (39) by interchanging  $g$  and  $h$ .

## APPENDIX II

### RECTANGULAR LINE HAVING THIN INNER CONDUCTOR

If the two sides of the rectangular line are short compared with the conductor spacings, half of the cross section shown in Fig. 14 should be considered. The appropriate transformations are<sup>5</sup>

$$z = \int \frac{(1 - t^2)^{1/2}}{(1 - k^2 t^2)^{1/2} (1 - k^2 \operatorname{sn} \alpha \cdot t^2)} dt, \quad (40)$$

and

$$w = u + jv = \frac{1}{\pi} \log \frac{\left( \frac{1}{k \operatorname{sn} \alpha} - t \right)}{\left( \frac{1}{k \operatorname{sn} \alpha} + t \right)}. \quad (41)$$

Here,  $k$  is the modulus of elliptic functions,  $\operatorname{sn} \alpha$  is one of the Jacobian elliptic functions, and  $\alpha$  is a complex quantity.

These transformations yield the line capacitance as

$$C = 4(\overline{AC} + \overline{CD} + X)/g \text{ farad per meter}, \quad (42)$$

in which  $X$  is the correction for the sides at one corner resulting from the field distortion and is given by an expression comprising elliptic and other higher functions.

For the case  $\alpha = K - jK'$ , and for values of  $k$  from 0.5 to unity, the equation for  $X$  reduces to (16), and  $g$  does not differ substantially from  $h$ . The fringing capacitance at one corner has been plotted in Fig. 8 as a function of  $b/g$  in the form

$$C_f/\epsilon = X/g. \quad (43)$$

## APPENDIX III

### SHIELDED SEMI-INFINITE PLATE

Fig. 15(a) shows a semi-infinite plate of finite thickness and rectangular cross section placed midway between two infinite plates. The two parallel infinite plates are at zero potential, and the semi-infinite plate is at potential  $V$ . The values of  $t$  chosen at the corners of the  $z$ -plane polygon are indicated in Fig. 15, both (a) and (b). The internal angles of the polygon are 0 when  $t = \pm 1$ , and  $3\pi/2$  when  $t = \pm a$ . The differential equation which transforms the boundary of the  $z$  diagram into the real axis of the  $t$  plane is<sup>3</sup>

$$\frac{dz}{dt} = A_1(t + a)^{1/2}(t - a)^{1/2}(t + 1)^{-1}(t - 1)^{-1}. \quad (44)$$

The diagram in the  $w$  plane consists of one straight line and the two sides of another parallel line, as shown in Fig. 15(c). The internal angles occur at points corresponding to  $t = -1$  and  $t = 1$  and are both zero. The transformation which turns the diagram in the  $w$  plane

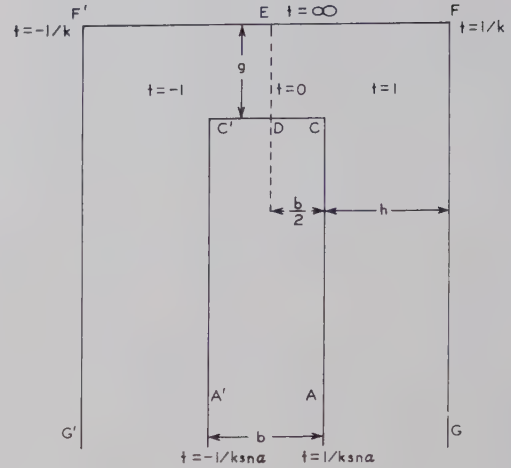


Fig. 14—Transformation for half cross section of a rectangular line.

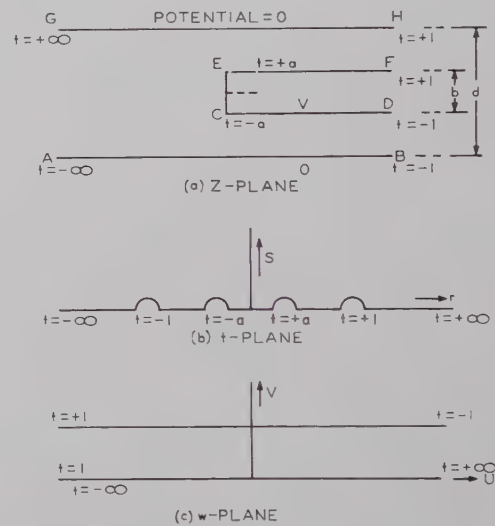


Fig. 15—Schwarz-Christoffel transformation for shielded semi-infinite plate.

to the real axis in the  $t$  plane is

$$\frac{dw}{dt} = B_1(t + 1)^{-1}(t - 1)^{-1}. \quad (45)$$

After (44) and (45) are integrated and the integration constants are determined by application of the boundary conditions, the fringing capacitance for one corner of the semi-infinite plate is given by (24).

## APPENDIX IV

### INNER CONDUCTOR WITH ROUNDED EDGES

The case considered is that of two coaxial rectangular conductors, the edges of the inner conductor being rounded. A potential difference  $\pi$  is maintained between the conductors, each of which forms an equipotential surface. The distances  $g$  and  $h$  are assumed to be small compared with the sides  $AB$  and  $CD$  of Fig. 16(a), so that the  $z$ -plane polygon consists of one corner, the sides of which are assumed to extend to infinity. The



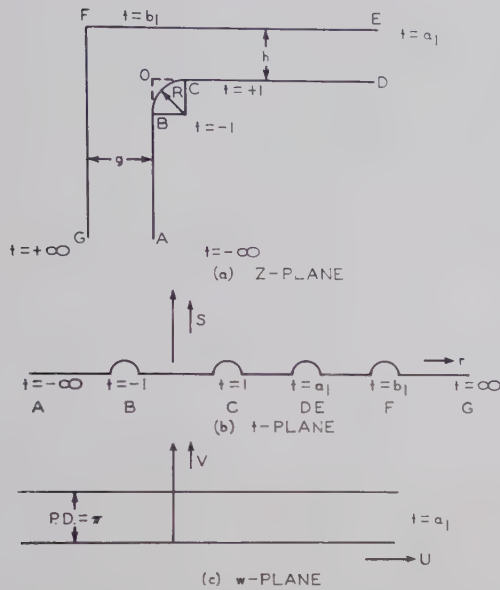


Fig. 16—Conformal transformation of a rounded bend.

differential equation which transforms the polygon  $ABCDEGA$  in the  $z$  plane to the upper half of the  $t$  plane is<sup>5</sup>

$$\frac{dz}{dt} = A_1 \frac{(t+1) + m(t-1)}{(t-a_1)(t-b_1)^{1/2}}. \quad (46)$$

The two terms in the numerator have the effect of turning the path of  $z$  through  $90^\circ$  as  $r$  in the  $t$  plane of Fig. 16(b) varies between  $-1$  and  $+1$ . If the factor  $m$  is chosen as

$$m = (b_1 + 1)^{1/2} / (b_1 - 1)^{1/2}, \quad (47)$$

then the variation of the electric field intensity is uniform along the curved boundary  $BC$ .

It is necessary to put an electric field into the  $t$  plane such that from  $t = -\infty$  to  $t = a_1$ , the horizontal line is at one potential and the horizontal line from  $t = a_1$  to  $t = +\infty$  at another potential. This is accomplished by opening up the two parallel lines in Fig. 16(c) to form the two lines  $AD$  and  $EG$  in the  $t$  plane. The transformation is

$$\frac{dw}{dt} = \frac{B_1}{t - a_1}. \quad (48)$$

After integration and evaluation of the total charge on the inner conductor as  $z$  takes infinite real and imaginary values; that is, as  $t$  varies from  $-\infty$  to  $+\infty$ , the total charge per unit length is given by

$$Q = \epsilon\pi \left[ \frac{(OA + X_1)}{g} + \frac{(OD + X_2)}{h} \right], \quad (49)$$

where  $OA$  and  $OD$  are, respectively, half the depth and half the width of the inner conductor. The expressions for the correction lengths  $X_1$  and  $X_2$  have been derived by Cockcroft, and the excess or fringing capacitance for one rounded corner is found from

$$C_f = \frac{Q}{\pi} = \epsilon \left[ \left( \frac{X_1}{g} + \frac{X_2}{h} \right) \right]. \quad (50)$$

The most usual case is for  $g = h$ . Under this condition,

$$\frac{b_1 - a_1}{a_1 - 1} = \frac{b_1 + 1}{b_1 - 1} = \frac{a_1 + 1}{b_1 - a_1} = m^2, \quad (51)$$

and

$$g = h = \pi(1 + m). \quad (52)$$

The radius of the round corner is given by

$$R = 2 \arctan i - m \log \frac{1+f}{1-f}, \quad (53)$$

in which the expressions for  $f$  and  $i$  are, respectively,

$$f = \left( \frac{2}{b_1 + 1} \right)^{1/2} \quad \text{and} \quad i = \left( \frac{2}{b_1 - 1} \right)^{1/2}.$$

The expression for the total correction length and the fringing capacitance for one rounded corner reduce to

$$\begin{aligned} X = & 2\pi + 4(m-1) \arctan \left( \frac{1}{m} \right) - 2(1+m) \log 4 \\ & + 2(1+m) \log 2b_1 - 2m \log (b_1 + 1) \\ & - 2 \log (b_1 - 1), \end{aligned} \quad (54)$$

and

$$C_f = \frac{\epsilon X}{g}. \quad (55)$$

The values of  $C_f/\epsilon = X/g$  are plotted in Fig. 12 as a function of  $R/g$ . In general, when  $g$  is not equal to  $h$ , the results are far more complex than those given by the previous equations and the curved boundary at the corner of the inner conductor does not assume a circular form.

## VIII. ACKNOWLEDGMENT

Acknowledgment is due W. N. Parker, Electron Tube Division, RCA, Lancaster, Pa., for very helpful discussions and for providing his results obtained by relaxation method on rectangular lines.

# The Analysis of a Broad-Band Circular Polarizer Including Interface Reflections\*

S. ADACHI†, MEMBER, IRE, AND E. M. KENNAUGH, ASSOCIATE MEMBER, IRE†

**Summary**—Transmission characteristics of a broad-band circular polarizer consisting of anisotropic dielectric plates are rigorously analyzed. The transmitted wave is formulated in terms of the incident wave including interface reflections. The influence of the interface reflections on the axial ratio of the polarization is numerically shown vs frequency. Frequency dependence of the power transmission ratio is also obtained. From the above analysis, it can be concluded that a circular polarizer of this type is promising as a new broad-band circular polarizer.

## INTRODUCTION

IT WAS shown by Pancharatnam<sup>1</sup> that a combination of birefringent plates transforms linear polarization to circular polarization over a very broad optical frequency band. The possibility of applying this principle to a circular polarizer in the microwave frequency range was discussed in detail by Long.<sup>2</sup>

This circular polarizer consists of three cascaded half-and/or quarter-wave birefringent plates, or anisotropic dielectric plates with their axes oriented at definite angles with respect to the incident polarization. Complete circular polarization can be obtained at three different points of frequency by using three plates, each having a different tilt angle with respect to the incident plane wave. Generally, it will be possible to design an  $n$ -plate circular polarizer having an axial ratio of 1 at  $n$  different frequencies.

Analyses by Pancharatnam and Long are confined to the ideal cases where the interface reflections are neglected. The reflections at these interfaces are inevitable in practical use, particularly for a polarizer consisting of relatively thin plates with high dielectric constant. It is easily conceivable that even small reflections have significant effects on the axial ratio of the emerging wave.

In this report, the transmission characteristics of the circular polarizer, including interface reflections, are rigorously analyzed. The influence of the interface reflections on axial ratio vs frequency is numerically shown. Frequency dependence of the power transmission ratio is also obtained.

## BIREFRINGENT-PLATE CIRCULAR POLARIZER

The mechanism of the birefringent-plate circular polarizer can be well described by a geometrical representation on the Poincaré Sphere.<sup>3,4</sup> An elliptical polarization with axial ratio  $r$  ( $\geq 1$ ) and tilt angle  $\beta$  ( $0^\circ \leq \beta \leq 180^\circ$ ) between the major axis and a reference axis can be uniquely represented by a point having  $2\beta$  and  $2\alpha = \pm 2 \cot^{-1} r$  as longitude and latitude, respectively, on a sphere. A positive sign is chosen for  $\alpha$  when the polarization is of left-hand sense; a negative sign is chosen for  $\alpha$  when the polarization is of right-hand sense. Such a sphere is called the Poincaré Sphere, and is shown in Fig. 1. The equator represents linear polarizations. All polarizations of left-hand sense lie in the upper hemisphere ( $0^\circ \leq 2\alpha \leq 90^\circ$ ) and all polarizations of right-hand sense lie in the lower hemisphere ( $-90^\circ \leq 2\alpha \leq 0^\circ$ ). A change from one state of polarization to another is represented by a rotation of the sphere about an appropriate diameter, so long as the transmission is lossless. For instance, passage of any polarization through a half-wave birefringent plate corresponds to a rotation of  $180^\circ$  about an axis in the equatorial plane. Similarly, passage through a quarter-wave plate corresponds to rotation of  $90^\circ$  about an axis in the equatorial plane. In particular, the passage of a linearly polarized wave through a quarter-wave plate whose axes are at  $45^\circ$  to the direction of polarization results in circular polarization, represented by the pole of the sphere. The transformation of a linearly polarized wave into a circularly polarized wave by the three-birefringent plate-

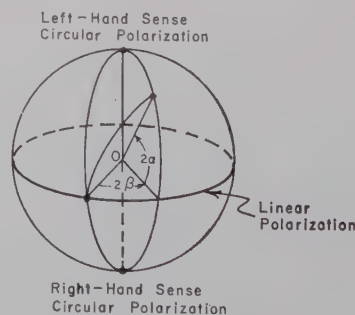


Fig. 1—Poincaré Sphere.

\* Received by the PGMTT, March 21, 1960; revised manuscript received, June 13, 1960.

† Antenna Lab., Dept. of Elec. Engrg., The Ohio State University, Columbus.

<sup>1</sup> S. Pancharatnam, "Achromatic combination of birefringent plates," *Proc. Indian Acad. Sci., Sec. A*, vol. 41, p. 130 ff.; April, 1955.

<sup>2</sup> R. K. Long, "Some methods of obtaining circular polarization over a broad band of frequencies by the use of birefringent plates," Antenna Lab., The Ohio State Univ. Res. Foundation, Contract AF 33(616)-5078, Wright Air Dev. Ctr., Wright-Patterson A.F.B., Dayton, Ohio. (AD 203827), Rept. No. 768-2; June 1, 1958.

<sup>3</sup> H. Poincaré, "Theorie Mathematique de la Lumière," g. Carré, Paris; 1889.

<sup>4</sup> G. A. Deschamps, "Techniques for handling elliptically polarized waves with special reference to antennas," *Proc. IRE*, vol. 39, pp. 540-544; May, 1951.



circular polarizer is illustrated by the Poincaré Sphere in Fig. 2. At the central wavelength  $\lambda_0$ , the incident linearly polarized wave represented by a point  $P$  is transformed to a point  $Q$  by passage through half-wave plate No. 1 (rotation of  $180^\circ$  about axis  $00_1$ ), and next, to a point  $R$  by passage through half-wave plate No. 2 (rotation of  $180^\circ$  about axis  $00_2$ ). Finally, the linear polarization  $R$  is transformed to circular polarization at the point  $S$  by passage through a quarter-wave plate (rotation of  $90^\circ$  about axis  $00_3$ ). The axes  $00_1$ ,  $00_2$ , and  $00_3$  are determined by the orientation of the fast axes of the individual plates with respect to the reference direction. At the equideviated wavelengths  $\lambda_1$  and  $\lambda_2$  from the central wavelength, the point  $P$  is transformed through points  $Q_1$ ,  $R_1$ , (rotations of  $180^\circ - 2\delta$  about  $00_1$ ,  $00_2$ ), or  $Q_2$ ,  $R_2$  (rotations of  $180^\circ + 2\delta$  about  $00_1$ ,  $00_2$ ), respectively, to the same point  $S$  (rotations of  $90^\circ - \delta$  or  $90^\circ + \delta$  about  $00_3$ ). Thus, it is possible to design a three-plate circular polarizer such that a fixed direction of linear polarization is transformed to complete circular polarization at three different frequencies. However, this analysis (originally given by Pancharatnam) does not include the effect of interfacial reflections.

#### RIGOROUS ANALYSIS OF A BROAD-BAND CIRCULAR POLARIZER

The plates are assumed to be infinite, and the direction of propagation of the incident wave is assumed to be normal to the plate. In Fig. 3, the plate is tilted by an

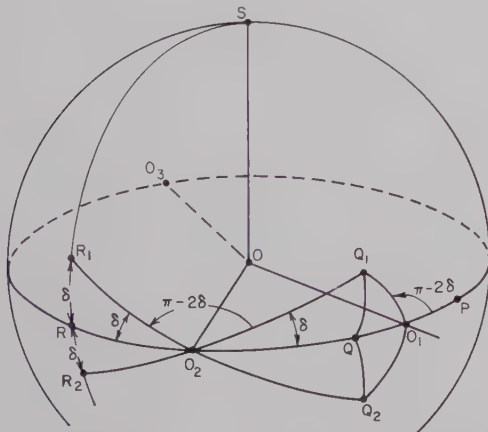


Fig. 2—Map of three-plate circular polarizer on the Poincaré sphere.

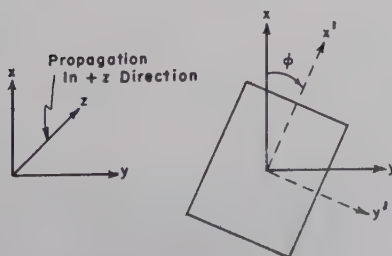


Fig. 3—Coordinate system.

angle  $\phi$  with respect to the coordinate  $x$ . Coordinates  $x'$  and  $y'$  are the fast and slow axes of the plate, respectively. The "fast" axis is referred to the polarization direction of the wave which has the highest phase velocity, or the direction along which the dielectric constant is minimum. A right-hand coordinate system is used.

Transmission matrices  $\mathbf{A}_{1f}$  and  $\mathbf{A}_{1s}$ , associated with fast and slow axes of the plate 1 respectively, are defined as follows:

$$\mathbf{A}_{1f} = \begin{pmatrix} \cos k_{1f}d_1 & jZ_{1f} \sin k_{1f}d_1 \\ \frac{j}{Z_{1f}} \sin k_{1f}d_1 & \cos k_{1f}d_1 \end{pmatrix}, \quad (1)$$

and

$$\mathbf{A}_{1s} = \begin{pmatrix} \cos k_{1s}d_1 & jZ_{1s} \sin k_{1s}d_1 \\ \frac{j}{Z_{1s}} \sin k_{1s}d_1 & \cos k_{1s}d_1 \end{pmatrix}, \quad (2)$$

where  $k_{1f}$ ,  $k_{1s}$  are phase constants associated with fast and slow axes respectively, and  $Z_{1f}$ ,  $Z_{1s}$  are normalized characteristic impedances of the respective media with reference to the free-space characteristic impedance. The thickness of plate 1 is given by  $d_1$ .

Since linearly polarized plane waves along each of the perpendicular axes  $x'$  and  $y'$  travel independently, we obtain the following relation using the transmission matrices defined above:

$$\begin{bmatrix} E_x' \\ H_y' \\ E_y' \\ -H_x' \end{bmatrix}_{z=0} = \mathbf{T}_{10} \begin{bmatrix} E_x' \\ H_y' \\ E_y' \\ -H_x' \end{bmatrix}_{z=d_1}, \quad (3)$$

where

$$\mathbf{T}_{10} = \begin{pmatrix} \mathbf{A}_{1f} & \mathbf{0} \\ \mathbf{0} & \mathbf{A}_{1s} \end{pmatrix}, \quad (4)$$

and where  $\mathbf{0}$  is a zero matrix of 2 rows and 2 columns. The coordinate transformation matrix  $\phi_1$  from coordinates  $(x', y', z')$  into coordinates  $(x, y, z)$  is expressed as follows:

$$\phi_1 = \begin{pmatrix} \cos \phi_1 \mathbf{I} & -\sin \phi_1 \mathbf{I} \\ \sin \phi_1 \mathbf{I} & \cos \phi_1 \mathbf{I} \end{pmatrix}, \quad (5)$$

where  $\mathbf{I}$  is a unit matrix of 2 rows and 2 columns. By using the above matrix, the following transmission equation for the field components referred to the unprimed coordinate system is obtained:

$$\begin{bmatrix} E_x \\ H_y \\ E_y \\ -H_x \end{bmatrix}_{z=0} = \mathbf{W}_{10} \begin{bmatrix} E_x \\ H_y \\ E_y \\ -H_x \end{bmatrix}_{z=d_1}, \quad (6)$$

where

$$W_{10} = \phi_1 T_{10} \phi_1^{-1}, \quad (7)$$

and where  $\phi_1^{-1}$  is the inverse matrix of  $\phi_1$ .  $W_{10}$  is the transmission matrix associated with the plate 1 whose fast axis is tilted by angle  $\phi_1$  from the  $x$  axis toward the  $y$  axis.

Carrying out the matrix calculation of (7), the following expression results for  $W_{10}$ :

$$2W_{10} = \cos 2\phi_1 \begin{pmatrix} A_1 & 0 \\ 0 & -A_1 \end{pmatrix} + \sin 2\phi_1 \begin{pmatrix} 0 & A_1 \\ A_1 & 0 \end{pmatrix} + \begin{pmatrix} B_1 & 0 \\ 0 & B_1 \end{pmatrix}, \quad (8)$$

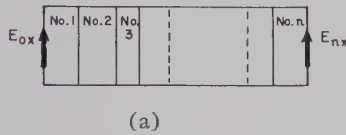
where

$$\begin{aligned} A_1 &= A_{1f} - A_{1s}, \\ B_1 &= A_{1f} + A_{1s}. \end{aligned} \quad (9)$$

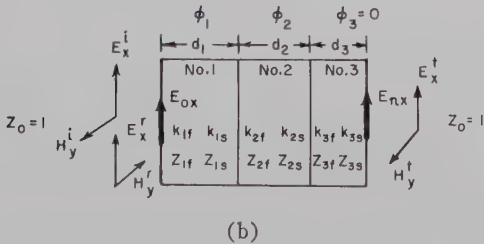
The transmission through a circular polarizer consisting of  $n$  plates is represented by the  $n$  products of matrices of the above type; that is,

$$\begin{bmatrix} E_{ox} \\ H_{oy} \\ E_{oy} \\ -H_{oz} \end{bmatrix} = W_{01} W_{12} \cdots W_{n-1n} \begin{bmatrix} E_{nx} \\ H_{ny} \\ E_{ny} \\ -H_{nz} \end{bmatrix}, \quad (10)$$

where subscripts  $o, n$  are referred to the fields at sending and receiving end-surfaces respectively as illustrated in Fig. 4(a).



(a)



(b)

Fig. 4—(a) An  $n$ -plate circular polarizer, (b) A three-plate circular polarizer.

Now let  $E_{ox}$ ,  $E_{nx}$ , etc., be expressed in terms of the incident, reflected, and transmitted fields as follows:

$$\begin{aligned} E_{ox} &= E_x^i + E_x^r, \\ E_{oy} &= E_y^i + E_y^r, \\ H_{oy} &= H_y^i - H_y^r = E_x^i - E_x^r, \\ -H_{oz} &= H_x^i - H_x^r = E_y^i - E_y^r, \end{aligned} \quad (11)$$

and

$$\begin{aligned} E_{nx} &= E_x^t, \\ E_{ny} &= E_y^t, \\ H_{ny} &= H_y^t = E_x^t, \\ -H_{nz} &= H_x^t = E_y^t. \end{aligned} \quad (12)$$

It is noted here that since input and output media are assumed to be free space, their normalized characteristic impedances are equal to 1.

Substituting (11) and (12) in (10) yields the following equation for a three-plate circular polarizer:

$$\begin{bmatrix} E_x^i + E_x^r \\ E_x^i - E_x^r \\ E_y^i + E_y^r \\ E_y^i - E_y^r \end{bmatrix} = W_{01} W_{12} W_{23} \begin{bmatrix} E_x^t \\ E_x^t \\ E_y^t \\ E_y^t \end{bmatrix}. \quad (13)$$

It is possible to set  $\phi_3 = 0$  without losing generality; therefore,

$$W_{23} = T_{23}.$$

Carrying out matrix multiplications yields

$$4W_{01} W_{12} W_{23} = \begin{pmatrix} A & C \\ B & D \end{pmatrix}, \quad (14)$$

where

$$\begin{aligned} A &= [\cos 2(\phi_1 - \phi_2) A_1 A_2 + \cos 2\phi_1 A_1 B_2 \\ &\quad + \cos 2\phi_2 B_1 A_2 + B_1 B_2] A_{3f}, \\ B &= [\sin 2(\phi_1 - \phi_2) A_1 A_2 + \sin 2\phi_1 A_1 B_2 + \sin 2\phi_2 B_1 A_2] A_{3f}, \\ C &= [-\sin 2(\phi_1 - \phi_2) A_1 A_2 + \sin 2\phi_1 A_1 B_2 \\ &\quad + \sin 2\phi_2 B_1 A_2] A_{3s}, \\ D &= [\cos 2(\phi_1 - \phi_2) A_1 A_2 - \cos 2\phi_1 A_1 B_2 \\ &\quad - \cos 2\phi_2 B_1 A_2 + B_1 B_2] A_{3s}. \end{aligned} \quad (15)$$

Solving (13) for the transmitted field ( $E_x^t, E_y^t$ ) in terms of the incident field ( $E_x^i, E_y^i$ ), yields

$$\begin{pmatrix} E_x^t \\ E_y^t \end{pmatrix} = 8 \frac{\begin{pmatrix} \sum_{ij} D_{ij} & -\sum_{ij} C_{ij} \\ -\sum_{ij} B_{ij} & \sum_{ij} A_{ij} \end{pmatrix}}{\begin{vmatrix} \sum_{ij} A_{ij} & \sum_{ij} C_{ij} \\ \sum_{ij} B_{ij} & \sum_{ij} D_{ij} \end{vmatrix}} \begin{pmatrix} E_x^i \\ E_y^i \end{pmatrix},$$

$$i = 1, 2; j = 1, 2, \quad (16)$$

and for the reflected field

$$\begin{pmatrix} E_x^r \\ E_y^r \end{pmatrix} = \frac{1}{8} \begin{pmatrix} \sum_j A_{1j} - \sum_j A_{2j} & \sum_j C_{1j} - \sum_j C_{2j} \\ \sum_j B_{1j} - \sum_j B_{2j} & \sum_j D_{1j} - \sum_j D_{2j} \end{pmatrix} \begin{pmatrix} E_x^i \\ E_y^i \end{pmatrix}, \quad (17)$$



where  $A_{ij}$ , etc., indicate matrix elements of matrices  $\mathbf{A}$ , etc. Right- and left-circularly polarized components of the transmitted wave are given by the following form:

$$R = \frac{1}{2} (1 - j) \begin{pmatrix} E_x^t \\ E_y^t \end{pmatrix},$$

$$L = \frac{1}{2} (1 + j) \begin{pmatrix} E_x^t \\ E_y^t \end{pmatrix}. \quad (18)$$

Axial ratio of polarization of the transmitted wave, A.R., is calculated by

$$\text{A.R.} = \frac{|L| + |R|}{|L| - |R|}. \quad (19)$$

Power transmission ratio, P.T.R., is given by

$$\text{P.T.R.} = \frac{|E_x^t|^2 + |E_y^t|^2}{|E_x^i|^2 + |E_y^i|^2}. \quad (20)$$

#### SOME NUMERICAL RESULTS

Numerical calculation has been carried out for a circular polarizer consisting of two half-wave plates (No. 1 and No. 2) and one quarter-wave plate (No. 3). Tilt angles  $\phi_1$ ,  $\phi_2$  and incident field components  $E_x^i$ ,  $E_y^i$  have been chosen such that in the absence of interface reflections, perfect circular polarization is obtained at three equispaced wavelengths:  $\lambda_0$  (central wavelength),  $\lambda_1$  and  $\lambda_2$ , where

$$\lambda_1 = \lambda_0 \left( 1 - \frac{\delta}{90^\circ} \right),$$

and

$$\lambda_2 = \lambda_0 \left( 1 + \frac{\delta}{90^\circ} \right). \quad (21)$$

This requires:<sup>1,2</sup>

$$\begin{aligned} \phi_1 &= \frac{1}{2}(90^\circ + 2a + e), \\ \phi_2 &= \frac{1}{2}(90^\circ + a), \\ E_x^i &= \cos \frac{1}{2}(90^\circ + 2a + 2e), \\ E_y^i &= \sin \frac{1}{2}(90^\circ + 2a + 2e), \end{aligned} \quad (22)$$

where  $a$  is a solution of the equation:

$$A \sin^2 a + B \sin a + C = 0, \quad (23)$$

and where

$$\begin{aligned} A &= 4 \cos^3 \delta (1 - \cos \delta), \\ B &= 4 \cos^2 \delta (\cos 2\delta - \cos \delta), \\ C &= 2 \cot^2 \delta (1 - \cos \delta) - \cos^2 2\delta, \end{aligned} \quad (24)$$

and  $e$  in (22) is given by

$$\sin e = \frac{2 \cos^2 \delta \sin a - \cos 2\delta}{2 \cos \delta}.$$

The characteristic values of four polarizers are shown in Table I, for several choices of dielectric constant along fast and slow axes and different values of  $\delta$  (which determines the bandwidth as well as the orientation angles of the plates). The composition of all plates in each example is assumed the same. The particular combination of the dielectric constants in (3) and (4) are those reported for a stratified polystyrene-styrofoam medium.<sup>5</sup>

TABLE I  
THE CHARACTERISTIC VALUES OF THE CIRCULAR POLARIZERS

No. of Example	(1)	(2)	(3)	(4)
$\epsilon_f' = \frac{\epsilon_f}{\epsilon_0}$	1.0	1.0	1.470	1.470
$\epsilon_s' = \frac{\epsilon_s}{\epsilon_0}$	1.2	1.5	1.795	1.795
$k_0 d_1 = \frac{\pi}{\sqrt{\epsilon_s'} - \sqrt{\epsilon_f'}}$	32.915	13.978	24.671	24.671
$\delta$	18°	18°	18°	23.5°
$\phi_1$	94.654°	94.654°	94.654°	92.493°
$\phi_2$	66.575°	66.575°	66.575°	65.172°
$\tan^{-1} \frac{E_y^i}{E_x^i}$	101.159°	101.159°	101.159°	99.642°

The axial ratios of the transmitted wave for the above four examples have been calculated by using the preceding equations. The calculation of the matrix products was programmed on the IBM 650 computer by H. W. Baeumler. The results are plotted in Figs. 5-8, and are compared with the axial ratios in the case of no reflection. These curves show very complex behavior for the frequency variation because of interference between multiply reflected waves. The effect of interference reflection is to increase the axial ratio of the output polarization, although in the worst case the resulting axial ratio is less than 1.075 over a 2:1 band of frequencies.

The axial ratio of polarizer No. 1 with the ratio of the dielectric constants,  $\epsilon_s/\epsilon_f = 1.2$  is much better than that of polarizer No. 3 with almost the same ratio,  $\epsilon_s/\epsilon_f = 1.22$ . This shows that the absolute value of the dielectric con-

<sup>5</sup> H. S. Kirschbaum and S. Chen, "A method of producing broad-band circular polarization employing an anisotropic dielectric," IRE TRANS. ON MICROWAVE THEORY AND TECHNIQUES, vol. MTT-5, pp. 199-203; July, 1957.

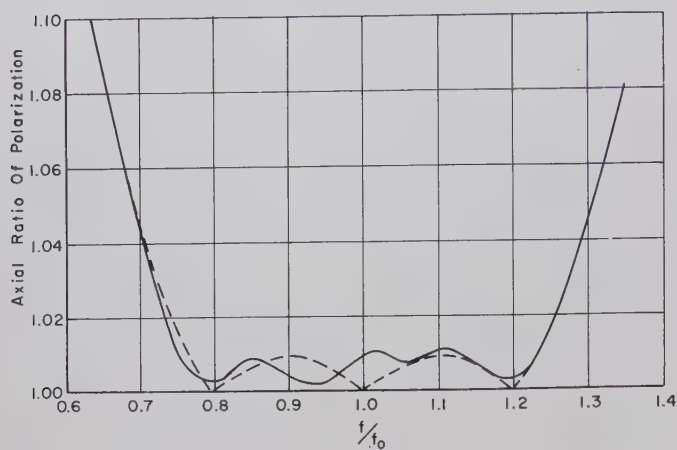


Fig. 5—Axial ratio of polarization vs frequency for Example (1).  
 — Interface reflection included; --- Interface reflection neglected.

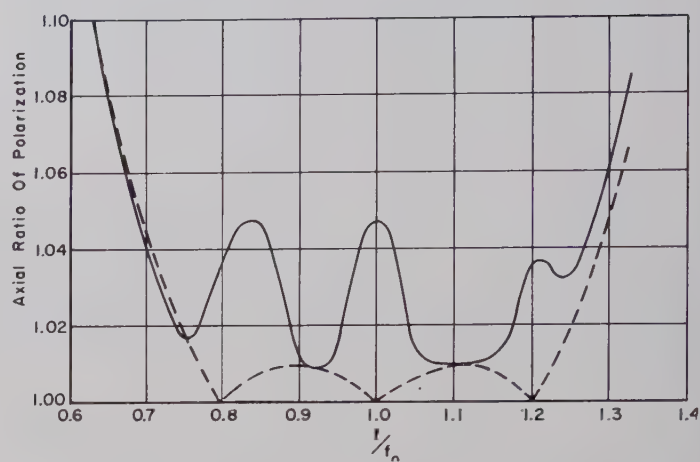


Fig. 6—Axial ratio of polarization vs frequency for Example (2).  
 — Interface reflection included; --- Interface reflection neglected.

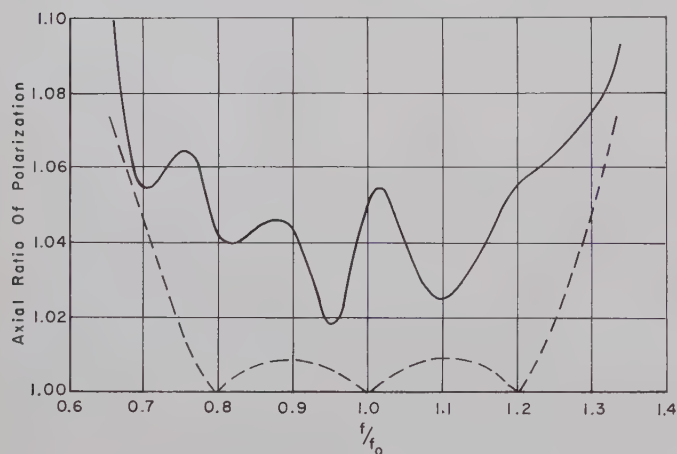


Fig. 7—Axial ratio of polarization vs frequency for Example (3).  
 — Interface reflection included; --- Interface reflection neglected.

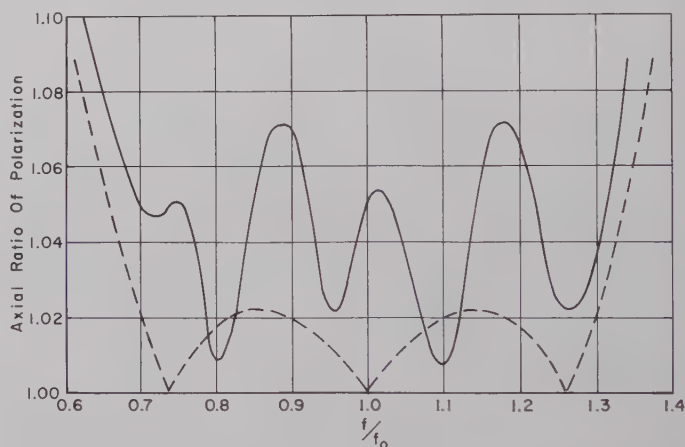


Fig. 8—Axial ratio of polarization vs frequency for Example (4).  
 — Interface reflection included; --- Interface reflection neglected.

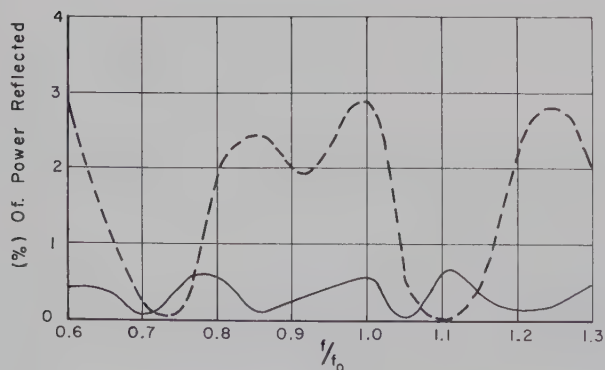


Fig. 9—Percentage of power reflected vs frequency.  
 — Example (1); --- Example (2).

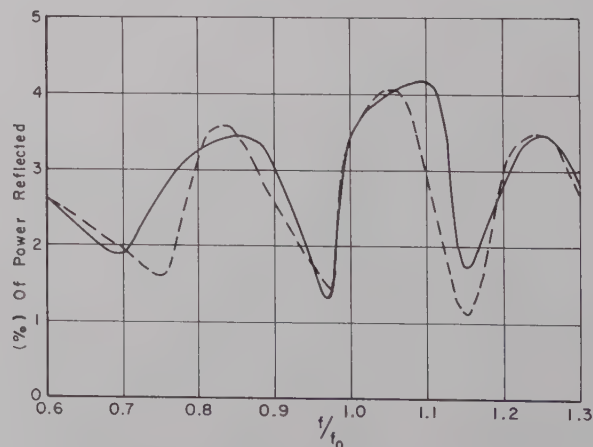


Fig. 10—Percentage of power reflected vs frequency.  
 — Example (3); --- Example (4).



stant is as important as the ratio,  $\epsilon_s/\epsilon_f$ , and must be as small as possible to obtain complete circular polarization. With the increase of the dielectric constants ( $\epsilon_s/\epsilon_f = \text{constant}$ ), the reflection at the receiving end surface (boundary between the plate No. 3 and the free space) increases and causes further multiple reflections and interactions between the sending and receiving end surfaces. It is noted also that the output axial ratio of polarizer No. 1 is extremely good, considering the depolarization which would be obtained for a circular polarized wave passing through a single plane interface. The above tells us that in this case the multiple reflections at the boundaries compensate each other as a whole so as to transmit a complete circular polarized wave over a wide frequency band.

The percentages of power reflected are plotted in Figs. 9 and 10. It is seen that better than 95 per cent transmission is obtained in all cases, and that the combinations yielding poorer axial ratios also exhibit the greater reflection.

## CONCLUSIONS

A broad-band circular polarizer consisting of three anisotropic dielectric plates has been rigorously analyzed under the assumption that each plate has constant (different) values of refractive index along the two principal axes. As a result, the transmitted wave has been formulated in terms of the incident wave including interface reflections. The frequency characteristics of the axial ratio of polarization and the power transmission ratio have been numerically shown. From the above analysis it can be concluded that a combination of this type is very promising as a broad-band circular polarizer. The axial ratio is less than 1.075 and the reflected power less than 5 per cent over more than a 2:1 band of frequencies for each of the anisotropic dielectric plate combinations chosen as examples in this paper.

## ACKNOWLEDGMENT

The assistance of Mrs. F. Phillips in the computation is gratefully acknowledged.

# Large Signal Analysis of a Parametric Harmonic Generator\*

KENNETH M. JOHNSON†

**Summary**—Large signal analysis of a harmonic generator using a semiconductor diode reveals a larger possible efficiency than a similar small signal analysis. As higher harmonic numbers are reached, large signal analysis becomes increasingly more important in predicting the maximum conversion efficiency. It is shown that there exists an optimum value for the diode bias voltage and an optimum coupling of the load and generator to the diode, and that the diode operating voltage should almost drive the diode into conduction. An expression is derived for the maximum conversion efficiency for any harmonic, and it is shown that the conversion loss increases with increasing harmonic number, approximately 2.9 db per  $n$  for large harmonic numbers in a typical case.

## INTRODUCTION

HARMONIC generators, unlike parametric amplifiers, are generally large signal devices; that is, the input signal traverses the entire dynamic range of the diode. For this reason, a large signal analysis must be used in the determination of the maximum conversion efficiency, especially at high harmonic numbers. Large signal analysis takes into account all the higher order contributions of the diode nonlinearity to the efficiency, and, as a result, a greater value for the

maximum efficiency is obtained than is revealed by small signal analysis. The large signal analysis is reduced to the small signal equivalent<sup>1</sup> when higher order terms are not considered. This paper describes the large signal analysis of a semiconductor diode operating as a frequency converter and discusses the conditions required for maximum conversion efficiency.

## SEMICONDUCTOR DIODE HARMONIC PRODUCTION

The Manley-Rowe<sup>2</sup> power relations indicate that a nonlinear reactance in a circuit can give rise to frequency conversion without losses. A back-biased semiconductor diode behaves as a nonlinear reactance in a circuit and, as a result, is useful for frequency conversion.<sup>3</sup> In this section we shall consider a diode as a harmonic generator to see how much energy conversion may be expected.

<sup>1</sup> D. B. Leeson and S. Weinreb, "Frequency multiplication with nonlinear capacitance—a circuit analysis," *Proc. IRE*, vol. 47, pp. 2076–2084; December, 1959.

<sup>2</sup> J. M. Manley and H. E. Rowe, "Some general properties of nonlinear elements—part I, general energy relations," *Proc. IRE*, vol. 44, pp. 904–913; July, 1956.

<sup>3</sup> D. Leenov and A. Uhler, "Generation harmonics and subharmonics at microwave frequencies with  $p$ - $n$  junction diodes," *Proc. IRE*, vol. 47, pp. 1724–1729; October, 1959.

\* Received by the PGMTT, April 6, 1960; revised manuscript received, June 28, 1960.

† Microwave Lab., Hughes Aircraft Co., Culver City, Calif.

The equivalent circuit for a semiconductor diode is shown in Fig. 1. The nonlinear capacitance of the diode  $C_D(V)$  is given by<sup>4</sup>

$$C_D(V) = C_0'(1 - V/V_c)^{-m}, \quad (1)$$

where  $C_0'$  is the zero bias capacitance,  $V_c$  is the contact potential,  $V$  is the bias voltage on the diode, and  $m$  is equal to  $\frac{1}{3}$  for a graded junction and  $\frac{1}{2}$  for an abrupt junction. A typical value for  $m$  is 0.46. The diode's nonlinear resistance  $G(V)$ , which arises because the diode conducts at forward bias voltages, is given as

$$G(V) = \frac{qI_s}{kT} \exp \frac{qV}{kT}, \quad (2)$$

in which  $q$  is the charge on an electron,  $V$  is the bias voltage, and  $I_s$  is the reverse saturation current.

At reasonably low frequencies  $C_s$  in Fig. 1 may be neglected; a typical value for  $C_s$  might be  $0.1 \mu\text{mf}$ . At negative bias voltages,  $G(V)$  may be neglected in comparison with  $r_s$ , the spreading resistance.

In Fig. 2 we have the general capacitance vs bias voltage variation. For negative bias voltage,  $G(V)$  is approximately zero and becomes significant at some forward voltage. Neglecting  $G(V)$  and  $C_s$ , the equivalent circuit may be reduced to Fig. 3, where  $G_D$  is the parallel equivalent of  $r_s$  and therefore is frequency dependent. At reasonably high frequencies and for high diode  $Q$ ,  $G_D$  is related to  $r_s$  and diode  $Q$  by

$$Q_D = \frac{\omega C}{G_D} = \frac{1}{\omega C r_s}. \quad (3)$$

Let  $V_B$  be the sum of the self bias and the applied dc voltage. If we define  $V_0 = V_c - V_B$  and  $K = C_0' V_c^m$ , then (1) becomes

$$C_0 = K V_0^{-m} \quad (4)$$

in which  $C_0$  is the operating point capacitance.

The diode, when operating as a harmonic generator, has only two sinusoidal voltages across it; all other frequencies are shorted out. One voltage,  $V_1 \cos \omega_1 t$ , appears at the fundamental frequency,  $\omega_1$ , and the other voltage,  $V_n \cos n\omega_1 t$ , appears at  $n\omega_1$ , the  $n$ th harmonic. It will be shown later that when the diode operates at low efficiencies and at high harmonic numbers,  $V_n$  may be neglected in comparison with  $V_1$ .

If we assume a fixed bias on the diode and let  $\phi_n$  be the phase difference which exists between  $V_1$  and  $V_n$ , then the total voltage which appears on the diode is given as

$$V = V_B + V_1 \cos \omega_1 t + V_n \cos (n\omega_1 t + \phi_n). \quad (5)$$

We may now calculate the charge stored on the semiconductor junction due to these voltages. This charge

is  $q = \int C(V) dV$ , or

$$q = -\frac{C_0 V_0}{1-m} \left[ 1 + \frac{V_1}{V_0} \cos \omega_1 t + \frac{V_n}{V_0} \cos (n\omega_1 t + \phi_n) \right]^{1-m} + q_0. \quad (6)$$

The charge may be represented in a Fourier series as

$$q = \frac{c_0}{2} + \sum_{n=1}^{\infty} (c_n \cos n\omega_1 t + d_n \sin n\omega_1 t). \quad (7)$$

This series may also be expressed in terms of complex exponentials as

$$q = \frac{1}{2} \sum_{n=-\infty}^{\infty} \alpha_n e^{in\omega_1 t} \quad (8)$$

The following relations exist between  $\alpha_n$ ,  $c_n$ , and  $d_n$ :

$$|\alpha_n| = \sqrt{c_n^2 + d_n^2}. \quad (9)$$

We may rewrite the charge using a phase as

$$q = \frac{a_0}{2} + \sum_{n=1}^{\infty} a_n \cos (n\omega_1 t - \Psi_n), \quad (10)$$

in which

$$\Psi_n = \tan^{-1} \frac{d_n}{c_n} \quad \text{and} \quad a_n = |\alpha_n|. \quad (11)$$

The reason for utilizing this form will be obvious later.

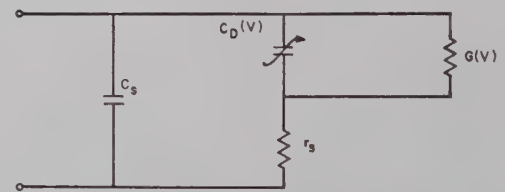


Fig. 1—Diode equivalent circuit.

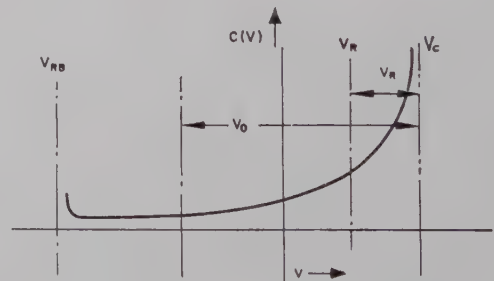


Fig. 2—Diode capacitance vs bias voltage.

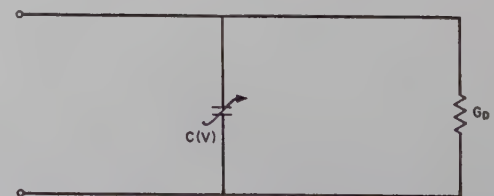


Fig. 3—Reduced diode equivalent circuit.

<sup>4</sup> A. Uhler, "The potential of semiconductor diodes in high frequency communication," *Proc. IRE*, vol. 46, pp. 1099-1115; June, 1958.



For arbitrary values of  $V_1$ ,  $V_n$  and  $\phi$ , the Fourier integrals for  $d_n$ ,  $c_n$ , and  $d_n$  can only be evaluated numerically or by series technique. However, since  $V_n$  is a direct result of  $V_1$  and the driving source, the phase associated with  $V_n$  and the magnitude of  $V_n$  may be related to  $V_1$ ,  $d_n$  and  $c_n$ . This will help fix the value of  $V_n$  and  $\phi_n$  for maximum efficiency. A relatively simple technique for numerical integration of the Fourier integrals will be indicated in Appendix I. A series solution for these integrals is also possible. When  $V_n$  can be neglected, then  $a_n = c_n$  and  $d_n = 0$ . The equation for  $c_n$  becomes

$$c_n = a_n = -\frac{C_0 V_0}{(1-m)\pi} \int_{-\pi}^{\pi} \left[ 1 + \frac{V_1 \cos \omega_1 t}{V_0} \right]^{1-m} \cdot \cos n\omega_1 t d(\omega_1 t). \quad (12)$$

This integral may be evaluated exactly by series technique, and for  $V_1/V_0 = 1$  it may be integrated directly. By use of the binomial expansion we may obtain the following series solution to the integral. Let  $1-m = \gamma$ , then

$$c_n = a_n = \frac{C_0 V_0 (-1)^n (n - \gamma - 1)!}{2^{n-1} n! (-\gamma)!} \left( \frac{V_1}{V_0} \right)^{n-1} \cdot \left[ 1 + \sum_{k=1}^{\infty} \frac{n!(n - \gamma - 1 + 2k)!}{k!(n+k)!(n - \gamma - 1)!} \left( \frac{V_1}{2V_0} \right)^{2k} \right]. \quad (13)$$

This series converges very slowly for  $V_1/V_0$  close to unity. However, for  $V_1/V_0 < 0.5$  it may be evaluated quite easily. In fact, the higher order terms in  $k$  may be neglected. Neglecting these higher order terms gives essentially the small signal approximation.

A better evaluation of the charge can be made by representing it in a hypergeometric series. Sensiper and Weglein<sup>5</sup> have shown that the charge in (7) may be expressed in terms of a rapidly convergent hypergeometric series regardless of the value of  $V_1/V_0$ . For  $\gamma = \frac{1}{2}$ , the hypergeometric series reduces to complete elliptical functions which are available in tables.<sup>6</sup> The hypergeometric series which is rapidly convergent for  $V_1/V_0 < 0.5$ , is

$$q = \frac{-2C_0 V_0}{\gamma} (1 + t^2)^{-\gamma} t^n \cdot \frac{\Gamma(n - \gamma)}{\Gamma(-\gamma)\Gamma(n + 1)} {}_2F_1(-\gamma, n - \gamma, n + 1, t^2), \quad (14)$$

in which  ${}_2F_1$  represents the hypergeometric series,  $\Gamma$  stands for the gamma function and  $t$  is defined from

$$\frac{V_1}{V_0} = \frac{2t}{1 + t^2}. \quad (15)$$

Although for this hypergeometric series there are no tables available, it converges so quickly that it can easily be evaluated in a few terms.

### GENERAL POWER RELATIONS

In this section we shall consider the general power relations for a harmonic generator to show the necessary circuit and the general equation for efficiency. In later sections we shall see how we may optimize the efficiency.

Fig. 4 shows the equivalent circuit for a harmonic generator.<sup>7</sup> The input circuit is resonant at  $\omega_1$  and coupled through a nonlinear capacitor to an output circuit resonant at  $n\omega_1$ , some multiple of  $\omega_1$ . The input circuit consists of a resonant tank circuit  $T_1$ , resonant at  $\omega_1$  with a conductance  $G_1$ . Power is supplied by a current generator  $I_g$ , with generator conductance  $G_g$  across it. The output circuit consists of a tank circuit  $T_2$ , resonant at  $n\omega_1$ , with a loss conductance  $G_2$  and a load conductance  $G_L$  across it. These circuits are coupled through the nonlinear capacitor  $C_D$  with a loss conductance  $G_D$  across it.

We shall assume that  $T_1$  and  $T_2$  are ideal filters. That is,  $T_1$  presents a short circuit to current flowing at  $n\omega_1$  and  $T_2$  presents a short circuit to current flowing at  $\omega_1$ . We may then represent the input circuit by Fig. 5, and the output circuit by Fig. 6, in which  $G_p$  is a positive conductance leading to energy transfer to the multiplied frequency and  $i_n$  is a current source at the  $n$ th harmonic due to the energy from  $G_p$ . We shall now determine  $G_p$  and  $i_n$  and apply them to the determination of the efficiency.

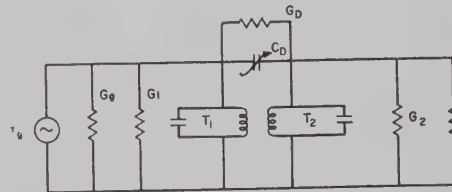


Fig. 4—Harmonic generator equivalent circuit.

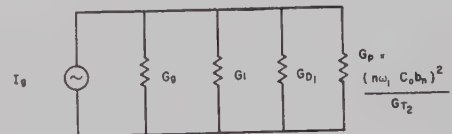


Fig. 5—Signal circuit equivalent circuit.

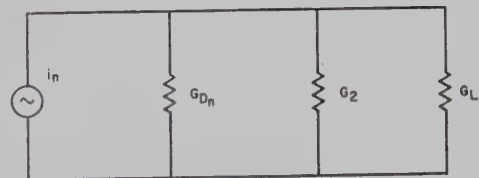


Fig. 6—Output circuit equivalent circuit.

<sup>5</sup> S. Sensiper and R. D. Weglein, "Capacitance and charge coefficients for parametric diode devices," *J. Appl. Phys.* (to be published).

<sup>6</sup> P. F. Byrd and M. D. Freidman, "Handbook of Elliptic Integrals for Engineers and Physicists," Springer-Verlag, Berlin, pp. 192-193; 1954.

<sup>7</sup> K. K. N. Chang, "Harmonic generation with nonlinear reactances," *RCA Rev.*, vol. 19, pp. 455-464; September, 1958.

The only frequencies which can exist are at  $\omega_1$  and  $n\omega_1$ ,<sup>8</sup> so the charge on the nonlinear capacitor at  $n\omega_1$  is simply given as

$$q_n = a_n \cos(n\omega_1 t - \Psi_n). \quad (16)$$

If we define  $\phi_n = -(\Psi_n + 90^\circ)$ , then the current flow out of the capacitor at the right is

$$\begin{aligned} i_n &= -\frac{dq_n}{dt} = n\omega_1 a_n \sin(n\omega_1 t - \Psi_n) \\ &= n\omega_1 a_n \cos(n\omega_1 t + \phi_n). \end{aligned} \quad (17)$$

This current supplies power to the output circuit conductances,  $G_L$ ,  $G_{Dn}$  and  $G_2$ . We may calculate the power supplied by the diode at the multiplied frequency as

$$P_D = \frac{i_n^2 \text{ eff}}{G_{T_2}} = \frac{n^2 \omega_1^2 a_n^2}{2G_{T_2}}, \quad (18)$$

where

$$G_{T_2} = G_L + G_{Dn} + G_2. \quad (19)$$

This power is supplied by  $V_1$  at the fundamental frequency and is transferred through the positive conductance  $G_p$ .

For convenience let us define  $b_n$  such that

$$a_n = C_0 V_1 b_n. \quad (20)$$

We may now calculate the positive conductance  $G_p$  from (18) and (20),

$$G_p = \frac{n\omega_1 C_0 b_n^2}{G_{T_2}}. \quad (21)$$

If we define  $I_n$  as the magnitude of the current  $i_n$  flowing out of the diode and define  $V_n$  as the magnitude of the output voltage at the  $n$ th harmonic, then  $I_n = V_n G_{T_2}$ . The power taken off at the load is calculated as  $V_n^2 G_L / 2 = P_{\text{out}}$ . The current generator  $I_g$  must supply all the input circuit conductances,  $G_g$ ,  $G_1$ ,  $G_{D_1}$  and  $G_p$ . The power available from the current generator is

$$P_{\text{av}} = \frac{I_g^2}{8G_g} = \frac{V_1^2 (G_{T_1} + G_p)^2}{8G_g}, \quad (22)$$

where

$$G_{T_1} = G_1 + G_{D_1} + G_g. \quad (23)$$

The efficiency may now be calculated as

$$\eta = \frac{P_{\text{out}}}{P_{\text{av}}} 100 = \frac{2G_L G_g}{G_{T_1} G_{T_2}} \cdot \frac{100}{\left[ 1 + \frac{(n\omega_1 C_0 b_n)^2}{2G_{T_1} G_{T_2}} + \frac{G_{T_1} G_{T_2}}{2(n\omega_1 C_0 b_n)^2} \right]}. \quad (24)$$

#### MATCHING CONDITIONS FOR OPTIMUM EFFICIENCY

Let us investigate the equation for efficiency, to determine the conditions for optimum efficiency, by using the following definitions for coefficients and  $Q$ 's:<sup>9</sup>

$$\begin{aligned} Q_g &= \frac{\omega_1 C_0}{G_g} \\ &= \text{external } Q \text{ of signal circuit loaded only by } G_g, \\ Q_L &= \frac{n\omega_1 C_0}{G_L} \\ &= \text{external } Q \text{ of output circuit loaded only by } G_L, \\ Q_{D_1} &= \frac{\omega_1 C_0}{G_{D_1}} \\ &= \text{external } Q \text{ of signal circuit loaded only by } G_{D_1}, \\ Q_{D_n} &= \frac{n\omega_1 C_0}{G_{D_n}} \\ &= \text{external } Q \text{ of output circuit loaded only by } G_{D_n}, \\ \mu &= \frac{Q_{D_1}}{Q_g}, \\ \nu &= \frac{Q_{D_n}}{Q_L}. \end{aligned}$$

For maximum efficiency, we must minimize the circuit losses  $G_1$  and  $G_2$  so that  $G_1 \ll G_{D_1}$ ,  $G_1 \ll G_g$ ,  $G_2 \ll G_{D_n}$ , and  $G_2 \ll G_L$ . In most microwave or UHF circuits these conditions are met. That is,  $G_1$  and  $G_2$  are usually negligible. By assuming this to be the case and realizing that in a physical diode  $Q_{D_n} = Q_{D_1}/n$ , we may write the efficiency as

$$\eta = \frac{2\mu\nu}{(1+\mu)(1+\nu)} \cdot \frac{100}{\left[ \frac{1 + Q_{D_1}^2 b_n^2}{2(1+\mu)(1+\nu)} + \frac{(1+\mu)(1+\nu)}{2Q_{D_1}^2 b_n^2} \right]}. \quad (25)$$

<sup>8</sup> J. Hilibrand and W. R. Beam, "Semiconductor diodes in parameter oscillators," *RCA Rev.*, vol. 20, pp. 229-253; June, 1959.

<sup>9</sup> R. C. Knechtli and R. D. Weglein, "Low noise parametric amplifier," *Proc. IRE*, vol. 47, p. 584; April, 1959.



By differentiating (25) with respect to  $\mu$  and setting it equal to zero, we obtain the optimum value of  $\mu$ . Doing this, we find that the generator conductance should be matched to the other signal circuit conductances, *i.e.*,  $G_g = G_{D_1} + G_1 + G_p$ . This is rather obvious, since for maximum power transfer the generator is always matched to the input circuit.

For the output circuit we would expect  $\nu$  or  $G_L/G_{D_n}$  to be at a maximum in order to minimize losses in  $G_{D_n}$ . However, since  $G_L + G_{D_n} + G_2$  enters into the value of  $G_p$ , which was to be made large in order to minimize losses due to  $G_1$  and  $G_D$ , then  $G_{T_2}$  must be small. Thus  $\nu$  has an optimum value which may be determined in the same manner as for  $\mu$ . This turns out to be a function of  $\mu$ , and when  $\mu = \mu_{\text{opt}}$  and  $\nu = \nu_{\text{opt}}$ , it may be written

$$\mu = \mu_{\text{opt}} = \nu = \nu_{\text{opt}} = \sqrt{1 + Q_{D_1}^2 b_n^2} \quad (26)$$

and

$$\eta_{\text{opt}} = \frac{\mu_{\text{opt}} - 1}{\mu_{\text{opt}} + 1} = \frac{\sqrt{1 + Q_{D_1}^2 b_n^2} - 1}{\sqrt{1 + Q_{D_1}^2 b_n^2} + 1} \quad (27)$$

From this expression it may be seen that for maximum efficiency  $Q_{D_1} b_n$  should be as large as possible. In Fig. 7 we have plotted  $\eta$  vs  $Q_{D_1}$  for various values of  $b_n$ .

In Fig. 8 we have plotted  $\eta$  vs  $\nu$  assuming  $\mu = \sqrt{Q_{D_1}^2 b_n^2 + 1}$ , to show the importance of  $\nu$ . Since  $\nu$  is always somewhat greater than unity, the load should be overcoupled to the diode.

We shall now consider the diode itself to see how factor  $Q_{D_1} b_n$  can be maximized in order to obtain greater efficiencies.

#### OPTIMIZING THE DIODE PARAMETERS

The maximum value of the factor  $Q_{D_1} b_n$  for any particular circuit is dependent only on the diode and its bias voltage. To maximize the diode  $Q$  alone, a diode should be chosen with a low series resistance and low capacitance. Since the diode  $Q$  is defined at the operating point capacity  $C_0$ , and not at the zero bias capacity, a diode should be chosen with as large a reverse breakdown voltage  $V_{RB}$  as possible, so that  $C_0$  will be small. Thus, the maximum value  $V_0$  may take is approximately  $V_{RB}/2$ .

From (9), (10), and (17) it is readily seen that to maximize  $b_n$ ,  $V_1$  (or the sum of  $V_1$  and  $V_n \cos \phi$  at  $\omega t = \pi$ ) must approach  $V_0$ . That is, we want to drive the capacity to infinity. However, as the capacitance goes to infinity, so do the forward conduction losses  $G(V)$ . Thus, the diode voltages may be limited<sup>8</sup> by some voltage  $V_R$  at which point the forward losses become so excessive as to reduce the diode  $Q$ . We may define  $V_R$  as the voltage where the diode  $Q$  is reduced to

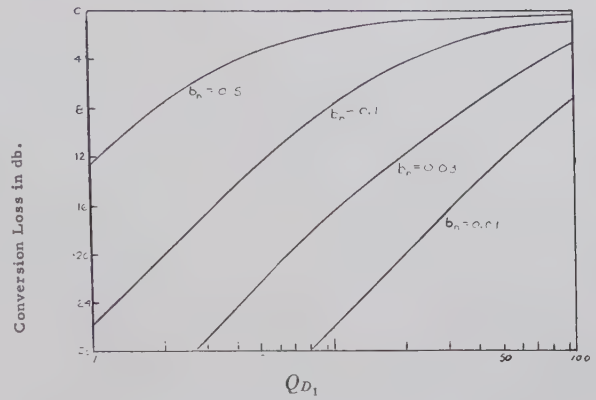


Fig. 7—Conversion loss vs diode  $Q$  for various values of the Fourier coefficient  $b_n$ .

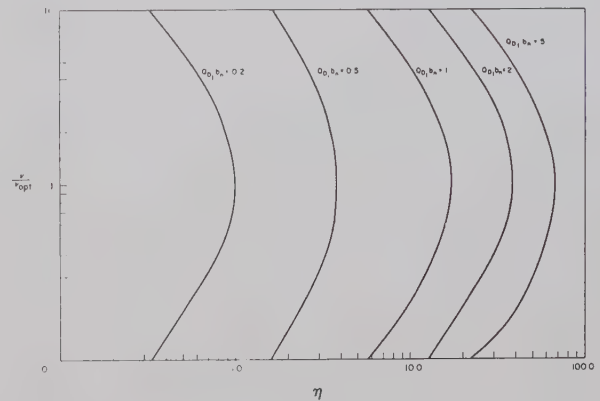


Fig. 8—Efficiency vs normalized load to diode conductance coupling.

half its original value due to the presence of  $G(V)$ . From Fig. 1 we can compute the total  $Q$  of the diode considering the effects of  $G(V)$  and  $r_s$ :

$$\frac{1}{Q_{DT}} = \frac{1}{Q_{D_1}} + \frac{1}{Q_{DG}} \quad (28)$$

where

$$Q_{DT} = \text{total diode } Q$$

$$Q_{D_1} = \frac{1}{\omega C(V) r_s} = \text{diode } Q \text{ due to } r_s \text{ only}$$

$$Q_{DG} = \frac{\omega C(V)}{G(V)(1 + r_s G(V))}$$

Measured from  $V_0$ ,  $V_R$  is then defined as the voltage where  $Q_{D_1} = Q_{DG}$ . Normally  $r_s G(V) \ll 1$  so  $V_R$  may be defined under the condition that

$$C(V) = \omega^2 C^2(V) r_s, \quad (29)$$

or for  $m = \frac{1}{2}$  when

$$\frac{kT\omega^2 C_0'^2 \phi r_s}{q i_s} = V_R \exp \frac{q(\phi - V_R)}{kT} \quad (30)$$

The instantaneous sum of the applied voltage at  $\omega_1 t = \pi$  may be written by inspection of (6) as  $V_1 = (-1)^{(n-1)} V_n \cos \phi_n$ . The maximum value of this in terms of  $V_R$  may be written

$$\left[ \frac{V_1 + (-1)^{n-1} V_n \cos \phi}{V_0} \right]_{\max} = 1 - \frac{V_R}{V_0} = 1 - \frac{2V_R}{V_{RB}} \quad (31)$$

For a maximum  $b_n$ , we want then a diode with a large  $V_{RB}/2V_R$ . The importance of this large value is shown in Fig. 9 where we have plotted  $V_{RB}/2V_R$  as a function of  $b_n$  assuming  $V_n = 0$ . The assumption that  $b_n = 0$  applies only to the case of low efficiencies as will be shown in the next section. When  $V_n$  is considered, the value of  $b_n$  becomes somewhat larger and the effect of  $V_{RB}/2V_R$  becomes less pronounced. In Fig. 10 we have shown how  $b_n$  may vary as a function of  $V_1/V_n$  for the particular case that  $V_1 + (-1)^{n-1} V_n \cos \phi_n = V_0$ .

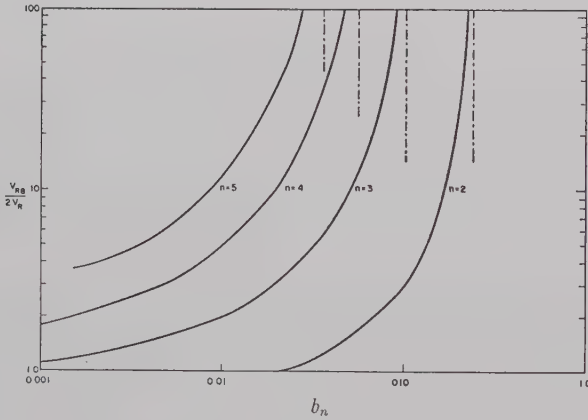


Fig. 9—Variation of Fourier coefficient with the diode parameter  $V_{RB}/2V_R$ .

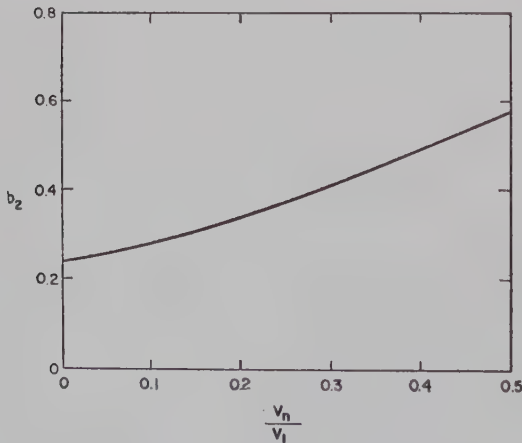


Fig. 10—Ratio of harmonic voltages vs normalized Fourier coefficient  $b_n$ .  
 $V_1 + (-1)^{n-1} V_n \cos \phi = V_0$

#### MAGNITUDE OF $N$ TH HARMONIC VOLTAGE

We shall show from the general circuit equations how  $V_1$  is related to  $V_n$  so that we may determine whether or not  $V_n$  may be omitted from (6).

Since we are ordinarily concerned with operation at maximum efficiency, we use the general circuit equations for optimum efficiency to relate  $V_1$  to  $V_n$ . From (14) and the fact that  $I_n = V_n G_{T_2}$  we may write

$$\frac{V_n}{V_1} = \frac{n\omega_1 C_0 b_n}{G_{T_2}} \quad (32)$$

Now

$$G_{T_2} = G_{D_n}(1 + \gamma_{\text{opt}}) = G_{D_n}[1 + \sqrt{1 + Q_{D_1}^2 b_n^2}], \quad (33)$$

so that

$$\frac{V_n}{V_1} = \frac{Q_{D_1} b_n}{n[1 + \sqrt{1 + Q_{D_1}^2 b_n^2}]} = \frac{\sqrt{\eta}}{n} \quad (34)$$

Therefore  $V_n/V_1$  is always less than  $1/n$  and, when operating with low efficiencies,  $V_n \ll V_1$ . Thus for  $n > 10$  and efficiencies less than 1 per cent,  $V_n/V_1 < 0.01$  and may be neglected without appreciably changing the determined value for efficiency. In the next section we shall show how the efficiency may be determined from the foregoing equations.

#### DETERMINATION OF EFFICIENCY

When  $V_n$  is negligible in the case of low efficiencies, we may use the value of  $b_n$  as determined from the hypergeometric series. Knowing, then, the diode  $Q$  we can solve for the efficiency from (27). If we consider the effect of  $V_n$ , then the equation we use for the "normalized" Fourier coefficient  $b_n$  as given from (7), (9) and (20) is given as

$$b_n = \sqrt{c_n'^2 + d_n'^2}, \quad (35)$$

where

$$c_n' = \frac{-V_0}{V_1 \pi (1 - m)} \int_{-\pi}^{\pi} \left[ 1 + \frac{V_1 \cos \omega_1 t}{V_0} + \frac{V_n}{V_0} \cos (n\omega_1 t + \phi_n) \right]^{1-m} \cos n\omega_1 t \cdot d\omega_1 t. \quad (36)$$

$$d_n' = \frac{-V_0}{V_1 \pi (1 - m)} \int_{-\pi}^{\pi} \left[ 1 + \frac{V_1 \cos \omega_1 t}{V_0} + \frac{V_n}{V_0} \cos (n\omega_1 t + \phi_n) \right]^{1-m} \sin n\omega_1 t \cdot d\omega_1 t. \quad (37)$$

Recall that

$$\phi_n = - \left( 90^\circ + \tan^{-1} \frac{d_n'}{c_n'} \right). \quad (38)$$



We may now solve for  $b_n$  if  $V_1$  and  $V_n$  are known. Eq. (34) is another equation relating  $V_1$  and  $V_n$  to  $b_n$ . This equation may be expressed in a more useful form as

$$b_n = \frac{2nV_n}{Q_{D1}V_1} \frac{1}{1 - \frac{n^2V_n^2}{V_1^2}}. \quad (39)$$

To solve for  $b_n$  and  $\eta$ , it is necessary to try various values of  $V_1$  and  $V_n$  until (34) and (35) are satisfied. Essentially, then, we must solve by trial and error (36), (37), (38), and (39) for any particular diode  $Q$ . Although this may seem quite tedious, it can be done. In the following section we shall show how important it is to consider  $V_n$  in a practical case. The appendixes provide the means for solution of the integrals. A series technique is useful if one has access to a computer.

### MAXIMUM EFFICIENCY

In this section we shall consider a practical diode to show what the maximum efficiency would be as a function of harmonic number.

Let us consider a typical Hughes parametric amplifier diode, the HPA 2800 diode, with an operating point capacity of  $1 \mu\text{mf}$ , a  $r_s$  of 4 ohms, and  $V_{RB}/2V_R$  of 40. Instead of including  $G_1$  and  $G_2$  in the equation for efficiency, we shall assume for simplicity that the input and output filters have a total loss of 0.3 db. By numerical integration of the integral for the Fourier coefficient, we are able to plot conversion loss vs  $n$  for a fundamental frequency of 1 kmc; this is done in Fig. 11. The dotted portion of the curve shows the effect when

$V_n$  is neglected and only the hypergeometric series used. It may be seen that the conversion loss increases as would be expected and for large  $n$  the conversion loss increases approximately 2.9 db per  $n$ .

Experimental work that the author has done has indicated that it is difficult to obtain efficiencies much greater than those indicated by the equations which neglect  $V_n$  for harmonics greater than the second. This may have been due to some fault in the diode used which showed itself at higher microwave frequencies, or perhaps to a poor estimation of the  $Q$  of the diode used. However, comparison was made with the results of Chang<sup>7</sup> and these give a little better agreement with the theory. Using the values they give for diode  $Q$  and assuming that the parameter  $V_{RB}/2V_R$  for their diode was equal to 10, the following calculations were made: The diode  $Q$  for  $n=2$  was calculated to be about 5, for  $n=3$  to be about 7.5. The Fourier coefficients  $b_2$  and  $b_3$  were calculated to be 0.250 and 0.053 respectively. This gave a maximum efficiency for doubling of 23 per cent and for tripling of 3.65 per cent. If the filter losses were about 0.2 db, then the expected efficiencies are 22 per cent and 3.47 per cent. This is to be compared with the experimental results of 22 per cent for doubling and 2 per cent for tripling. Thus, the accuracy is quite good for doubling and not quite as good for tripling.

### CONCLUSION

Good efficiencies may be obtained if the harmonic generator is operated so that the signal drives the diode somewhat into conduction and uses as large a bias voltage as possible on the diode. A diode should be chosen which has a large  $Q$ , a large reverse breakdown voltage, and a small voltage difference between the point of infinite capacity and high forward conduction. If the coupling of the load to the diode is optimized and the generator is critically coupled to the signal circuit, optimum matching conditions are achieved. As operation is extended to higher and higher harmonic numbers, the nonlinear contribution to the efficiency becomes exceedingly important and the diode chosen must have a high reverse breakdown voltage and low voltage difference between infinite capacity and high forward conduction.

By following these principles, it is possible to obtain efficiencies at least as good as those indicated by the equations which neglect  $V_n$ . As better diodes are obtained, it is likely that it will be possible to achieve the theoretical maximum efficiency for all harmonics. Because of the good efficiencies which this analysis shows are possible for large harmonic numbers, it may be, in some cases, just as efficient to convert directly to a large harmonic number as to use several doublers or triplers in cascade. This will give a saving on the quantity of diode and filters required.

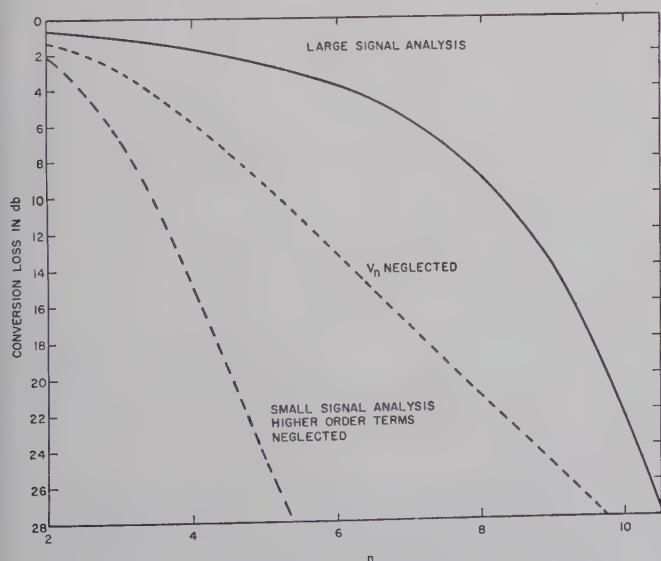


Fig. 11—Theoretical curves of conversion loss vs harmonic number for a typical Hughes diode.  $C_0 = 1 \mu\text{mf}$ ;  $r_s = 4$  ohms;  $V_{RB}/2V_R = 40$ , which corresponds for  $n=2$  to  $P_{in} \approx 13$  milliwatts; 0.3-db filter losses.

## APPENDIX I

In this appendix we shall indicate a technique for numerical integration of (36) and (37). Since the graph of the function to be integrated is merely a cosine wave in  $n\omega_1 t$ , modulated by a uniformly varying function, it is only necessary for the most part to determine the magnitude of the amplitude of the cosine wave from  $\omega_1 t = 0$  to  $\omega_1 t = \pi$ . At  $\omega_1 t = \pi$  an additional correction may have to be made if  $V_{RB}/2V_R$  is not  $\infty$ . The integral of the function will be proportional to the sum of these amplitudes, provided that the distance over which the half cosine waves occur is taken into consideration.

As a simple example, if we consider (12) for  $n=2$  and  $V_1/V_0=1$ , we find we have three peaks occurring approximately at 0,  $\pi/2$  and  $3\pi/8$ . This function is represented in Fig. 12. The respective magnitudes are 2, -1, and 0.19. The integral is then given by

$$b_2 = \frac{4}{\pi} \left[ \frac{\sqrt{2}}{2} - 1.0 + \frac{0.19}{2} \right] = 0.252.$$

The actual value by direct integration is  $b_2=0.240$ ; we see the accuracy is fairly good.

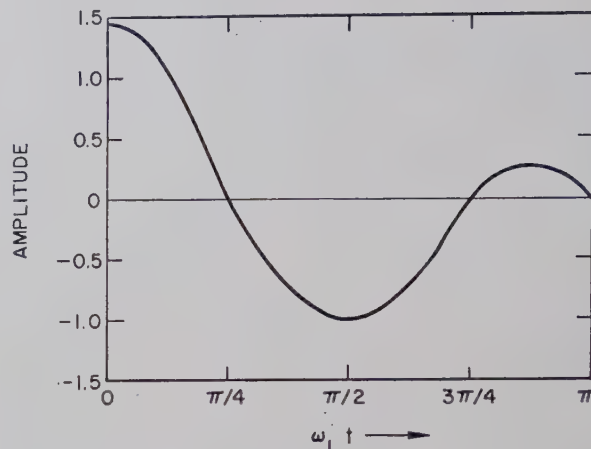


Fig. 12—Variation of second harmonic charge for computation of normalized Fourier coefficient  $b_n$ .

## ACKNOWLEDGMENT

The author is indebted to C. E. Nelson and M. T. Weiss of the Microwave Laboratory, to B. J. Leon and D. R. Anderson of the Research Laboratories, Hughes Aircraft Co., Culver City Calif., for their helpful comments and suggestions.

## A Waveguide Switch Employing the Offset Ring-Switch Junction\*

R. C. JOHNSON<sup>†</sup>, A. L. HOLLIMAN<sup>†</sup> AND J. S. HOLLIS<sup>‡</sup>, MEMBER, IRE

**Summary**—This paper describes an X-band microwave ring switch employing a junction of new design. The insertion loss is less than  $\frac{1}{4}$  db over the design band of 9.0–9.6 kmc; this low loss was obtained through the use of a coupling junction which is designated the offset ring-switch junction. A physical description, the electrical characteristics of the switch, and a qualitative theoretical discussion of the junction are included.

## INTRODUCTION

**R**APID scanning of a sector at a constant rate with a narrow beam antenna, by movement of the complete antenna or by motion of a feed mechanism, imposes the problem of minimizing the

dead-time between scans. Many scanning antennas employ multiple feeds or dishes which rotate at constant speed to limit the dead-time to a reasonable value without forcing the antenna or scanning mechanism to undergo rapid acceleration between scans. Several types of microwave switches have been employed for sequentially switching the input waveguide of such antennas to each of the several feeds or dishes. Waveguide ring switches are often employed for this purpose.

Peeler and Gabriel reported a waveguide ring switch<sup>1</sup> which is based on an annular rotary joint patented by Breetz.<sup>2</sup> This switch employs right-angle bends made of interleaving pins which project into the ring waveguide parallel to the  $E$  field, and couple energy into, and out of, the ring guide. This coupling junction requires the

\* Received by the PGMTT, May 12, 1960; revised manuscript received, June 20, 1960. The work on the switch was supported by the Diamond Ordnance Fuze Laboratories, Washington, D. C., under Contract No. DA-49-186-502-ORD-709; the development of the junction was supported by the U. S. Army Signal Engineering Laboratory, Fort Monmouth, N. J., under Contracts Nos. DA 36-039 SC-72789 and DA 36-039 SC-74870.

<sup>†</sup> Engineering Experiment Station, Georgia Inst. Tech., Atlanta, Atlanta, Ga.

<sup>‡</sup> Scientific-Atlanta, Inc., Atlanta, Ga.

<sup>1</sup> G. D. M. Peeler and W. F. Gabriel, "A volumetric scanning GCA antenna," 1955 IRE NATIONAL CONVENTION RECORD, pt. I, pp. 20–27.

<sup>2</sup> L. D. Breetz, U. S. Patent No. 2,595,186, April 29, 1952. Also, L. D. Breetz, "A Waveguide Rotary Joint with Waveguide Feed," Naval Res. Lab., Washington, D. C., NRL Rept. 3795; January 18, 1951.



ring waveguide to be split longitudinally along two corners. Since the current density across the corners is large, efficient chokes are required along the gaps to prevent excessive loss; these chokes are serrated to prevent longitudinal propagation of energy in the choke grooves.

Tomiyasu reported a waveguide rotary joint<sup>3</sup> which can be adapted for a ring switch. This joint is based upon the use of cascaded Transvar couplers which couple energy into, or out of, the ring waveguide; since the ring waveguide is split longitudinally along high cross-current lines, serrated chokes are employed as in the Breetz rotary joint.

In the design of a waveguide ring switch, it is desirable to make the longitudinal split in the ring guide at the center of the  $H$ -plane wall, since the only currents that exist across the gap with this configuration are located in the immediate vicinity of the junction. Configurations of this type were proposed independently by Hollis and Long<sup>4</sup> at Georgia Tech, Atlanta, and by Coleman<sup>5</sup> at the U. S. Navy Electronics Laboratory. A  $K_u$ -band switch based upon this principle was fabricated at Georgia Tech.<sup>6</sup> This switch operated satisfactorily; however, the bandwidth was limited to about 2 per cent by the impedance characteristics of the input and output junctions. An alternate coupling configuration has been developed at Georgia Tech, which has inherent broad bandwidth characteristics, and which can be scaled for use at any frequency in the microwave region; this coupling junction is called the *offset ring-switch junction*.<sup>7</sup> The switch described in this paper employs junctions of this type.

### OFFSET RING-SWITCH JUNCTION

The offset junction consists of a cavity, of length  $a$  and width  $b$ , which is used as a coupling device between two rectangular waveguides as illustrated by the section, through a typical junction, in Fig. 1. The lines down the center of the upper waveguide represent a mechanical separation which permits relative motion between sections  $A$  and  $B$ .

The junction has a simple geometrical configuration which requires no additional matching devices. Its performance is independent of the  $E$  dimension, since all discontinuities are parallel to the  $E$  field. In the junction cavity, the width  $b$ , which is approximately one and a half times the width of the coupled guides, is

large enough to propagate both the  $TE_{10}$  and  $TE_{20}$  modes; the impedance characteristics of the junction result from interaction of the energy in these modes. A rigorous theoretical analysis of the junction has not been completed; however, the following semiquantitative analysis serves to indicate the principle of operation.

The offset junction is a bilateral device; however, in this discussion it will be assumed that the energy is coupled from guide 1 into guide 2. At the discontinuity between guide 1 and the cavity, all  $TE_{m0}$  modes are excited; but only the  $TE_{10}$  and  $TE_{20}$  modes are above cutoff frequency. Consider the behavior of these two modes. The  $TE_{10}$  mode energy has a lower phase velocity than the  $TE_{20}$  mode energy; therefore, their relative phase changes as they propagate down the cavity. If the total relative phase shift in the cavity is  $\pi$ , all the energy is coupled from guide 1 into guide 2. This situation is illustrated in Fig. 2; notice that the boundary conditions at the ends of the cavity are roughly satisfied if the phase and amplitude of each mode are as illustrated.

The total relative phase shift in the junction cavity is

$$\theta_r = \theta_{10} - \theta_{20}$$

or

$$\theta_r = 2\pi a_e \left( \frac{1}{\lambda_{g10}} - \frac{1}{\lambda_{g20}} \right), \quad (1)$$

where  $\theta_{10}$  and  $\theta_{20}$  are the phase changes of the  $TE_{10}$  and  $TE_{20}$  modes, respectively;  $a_e$  is the electrical length of the cavity, and  $\lambda_{g10}$  and  $\lambda_{g20}$  are the guide wavelengths in the cavity of the  $TE_{10}$  and  $TE_{20}$  modes, respectively. Because of the cavity end effects, the electrical length of the cavity  $a_e$ , is slightly longer than the physical length  $a$ .

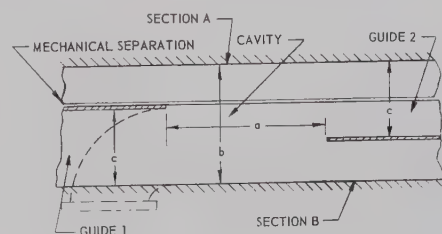


Fig. 1—The basic geometry of the offset junction. The  $E$  field is perpendicular to the plane of the page; therefore,  $c$  is the  $H$  dimension of guide 1 and guide 2. The dashed lines indicate the possible addition of an  $H$ -plane bend to guide 1 for use in a ring switch.

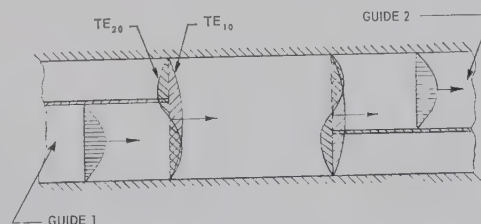


Fig. 2—The propagating modes in the offset junction. The curves represent the  $E$ -field amplitude, and the arrows represent the direction of propagation.

<sup>3</sup> K. Tomiyasu, "A new annular waveguide rotary joint," *Proc. IRE*, vol. 44, pp. 548-553; April, 1956.

<sup>4</sup> R. E. Horner, J. S. Hollis, M. W. Long, et al., "Two-Beam 16,000-mc Modified Luneberg Lens Scanning System," Georgia Inst. Tech., Atlanta, Final Rept., Contract No. DA 36-039 SC-15566, p. 13; February 15, 1953. U. S. Patent No. 2,826,742, March 11, 1958.

<sup>5</sup> G. M. Coleman, U. S. Navy Electronics Lab., San Diego, Calif., unpublished memoranda.

<sup>6</sup> R. D. Hayes and J. S. Hollis, "A Modification Kit for the Two-Beam 16,000-mc Modified Luneberg Lens Scanning System," Georgia Inst. Tech., Atlanta, Final Rept., vol. III, Contract No. DA 36-039 SC-42707; September 15, 1955.

<sup>7</sup> J. S. Hollis, patent pending.

The magnitude of the reflection coefficient has been measured for offset junctions having various cavity lengths  $a$ , with  $b=1.400$  inches and  $c=0.900$  inch. The  $E$  dimension was 0.400 inch throughout, and the interior walls had a thickness of 0.040 inch. In offset junctions with these dimensions, the electrical length of the cavity appeared to be about  $13\frac{1}{2}$  per cent of a free-space wavelength longer than the physical length. A curve of the magnitude of the reflection coefficient,  $|\Gamma|$ , vs frequency for a typical junction is shown in Fig. 3(a). The total relative phase shift in this cavity was calculated to be  $\pi$  for a frequency of 11.12 kmc; note that the

junction operates well in a region near this frequency. The three resonances in the band occur at frequencies such that the electrical length of the cavity is an integral number of half-wavelengths for the  $TE_{20}$  mode. This same type of impedance vs frequency characteristic with regularly spaced  $TE_{20}$  mode resonances has been observed for many junctions of various cavity lengths.

In practice, it has been found that the  $TE_{20}$  mode resonance is greatly reduced, or not present, if the electrical length of the cavity is simultaneously  $n$  half-wavelengths long for the  $TE_{20}$  mode and  $n+1$  half-wavelengths long for the  $TE_{10}$  mode, where  $n$  is a posi-

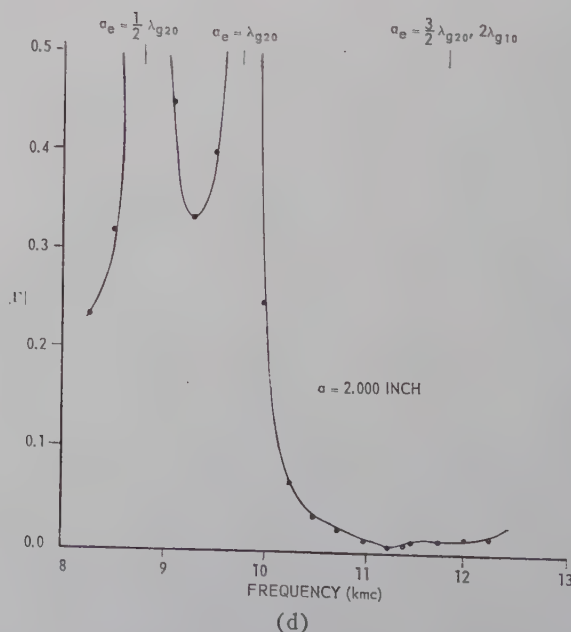
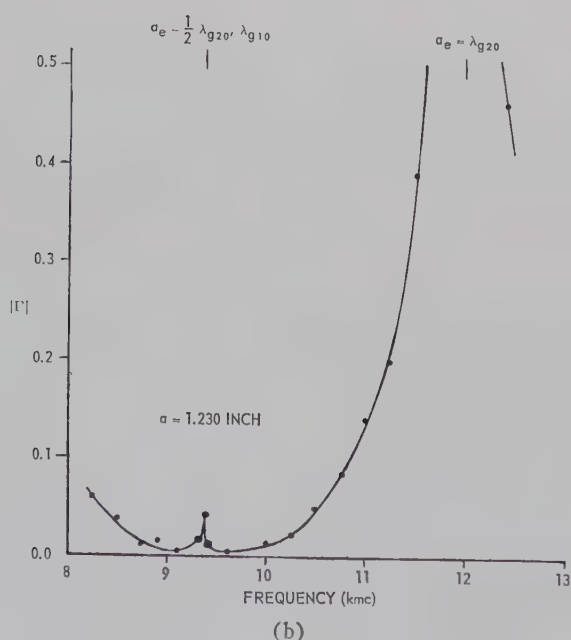
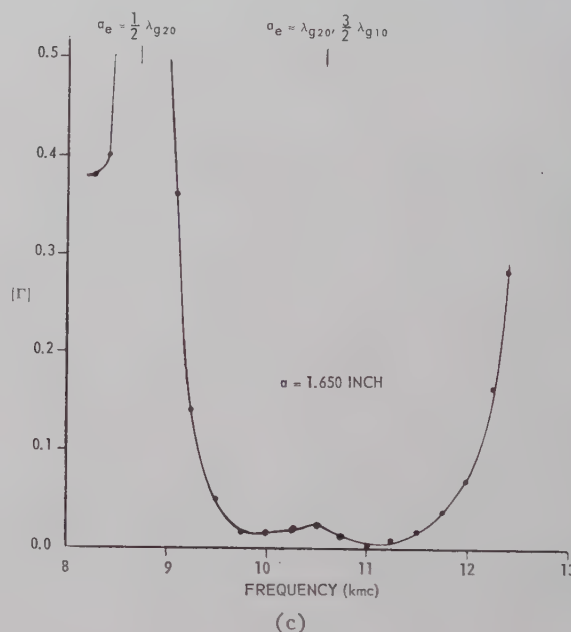
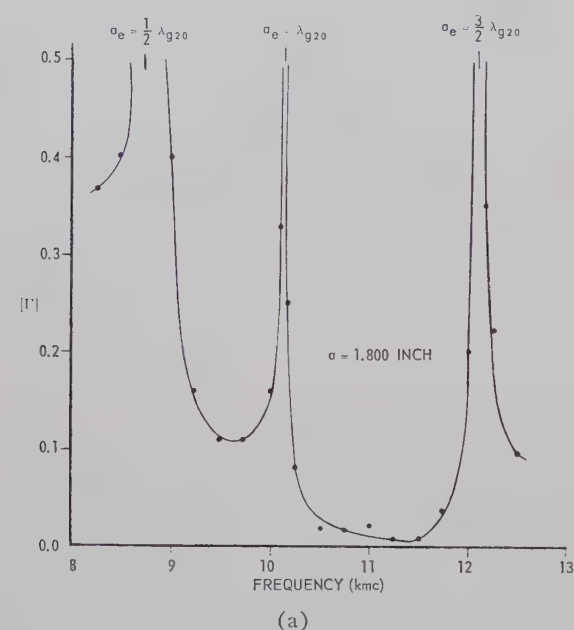


Fig. 3—The magnitude of the reflection coefficient,  $|\Gamma|$ , vs frequency for junctions having cavity widths  $b=1.400$  inches and cavity lengths  $a$  as indicated;  $a_e$ =electrical length of cavity.



tive integer. This condition can be expressed mathematically as two simultaneous equations,

$$a_e = \frac{n\lambda_{g20}}{2} = \frac{n\lambda}{2\sqrt{1 - (\lambda/b)^2}} \quad (2)$$

$$a_e = \frac{(n+1)\lambda_{g10}}{2} = \frac{(n+1)\lambda}{2\sqrt{1 - (\lambda/2b)^2}} \quad (3)$$

where  $\lambda$  is the free space wavelength. Solving these equations, it is found that the electrical length and the width of the cavity must be the following:

$$a_e = \lambda \left[ \frac{3n^2 + 8n + 4}{12} \right]^{1/2} \quad (4)$$

$$b = \lambda \left[ \frac{3n^2 + 8n + 4}{8n + 4} \right]^{1/2} \quad (5)$$

If  $b$  is equal to 1.400 inches, (4) and (5) give the values of  $a_e$  in Table I. The frequency,  $f_0$ , corresponds to a free space wavelength of  $\lambda$ , and the physical length,

TABLE I

$n$	$\lambda$ (inch)	$f_0$ (kmc)	$a_e$ (inch)	$b$ (inch)	$a$ (inch)
1	1.252	9.43	1.400	1.400	1.231
2	1.107	10.66	1.807	1.400	1.658
3	0.999	11.81	2.139	1.400	2.004

$a$ , was estimated by subtracting  $0.135\lambda$  from the electrical length,  $a_e$ . The magnitude of the reflection coefficient was measured over a wide band of frequencies for three junctions having dimensions close to those given in Table I. The  $TE_{20}$  mode resonance was not observed for the cases  $n=2$  and 3, as shown in Figs. 3(c) and 3(d), respectively, and it was greatly reduced for the case  $n=1$ , as shown in Fig. 3(b). It is possible that the latter resonance can be eliminated by a slight change in the dimension  $a$ . Experimental evidence indicated that the resonances for junctions corresponding to cases 1, 2, and 3 tend to occur at frequencies which are 0.3, 0.8 and 2.5 per cent, respectively, lower than theoretically predicted in Table I.

The three cavities of Table I produced wide bandwidth junctions which can be scaled to other frequencies. The power handling capacity is limited at the resonant frequency  $f_0$ ; but there is a relatively wide band of frequencies on each side of  $f_0$  where the junction will transmit high power. In low-power devices, such as radiometers, this power limitation at  $f_0$  is not a disadvantage.

A qualitative argument for the wide bandwidth characteristics of the offset junction is illustrated in Fig. 4; the phase shift of each mode and the relative phase shift are shown as functions of frequency for a junction corresponding to  $n=2$  in Table I. It should be noted that the relative phase shift is more nearly constant than the phase shift of either mode. The electrical

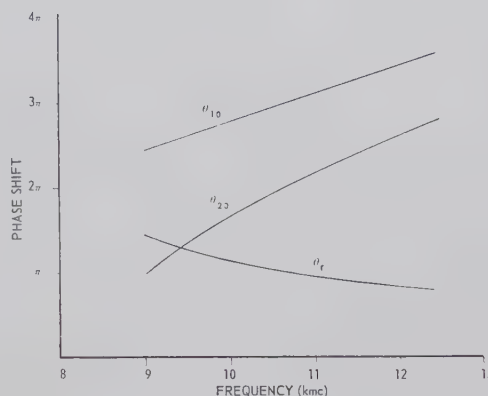


Fig. 4—The total phase shift for the  $TE_{10}$  and  $TE_{20}$  modes and their relative phase shift in a junction cavity having dimensions  $a_e=1.807$  inches and  $b=1.400$  inches.

length of the cavity was assumed to be constant and identical for both modes; however, in a more detailed analysis,  $a_e$  is a function of frequency and of the mode of propagation.

### CURVED JUNCTION

Fig. 1 illustrates the manner in which the offset ring-switch junction can be split for use in a ring switch. In this case, guide 2 represents the ring guide which is split down the center of the  $H$  dimension. Since the currents in the guide walls are parallel to the split, except in the junction cavity, chokes are required only in this region, and the loss in the split ring guide is almost as small as that in ordinary waveguide.

The offset junctions described in the previous section were constructed from straight sections of rectangular waveguide; however, the junction performance is not greatly affected if the cavity is curved in the  $E$  plane, as long as the mean cavity length is not changed. To meet physical limitations, the ring guide for the switch which is described below was curved in the  $E$  plane with a mean radius of 4.5 inches (approximately 3.5 wavelengths); the  $E$  dimension was made 0.600 inch to increase power transmission capability and to reduce loss.

The junction cavity selected for this switch had a mean length and width approximately proportional to those used for Fig. 3(b); however, to prevent the occurrence of the resonant peak in the design band of the switch, the cavity dimensions were scaled downward to put the resonance at the high end of the band. This required the  $H$  dimension of the ring guide to be 0.880 inch rather than 0.900 inch of standard RG-52/U waveguide. The magnitude of the reflection coefficient vs frequency for a typical curved junction with this configuration has the same general shape as that for a straight junction.

### PHYSICAL DESCRIPTION OF SWITCH

The ring switch is shown in Fig. 5 (assembled) and in Fig. 6 (disassembled). The sub-assemblies shown in Fig. 6 were machined from yellow brass, softsoldered

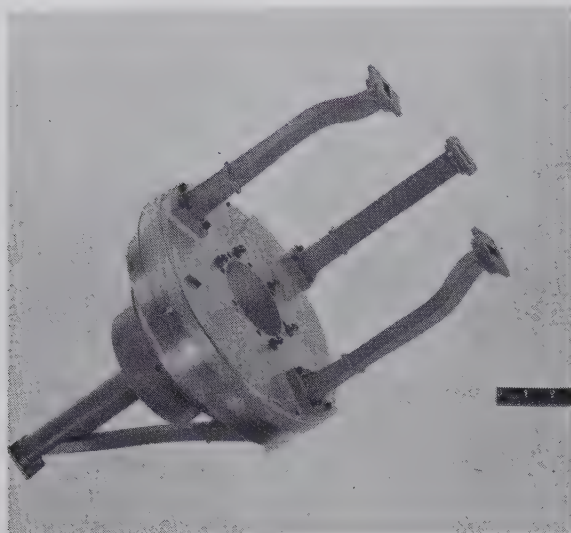


Fig. 5—The ring switch and connecting waveguide assemblies.

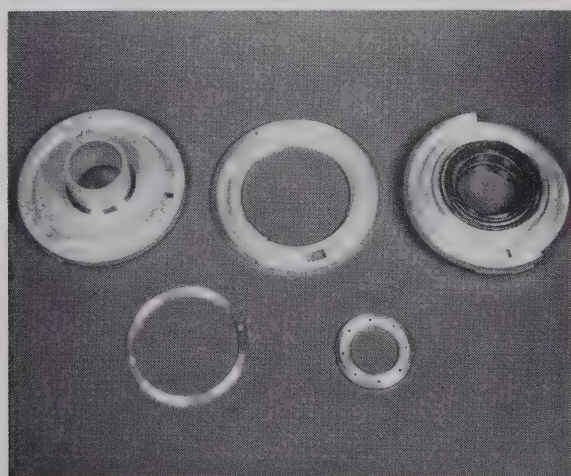


Fig. 6—The ring switch (disassembled).

together, and silver plated. In Fig. 5, the three output arms can be seen on the top surface of the switch, and the input arm is visible at the bottom. The general configuration of the switch and arms was required for compatibility with existing Diamond Ordnance Fuze Laboratories equipment.

Fig. 7 (opposite) is an isometric section of the ring switch, shown with four output arms rather than three, to show the junctions more clearly. The switch is constructed of three principal parts: Part *A*, the lower section, is stationary, and its input junction is connected to a transmitter-receiver system (see Fig. 5); Part *B*, the center section, can be manually rotated through  $150^\circ$  to adjust the center of the  $75^\circ$ -degree active sector; Part *C*, the upper section, rotates at 40 rpm. As the switch rotates, the energy is sequentially switched from one output junction to the next. Fig. 8 (opposite) is an orthographic section through the energy path of the

switch; the dashed line represents the path followed by microwave energy as it propagates through junctions *A*, *B*, and *C* of the switch.

The mean radius of the bend *D*, and the length of the taper *E*, in Fig. 7, connecting each of the switch junctions to the external waveguide, were designed to have minimum practical VSWR.

Serrated chokes were used to reduce radiation loss through the gaps between the center section of the switch and the upper and lower sections (see Fig. 6). Those chokes are required only in the vicinity of the junctions, as previously mentioned.

### SWITCH PERFORMANCE

This ring switch has three output arms spaced  $120^\circ$  apart, and activated sequentially through an active sector of  $75^\circ$ , with the position of the sector adjustable throughout a range of  $150^\circ$ . After the switch had been constructed, electrical measurements were made to determine the following three characteristics of the switch: voltage standing wave ratio, insertion loss, and power transmission capability.

The maximum VSWR was measured for representative frequencies over the operating band and is shown in Fig. 9. The energy transmission path (see Figs. 5, 7 and 8) consisted of the input waveguide, the input taper, a  $90^\circ$  *H*-plane bend, the input junction, the center section junction, one of the three output junctions, a  $90^\circ$  *H*-plane bend, an output taper, and the output waveguide terminated with a sliding load. The positions of the center ring and output ring were varied to determine the maximum VSWR at each frequency. The higher VSWR with output arm number 1 is believed to be caused by a nonuniformity in its output waveguide assembly, since before the input and output waveguide assemblies were installed, the maximum VSWR of the switch, with input and output  $90^\circ$  bends and tapers but without the combination twist-bend sections, was 1.12. The limited time available for the development of this switch did not permit additional tests and improvement of the waveguide sections.

The loss through the entire ring switch, including the input and output waveguides, was measured by the substitution method and found to be less than  $\frac{1}{4}$  db over the design band for representative switch positions.

The switch transmitted 200 kilowatts of peak power at atmospheric pressure without breakdown. Since this was the largest power source available for test purposes, the breakdown power could not be measured. With 15-psig pressurization, it is estimated that the switch will transmit a peak power greater than 600 kw.

Approximately  $45^\circ$  of switch rotation is required for switching between successive output arms; thus, the maximum usable scan sector is approximately  $75^\circ$ .



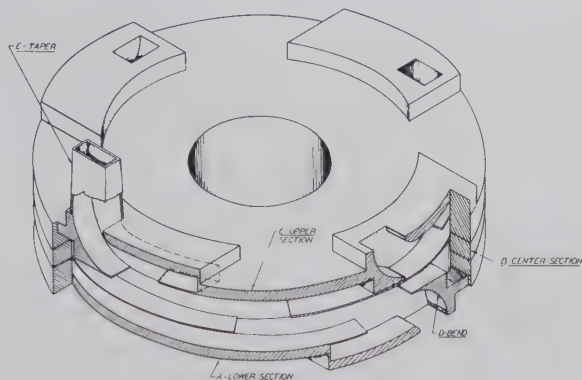


Fig. 7—An isometric section of the X-band microwave ring switch shown with four output arms, rather than three, in order to show junctions more clearly.

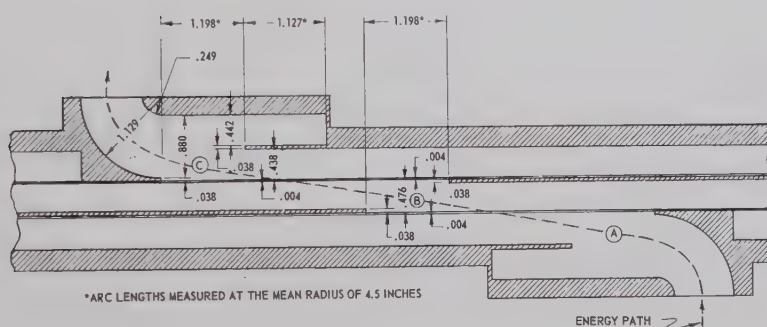


Fig. 8—A section through the energy path of the switch. Junctions A, B, and C are shown.

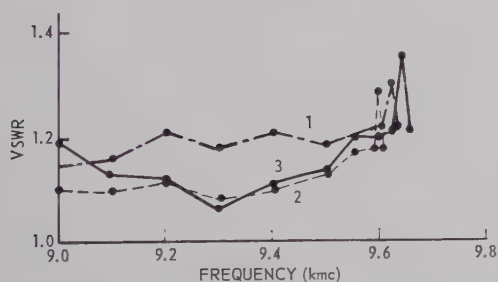


Fig. 9—The maximum VSWR vs frequency for each of the output arms. The energy path includes the total path through the ring switch and external waveguide as shown in Fig. 5.

### CONCLUSIONS

The waveguide ring switch described in this paper has electrical characteristics which are made possible by the use of the offset ring-switch junction. This junction has a larger switching angle than some other junctions which have been employed in ring switches; however, this fact is more than compensated by the following advantages. 1) The junction has low-loss, wide-bandwidth characteristics. 2) It has a simple geometrical configuration which requires no additional matching devices; this allows the junction to be fabricated with

relative ease for use at millimeter wavelengths. At these wavelengths, the switch diameter is much greater than a wavelength, and the switching angle becomes less significant. 3) The ring-guide is split down the center of the  $H$  dimension; this eliminates the need for chokes, except in the vicinity of the junction cavity, and it reduces the losses in the split ring-guide. 4) The junction operation is independent of the  $E$  dimension. In many applications, losses in the ring-guide can be reduced considerably by making the  $E$  dimension greater than half a wavelength; this is particularly useful at millimeter wavelengths. An increased  $E$  dimension also reduces the current density orthogonal to the split in the cavity; low-loss junctions have been fabricated without the use of chokes by making the  $E$  dimension  $1\frac{3}{8}\lambda$ . 5) The offset ring switch junction is capable of handling high power, except at the resonant frequency.

A simplification of the mechanical design and fabrication of this switch could be made by locating the serrated chokes only on the center section of the switch (see Fig. 6); it would then be possible to electroform the upper and lower sections of the switch as integral units. This design change would reduce the required machine work and eliminate almost all of the soldered mechanical joints along the boundaries of the energy path.

# Some Limitations on Parametric Amplifier Noise Performance\*

R. D. WEGLEIN†, SENIOR MEMBER, IRE

**Summary**—Now that the precursory period following the solid-state parametric amplifier invention has given way to an era of determined effort to reduce to practice some of the early, optimistic predictions, practical limitations setting an upper bound to the performance of this ingenious communications device have become apparent. In this paper, two such limitations are discussed: First, for a given diode  $Q$  and junction geometry, there exists a noninfinite idler frequency, which determines the lowest radar noise temperature.<sup>1</sup> Second, because of its extreme noisiness the reverse-breakdown current limits the maximum capacitance swing at both extremes and consequently the minimum noise performance. It is suggested that in certain cases refrigeration may be a partial remedy to both limitations.

## I. INTRODUCTION

IT IS commonly assumed that the minimum radar noise temperature of a parametric amplifier is obtained when the idler-to-signal-frequency ratio approaches infinity. While this notion is indeed a direct consequence of the energy conservation rules formulated by Manley and Rowe,<sup>2</sup> the presence of loss modifies this condition and a noninfinite ratio of idler to signal frequency results. Although the existence of this optimum ratio has already been pointed out,<sup>3</sup> it has not been adequately discussed in view of practical consequences. While in many cases this optimum ratio of idler to signal frequency is sufficiently large to demand more pump power than the diode can dissipate, there may be instances, especially at the lower frequencies, where some benefit can be derived from this knowledge. Since the detailed derivation of the expressions for noise temperature have been derived elsewhere,<sup>3</sup> they will be given here without proof as basis for further development.

## II. OPTIMUM RATIO OF IDLER TO SIGNAL FREQUENCY

The radar noise temperature  $T_{n1}$ , which in the most general case depends on circuit and diode losses at

signal and idler frequencies as well as on the degree of coupling of an external idler termination, may be simplified by consideration of only the pertinent losses. These are the signal and idler diode conductances derived from the actual series equivalent circuit, under the assumption that  $Q_d$  is independent of frequency and  $\gg 1$

$$G_{ds} = \frac{\omega_s \bar{C}}{Q_d}; \quad G_{di} = \frac{\omega_s \bar{C}}{Q_d} \Omega^2. \quad (1)$$

Assuming a perfect circulator to separate input and output terminals in the signal port and high gain, one finds for the radar noise temperature

$$T_{n1} \simeq \left[ \frac{1}{\mu_{s1}} + \frac{1}{\Omega} \left( 1 + \frac{1}{\mu_{s1}} \right) \right] T_d. \quad (2)$$

(All symbols are defined at the conclusion of the report.) The maximum  $\mu_{s1}$  for a given diode is determined by

$$\mu_{s1} \leq \left( \frac{\Delta C}{2\bar{C}} \right)^2 \left( \frac{f_c}{f_s} \right)^2 \frac{1}{\Omega} - 1. \quad (3)$$

Substituting (3) into (2) with the additional definition,

$$K = \left( \frac{1}{2} \frac{\Delta C}{\bar{C}} \right) Q_d, \quad (4)$$

(hereafter referred to as diode parameter or figure-of-merit) shows the explicit dependence of  $T_{n1}$  on the diode parameters and the idler-to-signal-frequency ratio  $\Omega$ :

$$\frac{T_{n1}}{T_d} \simeq \frac{1}{\frac{K^2}{\Omega} - 1} + \frac{1}{\Omega} \left( 1 + \frac{1}{\frac{K^2}{\Omega} - 1} \right). \quad (5)$$

The radar noise temperature exhibits a minimum value, where

$$\frac{\partial T_{n1}}{\partial \Omega} = 0. \quad (6)$$

Carrying out the differentiation indicated in (6), one obtains the optimum idler-to-signal-frequency ratio

$$\Omega_{opt} = \sqrt{1 + K^2} - 1. \quad (7)$$

\* Received by the PGMTT, May 3, 1960; revised manuscript received, June 17, 1960.

† Research Labs., Hughes Aircraft Co., Malibu, Calif.

<sup>1</sup> Radar noise temperature (figure) is suggested (and used henceforth) to indicate reception in the vicinity of one carrier frequency, even though one or more additional frequency ports may receive and generate thermal noise; the complementary method of reception using all available frequency ports will be christened radiometer noise temperature (figure). In the past, single-channel noise figure and double-channel noise figure, respectively, have often been used to describe the two methods of reception.

<sup>2</sup> J. M. Manley and H. E. Rowe, "Some general properties of nonlinear elements—pt. I. general energy relations," *PROC. IRE*, vol. 44, pp. 904–913; July, 1956.

<sup>3</sup> R. C. Knechtli and R. D. Weglein, "Low-noise parametric amplifier," *PROC. IRE*, vol. 48, pp. 1218–1226; July, 1960.



The minimum radar noise temperature that can be obtained from this diode (described by  $K$ ) is

$$\left. \frac{T_{n1}}{T_d} \right|_{\min} \geq \frac{\frac{K^2}{\sqrt{1+K^2}-1} + 1}{K^2 - \sqrt{1+K^2} + 1} \quad (5a)$$

In Figs. 1 and 2, the optimum  $\Omega$  and the minimum  $T_{n1}$  are plotted as a function of the diode parameter  $K$ ; these curves are easily interpreted. Recalling the mean-

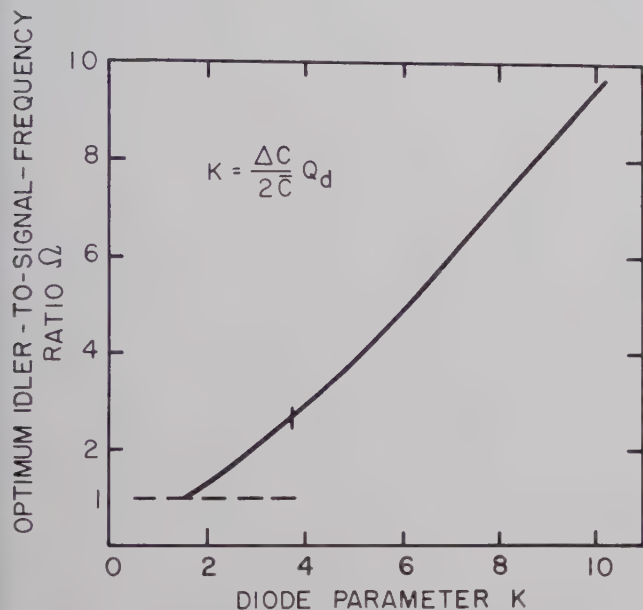


Fig. 1—Idler-to-signal-frequency ratio at which minimum noise temperature results.

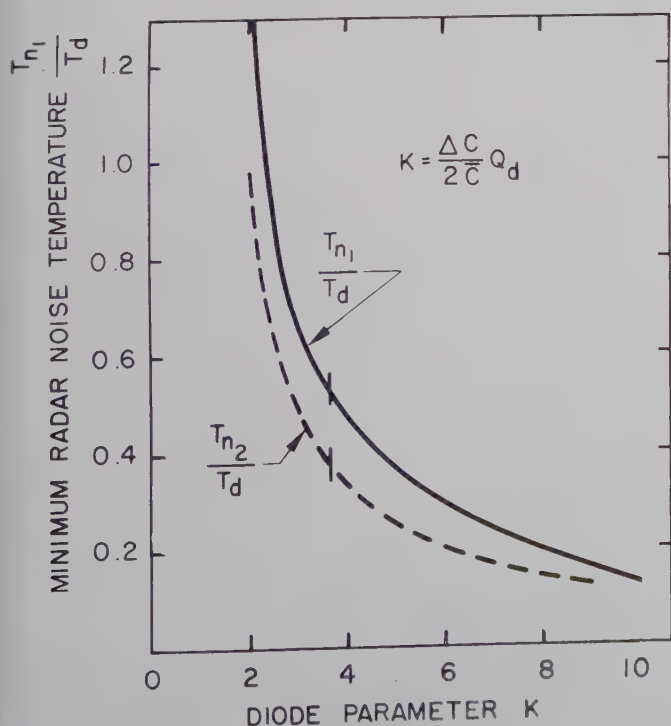


Fig. 2—Minimum noise temperature resulting from optimum choice of ratio of idler to signal frequency.

ing of the diode parameter  $K$  from (4), one may now obtain an estimate of the lowest noise temperature that a given diode can produce under optimum conditions: These are optimum coupling conditions and no circuit residual losses. Fig. 3, showing  $T_{n1}$  as a function of  $\Omega$ , for several values of  $K$ , gives an estimate of the penalty one pays for operating at an  $\Omega$  other than  $\Omega_{\text{opt}}$ . Note that for large  $K$  the minimum  $T_{n1}$  becomes less sensitive to  $\Omega$ . The parameter  $K$  can be determined with relative ease; the maximum normalized capacitance swing can be computed for any type junction,<sup>4</sup> and the  $Q$  at the signal frequency can be measured by determining the cutoff frequency. Fig. 1 then shows the idler-to-signal-frequency ratio at which the minimum radar noise temperature is obtained, and Fig. 2 gives its value in terms of the diode body temperature  $T_d$ . It is interesting to observe that Fig. 1 shows solutions for the idler frequency lower than the signal frequency. This indicates that the diode parameter  $K$  is too small for such an application, if low noise is the objective.

If, on the other hand, the amplifier is operated as a radiometer and signal and idler frequencies are near each other and both are coupled to the source, a radiometer noise temperature can be defined. This is given by

$$T_{n2} \simeq \frac{1}{\mu_{s2}} T_d, \quad (8)$$

<sup>4</sup> S. Sensiper and R. D. Weglein, "Capacitance and charge coefficients for parametric diode devices," *PROC. IRE*, vol. 48, pp. 1482-1483; August, 1960.

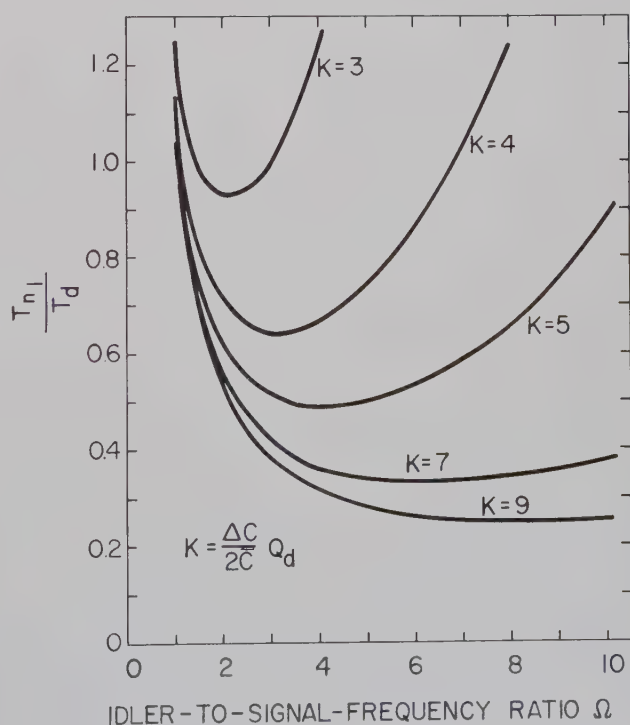


Fig. 3—The effect of the diode parameter  $K$  on the variation of the noise temperature (5) with idler-to-signal-frequency ratio  $\Omega$ .

and the maximum  $\mu_{s2}$  that can be achieved with a given diode is

$$\mu_{s2} \leq K - 1. \quad (9)$$

The minimum realizable radiometer noise temperature is shown in Fig. 2.

Finally, it is of interest to compute approximately the required pump power needed to obtain the results of Figs. 1 and 2. Expressions for the critical pump power  $P_{cr1}$  have been derived elsewhere<sup>3</sup> and are stated here under the assumptions that circuit losses are again negligible and the pump is matched to the diode:

$$P_{cr1} \geq \frac{\omega_s \bar{C}}{2Q_d^3} \left( \frac{C}{\varepsilon} \right)^2 \left( \frac{f_p}{f_s} \right)^2 \Omega (1 + \mu_{s1}). \quad (10)$$

This expression can be reduced to normalized form by noting that

$$\frac{\bar{C}}{\varepsilon} \simeq \left( \frac{\bar{C}}{\Delta C} \right) \Delta V, \quad \text{where } C = \bar{C} + \varepsilon V, \quad (11)$$

where  $\Delta V$  is the maximum permissible peak-to-peak voltage swing at the pump frequency. Then (10) can be rewritten as

$$\frac{P_{cr1}}{(\omega_s \bar{C}) \left( \frac{\Delta C}{2\bar{C}} \right) (\Delta V)^2} \geq \frac{1}{8} \left( K + \frac{1}{K} \right), \quad (12)$$

where (7), (3), and (4) have been substituted. It is perhaps more instructive to observe how this pump power varies with the optimum frequency ratio. Fig. 4 shows this variation, where both  $K$  and  $\Omega$  are indicated on the abscissa. Similarly, the normalized pump power of the degenerate case ( $\Omega \approx 1$ ) can be computed. If, instead of  $\mu_{s1}$ ,  $\mu_{s2}$  from (9) is substituted in (10), the normalized pump power for the degenerate case is given by

$$\frac{P_{cr2}}{(\omega_s \bar{C}) \left( \frac{\Delta C}{2\bar{C}} \right) (\Delta V)^2} \geq \frac{1}{2K}. \quad (12a)$$

This is shown by the dashed curve in Fig. 4.

#### A. Discussion

An examination of these four figures reveals the sensitivity of the amplifier performance to the diode parameter. If one refers, in particular, to Fig. 1 and Fig. 2, the strong dependence on the optimum idler-to-signal-frequency ratio and the resulting minimum noise temperature is evident. It is useful to consider a concrete example. (See Figs. 1, 2, and 4.) For currently available variable-capacitance diodes, a representative number for  $\Delta C/\bar{C}$  at some back bias is of the order of 0.6. In order to obtain a relative radar noise temperature of 0.5 (150°K without cooling of the diode), Fig. 2 im-

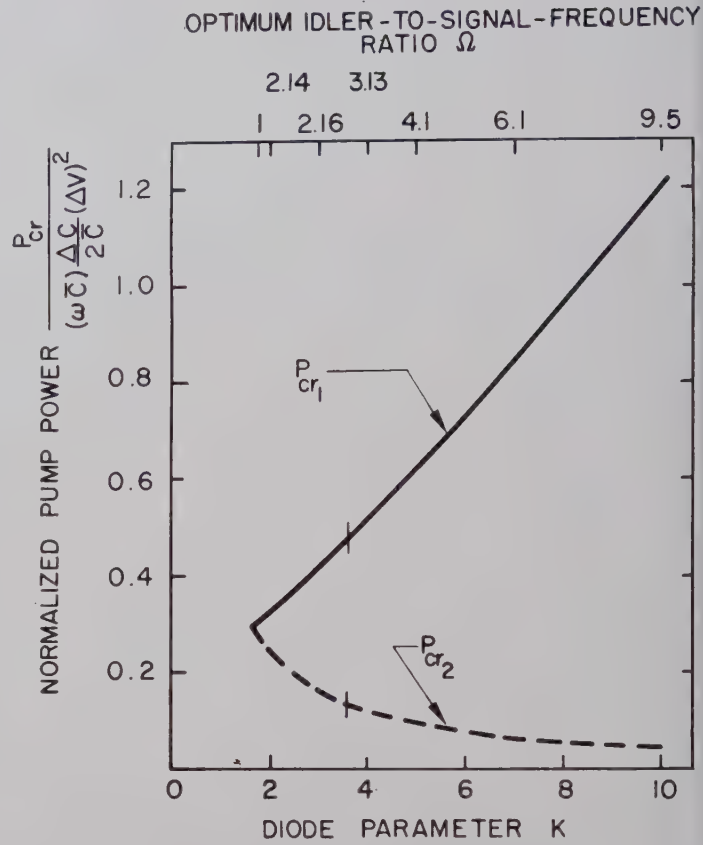


Fig. 4—Normalized pump power required to maintain high gain and the noise temperatures of Fig. 2.

plies a diode parameter  $K = 3.7$ , from which a diode  $Q$  of greater than 12 is calculated. Fig. 1 requires the idler-to-signal-frequency ratio to be about 2.7. The relative radiometer noise temperature for this diode is seen from Fig. 2 to be 0.37. Referring now to Fig. 4, one can make an estimate of the pump power necessary to attain these results. To obtain the radar noise temperature, a relative pump power of 0.48 is needed. Assuming a diode impedance level of 10 ohms and a peak-to-peak voltage swing of 4 volts, approximately 200 milliwatts are necessary (ideally). The corresponding degenerate amplifier needs only about 60 milliwatts. In practice, somewhat larger power is required, either because of losses that have not been accounted for or because of improper matching. In order that (3) or (9) holds, it should be kept in mind that the relations set forth here are valid only if the amplifier has been optimized—optimum coupling to the diode and maximum capacitance swing.

How does this optimum frequency ratio change if, in addition to the diode losses, an external idler termination is admitted? When it is recalled that the diode has been optimized with respect to coupling and capacitance swing to minimize the noise contribution due to its conductance, and the idler-to-signal-frequency ratio has been adjusted to produce approximately equal con-



tributions from both terms on the right-hand side of (5), it is evident that any additional conductance loading, whatever its origin, must of necessity result in a degradation of the noise performance. This, in turn, results in a new idler-to-signal-frequency ratio, which is sufficiently low to equalize again the contribution from the two competing terms in (5). The resulting radar noise temperature  $T_{n_1}$  will be higher than that obtained in the absence of the external idler load.

A scheme of this kind can be used to advantage in certain cases. In the above cited example, increase in bandwidth has been achieved at the expense of cooling an external load. If, for example, the diode cannot be cooled, as has been the case with silicon diodes,<sup>5</sup> the benefits resulting from deliberately reducing the idler-to-signal-frequency ratio in order to permit a "heavy" external idler load, which *can* be cooled, may be significant.

It may not always be practical to place the idler frequency at the optimum value, either because of bandwidth considerations (it is usually more difficult to attain bandwidth at higher idler-to-signal-frequency ratios) or because of possible spurious responses. The use of an external idler load in these cases may lead to more flexibility in design and, perhaps, improved performance.

### III. REVERSE CURRENT-INDUCED NOISE

In order that a parametric amplifier may give the optimum performance, which can be estimated from the knowledge of the figure of merit of the diode [*e.g.*, see (4)], the capacitance of the diode must swing over its entire permissible range. To achieve this maximum swing, the pump voltage (power) is increased until the diode is driven into the forward conduction region, where minority carriers are injected, or into the reverse breakdown region, where either avalanche multiplication or internal field emission limits the maximum voltage and capacitance excursion.<sup>6</sup> The measured noise power, due to reverse current in some diodes, is sufficiently high, even for currents of the order of 5 microamperes, to cause significant deterioration in the noise performance of an amplifier adjusted for optimum performance. Thus, in attempting to optimize an amplifier as outlined in the previous section, one encounters a new limitation to the noise and the bandwidth performance, these quantities being indirectly related when optimization is attempted simultaneously.

<sup>5</sup> To the best of the author's knowledge, on cooling silicon variable-capacitance diodes the series resistance increases as the temperature is decreased, so as to enhance the thermal noise power emanating from the diode.

<sup>6</sup> These and other noise sources have been suggested as possible causes for the observed increase of measured noise performance above theoretical predictions by M. Uenohara, "Noise consideration of the variable-capacitance parametric amplifier," *Proc. IRE*, vol. 48, pp. 169-179; February, 1960.

#### A. The Magnitude of Reverse Current-Induced Noise

Reverse breakdown in *p-n* junctions can occur in a variety of ways. Two mechanisms discussed in the literature are the field or tunneling effect<sup>7</sup> (Zener breakdown) and the avalanche or multiplication effect,<sup>8</sup> the latter analogous to the Townsend discharge in gases at high field strength. These two effects can appear as either surface or volume effects. Although either effect may govern the reverse behavior of the junction as dictated by its parameters, the nature of the mechanism is immaterial for the purpose of this discussion, since the primary concern is the magnitude and spectral density of the breakdown-induced noise power relative to thermal noise emanating from the diode. The measured relative magnitude of this noise in a small frequency band in the vicinity of 8.5 kMc is reported here, in an effort to obtain an exploratory estimate in an area where published data are conspicuously nonexistent.

The measurement was performed in the following way. (Fig. 5 illustrates experimental arrangement.) A low-noise parametric amplifier tuned to approximately 8.5 kMc with a bandwidth of 50 Mc followed by a mixer and a 30-Mc IF amplifier, fed a linear power detector, which, in this case, consisted of an automatic noise figure meter operated in the "manual" position. The input to the parametric amplifier was connected alternately to a broad-band matched waveguide termination and to a waveguide diode holder containing a diode adjusted to a particular bias voltage, and matched to the line over a narrow band using a standard *E-H* tuner. The waveguide match was a broad-band termination from which *kt* watts per unit bandwidth noise power emanated [ $T$ =nominal room temperature (300°K)]. When connected to the amplifier input, it provided a power-output reference level, which is to be compared with the alternate input—the matched diode holder. The bias voltage was set to cause various amounts of current to flow through the diode. A voltage-current characteristic for a typical diode is shown in Fig. 6. At each bias voltage, the diode was matched to the line by using both the variable short in the holder and an external *E-H* tuner to achieve a VSWR of 1.02 over a bandwidth in excess of the IF bandwidth. The noise-power-output indication, when the diode holder was switched to the input of the receiver, was compared with the corresponding indication when the matched termination furnished the input. Because of the difference in "noise" bandwidth between the two inputs, it was necessary to establish a reference on the basis of which an equiv-

<sup>7</sup> K. B. McAfee, E. J. Ryder, W. Shockley, and M. Sparks, "Observations of Zener current in germanium *p-n* junctions," *Phys. Rev.*, vol. 83, p. 650; August, 1951.

<sup>8</sup> K. G. McKay, "Avalanche in silicon," *Phys. Rev.*, vol. 94, pp. 877-884; May, 1954.

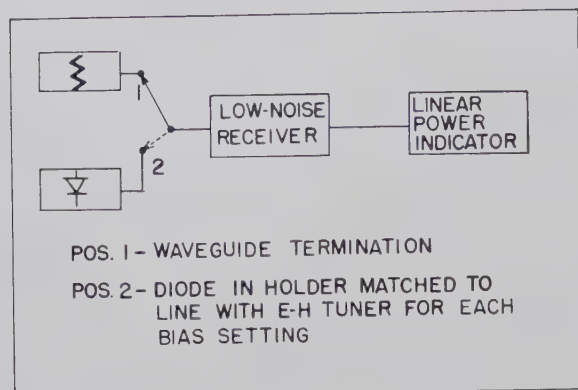


Fig. 5—Experimental arrangement for measuring diode excess noise.

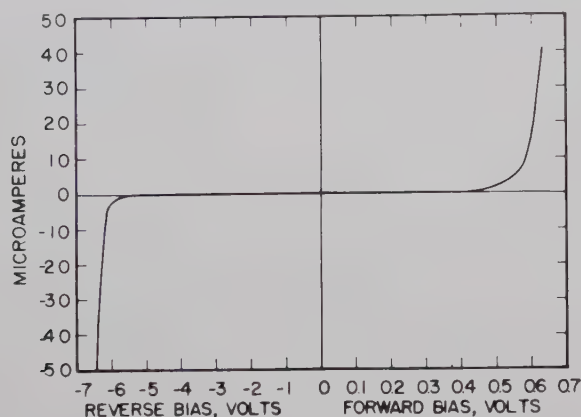
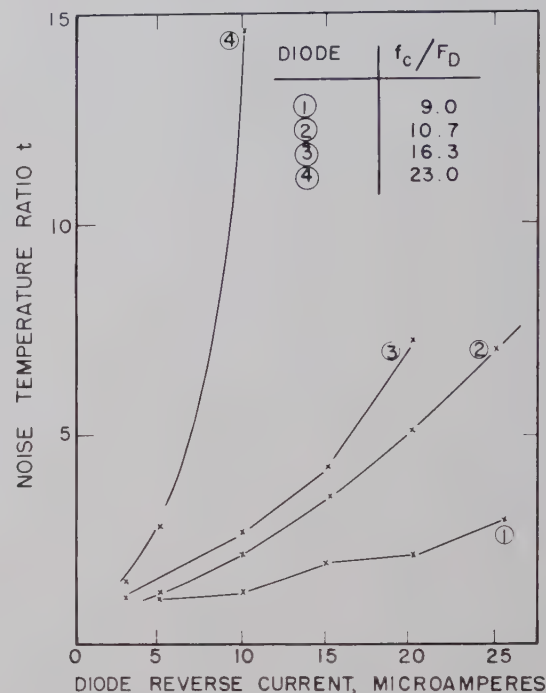


Fig. 6—Typical voltage-current curve of diode used in noise experiment.

alent "noise-temperature ratio" could be defined. The meaning of this term is as follows: Since, for purposes of evaluating noise performance a matched termination can be described in terms of a temperature<sup>9</sup> (which for a passive device corresponds to the ambient temperature), the noise temperature of a matched active device can be similarly defined. The active device, in this case the diode, then will radiate  $t$  times the noise power per unit bandwidth of the passive device. For the purpose of these measurements, the ratio of noise powers resulting from the two inputs when the diode bias voltage was set to zero (no current) was arbitrarily defined as a noise-temperature ratio of unity. Experimentally, this ratio remained constant, as was expected, as long as no current flowed through the diode. The noise-temperature ratio  $t$  can be related to the observed ratio of indicated noise powers  $N$  and the noise figure of the receiver  $F$  as follows:

$$t \simeq (N - 1)F + 1. \quad (13)$$

The measured noise figure for this experiment was 5.6 db. Variation of  $t$  with indicated diode reverse current for four silicon mesa diodes is shown in Fig. 7.

Fig. 7—Noise-temperature ratio  $t$  vs indicated diode current. Parameter is  $f_c/F_D$ ;  $f_c$  is cutoff frequency of particular diode, and  $F_D$  is noise figure of a parametric amplifier using this diode.

In addition to these measurements, an attempt was made to record the variation of the noise-temperature ratio with forward current. This attempt failed in that for currents up to 50 microamperes no change was observed in the indicated noise-power output. One may conclude from this that, compared with reverse current on a per unit current basis, the forward current gives rise to a negligible amount of noise, and for this regime a noise-temperature ratio of unity is a good approximation.

### B. Discussion

To form some basis for comparison of the "noisiness" of this reverse current, one could naively assume this current to produce shot noise flowing through the series resistance of the diode. In this case, the noise-temperature ratio<sup>10</sup> is given by

$$t \simeq 1 + 20IR, \quad (13a)$$

where  $I$  is the current in amperes, which flows through  $R$ , the series resistance in ohms. For currents up to the order of milliamperes, the second term in (13a) is negligible. Since the measured contribution of the forward current reported above was indeed negligible, one may conclude that this current produces shot noise.

On the other hand, the situation is vastly different when the current is produced by reverse breakdown.

<sup>9</sup> H. C. Torey and C. A. Whitmer, "Crystal Rectifiers," Rad. Lab. Series, McGraw-Hill Book Co., Inc., New York, N. Y., vol. 15, p. 30; 1948.

<sup>10</sup> In mixer-diode noise theory and practice, this term is often erroneously called noise temperature. Eq. (13a) is valid for a current source causing mean squared shot-noise current  $\bar{i}^2 = 2eIB$  to flow through a resistance  $R$  connected across it.



In this case, it is seen from a glance at Fig. 7 that an equivalent noise-series resistance several orders of magnitude in excess of the actual diode-series resistance must be postulated, in order to account for the large noise temperature resulting from the relatively small current. This probably means that a different mechanism, which gives rise to this excessive noise-power density, is at work. Nevertheless, it is not surprising to find the large noise contribution from the reverse current, since it has long been known that analogous high-field effects in gases and dielectrics have similar properties. A detailed study of the effects of temperature and a measurement of the spectral density over a broad band of frequencies coupled with analysis is necessary for further understanding of this noise-generating mechanism.

An additional observation deserves mention. It is noted from Fig. 7 that the diode with the highest cutoff frequency and the lowest noise figure appears to radiate appreciably more noise per unit current than any other. One can speculate, though perhaps prematurely, that this is as it should be. For a given magnitude of generated noise power in the junction, minimum absorption takes place in the losses of the diode with highest  $Q$  and, consequently, maximum radiation results.

#### C. Effect on Amplifier Performance

It has already been noted that the best amplifier performance that can be obtained with a given diode results when the diode capacitance excursion is maximized. The useful maximum excursion is limited to the region in which no appreciable reverse current flows through the diode. To the extent that the dc voltage-current characteristic of the diode is curved in the neighborhood of reverse-breakdown, the maximum permissible capacitance swing is restricted. This limitation alone is not as serious as it seems, since the capacitance variation near breakdown is quite small and the increase in capacitance swing, which would result from a sharp cutoff voltage-current curve, is not significant in most cases. It is found in some variable-capacitance diodes, however, that reverse current results on the application of the pump voltage, even if the dc bias is adjusted much closer to the forward conduction point than to the reverse-breakdown point. This phenomenon has been observed in our laboratory both at  $S$  band and at  $X$  band with silicon, as well as germanium, diodes. Recently, a plausible mechanism believed to be responsible for this curious behavior has been suggested.<sup>11</sup> It appears that the lifetime of minority carriers which are injected when the instantaneous voltage swings into the forward-conduction region, can be considerably longer than a period of the pump fre-

quency. The free electron injected into the junction by forward conduction thus remains free as the pump voltage reverses and, during the negative half cycle, precipitates avalanche multiplication through impact ionization. In this way, a net reverse current is produced with its accompanying high noise generation, even though the combined dc and ac voltage is insufficient to establish the critical avalanche field.<sup>12,13</sup> Consequently, in these diodes, the maximum capacitance swing is further restricted. In this case, the limitation is severe, since the relative capacitance swing using the forward voltage region could result in significant increase in the diode figure-of-merit  $K$ , particularly in semiconductors with large band-gap voltages.

#### D. Effect of Refrigeration

It has been amply demonstrated in the literature,<sup>14,15</sup> that the thermal noise power originating in the series resistance of a variable-capacitance diode can, in certain cases, be materially reduced by lowering the diode temperature. These experiments and others conducted in this laboratory proved successful, because the equivalent circuit parameters of the diode did not change materially as the temperature was reduced. Based on these experiments, it can be stated that when refrigeration is applied there will always be an accompanying reduction in noise temperature, provided that the impurity levels below the conduction band and above the valence band are sufficiently "shallow" (*i.e.*, when their "ionization energy" is small compared to  $kt$  electron volts at, say, room temperature).

In addition to the beneficial application of cooling described above, a further advantage results because the figure of merit improves at a lower temperature; this is partially caused by the increased maximum permissible capacitance swing. The temperature dependence of variable-capacitance diodes stems primarily from the diffusion potential, which influences the capacitance variation as well as the forward current variation with applied voltage.<sup>16</sup> This diffusion potential is an inverse function of the temperature for the metal-semiconductor junction as well as for the  $p$ - $n$  junction. Thus, the point of incipient forward conduction increases with decreasing temperature, and the capacitance at a given bias is reduced accordingly. These predictions are borne out by experiment as shown in Figs. 8 and 9, which show the current-voltage and capacitance-voltage characteristics of a gold-bonded ger-

<sup>12</sup> This effect should be absent in diodes that show high rectification efficiency at the particular frequency range involved. An example of this type is a recently developed GaAs point-contact diode.

<sup>13</sup> W. M. Sharpless, "High-frequency gallium arsenide point-contact rectifiers," *Bell Sys. Tech. J.*, vol. 38, pp. 259-269; January, 1959.

<sup>14</sup> M. Uenohara and W. M. Sharpless, "An extremely low-noise 6-kmc parametric amplifier using GaAs point-contact diodes," *PROC. IRE*, vol. 47, p. 2114; December, 1959.

<sup>15</sup> R. C. Knechtli and R. D. Weglein, "Low-noise parametric amplifier," *PROC. IRE*, vol. 47, p. 584; April, 1959.

<sup>16</sup> E. Spenke, "Electronic Semiconductors," McGraw-Hill Book Co., Inc., New York, N. Y., ch. 4; 1958.

<sup>11</sup> D. K. Breitner, *et al.*, "Fifth Quarterly Progress Report, Application of Semiconductor Diodes to Low-Noise Amplifiers, Harmonic Generators, and Fast-Acting TR Switches," Airborne Instruments Lab., Huntington, L. I., N. Y., Rept. No. 4589-1-5, sec. E, Contract 30(603)-1854; September, 1959.

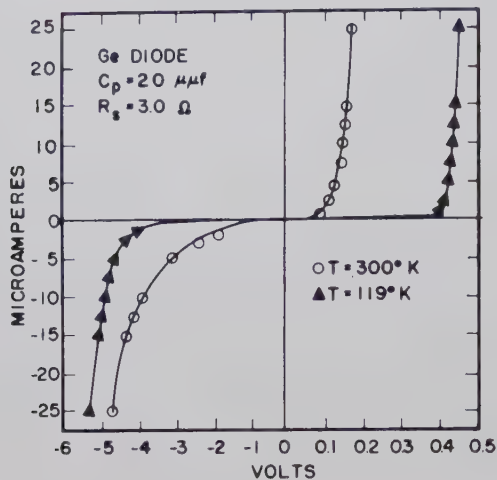


Fig. 8—Temperature dependence of voltage-current curve of germanium alloy junction.

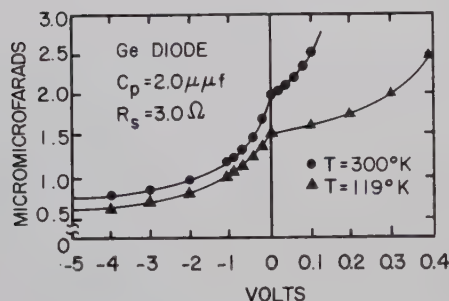


Fig. 9—Temperature dependence of voltage-capacitance curve of germanium alloy junction.

manium diode at two different temperatures. It is seen that the maximum voltage swing at the low temperature is significantly larger than that at room temperature. The resultant increase in capacitance swing, at least from these capacitance measurements (performed at 100 kc), would then be primarily due to the improvement in the reverse-biased region. There is some question as to whether these low-frequency capacitance measurements are valid at microwave frequencies. For example, refrigeration of such a diode in an S-band parametric amplifier experiment<sup>3</sup> did not result in any measurable detuning effects such as would be predicted

from the change in capacitance in Fig. 9. It is estimated from these considerations that in some cases more than a 20 per cent increase in the normalized capacitance swing can be realized. In view of expressions (5a) and (8), this increase would lead to an equivalent decrease in the noise temperature.

#### IV. CONCLUSION

The two limitations that are discussed in this report will be encountered, if an attempt is made to realize the optimum performance from a given diode. In most practical cases, approach to this optimum diode performance may not be preferred, because of difficulties that arise from increased interdependence of the relevant parameters, such as noise temperature and bandwidth. The previous material should, therefore, serve more as a guide in the design of a particular system, rather than be taken literally, since no attempt has been made to exhaust each subject. Finally, the reader should reflect, once again, on the assumed lumped low-frequency model,<sup>3</sup> which lends validity to the work. This should help to abate disappointment in the discovery that this information may only hold qualitatively at microwave frequencies, where the reader may wish to apply these results.

#### GLOSSARY OF SYMBOLS

$G_{ds}$  = diode shunt conductance at signal frequency.

$G_{gs}$  = effective source conductance at signal frequency.

$\mu_s = G_{gs}/G_{ds}$ .

$\omega_i = 2\pi f_i$ .

$s, i, p$  = subscripts designating signal, idler, pump frequency, respectively.

$\Omega = f_i/f_s$ .

$f_c$  = diode cutoff frequency at given bias.

$Q_d = f_c/f_s$ .

$\bar{C}$  = diode mean capacitance.

$\Delta C$  = maximum capacitance swing.

$T_d$  = diode temperature (°K).

$T_{n1}$  = radar noise temperature (°K).

$T_{n2}$  = radiometer noise temperature (°K).



# TE Mode Excitation on Dielectric Loaded Parallel Plane and Trough Waveguides\*

M. COHN†, MEMBER, IRE, E. S. CASSEDY‡, MEMBER, IRE, AND M. A. KOTT||, MEMBER, IRE

**Summary**—A theoretical and experimental study of the launching of TE surface wave modes on dielectric loaded parallel plane and trough waveguides has been performed. The source is a linear transverse current filament perpendicular to and extending across the space between the parallel side walls. Families of curves are presented, which show the bidirectional launching efficiencies for the dominant TE modes of these two transmission lines as a function of dielectric constant, dielectric slab thickness, and current filament location. Measured bidirectional efficiencies are compared to the theoretically predicted values. Measured unidirectional launching efficiencies as high as 97 per cent were obtained for the case where a short circuit is located on one side of the current filament.

## INTRODUCTION

THE FIELDS produced by a time varying current filament 1) embedded in an infinite dielectric slab of finite thickness, and 2) above and parallel to an infinite dielectric coated conducting plane have been analyzed respectively by Whitmer<sup>1</sup> and Tai.<sup>2</sup> The purpose of this extension of the works of Whitmer and Tai is to investigate the efficiency with which particular surface wave modes can be launched on these structures.

In the mathematical formulation of these problems,<sup>1,2</sup> physically unrealizable geometries and excitation conditions are assumed. The method of excitation is unrealizable since the current filament is assumed to be infinite in length and independent of the coordinate in the direction of current flow. If two parallel conducting planes, spaced a finite distance apart, are located on the above structures so as to be perpendicular to the current filaments, then the physically realizable dielectric loaded parallel plane<sup>3,4</sup> and through waveguides result.

\* Received by the PGM-TT, May 16, 1960; revised manuscript received July 6, 1960. Research supported by the U. S. Air Force, through WWRNGW of the Wright Air Dev. Div. of the Air Res. and Dev. Command.

† Electronic Communications, Inc., Timonium, Md.

‡ Microwave Res. Inst., Polytechnic Inst. of Brooklyn, Brooklyn, N. Y.

|| Radiation Lab., The Johns Hopkins University, Baltimore, Md.

<sup>1</sup> R. M. Whitmer, "Fields in nonmetallic waveguides," *PROC. IRE*, vol. 36, pp. 1105-1109; September, 1948.

<sup>2</sup> C. T. Tai, "The effect of a grounded slab on the radiation from a line source," *J. Appl. Phys.*, vol. 22, pp. 405-414; April, 1951.

<sup>3</sup> M. Cohn, "Propagation in a dielectric-loaded parallel plane waveguide," *IRE TRANS. ON MICROWAVE THEORY AND TECHNIQUES*, vol. MTT-7, pp. 202-208; April, 1959.

<sup>4</sup> M. Cohn, "TE modes of the dielectric loaded trough line," *IRE TRANS. ON MICROWAVE THEORY AND TECHNIQUES*, vol. MTT-8, pp. 449-454; July, 1960.

The fields which existed on the original unrealizable structures are undisturbed by the addition of the two parallel conducting planes, but the total power emanating from the unit current filament is now finite. The current filament can be energized from a coaxial line feeding through one of the side conducting walls, with only the center conductor crossing the lines and contacting the opposite wall. The variation of the current strength in the direction of its length can be made arbitrarily small by making the distance between the two parallel planes of the parallel plane (or trough) waveguide sufficiently small compared to the free space wavelength. It is thus possible to approximate closely the theoretically assumed conditions on practical transmission lines capable of supporting surface wave propagation. The existence of these surface wave structures provides the motivation for investigating efficient launching methods.

## TE<sub>20</sub> MODE EXCITATION AND DIELECTRIC LOADED TROUGH WAVEGUIDE

An analysis of the fields produced by a periodic time varying current filament above and parallel to a dielectric coated conducting plane has been performed by Tai.<sup>2</sup> Although Tai's analysis takes account of the existence of surface wave modes, his paper is primarily concerned with the effect on the radiation pattern caused by the introduction of the dielectric coating on the ground plane.

Tai has solved the inhomogeneous wave equation in the space shown in Fig. 1(a) to determine the electric field in region 2 ( $E_{y2}$ ) created by the filamentary unit current element located along the line  $x=d$ ,  $z=0$ . This method of excitation is unrealizable since the current is assumed to be independent of  $y$  and infinite in extent in the  $y$ -direction. The only field components that can exist, therefore, are  $E_y$ ,  $H_x$ , and  $H_z$ . These field components will also be independent of  $y$ . If conducting planes are placed at  $y=0$  and  $y=b$ , the above fields are undisturbed, and the physically realizable trough line configuration<sup>3,4</sup> of Fig. 1(b) results.

Tai has shown that the electric field in the region above the current filament ( $x>d$ ) is given by

$$E_{y2}(x, z) = \frac{j\omega\mu_0}{2\pi} \int_{-\infty}^{\infty} \frac{k_1 \sinh k_2(d-a) + k_2 \tanh k_1 a \cosh k_2(d-a)}{k_2(k_1 + k_2 \tanh k_1 a)} e^{k_2(a-x)} e^{j\beta z} d\beta, \quad (1)$$

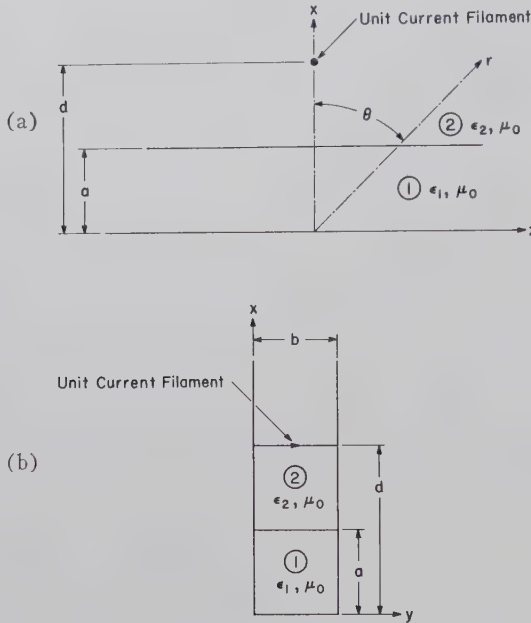


Fig. 1—(a) Dielectric coated conducting plane excited by an infinitely long unit current filament. (b) Dielectric loaded trough line excited by a unit current filament.

where  $k_1$  and  $k_2$  are the  $x$ -direction wave numbers of regions 1 and 2, which are related to the propagation constant ( $\beta$ ), angular frequency ( $\omega$ ), permeability ( $\mu_0$ ) and permittivity ( $\epsilon_1$  or  $\epsilon_2$ ) by the following equations:

$$k_1^2 = \beta^2 - \omega^2 \mu_0 \epsilon_1, \quad (2)$$

$$k_2^2 = \beta^2 - \omega^2 \mu_0 \epsilon_2. \quad (3)$$

The real integral (1) is evaluated by considering it to be a contour integral in the complex  $\beta$  plane and applying the Cauchy Residue Theorem. The integrand of (1) is multiple valued at  $k_1=0$  and  $k_2=0$ , but is an even function of  $k_1$ , and hence the only branch points occur at

$$\beta_b = \pm \omega \sqrt{\mu_0 \epsilon_2}, \quad (k_2 = 0).$$

The integrand of (1) has poles at  $\pm \beta_p$  determined by

$$k_{1p} + k_{2p} \tanh k_{1p} a = 0, \quad (4)$$

where  $k_{1p}$  and  $k_{2p}$  are the transverse wave numbers  $k_1$  where:

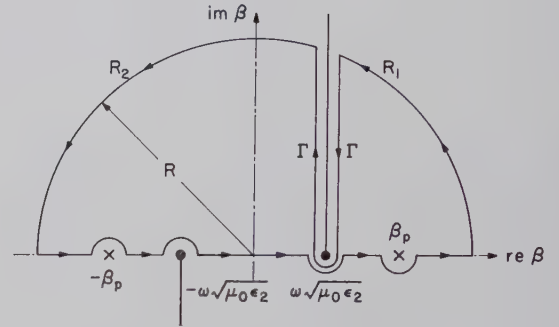


Fig. 2—Contour of integration in the  $\beta$  plane.

and  $k_2$  at the poles of (1). A path of integration in the complex  $\beta$ -plane which assures convergence of the integral is shown in Fig. 2. In the limit, as  $R \rightarrow \infty$ , the contributions to the integral from the circular arcs  $R_1$  and  $R_2$  approach zero. The integral (1) is therefore equal to the integral along the branch cut ( $\Gamma$ ) plus the residue due to the pole at  $\beta_p$ . Prior to evaluating the branch cut contribution, the path of integration is deformed from  $\Gamma$  to a new path of steepest descent, which passes through the saddle point of the integrand. The coordinates are transformed to the cylindrical coordinate system shown in Fig. 1, following the method of Tai<sup>2</sup> but using a different coordinate system. Upon performing the saddle point integration, which is valid for large  $r$ , the following formula is found for the branch cut contribution to the electric field.

$$E_y^R \cong j \sqrt{\frac{\omega \mu_0}{2\pi}} \left( \frac{\mu_0}{\epsilon_0} \right)^{1/4} F(\theta) \frac{e^{j\beta_b r}}{\sqrt{r}} \quad (5)$$

$$F(\theta) = \frac{\sqrt{K_1 - \sin^2 \theta} \sin \left[ \pi \left( \frac{2a}{\lambda_0} \right) \left( \frac{d}{a} - 1 \right) \cos \theta \right]}{\left\{ \sqrt{K_1 - \sin^2 \theta} - j \cos \theta \tan \left[ \pi \left( \frac{2a}{\lambda_0} \right) \sqrt{K_1 - \sin^2 \theta} \right] \right\} e^{j\pi (2a/\lambda_0) \cos^2 \theta}} + \frac{\cos \theta \tan \left[ \left( \frac{2a}{\lambda_0} \right) \sqrt{K_1 - \sin^2 \theta} \right] \cos \left[ \pi \left( \frac{2a}{\lambda_0} \right) \left( \frac{d}{a} - 1 \right) \cos \theta \right]}{\left\{ \sqrt{K_1 - \sin^2 \theta} - j \cos \theta \tan \left[ \pi \left( \frac{2a}{\lambda_0} \right) \sqrt{K_1 - \sin^2 \theta} \right] \right\} e^{j\pi (2a/\lambda_0) \cos^2 \theta}} \quad (6)$$

$$\epsilon_2 = \epsilon_0, \quad \epsilon_1 = K_1 \epsilon_0, \quad \beta_b = \omega \sqrt{\mu_0 \epsilon_0} = \frac{2\pi}{\lambda_0}.$$



Eq. (5) is recognized as the electric field of a radially propagating cylindrical wave. Eq. (6) is the field intensity radiation pattern of this wave. In the degenerate case, when  $a=0$ , the radiation pattern reduces to the well known solution for a current filament above a ground plane.

The evaluation of the pole residue contribution to the total field requires some interpretation. If the homogeneous wave equation for TE modes on the source free trough line is solved, one obtains (4) as the necessary condition to satisfy the boundary conditions at the dielectric-air interface. Furthermore, when one evaluates the contour integral (1), the residue contributions from the poles are in the following form:

$$F(d, a, \lambda_0) e^{k_{2p}(a-x)} e^{j\beta_p z}.$$

It has been previously shown<sup>3,4</sup> that the above solutions represent modal solutions, or surface waves propagating in the  $z$ -direction.  $\beta_p$  must be real for a dissipationless structure. In order to satisfy the radiation condition,  $k_{2p}$  must be real and positive, which requires that  $k_{1p}$  be pure imaginary and restricted to certain intervals. Let  $k_{1p} = jk_{1o}$  and  $k_{2p} = k_{2o}$ , where  $k_{1o}$  and  $k_{2o}$  are the symbols used for the transverse wave numbers describing the modal solutions. The subscripts "e" and "o" are used to denote respectively the modes having even and odd symmetry which can exist on the dielectric loaded parallel plane guide (only the odd modes can exist on the dielectric loaded trough line). By making use of (2), (3), and (4) and the fact that  $k_{1p} = jk_{1o}$ , the following result is obtained

$$\pi^2 \left( \frac{2a}{\lambda_0} \right)^2 (K_1 - 1) = \left[ \frac{k_{1o}a}{\sin k_{1o}a} \right]^2. \quad (7)$$

Solutions of (7) which yield the characteristics of the  $TE_{mo}$  modes on the trough line are available.<sup>3,4</sup> The even symmetry modes correspond to  $m$  being an odd integer and vice versa. In order for the  $TE_{mo}$  mode to propagate, the following inequality must be satisfied:

$$\frac{2a}{\lambda_0} > \frac{m-1}{2\sqrt{K_1-1}}. \quad (8)$$

In the remainder of this analysis, it is assumed that only the pole corresponding to the  $TE_{20}$  mode (dominant mode of the trough line) exists. Therefore, the analysis is valid only for the following interval:

$$\frac{1}{2\sqrt{K_1-1}} < \frac{2a}{\lambda_0} < \frac{3}{2\sqrt{K_1-1}}.$$

When the pole residue is evaluated, the following expression for the electric field of the  $TE_{20}$  mode in region 2 is obtained:

$$E_{y2}^s(x, z) = \omega\mu_0 \frac{(k_{1o}a) \sin^2 k_{1o}a}{(\beta_p a)(\tan k_{1o}a - k_{1o}a)} e^{-k_{2o}(d-2a+x)+j\beta_p z}, \quad (9)$$

where

$$\beta_p^2 = \omega^2\mu_0\epsilon_0 K_1 - k_{1o}^2 = \omega^2\mu_0\epsilon_0 + k_{2o}^2$$

and

$$\frac{\pi}{2} < k_{1o}a < \pi.$$

By the use of (9) and the required boundary conditions at the dielectric-air interface, it is a routine matter to determine the other field components of the  $TE_{20}$  mode in regions 1 and 2. The total surface wave power flowing in the positive  $z$ -direction ( $P_z$ ) can then be calculated, and when the power has been normalized with respect to the trough line width ( $b$ ) and free space wavelength ( $\lambda_0$ ), the following result is obtained:

$$\frac{P_z \lambda_0}{b} = 60\pi^2 \frac{(k_{1o}a)^2 \sin^2 k_{1o}a}{\sqrt{\pi^2 \left( \frac{2a}{\lambda_0} \right)^2 K_1 - (k_{1o}a)^2 (k_{1o}a - \tan k_{1o}a)}} e^{-2k_{2o}a(d/a-1)}. \quad (10)$$

The values of  $k_{1o}$  and  $k_{2o}$  to be used in (10) may be obtained from the previous results of Cohn.<sup>4</sup>

By the use of (5) and (6) the total radiated power can be calculated, and when normalized with respect to  $b$  and  $\lambda_0$ , it is given by the following expression:

$$\frac{P_R \lambda_0}{b} = 120\pi \int_0^{\pi/2} |F(\theta)|^2 d\theta, \quad (11)$$

where

$$|F(\theta)| = \frac{\sqrt{K_1 - \sin^2 \theta} \sin \left[ \pi \left( \frac{2a}{\lambda_0} \right) \left( \frac{d}{a} - 1 \right) \cos \theta \right]}{\sqrt{K_1 - \sin^2 \theta + \cos^2 \theta \tan^2 \left[ \pi \left( \frac{2a}{\lambda_0} \right) \sqrt{K_1 - \sin^2 \theta} \right]}} + \frac{\cos \theta \tan \left[ \pi \left( \frac{2a}{\lambda_0} \right) \sqrt{K_1 - \sin^2 \theta} \right] \cos \left[ \pi \left( \frac{2a}{\lambda_0} \right) \left( \frac{d}{a} - 1 \right) \cos \theta \right]}{\sqrt{K_1 - \sin^2 \theta + \cos^2 \theta \tan^2 \left[ \pi \left( \frac{2a}{\lambda_0} \right) \sqrt{K_1 - \sin^2 \theta} \right]}}. \quad (12)$$

$|F(\theta)|^2$  is the power radiation pattern produced by this configuration. Sample plots of  $|F(\theta)|^2$  vs  $\theta$  for various values of  $(d/a)$  and particular values of  $K_1$  and  $(2a/\lambda_0)$  are shown in Fig. 3. Since  $|F(\theta)|^2$  is an even function of  $\theta$ , it is only necessary to plot  $F(\theta)$  from  $0^\circ$  to  $90^\circ$ . Graphical techniques have been used on the many sets of curves like those in Fig. 3 to obtain the integral of  $|F(\theta)|^2$  and to determine  $P_R\lambda_0/b$  as a function of  $K_1$ ,  $(2a/\lambda_0)$ , and  $(d/a)$ . Use was made of (10) and the previously determined properties of the  $TE_{20}$  mode in order to calculate  $P_z\lambda_0/b$  as a function of  $K_1$ ,  $(2a/\lambda_0)$ , and  $(d/a)$ .

This method of launching the  $TE_{20}$  mode is inherently bidirectional, that is, equal amounts of surface wave power will be launched in the positive and negative  $z$ -directions. The bidirectional launching efficiency ( $\eta$ ) is defined as the ratio of the surface wave power in a desired direction to the total input power.

$$\eta = \frac{P_z}{2P_z + P_R} \quad (13)$$

It is thus apparent that even if the radiated power could be completely suppressed, the greatest efficiency possible, as defined above, is 50 per cent. A family of curves of the theoretical bidirectional launching efficiency as a function of normalized dielectric slab width  $(2a/\lambda_0)$

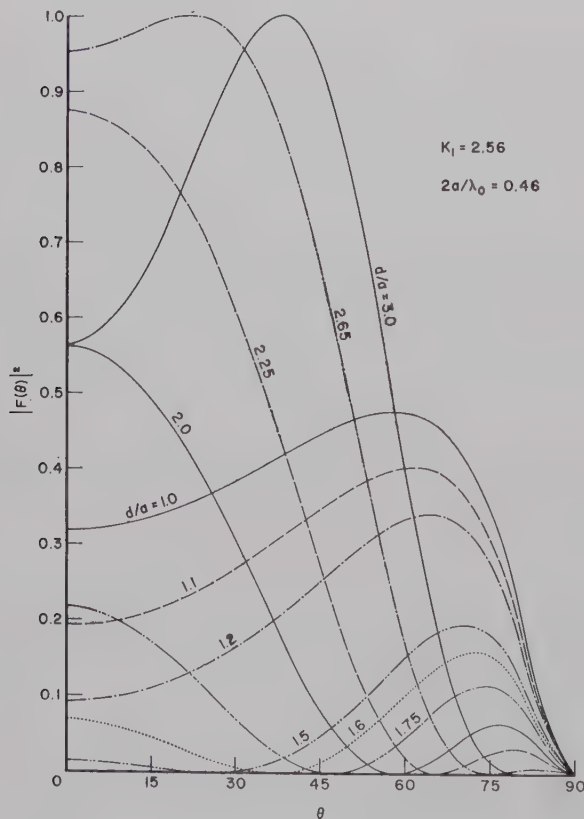


Fig. 3—Power radiation patterns produced by the unit current filament above the dielectric coated conducting plane for various filament locations.

and normalized current filament position  $(d/a)$  is shown in Fig. 4. These curves are for a dielectric constant of 2.56, which is being used in the experimental verification of this theoretical analysis. Similar sets of curves for other dielectric constants have been computed but will not be shown here.

#### TE<sub>10</sub> MODE EXCITATION ON A DIELECTRIC LOADED PARALLEL PLANE WAVEGUIDE

Whitmer<sup>1</sup> has solved the inhomogeneous wave equation for the case of the infinitesimally thin current filament embedded in the dielectric slab as shown in Fig. 5(a). The solution in this case has restrictions of exponential decay for increasing distance away from the slab in the outer region, but does not have the restriction of the ground plane present in the problem of Tai.<sup>2</sup> The solution found by Whitmer in the region

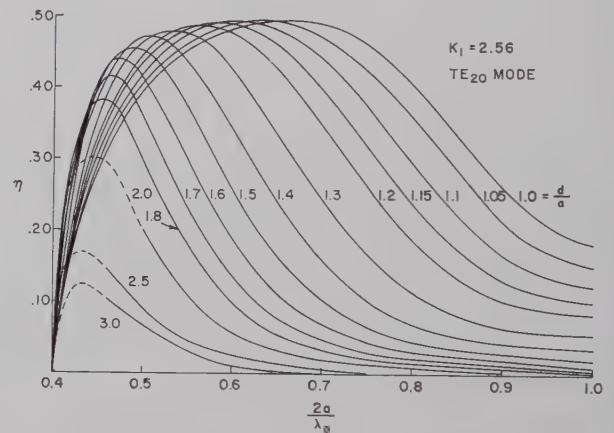


Fig. 4—Bidirectional launching efficiency as a function of dielectric slab width for various values of current filament location.

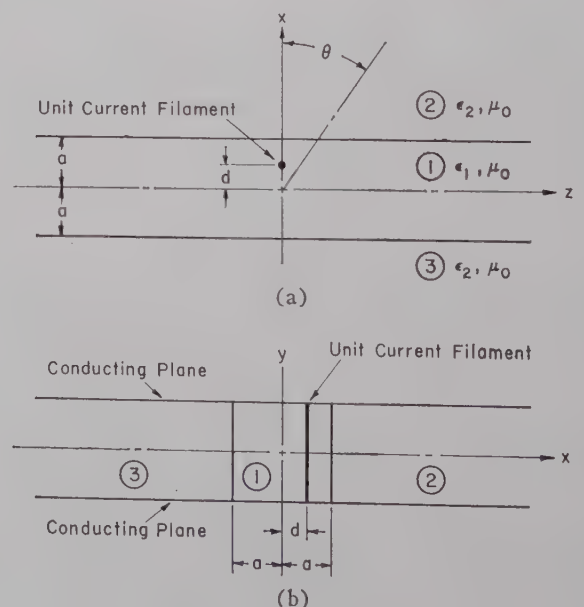


Fig. 5—(a) Infinite dielectric slab excited by an infinitely long unit current filament. (b) Dielectric loaded parallel plane waveguide excited by a unit current filament.



$x > a$ , may be written as follows:

$$E_{y2}(x, z) = \frac{j\omega\mu_0}{2\pi} \int_{-\infty}^{\infty} \frac{(k_1 + k_2)e^{k_1(a+d)} + (k_1 - k_2)e^{-k_1(a+d)}}{(k_1 + k_2)^2 e^{2k_1 a} - (k_1 - k_2)^2 e^{-2k_1 a}} \cdot e^{-k_2(x-a)} e^{j\beta z} d\beta, \quad (14)$$

where  $k_1$  and  $k_2$  are again the  $x$ -direction wave numbers of regions 1 and 2 and satisfy (2) and (3). Whitmer has discussed the contributions of poles and branch points in the integrand shown in (14). The same situation exists for this integral as did for the solution of Tai<sup>2</sup>, namely, that the poles contribute modal solutions, integration along the branch cut yields the radiation term, and the remainder of the path contributes a vanishing amount in the contour integration.

The integral, (14), has branch points at:

$$\beta_b = \pm \omega\sqrt{\mu_0\epsilon_2}, \quad (k_2 = 0) \quad (15)$$

and poles determined by:

$$(k_{1p} + k_{2p})e^{k_{1p}a} \pm (k_{1p} - k_{2p})e^{-k_{1p}a} = 0. \quad (16)$$

Following a path of integration similar to that shown in Fig. 2 we have found the following contribution for the radiated field after again deforming the path  $\Gamma$  to the path of steepest descents.

$$E_{yR} \cong j\sqrt{\frac{\omega\mu_0}{2\pi}} \left(\frac{\mu_0}{\epsilon_0}\right)^{1/4} f(\theta) \frac{e^{j\beta_b r}}{r^{1/2}}, \quad (17)$$

where:

$$f(\theta) = \frac{-j[(A-B)e^{jkaA(1+d/a)} + (A+B)e^{-jkaA(1+d/a)}]Be^{-jkaB}}{(A-B)^2 e^{j2kaA} - (A+B)^2 e^{-j2kaA}},$$

for

$$-\pi/2 \leq \theta \leq \pi/2$$

$$f(\theta) = \frac{j[(A+B)e^{jkaA(1-d/a)} + (A-B)e^{-jkaA(1-d/a)}]Be^{jkaB}}{(A+B)^2 e^{j2kaA} - (A-B)^2 e^{-j2kaA}},$$

for

$$\pi/2 \leq \theta \leq 3\pi/2$$

with

$$A = \sqrt{K_1 - \sin^2 \theta}$$

$$B = \cos \theta$$

$$\epsilon_1 = \epsilon_0 K_1, \quad k = 2\pi/\lambda_0.$$

Whitmer had only indicated this expression with unevaluated constants and for the special case of observation near the slab. Here, we have found asymptotic far field expressions for the radiation in any direction in the space external to the slab, for the purpose of determining the total radiated power.

The interpretation of the pole residue contribution is identical with that discussed in the previous section.

In order to satisfy the radiation condition,  $k_{2p}$  must again be real and positive and  $k_{1p}$  pure imaginary. We let  $k_{1p} = jk_{1e}$  and  $k_{2p} = k_{2e}$  in order to have pure real transverse wave numbers and to signify the modes of even ("e") symmetry. In the remainder of the analysis of this section, it will be assumed that only the residue of the pole corresponding to the TE<sub>10</sub>  $H$ -guide mode<sup>3</sup> exists. This condition may be assured by proper selection of the slab width according to (8). It has been shown<sup>3</sup> that the TE<sub>10</sub> mode is the dominant mode of the  $H$ -guide when the even symmetry modes are allowed to exist. The even modes may exist, of course, when the center vertical conducting plane (of the trough line) is not present. The TE<sub>10</sub> mode exists at all frequencies and exists as the sole mode of the  $H$ -guide at all frequencies less than the cutoff frequency of the TE<sub>20</sub> mode.

The condition for the pole becomes:

$$k_{2e} - k_{1e} \tan k_{1e}a = 0. \quad (18)$$

This is identical with that found for the TE<sub>10</sub> mode<sup>3</sup> and when combined with (2) and (3) yields the conditional equation found previously,<sup>3</sup> for this mode:

$$\pi^2 \left(\frac{2a}{\lambda_0}\right)^2 (K_1 - 1) = \left[\frac{k_{1e}a}{\cos k_{1e}a}\right]^2. \quad (19)$$

The solutions of this equation, found graphically,<sup>3</sup> yield the transverse wave number  $k_{1e}$  which exists for a given slab width ( $2a$ ) and dielectric constant ( $K_1$ ).

When the pole residue is evaluated, the following expression for the electric field of the TE<sub>10</sub> mode in region 2 is found:

$$E_{y2}^s(x, z) = \frac{-\omega\mu_0(k_{1e}a) \cos k_{1e}a \cos k_{1e}d}{2(\beta_p a)(k_{1e}a + \cot k_{1e}a)} e^{-k_{2e}(x-a)} e^{j\beta_p z}. \quad (20)$$

It is again a routine matter to determine the other surface wave field components in both the air and dielectric regions. The normalized total surface wave power may then be calculated:

$$\frac{P_z \lambda_0}{b} = \frac{30\pi^2(k_{1e}a) \cos^2 k_{1e}d}{(k_{1e}a + \cot k_{1e}a) \sqrt{\pi^2 \left(\frac{2a}{\lambda_0}\right)^2 - (k_{1e}a)^2}}. \quad (21)$$

The total radiated power in this case is given by:

$$\frac{P_R \lambda_0}{b} = 120\pi \int_0^\pi |f(\theta)|^2 d\theta. \quad (22)$$

$|f(\theta)|^2$  is the power radiation pattern of this configuration.

The bidirectional launching efficiency may be calculated by substituting (21) and (22) in (13). Fig. 6 shows the bidirectional launching efficiency computed for polystyrene ( $K_1 = 2.56$ ) as a function of  $2a/\lambda_0$  for various  $d/a \leq 1$ . Similar curves for other dielectric constants also show that maximum efficiency occurs for  $d = 0$ .

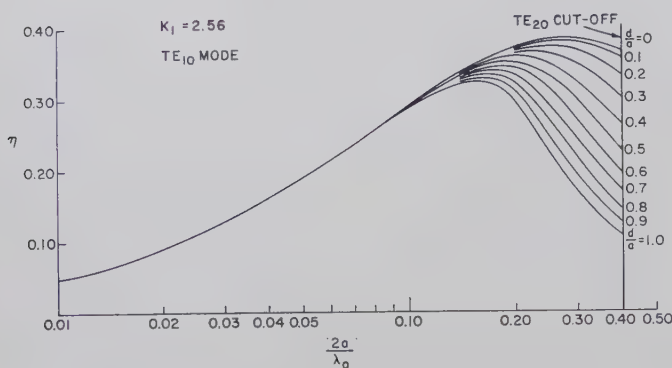


Fig. 6—Bidirectional launching efficiency as a function of dielectric slab width for various values of current filament location.

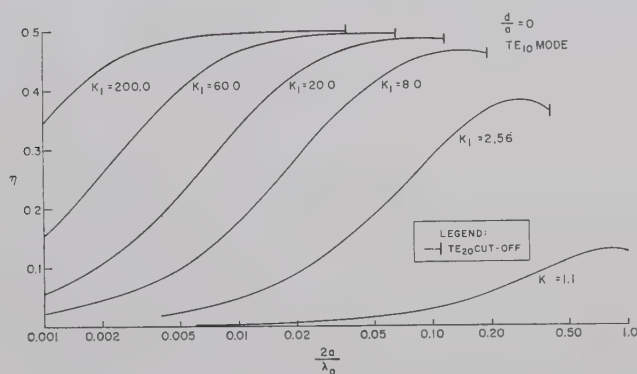


Fig. 7—Bidirectional launching efficiency as a function of dielectric slab width for various values of dielectric constant with center line excitation.

Fig. 7 shows the bidirectional launching efficiency for various dielectric constants vs  $2a/\lambda_0$  for  $d=0$ . Note that the higher dielectric constants have wide ranges of  $2a/\lambda_0$  where the efficiency is nearly 50 per cent. This may be verified by arguments of approximate analysis of rays emanating from the current filament. The rays become "trapped" into a mode-like behavior for angles of incidence on the interface greater than or equal to the angle of total internal reflection. Thus, the higher the dielectric constant, the smaller the angle of total reflection and, therefore, the more rays that will be "trapped" into the mode. It should also be noted that as the TE<sub>10</sub> cutoff ( $2a/\lambda_0=0$ ) is approached, the launching efficiency goes to zero.

#### LEAKY WAVE CONSIDERATIONS

In all the discussions above, concerning residue contributions from poles, it has been assumed that the longitudinal and transverse wave numbers had to be either pure real or pure imaginary. The residues from such poles have been defined as "surface waves." Barone<sup>5</sup> has shown that when the complex poles of the propagation constant  $\beta$  are considered, their residues yield "leaky waves." Although difficult to detect, these

leaky waves are physically realizable.

The discussion of these contributions is carried out in the transformed complex plane<sup>1,5</sup>  $\phi = \xi + i\eta$  (where  $\beta = k \sin \phi$ ), used previously as an aid to the steepest descent integration. In either (1) or (14), the surface wave poles lie along  $\xi = \pi/2$ ,  $\eta < 0$ , and the leaky wave poles lie in the region  $0 < \xi \leq \pi/2$ ,  $\eta > 0$ . Residues due to leaky wave poles must be included when the deformation of the path of integration into the steepest descent path causes the pole to be included within the contour integration. As such, the leaky waves merely constitute a portion of the field representation which one has when it is decided to use the saddle point evaluation as a representation of the field. The leaky waves excited by the line source attenuate exponentially along any radius from the origin, for angles within the region of definition.<sup>5</sup> It is therefore apparent that the leaky waves constitute part of the near field of the source in the particular field representation. Furthermore, orthogonality considerations<sup>6</sup> show that the leaky waves are a part of the continuous spectrum of the source, resulting from the evaluation of the field integral along the branch cut described previously. That is, orthogonality is found to exist between each of the surface waves, and between surface waves and the total continuous spectrum, but not between individual terms (saddle point terms and leaky wave terms) of the continuous spectrum.<sup>6</sup>

It then remains to determine if the near fields of the source, including both leaky waves and higher-order contributions of the saddle point evaluation, play any significant role in the experimental measurements described below. Barone<sup>5</sup> has calculated the lower-order waves for the case of our experiment, namely the current source above a grounded slab of polystyrene ( $K_1=2.56$ ). The leaky waves having the lowest rates of attenuation are those for the case of the thickest slab considered.<sup>5</sup> The greatest slab thickness considered in the present work is  $2a/\lambda_0=1$ , for which thickness, and less, only one leaky wave need be considered.<sup>7</sup> Barone has calculated the rate of attenuation of the leaky wave along the dielectric interface to be about one neper per free space wavelength for a slab thickness of  $2a/\lambda_0=1.08$ . The initial field strength of the leaky wave in this case has been calculated by the writers to be 19 times that of the surface wave. In seven wavelengths, therefore, the leaky wave will be approximately 35 db below the surface wave field strength at the slab interface. Further calculations of the leaky wave fields and the space wave components, as well as some sample experimental probing of the field within seven wavelengths of the current element in the case  $2a/\lambda_0=1.08$ , show that the surface wave is certainly dominant in the

<sup>5</sup> S. Barone, "Leaky Wave Contributions to the Field of a Line Source Above a Dielectric Slab," Microwave Res. Inst., Polytechnic Inst. of Brooklyn, N. Y., Rept. 532-56, PIB-462; November, 1956.

<sup>6</sup> L. B. Felsen and N. Marcuvitz, "Modal Analysis and Synthesis of Electromagnetic Fields," Microwave Res. Inst., Polytechnic Inst. of Brooklyn, N. Y., Rept. R726-59; June, 1959.

<sup>7</sup> Wave labeled  $N=3$  of Barone, *op. cit.*



vicinity of the slab for distances beyond seven wavelengths.

The absence of effects due to near field distortion should then be obvious in the experiments described below where all measurements of launching efficiency were made with at least seven wavelengths of unobstructed trough line and slab thickness  $2a/\lambda_0 \leq 1$ .

#### LAUNCHING EFFICIENCY MEASUREMENTS ON THE TROUGH LINE TE<sub>20</sub> MODE

Measurements of the bidirectional launching efficiency as a function of frequency and current filament location have been made on a trough line specified by the following parameters:  $K_1 = 2.56$ ;  $a = 3.33$  cm;  $b = 0.79$  cm. The method of measuring the launching efficiency is based upon the following scattering matrix analysis of the excitation structure. The trough line and current filament exciter can be considered equivalent to a four-port junction (Fig. 8); port 1 is the coaxial input, ports 2 and 3 are the two surface wave ports, and port 4 is an antenna to account for the radiation loss.

A triple stub coaxial tuner is included between port 1 and the trough line so that a matched input can always be achieved. Matched loads were placed in the trough line on both sides of the current filament and along the top of the trough line in order to provide reflectionless terminations for ports 2, 3, and 4. These loads consisted of tapered sections of white pine wood which were impregnated with a liquid containing suspended carbon. Since the junction is a reciprocal structure, and because of the symmetry between ports 2 and 3, the junction matrix is

$$\begin{bmatrix} b_1 \\ b_2 \\ b_3 \\ b_4 \end{bmatrix} = \begin{bmatrix} s_{11} & s_{12} & s_{12} & s_{14} \\ s_{12} & s_{22} & s_{23} & s_{24} \\ s_{12} & s_{23} & s_{22} & s_{24} \\ s_{14} & s_{24} & s_{24} & s_{44} \end{bmatrix} \begin{bmatrix} a_1 \\ a_2 \\ a_3 \\ a_4 \end{bmatrix}, \quad (23)$$

where the  $a$ 's,  $b$ 's and  $s$ 's are respectively the elements of the incoming, outgoing, and scattering matrices. The launching efficiency from port 1 to port 3 ( $\eta_{13}$ ) is defined as the ratio of the power delivered to a matched load at port 3 to the available power at port 1. With matched loads at ports 2, 3, and 4 ( $a_2 = a_3 = a_4 = 0$ ) and the input matched due to the tuner ( $s_{11} = 0$ ), it is apparent that

$$\eta_{13} = \frac{|b_3|^2}{|a_1|^2} = |s_{12}|^2. \quad (24)$$

If the matched load at port 3 is replaced by a movable short circuit, and if the triple stub tuner is not disturbed ( $s_{11}$  is still zero), a standing wave will exist on the coaxial line which feeds port 1. The magnitude of the voltage standing wave ratio will be a function of the position of the short circuit. Positions of the short can be found which will produce a maximum standing wave,

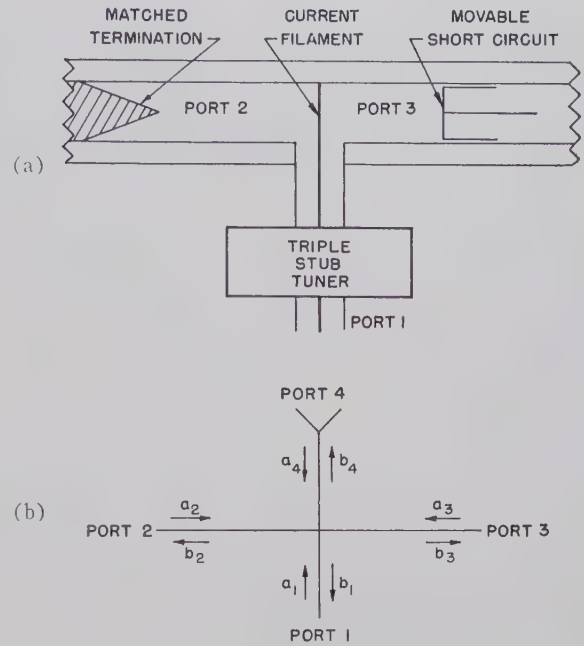


Fig. 8—(a) Top view of trough and current filament exciter. (b) Equivalent four-port junction for current filament exciter.

(VSWR)<sub>max</sub>, or a minimum standing wave, (VSWR)<sub>min</sub>. From (23) it can be shown that

$$\eta_{13} = |s_{12}|^2 = \frac{[(VSWR)_{\max} - 1][(VSWR)_{\min} - 1]}{(VSWR)_{\max} \cdot (VSWR)_{\min} - 1}. \quad (25)$$

The accuracy with which the launching efficiency can be measured depends upon how close the reflection coefficient ( $\rho$ ) of the short is to unity. It can be shown that

$$(\eta_{13})_{\text{measured}} = |\rho| (\eta_{13})_{\text{true}}. \quad (26)$$

Thus, any imperfection of the movable short circuit results in a pessimistic determination of the launching efficiency.

The above method of determining surface wave launching efficiency can be shown to be equivalent to the method of Deschamps<sup>8</sup> for determining the insertion loss of a waveguide junction. Deschamps' method has been used previously<sup>9</sup> to measure launching efficiency.

Launching efficiency was first measured with a short circuit which extended across the air region of the trough line and reached the air-dielectric interface. The resulting measured values of launching efficiency were all much lower than the theoretically predicted values. The short circuit and dielectric slab were modified so that the short extended through the dielectric slab to

<sup>8</sup> G. A. Deschamps, "Determination of reflection coefficients and insertion loss of a waveguide junction," *J. Appl. Phys.*, vol. 24, pp. 1046-1050; August, 1953.

<sup>9</sup> R. H. DuHamel, and J. W. Duncan, "Launching efficiency of wires and slots for a dielectric rod waveguide," *IRE TRANS. ON MICROWAVE THEORY AND TECHNIQUES*, vol. MTT-6, pp. 277-284; July, 1958.

nearly the bottom conducting wall of the trough line. Subsequent measurements of bidirectional launching efficiency were made by moving the short circuit and the dielectric slab as an integral unit. These measurements were made over a band of frequencies from 1.8 to 3.6 kmc and for a number of values of normalized current filament location ( $d/a$ ). Fig. 9 shows a comparison of the measured loss and predicted launching loss for the case where  $d/a = 1.11$ . The small discrepancy between the measured loss and calculated launching loss is probably due in part to the fact that a perfect short circuit has not yet been achieved.

Measurements were also taken to determine if unidirectional launching efficiencies approaching double those just reported for the bidirectional case could be achieved by properly locating a trough line short circuit on one side of the current filament. These measurements were made by comparing the surface wave power delivered to a matched detector at port 3 with and without a short circuit located at port 2. The power sampled by this detector was measured as a function of frequency. At the center frequency (2.7 kmc), the short was placed at port 2 and adjusted to maximize the power delivered to the detector. The triple stub tuner at the input port was readjusted to provide an input match for this new configuration. After this initial adjustment, the positions of the short and the tuning stubs were held fixed. The increased power delivered to the detector due to the addition of the short and readjustment of the stub tuner was recorded. Thereafter, the frequency was varied across the band and the increase in detected power over that obtained for the bidirectional launching case was measured. The results for this unidirectional launching case are also shown in Fig. 9. This curve shows that the power loss due to this method of launching the  $TE_{20}$  mode is extremely low over a broad band of frequencies and that the peak efficiency achieved was 97 per cent.

#### CONCLUSIONS

The bidirectional launching efficiencies of TE surface waves on dielectric loaded trough and parallel plane waveguides excited by a current filament have

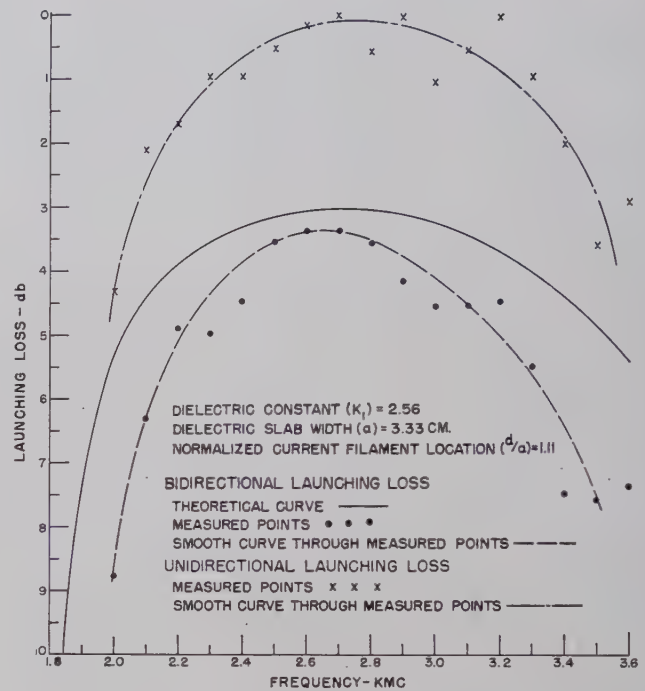


Fig. 9—Curves of unidirectional and bidirectional launching loss for the trough line excited by a current filament.

been derived. Results are shown which indicate the parameters for optimum efficiency. Experimental verification has been carried out in one case.

We conclude not only that there is a method of computing the bidirectional excitation efficiency but also that a unidirectional launching efficiency of 97 per cent can be achieved for this configuration of feed. Finally, these launching techniques are particularly applicable to high dielectric constant lines, where launching is normally difficult.

#### ACKNOWLEDGMENT

The authors should like to thank Prof. A. A. Oliner and Dr. A. Hessel of the Polytechnic Institute of Brooklyn for reference to the work on leaky waves; Dr. J. M. Kopper for his review of the manuscript; I. E. Pakulis, who performed the measurements; and Miss M. D. Velten for the numerical calculations and curve plotting.



# A New Semiconductor Microwave Modulator\*

H. JACOBS†, MEMBER, IRE, F. A. BRAND†, MEMBER, IRE, M. BENANTI†, MEMBER, IRE,  
R. BENJAMIN‡ AND J. MEINDL†, MEMBER, IRE

**Summary**—A new semiconductor device is proposed for use as an amplitude modulator for microwave transmission. The principle of action depends upon the increase of absorption with an increase of conductivity caused by the injection of excess minority carriers. Experiments conducted at 9600 Mc indicate little or no phase and frequency modulation. The mechanism of the modulation action and the device design are discussed here.

## INTRODUCTION

THERE has been an increased interest recently in the possibility of designing semiconductor devices for microwave applications. In some of the proposed schemes, a block of germanium is inserted in a waveguide, and, by modulating the conductivity of the semiconductor crystal, a change in microwave energy transmitted through the system is attained. In one suggestion,<sup>1</sup> a semiconductor slab is inserted through slits in a waveguide and oriented in a direction parallel to the electric vector in the TE<sub>0,1</sub> mode. By application of high pulse fields across the semiconductor, a decrease in mobility of the majority carriers occurs with a concurrent decrease in conductivity. This results in more power being transmitted through the waveguide. Here we have a possible microwave modulator device. In still another case, the modulation by light of the conductivity of a semiconductor inserted in a waveguide, together with the measurement of changes in microwave power absorption as a function of time, has resulted in a new method of measuring the lifetime of semiconductors with an electrodeless technique.<sup>2</sup> That one could expect absorption of electromagnetic radiation by increasing the conductivity of the semiconductor, can be seen by examining the classical equations derived from Maxwell's field theory.

For a plane wave traveling in unbounded dielectric,

$$\gamma = \sqrt{j\omega\mu(\sigma + j\omega\epsilon)} = \alpha + j\beta, \quad (1)$$

where  $\epsilon = 1.41664 \times 10^{-10}$ ,  $\mu = 1.257 \times 10^{-6}$ ,  $\omega = 2\pi 10^{10}$ ,  $\sigma$  is the conductivity,  $\alpha$  the attenuation constant, and  $\beta$  the phase constant. For low loss dielectric,

$$\sigma < \omega\epsilon$$

and (1) reduces to

$$\gamma = \frac{\pi}{\lambda} \left[ \frac{\sigma}{\omega\epsilon} \right] + j\omega\sqrt{\mu\epsilon} = \alpha + j\beta. \quad (2)$$

Hence, the attenuation constant is

$$\sigma = \frac{\pi}{\lambda} \left[ \frac{\sigma}{\omega\epsilon} \right] = \eta\sigma/2, \quad (3)$$

where  $\eta$  is the intrinsic impedance of the medium. The attenuation factor increases linearly with conductivity in the region where  $\sigma \ll \omega\epsilon$ . In Figs. 1 and 2, we see the results of calculating  $\alpha$  and  $\beta$  for germanium as a function of conductivity and frequency. These preliminary experiments and calculations form the basis of a new class of devices in which electromagnetic energy can be modulated. In particular, it now appears feasible to design an amplitude modulator with little or no frequency modulation or phase modulation. Such a device would be applicable to microwave communication systems, where it is desirable to maintain very narrow band transmission in order to communicate the maximum intelligence over a given portion of the electromagnetic spectrum.

To demonstrate modulation effects, experimental equipment was constructed in the following manner. In Fig. 3, we see the arrangement for mounting the semiconductor rod in the waveguide and the manner in which a probe, perpendicular to the electric field in the waveguide, can be used to inject additional minority carriers in the semiconductor. The microwave power at a frequency of 9600 Mc was transmitted through the waveguide and sample to the tuned diode. A semiconductor rod of germanium with dimensions of approximately  $0.3 \times 0.3 \times 3.5$  ohms was inserted through the waveguide. A small hole was cut in the side of the waveguide, through which a tungsten probe could be inserted. With this arrangement, considerable flexibility of the sample position was allowed. In addition, the sample could be tested as a point contact diode, or if a junction were made on the side of the sample, the tungsten could be located on the alloyed dot and injection characteristics could be measured. In Fig. 4, we find the over-all microwave system schematic diagram. In this arrangement, the klystron operated without modulation and supplied electromagnetic radiation which was transmitted through the germanium rod. Under these conditions, the oscilloscope displayed no variations in amplitude because of the input on the A channel. Next, if the pulse generator were turned on to

\* Received by the PGMTT, May 19, 1960.

† U. S. Army Signal Res. and Dev. Lab., Fort Monmouth, N. J.

‡ Monmouth College, West Long Branch, N. J.

<sup>1</sup> A. F. Gibson, "Progress in Semiconductors," John Wiley and Sons, Inc., New York, N. Y., vol. 2, p. 229; 1957.

<sup>2</sup> A. P. Ramsa, H. Jacobs, and F. A. Brand, "Techniques in measurement of lifetime in germanium," 1959 IRE NATIONAL CONVENTION RECORD, pt. 3, pp. 159-169. Also, *J. Appl. Phys.*, vol. 30, pp. 1054-1060; 1959.

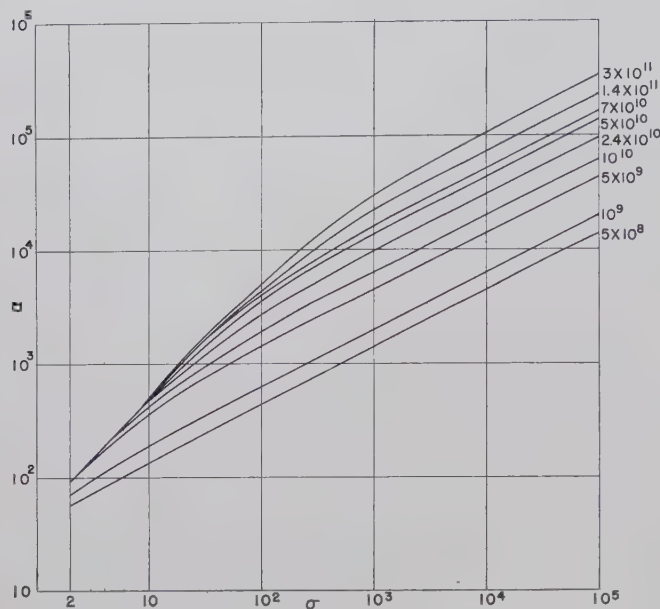


Fig. 1—Attenuation factor (nepers/meter) as a function of conductivity (mhos/meter) and frequency (cycles/second).

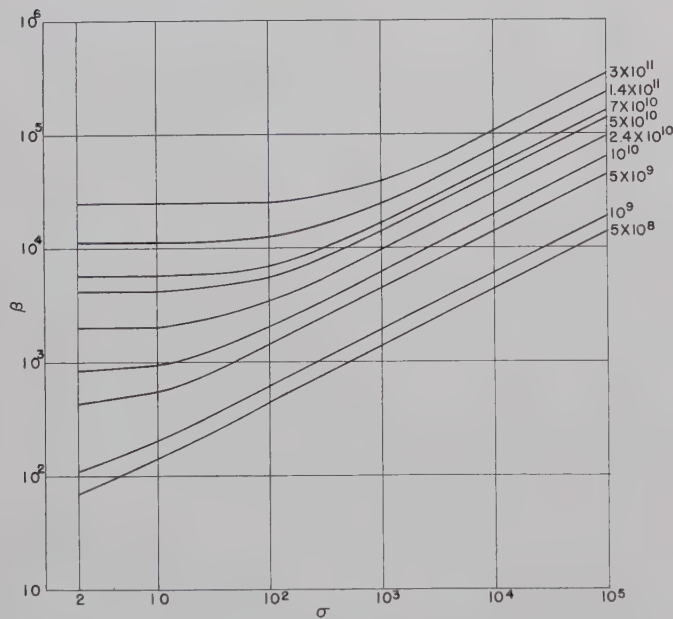


Fig. 2—Phase constant (radians/meter) as a function of conductivity (mhos/meter) and frequency (cycles/second).

give one to ten microsecond pulses to the probe in the forward direction, variations in the output of the detector diode could be readily observed. The voltage or current supplied to the probe could be monitored by the B channel. In this arrangement, an increase in the semiconductor conductivity could be displayed as a decrease in power on the A channel of the oscilloscope. At the cessation of the pulse, an exponential form of recovery was noted as the current from the detector diode increased back to equilibrium. It has been shown that this exponential characteristic is related to the "lifetime" of additional minority carriers.

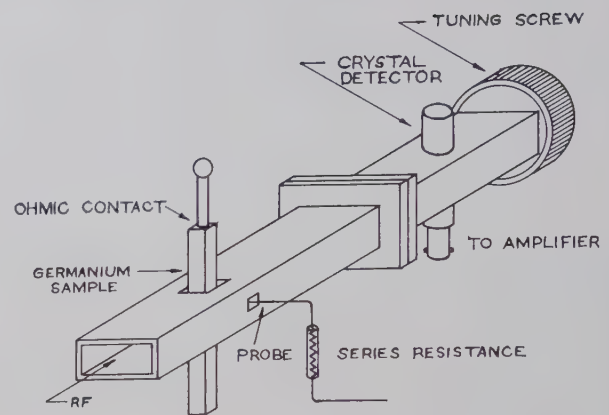


Fig. 3—Arrangement for location of sample in microwave power attenuation measurements.

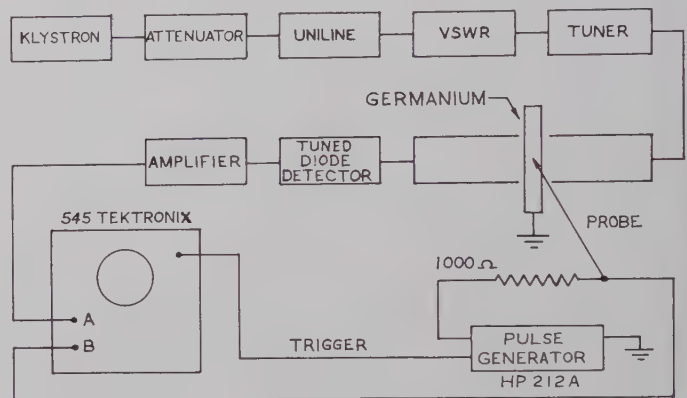


Fig. 4—Circuit diagram for microwave modulation.

During the remainder of this paper, we shall refer to the tuned diode feeding into the amplifier as the detector diode. It is also true that the probe making contact to the germanium rod which was under study makes another diode. This we shall refer to as the sample diode. In Fig. 5, we see a typical display of the oscilloscope presentation. Let us consider the sample diode now in more detail. In what follows, an alloyed dot was often made on the side of the semiconductor. The arrangement here is shown in Fig. 6. It is to be noted that the other contact of the sample, the ohmic contact, was not enclosed in the waveguide and, in fact, was more than two centimeters from the waveguide wall. This large distance was used to help prevent possible injection of minority carriers into the microwave field from the ohmic contact. In this manner only, one junction (the sample diode) could be studied without possible interference from the behavior of the ohmic contact.

Still another circuit arrangement was utilized. This we shall refer to as the *low-frequency amplitude modulation test*. Here, instead of using pulse voltages on the sample diode, 60-cycle ac voltage was applied to the probe. The circuit is shown in Fig. 7. In this arrangement, when 60-cycle ac voltage was applied to the probe the sample diode often rectified the current. The



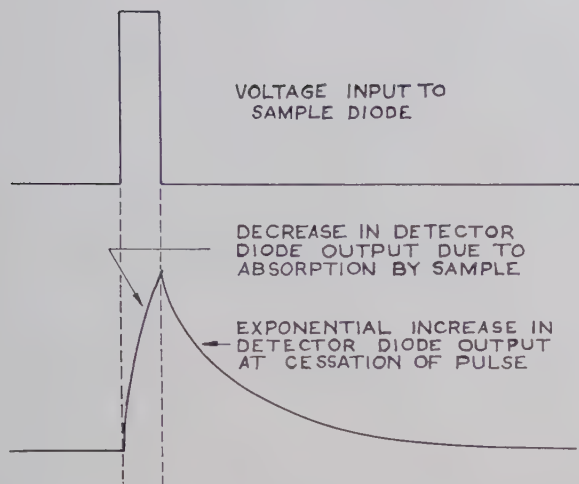


Fig. 5—Response of detector diode output to changes in power absorption. The polarity is such that an increase in oscilloscope voltage indicates an increase in absorption.

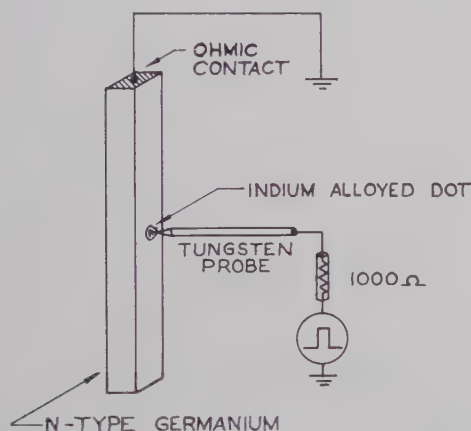


Fig. 6—Arrangement for study of alloy type of injection mechanisms.

output of the detector diode also showed a rectified sine wave characteristic.

In summary, the device to be considered is a germanium rod, the conductivity of which can be modulated by injected current carriers. An increase in conductivity will, in turn, cause a decrease of microwave power transmitted through the guide. In what follows, we shall describe the semiconductor preparation, some interesting physical effects observed during the testing, electrical characteristics and the design of the device.

#### SEMICONDUCTOR PREPARATION

Rods were cut to the approximate desired dimensions, then polished with 600 mesh carborundum and etched in CP-4 solution to a bright finish. The ends of the rod were then abraded to reduce the possibility of injected minority carriers and plated with nickel. Soldered contacts were made to both ends and the resistivity of the material was determined. The type was then checked using two methods: the hot point probe, and the rectification point contact characteristics. Some samples were deliberately doped with copper impurity, by diffusion or by introducing copper in the melt.

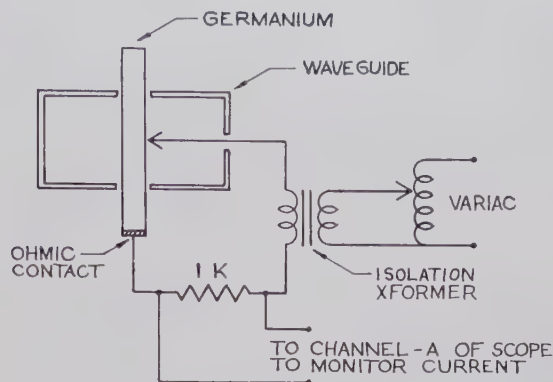


Fig. 7—Low-frequency modulation of germanium conductivity.

In relation to alloyed contacts for the sample diode, indium dots were fired on an N-type germanium crystal in an argon atmosphere, and for P-type material, alloyed dots were made with gold antimony. In general, the dots were about 1 mm in diameter. The samples were etched in CP-4 for 20–30 seconds, distilled-water washed, and then dried in air. Immediately after the etching, washing and drying steps, the samples were tested for diode characteristics. When the sample was placed in the waveguide, still another materials control was introduced. By injecting current into the sample with a 1–10 second pulse in the forward direction, one could observe the excess minority current carrier decay and from this deduce the lifetime. It has been shown in previous work<sup>3</sup> that the lifetime obtained in this manner is approximately the same as that obtained by more conventional photoconductive decay methods<sup>4</sup> or the microwave electrodeless techniques.

In Table I, there is a summary of samples tested in these experiments. It should be noted that some of the samples tested indicate a single lifetime. Others indicate more than one—a short lifetime and then a break in the recombination curve, followed by a longer lifetime. This longer lifetime was interpreted as being caused by deep traps of an unknown origin. This could be further checked by flooding the samples with light. Here the longer lifetime values changed considerably with variations in ambient light.

The deep trap samples could not be used for conventional design calculations of  $L_p$ , the diffusion length,  $D_p$ , the diffusion constant or  $\tau_p$ , the bulk lifetime. However, the sensitivity of these samples to light and particularly infrared light, when tested in the waveguide holder, indicates that they may find considerable use in device applications.

<sup>3</sup> A. P. Ramsa, H. Jacobs, and F. A. Brand, "Techniques in measurement of lifetime in germanium," 1959 IRE NATIONAL CONVENTION RECORD, pt. 3, pp. 159–169. Also, *J. Appl. Phys.*, vol. 30, pp. 1054–1060; 1959.

<sup>4</sup> D. T. Stevenson and R. J. Keyes, "Measurement of carrier lifetimes in Germanium and Silicon," *J. Appl. Phys.*, vol. 26, p. 190; February, 1955.

G. Bernski, "Lifetime of electrons in p-type Silicon," *Phys. Rev.*, vol. 100, p. 523; October, 1955.

J. S. Blackmore, "Lifetime in p-type Silicon," *Phys. Rev.*, vol. 110, p. 1301; January, 1958.

TABLE I  
PHYSICAL PROPERTIES OF SAMPLES

Number	Size in cm	Type	Resistivity ohm-cm	Lifetime in Microseconds	Comments
A	$0.41 \times 0.51 \times 3.7$	N	10.13	120–130	Single lifetime.
2	$0.297 \times 0.507 \times 3.42$	N	3.26	10	Single lifetime.
3	$0.357 \times 0.471 \times 4.0$	N	19.7	Two lifetimes noted. Longer lifetime 484 in room light.	Indication of deep traps.
4	$0.302 \times 0.325 \times 3.45$	N	33.6	Two lifetimes. Longer lifetime, roughly 1000 in room light.	Indication of deep traps.
5 90AE	$0.338 \times 0.386 \times 3.60$	N	35.2	1540	Single lifetime.
6	$0.216 \times 0.528 \times 3.75$	N	9.75	80	Single lifetime.
7	$0.338 \times 0.386 \times 3.60$	N	35.2	1540	Single lifetime.
Same rod as sample No. 5					
C	$0.330 \times 0.412 \times 3.62$	P	1.43	0.2 to 1.5	Single lifetime.
Same as A but copper doped at 700°C in argon.					

### PHYSICAL EFFECTS IN SEMICONDUCTORS

At this point, it would be best to describe the observation of physical effects. We do this for two reasons. First, in the experiments to be described, we have a novel method of observing semiconductor phenomena related to variations in carrier concentration, such as injection, extraction, lifetime, trapping levels, etc. Second, in order to understand the mechanism of the modulator device and to foresee new arrangements and modifications, we must understand the physical effects. The physical phenomena of interest can be listed as follows: 1) Correlation of lifetime and modulation, 2) notes on injection, 3) observation of extraction, 4) further lifetime effects. Let us consider first the correlation in lifetime and modulation efficiency. Referring again to Fig. 4, we see that the tests were run as a modification of this arrangement. First, the lifetime was measured by a dual trace technique, whereby the pulse generator voltage was fed into an RC network and from here to the B channel on the oscilloscope. This allowed a comparison of the RC time constant with the lifetime characteristic obtained from the sample. Second, low-frequency amplitude modulation was measured by using the arrangement shown in Fig. 7 on the sample. The dc power level,  $P$ , reaching the detector diode was measured and then the peak decrease in power,  $\Delta P$ , was determined for a given injection current (15 ma) into the sample. Power levels were measured using the output current of the detector diode through a 1000-ohm load resistor. This output of the detector diode was calibrated with a bolometer.

Now, consider the effects of injection in the forward direction. Assuming a low drift field, the minority carrier concentration will be given by

$$p_0 - p_n = p_n(e^{qv_{e0}/kT} - 1)e^{(X_n - X)/L_p}, \quad (4)$$

where

$$L_p = (D_p \tau_p)^{1/2} \quad (5)$$

and  $p_0 = p_n$  is the excess minority carrier concentration,  $p_n$  the equilibrium minority carrier concentration,  $v_{e0}$

TABLE II  
COMPARISON OF LIFETIME AND POWER MODULATION

Sample	$\Delta P$ (Relative Units)	$P$ (Relative Units)	$\tau$ Microseconds
A	0.12	1.55	120–130
2	0.02	0.85	10
3	0.25	1.6	Double lifetime. Longer lifetime 400.
4	1.15	2.9	Double lifetime. Longer lifetime >1000.
5	1.25	2.9	1540
6	0.23	2.3	80
C	0.01	0.85	0.2 to 1.5

the applied voltage,  $X_n$  the boundary of the junction and  $X$  the distance inward. Thus, the longer the diffusion length, or  $\tau_p$ , the greater the penetration of increased carrier concentration in the semiconductor rod. We should expect that, for long-lifetime samples, a longer time would be required for equilibrium to be established upon the advent of a forward bias voltage, and for a decrease in conductivity upon the cessation of the forward bias condition. In the low-frequency amplitude modulation test, the frequency was found to be low enough for equilibrium to be reached and the results were almost identical with dc effects of injection current upon transmitted power. In Table II, we find the data taken for the various samples studied. All numbers here refer to a point contact sample diode with 60-cycle voltage applied and providing 15 ma peak current through the sample.

By (4) and (5) we might expect an empirical relationship between  $\tau_p$  and  $\Delta P/P$ . A theoretical analysis is difficult because there are many other factors to consider. For instance, we must assume that the point contact at the sample has reasonable uniformity of efficiency of injection for all samples. In addition, the samples should be fairly uniform in geometry. Moreover, theoretical considerations<sup>2</sup> indicate that the lifetime measurement technique is more applicable to high-resistivity long-lifetime samples. The longer lifetimes



resulting from the deep traps precluded the use of these particular samples in assembling the data in Fig. 8. We further assume that the quantity  $\Delta P/P$  is constant for a given sample. Nevertheless, making these assumptions and choosing single lifetime samples A, 2, 5, 6, and C, we plotted the log  $\Delta P/P$  vs log  $\tau$ . The results indicate that a correlation exists in  $\Delta P/P$  with  $\tau$ . It may be suggested that this would provide a new technique in determining, by extrapolation, the lifetime for short-lifetime materials where measurements have been found difficult. In relating this to the design of the amplitude modulator, we should expect greater modulation efficiency with longer-lifetime semiconductors, provided the geometry is relatively constant. The situation for high drift fields will be discussed in a later section.

This technique of microwave absorption offers a novel method of inspecting injection phenomena which may be used to supplement more standard types of diode testing. For instance, double injection, with carriers being injected by a probe with either positive or negative polarities, can readily be observed by utilization of the microwave system. In the case of sample C (copper doped by diffusion at 700°C firing temperature), the sample was tested as a point contact diode with the standard circuit consisting of measuring current through a resistor. In this diode test, no rectification in the sample diode was demonstrated. One might conclude that the point contact formed an ohmic contact or that some other combination of circumstances prevented rectification. However, when the semiconductor block was inserted in the waveguide, one could observe the injection of carriers of both types and even get estimates of comparative injection efficiencies.

Referring to Fig. 9, we obtain the following data and interpretation. The upper line shows the oscilloscope trace representing current through the sample diode. No rectification was apparent and the peak current was set at 15 ma. In the second line, we see the result of double injection on the power absorption. The cusp points refer to the condition of no voltage and no injection, the downward path indicates absorption of microwave power due to injection. The larger absorption is due to injection of electrons, the smaller due to holes.<sup>5</sup> In this manner, comparative injection efficiencies can be demonstrated.

Another item of interest is that the microwave system allows a visual observation of extraction. This sometimes appears in the sample diode being reversed biased, with an increase in power transmitted.

Next, the effects of alloying on the lifetime of the sample were sought. A new indium alloyed dot was

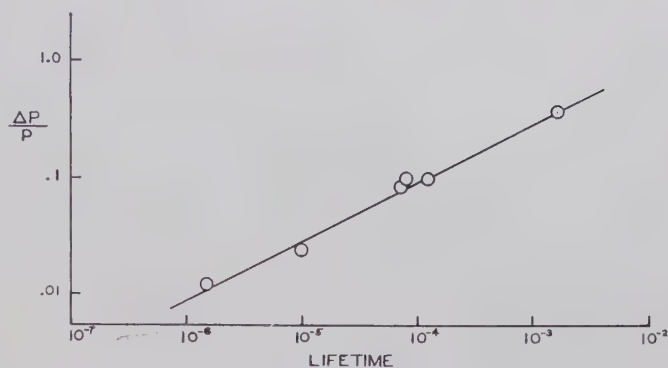


Fig. 8—The ratio of power absorbed by the semiconductor to the total power transmitted as a function of the bulk lifetime in seconds of the germanium specimen.

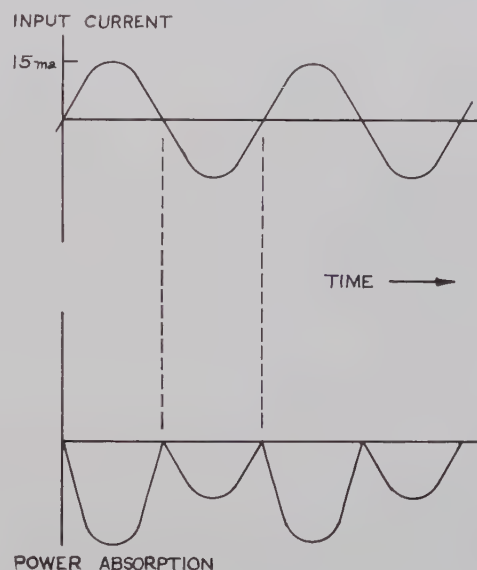


Fig. 9—Power absorption resulting from injection of carriers with alternating voltages on the probe.

formed on the side of germanium rod No. 4. The sample was then placed in the waveguide and contact was made to the indium. The apparent lifetime was measured and found to be 350  $\mu\text{sec}$ . This was the value of the longer lifetime resulting from the presence of traps. Then the probe was removed and a point contact was made to the germanium surface. The longer lifetime here was about 1000  $\mu\text{sec}$ . This indicates that the presence of the indium alloy shortened the lifetime related to deep traps by a factor of three. It was concluded from further experiments with samples No. 6 and No. 7 that alloying does usually shorten the lifetime under the alloyed dot by a factor of  $\frac{1}{3}$  to  $\frac{1}{4}$ , for germanium with the resistivity and lifetime in the ranges described above.<sup>6</sup>

<sup>5</sup> For reports on double injection, see W. G. Matthei and F. A. Brand, "On the injection of carriers into a depletion layer," *J. Appl. Phys.*, vol. 28, p. 513, April, 1957; and N. J. Harrick, "Metal to semiconductor contacts: injection or extraction for either direction of current flow," *Phys. Rev.*, vol. 115, p. 876, August, 1959.

<sup>6</sup> With the microwave absorption technique of lifetime measurement, it is shown by Ramsa, et al. ("Techniques in measurement of lifetime in germanium," *op. cit.*), that if the lifetime vs current curves are extrapolated to small current values, good agreement is found with the more conventional photoconductive decay methods. Experimental tests were run to confirm this conclusion, and the lower current values in Tables III and IV can be considered to provide the bulk lifetime values.

## ELECTRICAL CHARACTERIZATION

The electrical properties of the semiconductor rod running parallel to the  $E$  field in the  $TE_{0,1}$  mode were considered next. The microwave circuit was based on the arrangement of Fig. 4, with the following modifications. An  $EH$  tuner was used in place of the slide screw tuner and a bolometer was used in place of the detector diode. The sample diode current was supplied by a dc source consisting of a battery arrangement. In the following, the indium dot was used for injection.

For sample No. 6, the decrease in power,  $\Delta P$ , reaching the bolometer for various forward currents in the sample diode, is shown in Table III. These data have been normalized by our calculating the  $\Delta P/P$  ratio at different power levels. The data indicate that  $\Delta P/P$  is relatively constant for constant forward currents, with the power levels changing by a factor of ten. The VSWR during these measurements was in the order of 1.10.

In the same microwave system, the  $EH$  tuner was removed; in order to examine the electrical effects of the semiconductor alone inserted in the waveguide, with the transmitted power going to a matched load. The wavelength in the guide was found to be 4.32 cm., and the standing wave ratio showed very slight variations with current. By means of Smith chart analysis, the normalized impedance and VSWR were demonstrated as a function of input current to the sample diode. Results are shown in Table IV.

We next consider sample No. 7 with resistivity at 35.2 ohm cm. The microwave system was matched by means of the  $EH$  tuner with the sample inserted. Results indicated that for this sample 43 per cent of the power was removed as insertion loss. This sample was tested for power transmitted as a function of sample diode current. The results are shown in Table V.

Next, for sample No. 7 without the  $EH$  tuner, the sample diode current was found as a function of VSWR, normalized impedance and  $\Delta P/P$ . The data are indicated in Table V.

Samples were tested for frequency modulation by means of a resonant cavity inserted in the line. In addition, a microwave bridge was assembled with calibrated attenuators and phase shifter. With the sample current injected to reduce the power transmitted to less than fifty per cent of its initial value, a phase shift of less than five degrees was noted.

## DESIGN OF MODULATOR

In the design of the modulator, so far we have considered only the diffusion mechanism of injected minority carriers with relatively low drift fields. In fact, the samples were made deliberately long so that the ohmic contact to the germanium could be placed a considerable distance out of the waveguide. This was necessary in order to examine the physical effects of absorption,

TABLE III  
NORMALIZED DECREASE IN POWER TRANSMITTED AS A  
FUNCTION OF VARIOUS DC CURRENTS  
(SAMPLE NO. 6)

DC Current in Sample Diode (ma)	Normalized Decrease in Power Transmitted $\Delta P/P$				
	$P=0.3$ mw Level	0.49 mw Level	1.0 mw level	2.0 mw Level	3.0 mw Level
0	0.0	0.0	0.0	0.0	0.0
5.5	0.0834	0.0633	0.078	0.080	0.084
12.0	0.133	0.122	0.130	0.130	0.130
19.5	0.166	0.153	0.140	0.155	0.163
27.5	0.173	0.1838	0.180	0.185	0.190
36.0	0.190	0.202	0.195	0.200	0.206
46.0	0.200	0.220	0.210	0.210	0.220

TABLE IV  
NORMALIZED IMPEDANCE VS DC SAMPLE  
DIODE CURRENT (SAMPLE NO. 6)

Current in Milliamperes	VSWR	Normalized Impedance
0	3.59	$0.290 + j.140$
5.8	3.60	$0.283 + j.165$
12.5	3.68	$0.280 + j.180$
19.5	3.75	$0.275 + j.155$
27.5	3.80	$0.266 + j.154$
45.5	3.90	$0.261 + j.168$
(Drift noted due to temperature rise)		

TABLE V  
SAMPLE DIODE CURRENT VS VSWR AND NORMALIZED  
IMPEDANCE (SAMPLE NO. 7)

Current Bias (ma)	VSWR	Normalized Impedance	$\Delta P/P$
0	4.90	$0.21 - j.158$	0
2 ma	4.70	$0.008 - j.140$	0.12
4 ma	4.60	$0.208 - j.140$	0.2
7.5 ma	4.50	$0.205 - j.100$	0.2
10.0 ma	4.50	$0.202 - j.070$	0.36
15.0 ma	4.50	$0.202 - j.070$	0.43
20.2 ma	4.50	$0.202 - j.070$	0.48
25.0 ma	4.60	$0.202 - j.070$	0.51
30.0 ma	4.70	$0.202 - j.070$	0.54
(Drift starting due to temperature rise)			

reflection, etc., related to the sample diode alone. If one is not too concerned with the isolation of the sample diode and could insert a PIN diode in the waveguide, one might take advantage of high drift fields in the semiconductor to enhance the modulation effects.

For calculation of the properties of the PIN modulator, the lifetime, resistivity and distance become the key factors. Assume that the region from the sample diode to the ohmic contact of the specimen can be treated as a filament structure with a high enough field to neglect diffusion.

Following Shockley, the hole density varies as  $e^{-ax}$ , where  $a$  is the hole density attenuation factor.<sup>7</sup> The

<sup>7</sup> W. Shockley, "Electrons and Holes in Semiconductors," D. Van Nostrand, Inc., Princeton, N. J., p. 319; 1952.



term  $1/a$  is now the distance at which the density is  $e^{-1}$  of its initial value, assuming constant injection current, and

$$1/a = \tau_p \mu_p E. \quad (6)$$

Next consider the total number of minority carriers in the filament  $N'$ . Here we have

$$N' = \int_0^D N dx = \int_0^D K e^{-ax} dx, \quad (7)$$

where  $D$  is the distance,  $K$  a constant representing the density of injected minority carriers at the junction boundary, and  $N'$  the total number of carriers. If  $N'$  is in the waveguide and  $\sigma \alpha \omega \epsilon$ , we have seen that  $\alpha$  is linearly increased with  $\sigma$ . By (7),

$$N' = \frac{K}{a} [1 - e^{-aD}], \quad (8)$$

and as  $D$  becomes large compared to  $1/a$ ,

$$N' = \frac{K}{a} = K \tau_p \mu_p E. \quad (9)$$

Eq. (9) reveals that an increase of  $D$  and  $E$  increase  $N'$  and, hence, the attenuation  $\alpha$  of the semiconductor. However, there are practical limits. The limit on  $E$  is due to heating of the sample. This can be helped by the arrangement in Fig. 10, allowing more heat conduction. The other factor to be varied is the thickness of the sample  $D$ . This, however, can have the disadvantage of providing too high an insertion loss. It is desirable for  $D > 1/a$ , but not so much so that insertion losses at zero current bias conditions are impracticable.

The sample dimensions used in these tests are a compromise of temperature, insertion loss, lifetime and  $1/a$  considerations, with respect to physical measurements and device design. A proposed arrangement sim-

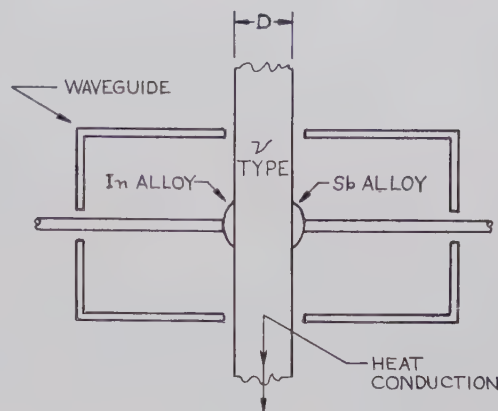


Fig. 10—Proposed method for enhancing the modulation efficiencies.

ilar to that of Fig. 10 should give improved device performance. In preliminary tests,  $\Delta P/P$  ratios of 70 per cent have been obtained, as compared with 50 per cent using samples arranged as shown in Fig. 6. Other preliminary tests, using differently oriented samples of various sizes entirely enclosed within the walls of the waveguide, indicated that an optimum amplitude modulator configuration is determinable.

The possibility of designing a device specifically for enhanced phase modulation, using the present techniques, is also being investigated. In addition, multiple alloy dot arrangements would be worth studying, since  $N'$  will increase linearly with area.

#### ACKNOWLEDGMENT

Acknowledgment should be made to Dr. G. Goubau, L. Hatkin, and Dr. W. Gärtner for their discussions in relation to this work, to the Bendix Semiconductor Division and the Philco Corporation for samples of single crystal germanium which they so kindly furnished, and to C. LoCascio for the design and construction of much of the equipment used.

# Theory and Measurement of $Q$ in Resonant Ring Circuits\*

HELLMUT GOLDE†

**Summary**—The loaded and unloaded  $Q$  of a resonant ring circuit are derived on the basis of the fundamental definition. Simple experiments are described to measure  $Q_0$ ,  $Q_L$ , and the ring power gain without additional coupling to the ring. A number of graphs are given which are useful for these measurements.

## INTRODUCTION

THE traveling-wave resonator or resonant ring circuit has been described by various authors [1–6]. Both directional and nondirectional coupling have been treated, as well as the effect of a lossless discontinuity in the resonant ring. Some applications for the resonant ring circuit have been given which show the general interest in the device [1], [2], [7], [8]. One important characteristic of the circuit is that the power level in the resonant ring may be higher than in the primary transmission line.

A few of the papers go briefly into a discussion of the  $Q$  of the circuit [3], [5]. These calculations are of an approximate nature, valid under the assumption of very low loss in the resonant ring. It is the purpose of this paper to derive more accurate relations for the unloaded and loaded  $Q$  of the circuit. The paper will further describe simple measurements for  $Q_0$ ,  $Q_L$ , and the ring power gain without additional coupling to the ring. This may be important in cases where the ring circuit wave cannot be readily monitored for reasons of size, or operation in a vacuum where a second coupling element should be avoided. The power loss in the ring circuit can also be determined by this measurement, since the power gain depends on the total losses in the ring. This information may be valuable, if the resonant ring is used to test certain components under high power levels and where the power loss in the component depends on the power level.

Only the case of directional coupling will be treated in this paper. The ideas relating to the determination of  $Q$ , the ring power gain, and the ring power loss can easily be applied to nondirectional coupling.

## BASIC EQUATIONS

Two basic configurations of the ring circuit are possible as originally described by Milošević and Vautey [2]. They are shown schematically in Figs. 1 and 2 and will be referred to as types I and II, respectively. The coupling element between the primary line and the

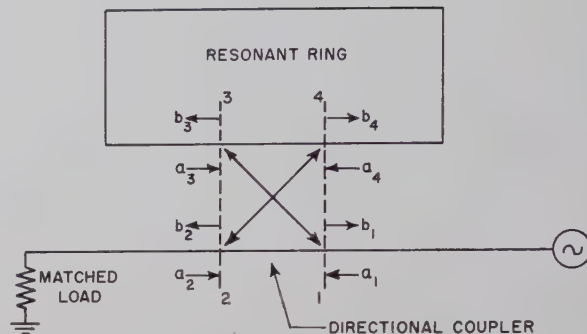


Fig. 1—Resonant ring circuit, type I.

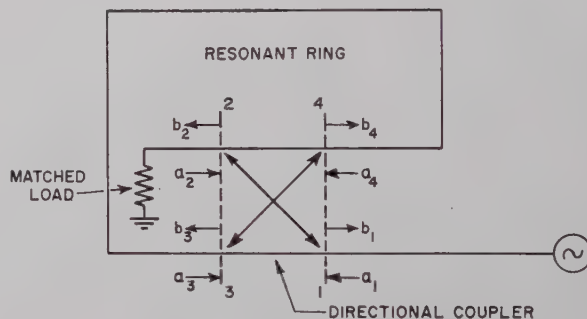


Fig. 2—Resonant ring circuit, type II.

ring circuit is a symmetrical dual directional coupler; other coupling elements like a magic tee or a circulator are equally possible.

No reflections are assumed to exist anywhere, the external load is matched to the transmission line, and the directional coupler has infinite directivity. To simplify the calculations, it will be further assumed that the coupling region between the reference planes is lossless and of infinitesimal length; any loss or phase shift resulting from the finite length of the directional coupler will be absorbed into the connecting transmission lines.

The relations between the incident and reflected waves at the reference planes of the coupler are uniquely determined by the matrix equation

$$b = S \cdot a, \quad (1)$$

where  $a$  is the matrix of the incident waves  $a_1 \cdots a_4$ ,  $b$  the matrix of the reflected waves  $b_1 \cdots b_4$ , and  $S$  the scattering matrix of the directional coupler. For a symmetrical, lossless directional coupler, the scattering matrix is given by

\* Received by the PGMTT, May 20, 1960; revised manuscript received June 29, 1960.

† Dept. of Electrical Engrg., University of Washington, Seattle.



$$S = \begin{vmatrix} 0 & k_1 & jk_2 & 0 \\ k_1 & 0 & 0 & jk_2 \\ jk_2 & 0 & 0 & k_1 \\ 0 & jk_2 & k_1 & 0 \end{vmatrix}, \quad (2)$$

where  $k_1$  and  $k_2$  are real due to the assumed infinitesimal length of the coupling region [9].

Conservation of energy demands that

$$k_1^2 + k_2^2 = 1. \quad (3)$$

It is common practice to express the amount of coupling between the primary and secondary branch of a directional coupler in db. From (1) and (2) and Figs. 1 and 2, it follows that

$$\text{Coupling} = 20 \log k_2 \text{ db (Type I circuit)} \quad (4a)$$

$$\text{Coupling} = 20 \log k_1 \text{ db (Type II circuit).} \quad (4b)$$

The two resonant ring circuits are sufficiently similar to be treated by the same equations. From the previous assumption, that no reflections occur anywhere, it follows for both circuits that

$$a_2 = a_3 = b_1 = b_4 = 0. \quad (5)$$

The relation between the wave amplitudes  $a_4$  and  $b_3$  is given by

$$a_4 = b_3 e^{-\gamma l}, \quad (6)$$

where

$$\gamma = \alpha + j\beta \quad (7)$$

is the propagation constant in the ring circuit of length  $l$  between the reference planes 3 and 4. It is convenient to define a loss factor  $A$  by

$$A = e^{-\alpha l}. \quad (8)$$

Eqs. (1), (2), and (6) can be solved for the power gain  $G$  between reference planes 3 and 1.

$$G = \left| \frac{b_3}{a_1} \right|^2 = \frac{1 - k_1^2}{|1 - k_1 A e^{-j\beta l}|^2}. \quad (9)$$

The power gain is a maximum if the phase shift around the ring is equal to  $2\pi n$ , where  $n$  is an integer; this resonant power gain is given by

$$G_r = \frac{1 - k_1^2}{(1 - k_1 A)^2}. \quad (10)$$

It is possible to optimize the power gain for a given value of  $A$  by a suitable choice of  $k_1$ .

$$G_{r,\text{opt}} = \frac{1}{1 - A^2} \quad (11)$$

with

$$k_{1,\text{opt}} = A. \quad (12)$$

Eq. (10) has been plotted by various authors [1-3]. For graphs of the power gain as a function of other parameters, which will be discussed in the following sections, see Figs. 7 and 8.

### THE UNLOADED $Q$

In general, the unloaded  $Q$  of a resonant cavity is defined by

$$Q_0 = \frac{\omega (\text{energy stored in cavity})}{\text{power loss in cavity}} = \frac{\omega W}{P_L}, \quad (13)$$

evaluated at resonance. The power balance for the ring circuit at resonance is given by

$$P_L = |a_1|^2 - |b_2|^2, \quad (14)$$

where  $|a_1|^2$  is the power delivered by the generator and  $|b_2|^2$  is the power dissipated in the external load. The power flow around the ring can be expressed in terms of the power level at reference plane 3 as

$$P(x) = |b_3|^2 e^{-2\alpha x}. \quad (15)$$

The total stored energy in the loop is given by

$$W = \int_3^4 \frac{|b_3|^2 e^{-2\alpha x}}{v_g} dx = \frac{|b_3|^2}{2\alpha v_g} (1 - A^2), \quad (16)$$

where  $v_g$  is the group velocity in the ring. Then

$$Q_0 = \frac{\omega}{2\alpha v_g} \frac{|b_3|^2 (1 - A^2)}{|a_1|^2 - |b_2|^2}. \quad (17)$$

Introducing relations between the wave amplitudes, (17) can be simplified to

$$Q_0 = \frac{\omega}{2\alpha v_g} = \frac{\pi n \lambda_g^2}{\alpha l \lambda_0^2}, \quad (18)$$

where  $n$  is the number of wavelengths in the ring,  $\lambda_0$  and  $\lambda_g$  are the free space wavelength and the guided wavelength in the ring, respectively. Tischler derived this expression as an approximation for small values of  $\alpha$  [3], [5]. However, (18) has been derived from the basic definition of  $Q_0$  without any approximations; it is therefore valid for any value of  $\alpha$ .

### THE LOADED $Q$

The loaded  $Q$  of a resonant circuit is defined by

$$Q_L = \frac{\omega (\text{energy stored in cavity})}{\text{power loss in cavity and external circuit}} = \frac{\omega W}{P_L + P_{\text{ext}}}, \quad (19)$$

evaluated at resonance.

Before we evaluate this expression for a resonant ring circuit, it is convenient to consider first the usual single-input resonant circuit, as shown schematically in Fig. 3. Here, the cavity is coupled to the input transmission line by a coupling network. It can easily be

shown that the ratio  $Q_L/Q_0$  can be obtained by measuring the voltage standing wave ratio (VSWR) on the line at resonance [10].

$$Q_L = \frac{Q_0}{1 + r}, \quad (20)$$

where  $r$  is the VSWR for an overcoupled cavity and the reciprocal of the VSWR for an undercoupled cavity. If we introduce the reflection coefficient  $\rho$ ,

$$|\rho| = \frac{\text{VSWR} - 1}{\text{VSWR} + 1}, \quad (21)$$

(20) reduces to

$$Q_L = \frac{Q_0}{2} (1 \pm |\rho|), \quad (22)$$

where the positive sign is for an undercoupled cavity, the negative sign for an overcoupled cavity. For critical coupling,  $\rho=0$ , and  $Q_L=Q_0/2$ .

Referring again to Figs. 1 and 2, it is obvious that the VSWR on the input transmission line is always unity under the idealizing assumptions made in this derivation. The power not coupled into a conventional resonant cavity is reflected toward the generator; the power not coupled into a resonant ring is absorbed in the external load. In order to apply the ideas above to the resonant ring, we must replace the

reflection coefficient  $\rho$  by the wave ratio  $b_2/a_1$ , the ratio of the uncoupled wave to the incident wave.

$$Q_L = \frac{Q_0}{2} \left( 1 \pm \left| \frac{b_2}{a_1} \right| \right), \quad (23)$$

where again the positive sign refers to an undercoupled cavity, the negative sign to an overcoupled cavity. From the definition of  $k_1$  and  $k_2$  it follows that overcoupling is characterized by  $k_1 < A$ , undercoupling by  $k_1 > A$ . In either case, if the wave ratio  $b_2/a_1$  is evaluated at resonance from (2) and (3) and substituted into (23), the loaded  $Q$  is given by

$$Q_L = \frac{Q_0(1 + k_1)(1 - A)}{2(1 - k_1A)}. \quad (24)$$

If the coupling between the primary line and the resonant ring is reduced to zero, *i.e.*,  $k_1=1$ ,  $Q_L=Q_0$ . For optimum or critical coupling,  $k_1=A$ , and  $Q_L=Q_0/2$ . Eq. (24) has been plotted in Fig. 4 as a function of the ring attenuation in db.

An approximate expression for the loaded  $Q$  can be derived from (9) for the power gain, since for reasonably large values of  $Q$  (19) reduces to

$$Q_L = \frac{\omega}{2\Delta\omega}, \quad (25)$$

where  $\omega$  is the resonant frequency, and  $\omega \pm \Delta\omega$  are the half-power frequencies. Thus,

$$|1 - k_1A e^{-j\Delta\beta l}|^2 = 2(1 - k_1A)^2, \quad (26)$$

assuming that the loss in the ring is constant for small frequency changes. Using the relation

$$\Delta\beta \simeq \frac{\partial\beta}{\partial\omega} \Delta\omega = \frac{\Delta\omega}{v_g}, \quad (27)$$

which is a good approximation for small values of  $\Delta\omega$ , (26) reduces to

$$\cos \frac{\Delta\omega l}{v_g} = 1 - \frac{(1 - k_1A)^2}{2k_1A}. \quad (28)$$

Since (25) is valid only for reasonably large  $Q_L$ , the cosine can be approximated by the first two terms of the power series expansion. Then (25) can be written

$$Q_L = Q_0 \frac{\sqrt{k_1A} \log_e (1/A)}{1 - k_1A} \quad (29)$$

Eq. (29) is an approximation for large values of  $Q_L$ . It can be compared with (24), which is an exact expression for  $Q_L$ . The two expressions agree within a few per cent if the loss in the ring circuit does not exceed 6 db, and  $k_1$  is larger than  $\frac{1}{2}$ . The latter condition implies

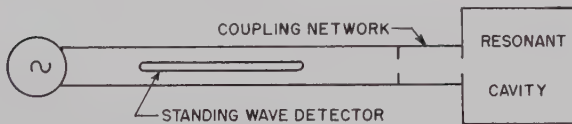


Fig. 3—Schematic diagram of conventional single-input resonant cavity.

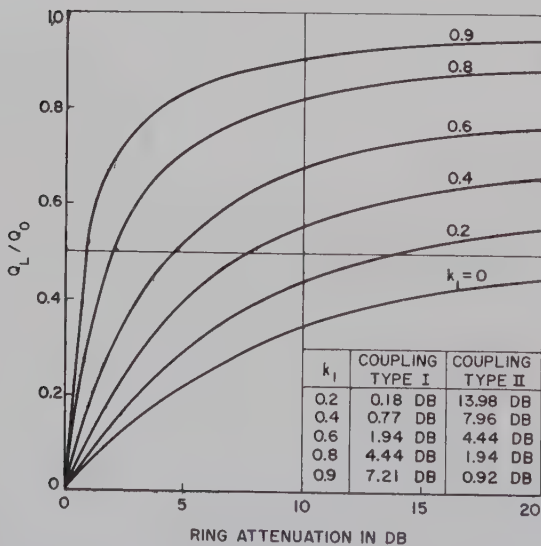


Fig. 4— $Q_L/Q_0$  vs ring attenuation with the coupling coefficient  $k_1$  as parameter.



that the directional coupler should couple less than 3 db of power from the primary to the secondary branch, if a type I circuit is used, and more than 3 db if a circuit of type II is used. Since directional couplers with more than 3 db coupling are scarcely available, it follows that (29) is not applicable for practical type II circuits. This is not too serious a limitation, since for low losses (less than 6 db) a circuit of type I gives a higher power gain than a circuit of type II with the same directional coupler.

### MEASUREMENT PROCEDURES

Eq. (23) suggests a simple measurement of the ratio  $Q_L/Q_0$ . One possible arrangement is shown in Fig. 5. The two power levels  $|b_2|_\omega^2$  and  $|a_1|_\omega^2$  are measured independently at the resonant frequency  $\omega$  by means of two bolometer bridges. If the two auxiliary directional couplers are equal, the two bolometer bridges can be replaced by a reflectometer, which measures the ratio  $|b_2/a_1|_\omega$  directly, or by a slotted line. The latter method is shown schematically in Fig. 6. The ratio  $|b_2/a_1|_\omega$  can be calculated from the measured VSWR using (21), if  $|\rho|$  is replaced by  $|b_2/a_1|_\omega$ . The resonance in the system is easily determined by noting that the ratio  $b_2/a_1$  is a minimum at resonance.

An independent measurement of the loaded  $Q$  is possible if the frequency dependence of the wave  $b_2$  is used. From (1) and (2),

$$\frac{b_2}{a_1} = \frac{k_1 - Ae^{-j\beta l}}{1 - k_1 Ae^{-j\beta l}} \quad (30)$$

At the half-power frequencies,  $\omega \pm \Delta\omega$ , this wave ratio is given by

$$\left| \frac{b_2}{a_1} \right|_{\omega \pm \Delta\omega} = \left[ \frac{k_1^2 + A^2 - 2k_1A \cos \frac{\Delta\omega l}{v_g}}{1 + k_1^2 A^2 - 2k_1A \cos \frac{\Delta\omega l}{v_g}} \right]^{1/2} \quad (31)$$

Introducing (27), the ratio  $b_2/a_1$  at the half-power points can be expressed by the same ratio measured at resonance.

$$\left| \frac{b_2}{a_1} \right|_{\omega \pm \Delta\omega}^2 = \frac{1}{2} \left( \left| \frac{b_2}{a_1} \right|_\omega^2 + 1 \right) \quad (32)$$

Thus, a measurement of the frequency deviation  $\Delta\omega$  which satisfies (32) yields a second independent measurement of  $Q_L$ . It should be noted that (32) is valid under the same restrictions as (29).

These two measurements determine both the loaded and the unloaded  $Q$ . It is then possible to eliminate both  $k_1$  and  $A$  from the expressions for the power gain and

express the power gain in terms of the two  $Q$  values.

$$G_r = \frac{4 \frac{Q_L}{Q_0} \left( 1 - \frac{Q_L}{Q_0} \right)}{1 - \exp \left( \frac{-2\pi n v_g}{Q_0 v_g} \right)} \quad (33)$$

The exponential term generally cannot be neglected. Eq. (33) has been plotted in Fig. 7. This method for measuring the ring power gain is accurate only for reasonably large values of  $Q_L$ . Since it is an indirect method, it should be used only in cases where a direct measurement of the ring power gain is not desirable or possible.

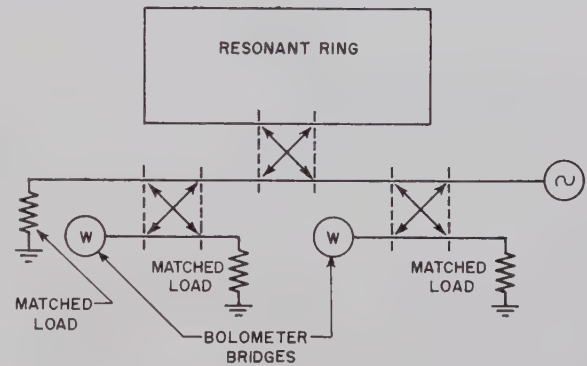


Fig. 5—Schematic diagram for the measurement of  $Q_L$  (type I resonant ring).

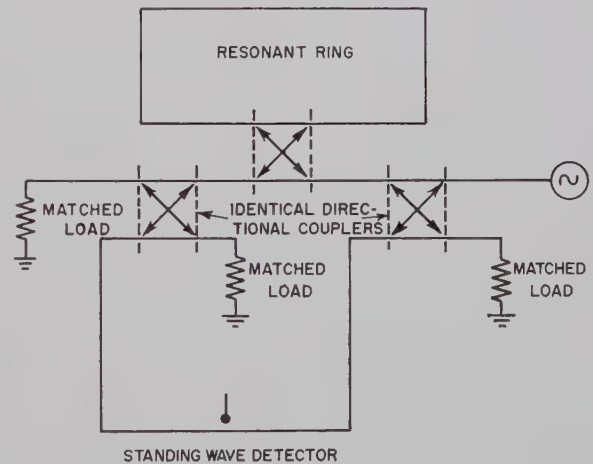


Fig. 6—Alternate setup for the measurement of  $Q_L$  (type I resonant ring).

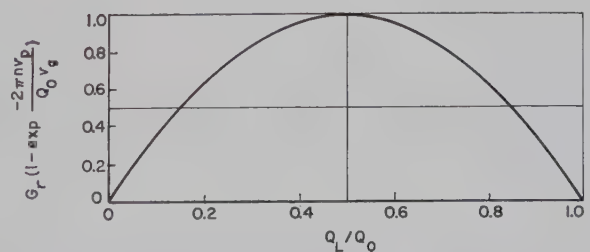


Fig. 7—Normalized ring power gain vs  $Q_L/Q_0$ .

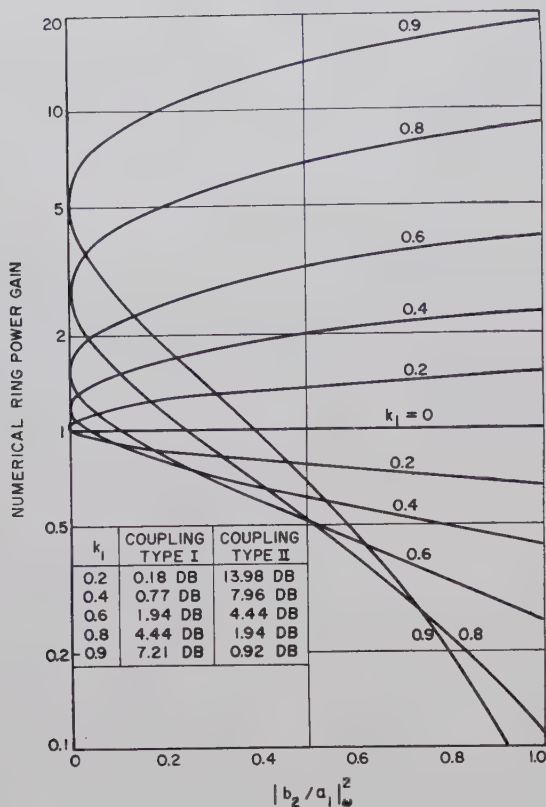


Fig. 8—Resonant ring power gain vs power ratio  $|b_2/a_1|\omega^2$ . (Upper branches are for an undercoupled circuit, lower branches for an overcoupled circuit.)

A variation of this method assumes a knowledge of the coupling coefficient  $k_1$ . It is then sufficient to measure  $|b_2/a_1|\omega$ , the wave ratio at resonance. Eliminating the loss factor  $A$  in (10), the power gain can be written in terms of this wave ratio as

$$G_r = \frac{(1 - k_1 |b_2/a_1|\omega)^2}{1 - k_1^2} \quad (34a)$$

for an overcoupled circuit, or as

$$G_r = \frac{(1 + k_1 |b_2/a_1|\omega)^2}{1 - k_1^2} \quad (34b)$$

for an undercoupled circuit.

The power gain is shown graphically in Fig. 8 as a function of the power ratio  $|b_2/a_1|\omega^2$  with  $k_1$  as a parameter. The upper branch of each curve is for an undercoupled circuit, the lower branch for an overcoupled circuit. This measurement is accurate for all values of the coupling coefficient  $k_1$ , since the two equations do not contain any approximations. Since the coupling coefficient can usually be determined accurately, while

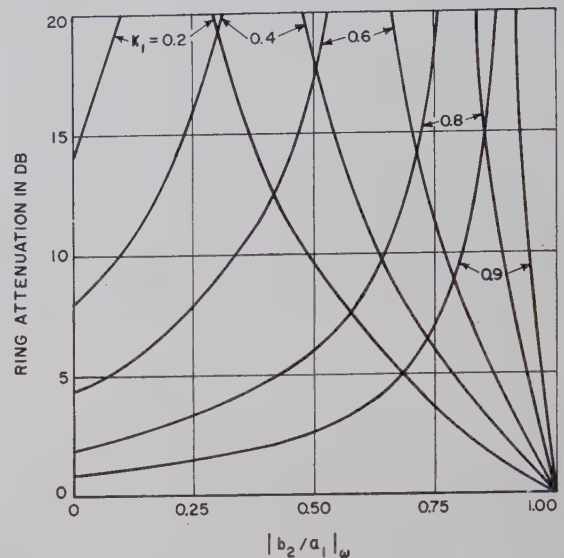


Fig. 9—Ring attenuation vs wave ratio  $|b_2/a_1|\omega$  with  $k_1$  as parameter.

the ring attenuation cannot, this measurement is very often sufficient to determine the power gain.

Note that these methods can be used to determine the ring attenuation. It can easily be shown that

$$A = e^{-\alpha l} = e^{-(\pi n v_p / Q_0 v_g)} = \frac{|k_1 - |b_2/a_1|\omega|}{1 - k_1 |b_2/a_1|\omega} \quad (35)$$

This expression is shown graphically in Fig. 9.

#### BIBLIOGRAPHY

- [1] P. F. Sferazza, "Traveling wave resonators," *Tele-Tech and Electronic Ind.*, vol. 14, pp. 84-85; November, 1955.
- [2] L. Milošević and R. Vautey, "Resonateur a ondes progressives," *Rev. tech. Comp. franc. Thomson-Houston*, no. 21, pp. 65-78; December, 1955; also "Traveling-wave resonators," *IRE TRANS. ON MICROWAVE THEORY AND TECHNIQUES*, vol. MTT-6, pp. 136-142; April, 1958.
- [3] F. J. Tisher, "Resonance properties of ring circuits," *IRE TRANS. ON MICROWAVE THEORY AND TECHNIQUES*, vol. MTT-5, pp. 51-56; January, 1957.
- [4] K. Tomiyasu, "Effect of a mismatched ring in a traveling-wave resonant circuit," *IRE TRANS. ON MICROWAVE THEORY AND TECHNIQUES*, vol. MTT-5, p. 267; October, 1957.
- [5] F. J. Tisher, "Resonant properties of nonreciprocal ring circuits," *IRE TRANS. ON MICROWAVE THEORY AND TECHNIQUES*, vol. MTT-6, pp. 66-71; January, 1958.
- [6] K. Tomiyasu, "Attenuation in a resonant ring circuit," *IRE TRANS. ON MICROWAVE THEORY AND TECHNIQUES*, vol. MTT-8, pp. 253-254; March, 1960.
- [7] H. Golde, "Extended interaction klystrons with traveling-wave cavities," Ph.D. dissertation, Stanford University, Stanford, Calif., 1959.
- [8] R. B. R. Shersby-Harvie and L. B. Mullet, "Traveling-wave linear accelerator with RF power feedback," *Proc. Phys. Soc.*, London, vol. 62, pp. 270-271; April, 1949.
- [9] C. G. Montgomery, R. H. Dicke, and E. M. Purcell, eds., "Principles of Microwave Circuits," McGraw-Hill Book Co., Inc., New York, N. Y., p. 302; 1948.
- [10] E. L. Ginzton, "Microwave Measurements," McGraw-Hill Book Co., Inc., New York, N. Y., p. 407; 1957.



# Correspondence

## Ferrite Shape Considerations for UHF High-Power Isolators\*

Ferrite isolators deteriorate at high microwave power levels due to the gyromagnetic saturation phenomena described by Suhl.<sup>1</sup> The onset of this deterioration is particularly detrimental to isolator performance when the main and subsidiary resonances coincide. At microwave frequencies the coincidence effect can generally be avoided if thin transversely magnetized ferrite slabs are used. However, at frequencies below 1 kMc, the finite slab thickness can contribute to main-subsidary resonance coincidence unless care is taken to choose the proper length and width dimensions of the slab. The following calculations specify the ferrite slab shape needed to avoid this coincidence in UHF ferrite isolators.

The main and subsidiary resonances occur at magnetizing fields  $H_{res}$  and  $H_{sub}$ , respectively. Coincidence effects are avoided provided that,

$$H_{res} \geq H_{sub} \quad (1)$$

where

$$H_{res} = \left( N_x - \frac{N_x + N_y}{2} \right) 4\pi M_s + \sqrt{\left( \frac{N_x - N_y}{2} \right) (4\pi M_s)^2 + \left( \frac{\omega}{\gamma} \right)^2} \quad (2)$$

$$H_{sub} = \frac{\omega}{2\gamma} + N_x 4\pi M_s \quad (3)$$

By substituting (2) and (3) into (1),

$$\frac{\omega}{\gamma} \geq \frac{4\pi M_s}{3} [N_x + N_y + \sqrt{N_x^2 + N_y^2 + 14N_x N_y}] \quad (4)$$

Where

$\omega$  = applied angular frequency

$\gamma$  = the gyromagnetic constant

$4\pi M_s$  = the saturation magnetization

$N_x + N_y + N_z = 1$  are the demagnetizing constants. The  $z$  direction is taken as the direction of magnetization.

The demagnetizing constants worked out by Osborn<sup>2</sup> for the general ellipsoid are used in calculating the minimum frequency prior to main-subsidary coincidence for particular ferrite shapes. The results are plotted on Fig. 1 and the ferrite-waveguide geometry is shown in Fig. 2.

Note that the minimum frequency for a particular material and  $T/L$  ratio occurs when  $W/L=1$ . Now, suppose it is desired to make a YIG 400 Mc high-power isolator with  $\frac{1}{8}$  inch thick slabs. The useful width

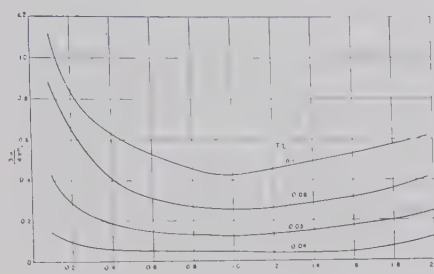


Fig. 1—Critical frequency ratio for the onset of main and subsidiary resonance coincidence as a function of ferrite shape.

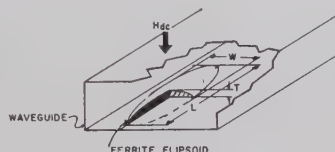


Fig. 2—Ferrite-waveguide geometry.

$W$  is on the order of 3 inches, and the  $4\pi M_s \approx 1800$  gauss,  $\gamma \approx 2\pi \times 2.8 \times 10^6$  radians per oersted. The value of  $3\omega/\gamma 4\pi M_s$  is 0.24, which is entered on the ordinate of Fig. 1. Only those shapes that fall below 0.24 should be considered for the isolator application. Thus, the  $T/L$  ratio should be less than 0.06 or  $L \geq 2$  inches. If a length of 4.2 inches is chosen, then  $T/L=0.03$ , and  $W \geq 0.84$  inch.

In conclusion, it has been shown that the ferrite thickness of a ferrite slab causes a contribution to the demagnetizing fields that may produce main-subsidary resonance coincidence at UHF frequencies. However, an appropriate slab geometry can be specified that eliminates this possibility.

E. STERN

Antennas and Microwave

Electronics Lab.

General Electric Co.

Syracuse, N. Y.

## Measurement Technique for Narrow Line Width Ferromagnets\*

Measurement of the line width of a ferromagnetic resonance curve using the now well-known cavity perturbation technique<sup>1</sup> offers some difficulty in the case of very narrow line width samples. Because of their large magnetic susceptibility, such samples produce a large effective filling factor with

respect to the cavity. For example, the filling factor for a small ferromagnetic sample in a nondegenerate rectangular cavity reduces to

$$\eta = \chi \left[ \frac{h^2 V_s / 2}{\int_{V_c} h^2 dv} \right] \propto \chi V_s / V_c$$

where  $\chi$  is the scalar magnetic susceptibility,  $V_s$  is the volume of the small sample,  $V_c$  is the cavity volume and  $h$  is the microwave magnetic field. Since the perturbation equations for cavity frequency shift and  $Q$  change are

$$\frac{\Delta\omega}{\omega} = \text{Re}(\eta) \alpha \chi' V_s / V_c$$

$$\Delta\left(\frac{1}{2Q}\right) = I_m(\eta) \alpha \chi'' V_s / V_c$$

large values of  $\chi$  must be offset by increasing the size of the test cavity in order to reduce the ratio  $V_s/V_c$  if the perturbation is to remain small. When a 0.020 inch yttrium-iron-garnet sphere of the order of 1-oersted line width is to be placed in a simple X-band brass cavity, it is found that a cavity length greater than  $50\lambda_0$  may be required to insure a sufficiently small perturbation of the fields in the cavity. The situation may be alleviated somewhat by rotation of  $H$ , the dc magnetic field, thereby reducing from  $90^\circ$  the angle between  $H$  and  $h$ . This procedure, which decouples the sample and effectively reduces  $V_s$ , normally precludes controlling the crystalline orientation of the sample under study.

The cavity perturbation method may be avoided if instead the sample is placed in a geometry whereby its magnetic resonance is characterized by reradiation of incident power into a region that is normally isolated when  $H$  is moved off-resonance.<sup>2,3</sup> An example of this idea is the cross-guide coupler suggested by Stinson.<sup>3</sup> By detection of the power coupled into the crossed guide, a resonance response curve is easily obtained from which the line width may be measured directly as the width at a certain fraction of the peak value of the curve. A possible disadvantage of this scheme is that the sample is located in a hole common to both guides and may be subject to undesirable nonuniform microwave fields. Furthermore, the mechanism for reradiation by the resonant spin system into the secondary guide may be accompanied by significant radiation damping which would show up as a line broadening in narrow line width samples.

The technique described below has been found satisfactory for line width measurements of fractional linewidth samples in the size range 0.015 inch or larger. As shown in the schematic of Fig. 1, the sample is placed in the transverse, uniform microwave magnetic field at a distance  $n\lambda_0/2$  from the short

\* Received by the PGMTT, May 9, 1960.

<sup>1</sup> H. Suhl, "The nonlinear behavior of ferrites at high microwave signal levels," *Proc. IRE*, vol. 44, pp. 1270-1284; October, 1956.

<sup>2</sup> J. A. Osborn, "Demagnetizing factors of the general ellipsoid," *Phys. Rev.*, vol. 67, pp. 351-357; June, 1945.

\* Received by the PGMTT, May 16, 1960.

<sup>1</sup> J. O. Artman and P. E. Tannenwald, "Microwave Susceptibility Measurements in Ferrites," M.I.T. Lincoln Lab., Lexington, Mass., Tech. Rept. No. 70; October 1954.

<sup>2</sup> J. I. Masters and R. W. Roberts, *J. Appl. Phys.*, vol. 30, pp. 1795-1805; April, 1959.

<sup>3</sup> D. C. Stinson, "Ferrite line width measurements in a cross-guide coupler," *IRE TRANS. ON MICROWAVE THEORY AND TECHNIQUES*, vol. MTT-6, pp. 446-450; October, 1958.

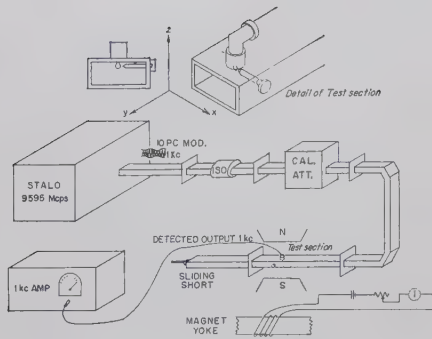


Fig. 1—Circuit for line width measurement

in a shorted X-band waveguide. A nearby pickup coil, which senses the precessing dipolar field of the magnetic sample, is oriented so that the plane of the loop and  $h$  are parallel, producing a negligible coupling to the transverse microwave field. When  $H$  is near resonance a voltage is induced in the loop. Since  $h$  is kept sufficiently small to insure linearity, this voltage is proportional to  $h$ .

The definition of line width depends on the type of response of  $m$  to  $h$  as dictated by the geometry of the system. In general, assuming  $h_x = h_0 e^{i\omega t}$ ,  $h_y = -j h_0 e^{i\omega t}$ ,  $h_z = 0$ ,  $m = (\chi) \cdot h$  where the elements of the anti-symmetric dyadic are complex, substitution yields the circular precession

$$m_x m_x^* = m_y m_y^* = h_0^2 \{ |\chi_{xx}|^2 + |\chi_{xy}|^2 + j\chi_{xx}\chi_{xy}^* - j\chi_{xy}\chi_{xx}^* \}.$$

However, in the use of linear polarization ( $h_x = h_0 e^{i\omega t}$ ,  $h_y = h_z = 0$ ) employed here, there results:

$$m_x m_x^* = h_0^2 |\chi_{xx}|^2 \quad m_y m_y^* = h_0^2 |\chi_{xy}|^2.$$

Now the spacial relationship of the loop and sample is such that only the projection of the motion along the  $y$  direction is effective. Therefore, the induced voltage depends upon the absolute value of the off-diagonal component of  $(\chi)$ , i.e.,  $E \propto h_0 \sqrt{|\chi_{xy}|^2}$  which may be expressed in terms of its absorptive component,  $\chi_{xy}'$ , whereby the line width may be defined. In general  $|\chi|^2 = \chi'^2 + \chi''^2$  where we have dropped the  $xy$  subscript for convenience. In particular,

$$|\chi|^2 \Delta H \cong [\chi'_{\max}/2]^2 + [\chi''_{\max}]^2 \cong 2[\chi'_{\max}/2]^2$$

when  $H$  is set for  $\frac{1}{2}$  of the peak of the absorption curve.<sup>4</sup> Also  $|\chi|_{\max}^2 = \chi_{\max}^{\prime 2}$ . The indicated approximations are very good for narrow line width samples yielding

$$|\chi_{xy}| \Delta H = |\chi_{xy}|_{\max} / \sqrt{2}.$$

However, since the measurement of the response is normally read from a calibrated attenuator, the observed response as  $H$  varies is of the form  $h_0^2 |\chi_{xy}|^2$ , and the line width is therefore measured at 3 db below the peak of the response curve.

A simple circuit assembled for these measurements is shown schematically in Fig. 1. The CW source is a Stalo, L. F. E. 814X-21, operated at 9600 Mc and internally modulated at 1 kc. The sensitivity

gained by modulation allows the use of signals as small as the order to 1 mV to avoid any saturation or heating effects. The signal is fed through an isolator and calibrated attenuator to a test section terminated in a sliding short. The correct position of the sliding short is found by substitution of an electric probe for the loop and adjusting for a null in the electric probe output. The correct loop orientation is then found by rotation of the loop for minimum leakage of the microwave field with  $H=0$ , which is about 30 db below the loop output when  $H$  is adjusted for resonance.

The loop output is demodulated by a tuned crystal detector and the remaining 1 kc signal is amplified and read on a voltmeter.

Line width measurements are made by noting the field required for resonance and the associated voltmeter readings at attenuator settings of 0 db and 3 db. Twice the difference between the field for resonance and the field required to produce the latter voltmeter reading with the attenuator set at 0 db is the measured line width. Measurements of  $\Delta H$  were made in this experiment by producing field increments with an accurately measured dc current passed through a coil of some 50 turns wound around the yoke of a 6-inch Varian magnet. An  $H$  vs current curve was established using a precision NMR gaussmeter and is a straight line for the current range in question. It has been found that the accuracy ( $\pm 0.01$  gauss) and ease of this method of measuring changes in  $H$  exceeds the method of direct measurements of  $H$  with the gaussmeter.

As anticipated, the distance between the loop and sample is an important consideration. The sample is cemented to a quartz post which may be extracted and rotated by known amounts. In a previous paper,<sup>5</sup> it has been shown that currents in the loop will produce fields that will damp the motion of the resonant sample. Although the formulas of this paper appear not to apply here because of the uncertainty in the phase relationship between loop voltage and current, decoupling of the sample and loop by increasing their spacing will reduce the damping. The sample is thus extracted as far from the loop as possible without reducing the signal-to-leakage ratio in the loop output below an arbitrary figure of 30 db. For two single crystal YIG sphere samples tested, a spacing of greater than 5-sphere diameters was used. The results of a comparison between the cavity perturbation method and the loop method are given below:

Sample	Diameter in Inches	X-Band Cavity	X-Band Loop Method
A	0.015	0.63 oe	0.65 oe
B	0.020	0.64 oe	0.67 oe

Sample A was grown in the Air Force Cambridge Research Center and polished by a novel manual process to be described in a later letter. Sample B was purchased as a polished sphere from Microwave Chemicals,

Inc., New York, N. Y. The dependence of line width on crystal orientation was eliminated from the comparison by averaging over many orientations in each case.

J. I. MASTERS  
Technical Operations, Inc.  
Burlington, Mass.  
B. R. CAPONE  
P. D. GIANINO  
AF Cambridge Res. Center  
Air. Res. and Dev. Command  
Laurence G. Hanscom Field  
Bedford, Mass.

## Multidiode Switches\*

The impedance of crystal diodes is known to depend on the applied bias voltage. This has suggested the use of diodes as switching elements in the control of microwave signal transmission. In the simplest form, the diode switch consists of a transmission line which is shunted by a diode. Coaxial cables<sup>1</sup> as well as waveguides<sup>2-5</sup> have been used for the transmission lines that are shunted by point-contact<sup>1-5</sup> and  $p-i-n$  diodes.<sup>6</sup> Slab line or coaxial switches where a diode is inserted in series with the center conductor of the line have also been developed.<sup>7</sup>

This note examines the feasibility of multidiode shunt or series type switches. After establishing equivalent circuits representative of the diodes in the "on" and "off" states of the switch, a specific realizable single diode switch is assumed for the calculations. Characteristics of a multipole switch which consists of a number of diodes in individual transmission line branches are derived for the two switch types. Several measurements made on an 8-diode series switch will be described thereafter.

### SHUNT-TYPE DIODE SWITCHES

The diode switch configuration consisting of a diode which shunts a transmission line will be considered first for multidiode

\* Received by the PGMTT, April 18, 1960; revised manuscript received, May 26, 1960. This note is based on a presentation at the 1959 National Symposium of the Professional Group on Microwave Theory and Techniques, Harvard University, Cambridge, Mass.

<sup>1</sup> D. J. Grace, "A Microwave Switch Employing Germanium Diodes," Appl. Elec. Lab., Stanford University, Stanford, Calif. Tech. Rept. No. 26; January, 1955.

<sup>2</sup> M. A. Armstead, E. G. Spencer, and R. D. Mather, "Microwave semiconductor switch," PROC. IRE, vol. 44, p. 1875; December, 1956.

<sup>3</sup> R. V. Garver, E. G. Spencer, and M. A. Harper, "Microwave semiconductor switching techniques," IRE TRANS. ON MICROWAVE THEORY AND TECHNIQUES, vol. MTT-6 pp. 378-383, October, 1958.

<sup>4</sup> M. R. Millet, "Microwave switching by crystal diodes," IRE TRANS. ON MICROWAVE THEORY AND TECHNIQUES, vol. MTT-6, pp. 284-290; July, 1958.

<sup>5</sup> M. Depoy and R. Lucy, "An Absorption Type Microwave Crystal Switch for High Speed Duplexing," Sylvania Electric Products, Inc., Waltham, Mass., Appl. Res. Memo. No. 140; July, 1958; also R. Lucy, "Microwave High Speed Switch," Proc. 1959 Electronic Components Conf., Philadelphia, Pa., May 6-8, 1959; pp. 12-25.

<sup>6</sup> A. Uhlir, Jr., "The potential of semiconductor diodes in high-frequency communications," PROC. IRE, vol. 46, pp. 1099-1115; June, 1959. (See especially pp. 1112-1113.)

<sup>7</sup> M. Bloom, "Single-Pole Double-Throw Wide-Band Microwave Switch," National Symposium of the Professional Group on Microwave Theory and Techniques, Harvard University, Cambridge, Mass.; 1959.

<sup>4</sup> A relationship between absorption and dispersion that approximately satisfies the Kramers-Kronig formula is assumed.

<sup>5</sup> N. Bloembergen and R. V. Pound, "Radiation damping in magnetic resonance experiments," Phys. Rev., vol. 95, pp. 8-12; July, 1954.



TABLE I\*  
PERFORMANCE OF SINGLE POLE SHUNT TYPE DIODE SWITCHES

Incident Power, Milliwatts		Armstead, <i>et al.</i> <sup>2</sup>	Millet <sup>4</sup>	Depoy and Lucy <sup>5</sup>	Sylvania <sup>8</sup>	Assumed Switch Characteristics
"on" Condition		0.1	0.5	0.1	1000 to 4000	1.25 - <i>jb</i>
	Admittance, Normal	0.95 - <i>j</i> 0.15	1.25 - <i>j</i> 0.05	1.25 - <i>j</i> 0.03	—	—
	Insertion Loss, db	1	1	1	0.5	1
"off" Condition		18 + <i>j</i> 15	8	2.2 - <i>j</i> 3.4	—	<i>y</i> <sub>off</sub>
	Admittance, Normal	18 + <i>j</i> 15	8	2.2 - <i>j</i> 3.4	—	—
	Reflected Power, Per cent	80	60	60	90	80
	Insertion Loss, db	25	21	22	25 to 19	<i>k</i>

\* The listed admittance figures include the admittance of a matched line termination.

switch applications. The data published by several authors<sup>2,4,6</sup> and recent experimental data of Sylvania<sup>8</sup> are summarized in Table I. The characteristics of the switch assumed for the subsequent analysis are indicated in the last column of the Table. The admittance of the "off" diodes should be commensurate with the 80 per cent power reflection figure, but is not further specified.

The equivalent circuit of a single pole diode switch to be used in a multipole switch synthesis must account for the experimental data of Table I. Although equivalent two-terminal network representations have been suggested for the switch during its "on" and "off" conditions,<sup>4</sup> such networks characterize the switch performance only qualitatively. The loading of the transmission line by the diode admittance may account for the insertion loss observed in most cases during the "on" condition, but one must resort to a four-terminal structure to represent the observed insertion loss during the "off" condition of the switch. The "on" condition of the switch is represented by an admittance *Y<sub>d</sub>* which shunts the transmission line. The normalized diode admittance

$$y_d = \frac{Y_d}{Y_0} = 0.25 - jb \tag{1}$$

when added to the matched line admittance *y<sub>0</sub>* = 1 provides the insertion loss listed in two cases<sup>4,6</sup> of Table I. With a standing wave ratio of approximately 1.2, the reflection loss is less than 0.1 db. Power division between the diode and the matched load provides the measured insertion loss of approximately 1 db. In the "off" condition, the equivalent shunt admittance provides the correct amount of reflected power, but it gives too small an insertion loss in all of the cases listed in Table I. Thus, 60 per cent of reflected power corresponds to a reflection coefficient |Γ| = 0.775 and to the normalized input admittances *y<sub>i</sub>* = 8 or 2.2 - *j*3.4 as listed in the Table.<sup>4,6</sup> The smallest amount of power is delivered to the load *Y<sub>0</sub>* if the real part of *Y<sub>d</sub>* has its maximum value which is the case for real *Y<sub>d</sub>*. With *y<sub>i</sub>* = 8 the power division between *Y<sub>0</sub>* and *Y<sub>d</sub>* is 1:7. The power delivered to the load *Y<sub>0</sub>* is thus 0.4:7 ≈ 0.057 of the incident power; the in-

sertion loss is no greater than 12.5 db which is almost 10 db short of the measured insertion loss. The insertion loss measured in the "off" condition can be accounted for by a four-terminal equivalent network. A *T*-type structure has been selected for the equivalent representations of multidiode switches.

A multidiode switch may be designed to connect a centrally located source to one of *n* possible loads. Such a switching device is designated as a distribution switch. Its equivalent diagram is shown in Fig. 1. The isolation and insertion losses of this switch have been calculated for the diode characteristics indicated in the last column of Table I. The total insertion loss relative to the load at the "on" diode (*L<sub>on</sub>*) consists of the reflection loss due to the mismatch of the central junction as seen from the incident wave, a power division loss between the (*n* - 1) "off" diodes and the "on" diode and of a further power division loss between the "on" diode and the load. The total insertion loss relative to the load at the "off" diode (*L<sub>off</sub>*) consists of the reflection loss from the central junction, a power division loss between the "off" diode on one side and the "on" diode and the (*n* - 2) "off" diodes on the other side, the nominal isolation (*k*) provided by a single "off" diode less the single "off" diode reflection loss (7 db for 80 per cent reflected power), since the latter part of the single diode isolation is accounted in the earlier power division losses. In designing the multidiode switch, the line length *l* between the central junction and the individual diodes is selected in such a way that the "off" diodes reflect minimum conductance across the central junction. This choice of line length minimizes the part of insertion losses *L<sub>on</sub>* caused by power division between the load and the "off" switches. As seen in Table I, the "off" switches exhibit a high input admittance. Therefore, the line length *l* will be very nearly an odd multiple of (λ/4). For a purely conductive input admittance of the "off" switches

$$l = (2m + 1)(\lambda/4) \tag{2}$$

where *m* is an integer or zero. The loss figures computed for this line length are indicated by solid curves in Fig. 2. For a complex input admittance of the "off" switches, the loss figures will lie within the shaded areas, close to the solid curves. The shaded areas are bounded by dashed curves that represent loss figures in the hypothetical case of *l*, a multiple of λ/2 for "off" switches of low

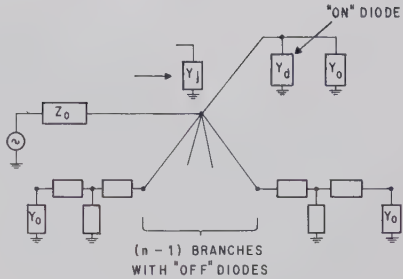


Fig. 1—Multidiode distribution switch.

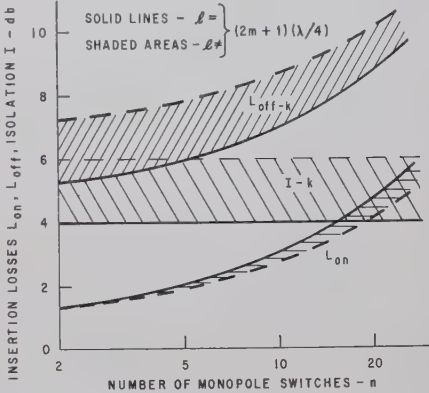


Fig. 2—Insertion losses and isolation of a shunt-type multidiode switch. Isolation *I* = *L<sub>off</sub>* - *L<sub>on</sub>*; *k* = "off" insertion loss of a one-diode switch.

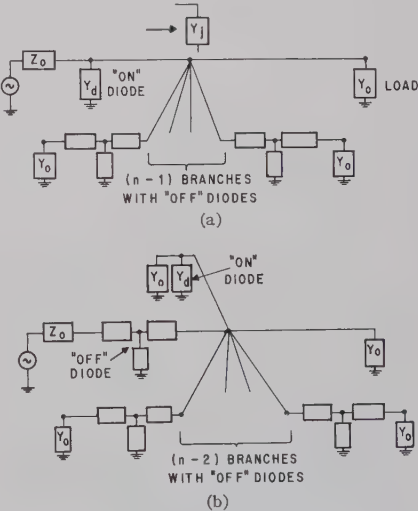


Fig. 3—Multidiode selector switch; (a) "on" condition (b) "off" condition.

purely conductive input admittance. It is seen that both the losses in the "on" and "off" conditions of the switch increase with an increasing number of diodes *n*. However, the isolation provided by the switch remains constant over the range of *n* indicated in Fig. 2.

In another switch configuration, a centrally located load may be connected to one of *n* possible locations of a single source (as in a scanning receiving antenna). Such a switching device is designated as a selection switch and its equivalent diagram is shown in Fig. 3. The same physical structure may be used for distribution and selection switches. The switches act as linear devices

\* Unpublished X-band measurements on 1N419 diodes, by the Appl. Res. Lab., Sylvania Electronic Systems, Inc., Waltham, Mass. No switch impedances were recorded in these tests.

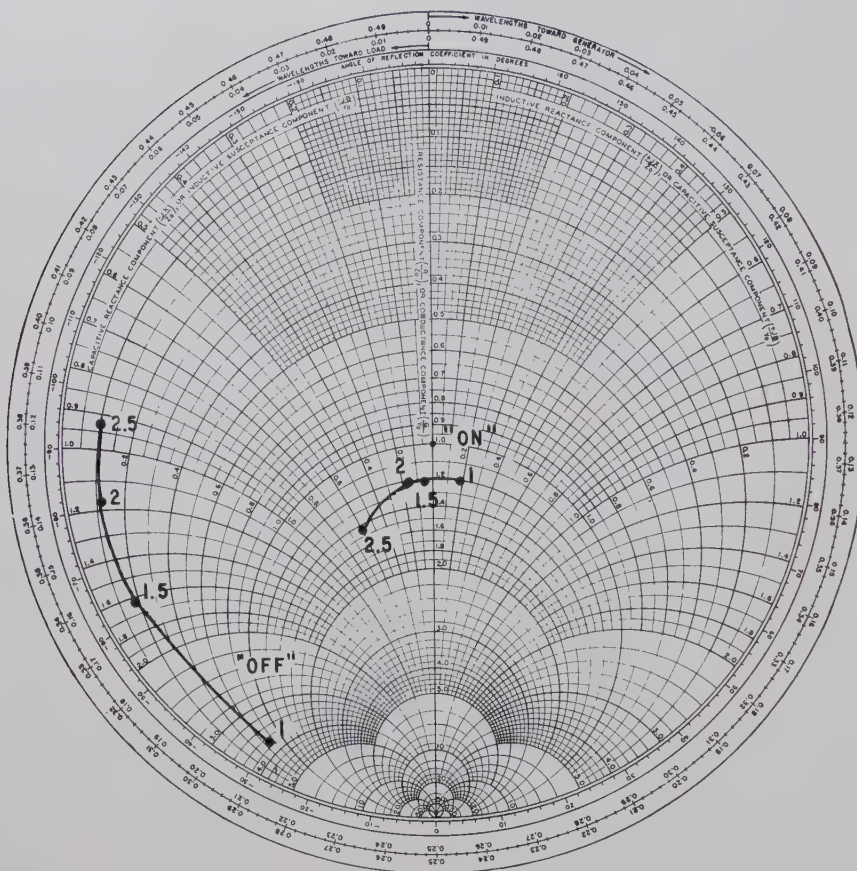


Fig. 4—Input impedance of a series-type diode switch. 50  $\Omega$  line termination, 1N118 diode, frequency in kMc.

during any of their possible states and the reciprocity theorem may be applied to show that the distribution and selection switches exhibit identical loss figures.<sup>9</sup>

#### SERIES-TYPE DIODE SWITCHES

A typical impedance plot of a single diode series type slab line switch is plotted in Fig. 4. The corresponding "on" condition insertion loss is 1 db. The isolation decreases from 29 to 21 db as the frequency is increased from 1 to 2.5 kMc.

The "on" condition of the switch is represented by an impedance in series with the transmission line. The impedance plotted in Fig. 4 provides a reflection loss of less than 0.1 db in the frequency range between 1 and 2.5 kMc. The power division between the diode and the matched load provides the measured insertion loss of approximately 1 db. The two-terminal equivalent representation does not provide the measured insertion loss in the "off" condition. Again a four-terminal structure may be used to characterize the "off" condition.

The equivalent representation of a series type multidiode switch is of the form indicated in Figs. 1 and 3 except for the "on" diode equivalent circuits. The shunt type "on" diodes should be changed to series type "on" diodes in the diagrams of Figs. 1 and 3. The computation of the loss figures of

the multidiode series switch follows closely the pattern of shunt diode computations. However, a significant distinction between the two switch types is their "off" impedance. The series type "off" diodes exhibit high impedance as seen from Fig. 4. In order to minimize the insertion losses caused by power division between the load and the "off" diodes, the line length  $l$  between the central junction and the "off" diodes must be an approximate multiple of  $(\lambda/2)$ . For a purely resistive impedance of the "off" diodes,

$$l = m\lambda/2 \quad (3)$$

where  $m$  is an integer or zero. The analysis shows that the loss figures of the series type switches are identical with those of the shunt type switches, provided the single diode insertion loss and isolation figures are identical and provided that the "on" diode shunt admittance of the shunt switch is equal to the series impedance of the series switch. Within these limitations, the loss curves indicated in Fig. 2 apply also to the shunt type switch except that the solid curves refer to series switches where the line length  $l$  is given by (3). For different line lengths, the loss figures will be within the shaded areas close to the solid curves.

#### DESIGN CONSIDERATIONS AND MEASUREMENTS

The previous discussion indicates that series and shunt type switches are equally

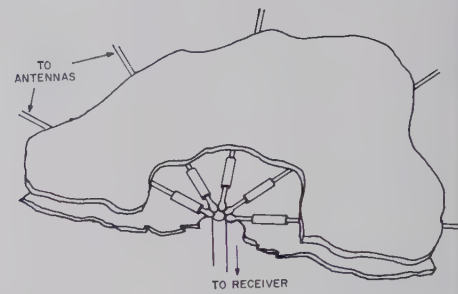


Fig. 5—Diode distribution network.

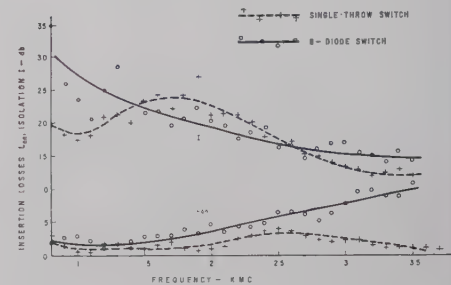


Fig. 6—Measured characteristics of series-type diode switches.

sued for synthesis of a multidiode switch, provided that their characteristics in single-diode switches are equivalent. The selection between the two switch types may be based on frequency characteristics, bandwidth considerations or fabrication problems.

The operation of series type switches is rapidly deteriorated with increasing operating frequency. This limitation is less pronounced with shunt type switches. A wide operation bandwidth may be achieved only with series type switches. By placing the series diode as close to the central junction as possible, small power division losses may be achieved over a frequency range exceeding an octave [ $m \approx 0$  in (3)]. The shunt diode which exhibits a low "off" impedance must be placed approximately an odd number of quarter wavelengths away from the central junction [ $m$  zero or integer in (2)]. This condition may be satisfied only over small fractional bandwidth to frequency ratios.

A slab line series type switch performs satisfactorily for frequencies up to 3 kMc. Also, the simplicity of its construction makes one favor this switch relative to shunt type switches. As shown in Fig. 5, the switch consists of a central junction and of a number of diodes connected around this junction. Such a switch consisting of 8 diodes has been designed and tested. Preliminary measurement data of Fig. 6 affirm several of the analytical results. The multidiode switch exhibits higher insertion losses, but it provides roughly the same isolation figures as a single-diode switch.

A more recent design of a multidiode switch has resulted in insertion losses that are less than 4 db over the frequency range indicated in Fig. 6.<sup>10</sup>

<sup>9</sup> A long-hand analysis of the selection switch thus provides a cross-check for the loss figure calculations of the distribution switch.

<sup>10</sup> Unpublished measurements on a five-diode switch by J. Kellett of Sylvania's Antenna and Microwave Laboratory.



## ACKNOWLEDGMENT

The experimental work on the 8-diode switch has been carried out under the direction of S. Miller. It was sponsored by USAF Cambridge Research Center.

JANIS GALEJS  
Sylvania Electronic Systems  
Waltham, Mass.

## Technique for Polishing Single Crystal Yttrium-Iron-Garnet Spheres\*

A simple method of polishing yttrium-iron-garnet spheres which produces samples of fractional oersted linewidths has been employed at the Air Force Cambridge Research Center. The technique consists of "hand-polishing" the crystal spheres in diamond pastes and aluminum oxide powders of diminishing grit sizes. This method significantly increases, both by greater pressure and efficiency of abrasive contact, the rate of removing material from the surface

3  $\mu$ -, 1  $\mu$ -, and 0.5  $\mu$ -diamond pastes, followed by dry aluminum oxide powders of grit size 0.3  $\mu$  and 0.1  $\mu$ . Toward the conclusion of the process, the aluminum oxide powder was mixed with acetone into a slurry, yielding an extremely high degree of polish.

At regular intervals within each polishing phase, a visual inspection under a 90X microscope was made and the linewidth of the sample was measured to compare the effectiveness of each grit size in narrowing the linewidth. Table I lists the measured linewidths of three YIG spheres for various grit sizes and polishing times.

Samples A and B were grown in the same batch in the laboratory, while sample C was purchased. Sample B, though adequately polished, appears to have solvent inclusions which probably account for its relatively large linewidth.

Each value listed in the preceding table is the average linewidth taken over many sample orientations, thereby eliminating any dependency of linewidth on crystal orientation. These values were obtained using both the cavity perturbation technique,<sup>2</sup> where appropriate, and a new method<sup>3</sup> designed especially for use with narrow linewidth samples.

TABLE I  
LINewidth IN OERSTEDS

At completion of coarse-polishing phase		Sample A	Sample B	Sample C
Grit Size	Hours	4.47	2.5	~3.0
6 $\mu$ -Diamond Paste	1	—	—	1.89
3 $\mu$ -Diamond Paste	1	2.72	1.28	1.39
	1	1.35	1.30	1.13
1 $\mu$ -Diamond Paste	1	1.27	—	1.16
	1	1.00	1.25	0.84
0.5 $\mu$ -Diamond Paste	1	1.05	—	—
	1	1.00	1.24	—
0.3 $\mu$ -Aluminum Oxide Powder	1	0.86	—	0.73
	1	0.95	1.25	—
	2	—	1.04	—
	3	—	1.03	—
0.1 $\mu$ -Aluminum Oxide Powder	1	0.80	—	—
	1	0.65	—	—
	2	—	1.07	—
	3	—	1.12	—
Final Diameters		0.015 inch	0.021 inch	0.014 inch

of the sample, which is fundamental in the polishing process. Results attest to a substantial reduction in fine-polishing time to a matter of hours. At present, fine-polishing using the more or less conventional technique of tumbling the sample in an air-cyclone chamber requires a period of days.

Rough samples are shaped into spheres and the coarse-polishing phase completed by either the previously mentioned air-cyclone chamber or metallurgical grinder<sup>1</sup> methods. Fine-polishing is initiated by rolling the spheres in a figure eight pattern under light finger pressure in 6  $\mu$ -grit diamond paste that has been dabbed on a metallurgical polishing cloth. Since a very small amount of material is removed by hand polishing, reasonable care insures uniform polish over the entire crystal surface and maintains sample sphericity. After approximately one hour of such polishing, the process is repeated with successively finer grits, viz.,

It is felt that further experience will reveal not only that one or more steps can be eliminated in the polishing procedure, but also that an optimum polishing time per stage can be determined.

To mechanize the process, a simple polishing machine consisting essentially of two reciprocating polishing plates is being developed.

P. D. GIANINO  
B. R. CAPONE  
E. KELLY  
AF Cambridge Res. Center  
Air Res. and Dev. Command  
Laurence G. Hanscom Field  
Bedford, Mass.  
J. I. MASTERS  
Technical Operations, Inc.  
Burlington, Mass.

<sup>2</sup> J. A. Artman and P. E. Tannenwald, "Microwave Susceptibility Measurements in Ferrites," M.I.T. Lincoln Lab., Lexington, Mass., Tech. Rept. No. 70, October, 1954.

<sup>3</sup> J. Masters, B. Capone, and P. Gianino, "Measurement technique for narrow linewidth ferromagnets," IRE TRANS. ON MICROWAVE THEORY AND TECHNIQUES, this issue, p. 330.

## Tunable Two-Mode Cavity with Capacitive Loading\*

A cavity with two independently tunable modes in the 4- to 9-kMc frequency range was needed for experiments in paramagnetic relaxation. It had to be small enough to fit inside a liquid helium dewar and had to possess a region of approximately uniform RF magnetic field common to both modes over part of its volume.

To meet these requirements a box shaped copper cavity of inside dimensions 0.670 inch  $\times$  0.670 inch  $\times$  0.866 inch was built, and its natural resonant frequencies were lowered into the required range by means of copper blocks mounted in the central region. If the cavity is regarded as the limiting case of an LC resonant circuit, the effect of such loading is to increase the capacity. The fundamental unloaded frequencies were 11.18 kMc in the two modes which were used and 12.48 kMc in the third mode. The 11.18-kMc modes were shifted to frequencies in the range from 4 to 9 kMc by an appropriate choice of loading block. The third mode was damped out by the joint in the cavity wall and by the brass rod used to support the center block. The cavity was tuned by moving dielectric plungers in and out of the region of the strong electric field. In most of the geometries tested, these regions were distinct for each mode so that changes in the tuning of one had comparatively little effect on the other.

The cavity was made in two parts joined along a central plane as shown in Fig. 1.

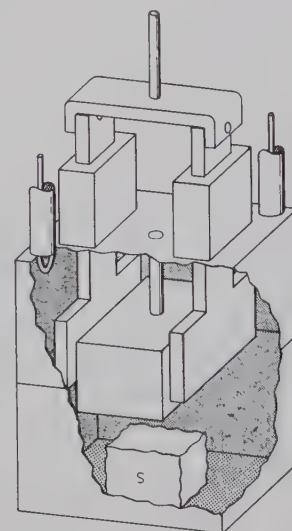


Fig. 1—Cutaway view of loaded cavity. In magnetic resonance experiments the sample (S) may be placed in the space below the loading block. For clarity, only one pair of dielectric tuning plungers are shown.

Dielectric plungers, loading blocks, and coupling loops were mounted in the upper part, the lower part being left for accommodation of the specimen. The plungers were made of SC24 ceramic (relative dielectric constant 9) and connected in pairs by brass brackets outside the cavity so that each

\* Received by the PGMTT, June 1, 1960.

<sup>1</sup> J. L. Carter, E. V. Edwards, and I. Reingold, "Ferrite sphere grinding technique," Rev. Sci. Instr., vol. 30, pp. 946-947, October, 1959.

\* Received by the PGMTT, June 1, 1960.

pair moved as a unit. The loading blocks were mounted in the center space by a 0.050-inch brass supporting tube clamped in the top of the cavity. Four blocks were tested (Fig. 2): one with a square cross section to give nearly equal frequencies, one with rectangular cross section to give moderate separation of frequencies, one I shaped block to give extreme separations, and the block shown in Fig. 2(d). The large horizontal dimensions of this last block make the space between block and cavity walls small, thereby providing high capacitive loading. The holes in the corners help conserve the effective inductance by allowing the magnetic field a near normal path. Each block had a vertical dimension of 0.280 inch (*i.e.*, about one third of the depth of the cavity). The other dimensions are shown in Fig. 2.

Power was introduced by two magnetic coupling loops which could be rotated or retracted. The two loops could be used to feed each mode independently, or one loop could be oriented to feed both and the other loop left as a tuning monitor.

Measured  $Q$  values corrected for coupling losses were 2000 to 3000. Tuning curves for the cavity when loaded with the rectangular block are shown in Fig. 3. Results for this and other blocks are summarized in Table I.

Ceramic plungers with a thickness of 0.120 inch (*i.e.*, two times the original thickness) were fitted and tested with the square cross section block [Fig. 2(a)]. This resulted in a tuning range from 5655 Mc to 7450 Mc for each mode. A block of quartz (relative dielectric constant 4) with a volume of 0.034 cubic inch was placed in the bottom of the cavity to estimate the amount of detuning likely to be caused by the presence of a paramagnetic or other sample in the cavity. The quartz occupied about one fourth of the total volume available for the sample and lowered the cavity frequency by less than one per cent.

Capacitive loading by centrally mounted copper blocks is free from lossy joints between conducting elements and does not lead to an excessive deterioration in  $Q$ . In magnetic resonance experiments, there may be an over-all gain in sensitivity due to the reduction in cavity volume and the increase in sample filling factor. For a given size cavity the operating frequencies may be chosen anywhere in a wide range and may be altered merely by substituting new loading blocks. Because of the effect of the block in concentrating the electric field between itself and the cavity wall, it is possible to obtain a fair degree of independence in the

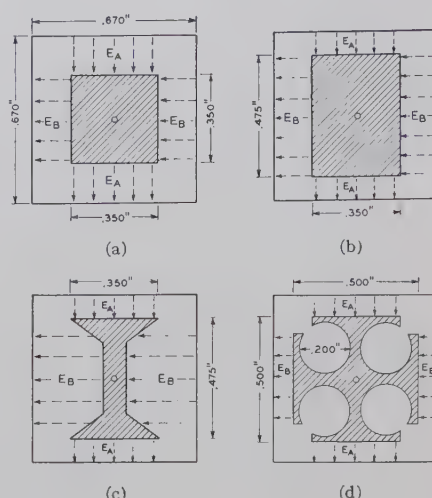
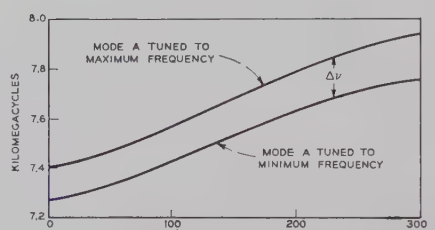
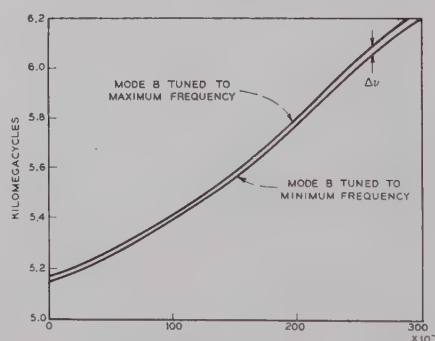


Fig. 2—Plan views of cavity with each loading block in place.  $E_A$  and  $E_B$  indicate the direction of electric field for modes A and B. Third dimension of all blocks in 0.280 inch.



(a) Displacement of mode B tuning plungers in inches.



(b) Displacement of mode A tuning plungers in inches.

Fig. 3—Tuning curves for each cavity mode when loaded with rectangular block [Fig. 2(b)]. Tuning plunger displacements are measured from the central position (*i.e.*, the position in which the plunger occupies the space between the loading block and the side wall). The two curves shown in each case correspond to the two extreme tuning settings in the remaining mode.  $\Delta\nu$  is a measure of the independence of tuning.

TABLE I\*

Type	High End	$\Delta\nu$	Low End	$\Delta\nu$	Tuning Range
Square Block Modes A and B	7700 Mc	50 Mc	7075 Mc	40 Mc	625 Mc
Rectangular Block Mode A	6220 Mc	25 Mc	5150 Mc	20 Mc	1070 Mc
Mode B	7940 Mc	190 Mc	7265 Mc	135 Mc	675 Mc
I Block Mode A	5280 Mc	25 Mc	4400 Mc	2 Mc	880 Mc
Mode B	9150 Mc	305 Mc	8500 Mc	255 Mc	650 Mc
Block of Fig. 2(d) Modes A and B	4950 Mc	30 Mc	3850 Mc	50 Mc	1100 Mc

\*  $\Delta\nu$  is a measure of independence of tuning. It is the change in frequency of one mode when the tuning control for the other mode is taken from one extreme end to the other. See Fig. 3.

tuning of the two modes and to cover a range up to twenty per cent without using large amounts of dielectric. The lower third of the cavity volume is left free for the mounting of samples and contains the region of strong magnetic field common to both modes.

J. D. MCGEE  
Bell Telephone Labs., Inc.  
Murray Hill, N. J.

## Unloaded $Q$ of Single Crystal Yttrium-Iron-Garnet Resonator as a Function of Frequency\*

The practical feasibility of constructing magnetically tunable broad-tuning range microwave filters using single crystal yttrium-iron-garnet resonators was demonstrated in a recent paper.<sup>1</sup> Experimental results were presented on one- and two-resonator filters which can be tuned by varying a dc magnetic field bias over a full waveguide bandwidth and greater, at the same time maintaining an insertion loss performance which is comparable to mechanically-tuned cavity filters. The crucial parameter of the resonant elements in a band-pass filter is the unloaded  $Q$ ,  $Q_u$ . With a spherical single crystal of yttrium-iron-garnet the  $Q_u$  decreases with frequency below X-band frequencies reaching very low values at frequencies around 2000 Mc.

Analytical formulas for  $Q_u$  ( $=2\pi \times \text{frequency} \times \text{total energy stored} / \text{power absorbed at resonance}$ ) have been developed.<sup>2</sup> First, formulas given by Lax<sup>3</sup> were used for the effective susceptibility, which relates the RF components of magnetization inside a ferrite to the external RF fields. Lax uses the original Landau-Lifshitz formulation of the equations of motion and makes the substitution  $\alpha = 1/\omega\tau$  for the original damping parameter  $\alpha$ , where  $\tau$  is a relaxation time, and  $\omega = 2\pi \times \text{frequency}$ . By using his susceptibility formula the following expression for  $Q_u$  of a sphere was obtained:

$$Q_u = \omega_0\tau/2 \text{ (Lax)}. \quad (1)$$

Recently an analytical formula for the effective susceptibility was developed<sup>4</sup> using the modified form of the Bloch equations of motion of magnetization which were given by Bloembergen.<sup>5</sup> Using this result a new re-

\* Received by the PGMTT, June 6, 1960. This work was supported jointly by Stanford Res. Inst. and by the U. S. Army Signal Res. and Dev. Lab., Fort Monmouth, N. J., under Contract DA 36-039 SC-74862.

<sup>1</sup> P. S. Carter, Jr., "Magnetically Tunable Microwave Filters Employing Single Crystal Garnet Resonators," IRE 1960 INTERNATIONAL CONVENTION RECORD, pt. 3, pp. 130-135.

<sup>2</sup> P. S. Carter, Jr., *et al.*, "Design Criteria for Microwave Filters and Coupling Structures," Stanford Res. Inst., Menlo Park, Calif., Tech., Rept. No. 8, SRI Project 2326, Contract DA 36-039 SC-74862; October, 1959.

<sup>3</sup> B. Lax, "Frequency and loss characteristics of microwave ferrite devices," *Proc. IRE*, vol. 44, pp. 1368-1386; October, 1956.

<sup>4</sup> C. Flammer, "Resonance Phenomena in Ferrites," unpublished memorandum.

<sup>5</sup> N. Bloembergen, "Magnetic resonance in ferrites," *Proc. IRE*, vol. 44, pp. 1259-1269; October, 1956. Eq. (5) (Bloch-Bloembergen equations of motion) contains an error. The term  $-M_0/\tau$  should be deleted.



lation was then obtained for  $Q_u$ :

$$Q_u = \left( \omega_0 - \frac{\omega_m}{3} \right) \frac{\tau}{2} \quad (2)$$

where

$\tau$  = relaxation time

$\omega_0$  = resonant angular frequency =  $2\pi$   $\times$  resonant frequency in cycles per second

$\omega_m = \gamma_0 M_0 = \mu_0 g(e/2m) M_0 = 2\pi f_m$  = angular frequency corresponding to the magnetization, in which

$\mu_0$  = intrinsic permeability of free space =  $1.256 \times 10^{-6}$  henries per meter

$g$  = Landé  $g$  factor  $\cong 2.00$  for electrons in most ferrites

$e/m$  = ratio of charge,  $e$ , to mass,  $m$ , of electron =  $1.759 \times 10^{11}$  coulombs/kg

$M_0$  = saturation magnetization of ferrite, amperes per meter.

This new formula for  $Q_u$  given above predicts that a value of  $Q_u = 0$  should occur at  $\omega_0 = \omega_m/3$ , thereafter increasing linearly with increasing frequency, provided that  $\tau$  is independent of frequency. According to the equation for  $Q_u$  derived using the Lax formula, the variation of  $Q_u$  is described by a straight line which intersects the origin,  $Q_u = 0$  at  $f_0 = 0$ . These two relations given by (1) and (2) are shown in Fig. 1 for the case  $\tau = 2 \times 10^{-7}$ . The only qualification that must be applied to these formulas is that the material must be fully magnetized. For a spherical shape this requires that the operating frequency should be somewhat greater than  $\omega_0 = \omega_m/3 = \gamma_0 H_0$ , since a sphere becomes unsaturated at biasing fields of this magnitude. For single crystal yttrium-iron-garnet this "saturation frequency" occurs at  $f_0 = f_m/3 = 1670$  Mc.

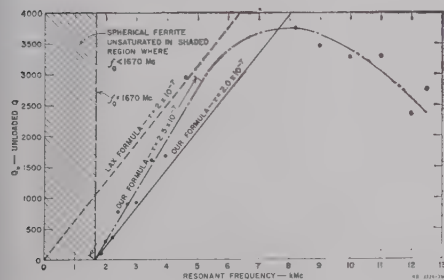


Fig. 1.

It is possible to reinterpret Lax's susceptibility formula so that it now becomes the same as the new formula. This is done by substituting for  $\tau$  in Lax's equation a new relaxation time  $(\omega_0 - N_z \omega_m) \tau / \omega_0$ , where  $N_z$  is the  $z$ -demagnetizing factor. In the case of the sphere,  $N_z = \frac{1}{3}$ . However, the new formula is obtained straightforwardly from the Bloch-Bloembergen equation of motion, and the equivalent circuit interpretation, without the artificial introduction of a relaxation time which in turn depends on a demagnetizing factor.

Measurements were made of the  $Q_u$  of a highly polished spherical single crystal of yttrium-iron-garnet, using the method de-

scribed by Ginzton.<sup>6</sup> The yttrium-iron-garnet sphere was mounted in a short-circuited waveguide or transmission line near the short circuited end. A 0.064-inch diameter single crystal yttrium-iron-garnet sphere was used in these measurements.

The experimental values of  $Q_u$  are shown as points in Fig. 1. An approximate fit to these data is given by the "dash-dot" curve. The lower frequency portion of this experimental curve between 1.67 kMc and about 5 kMc is a straight line which can be represented by the new formula, assuming  $\tau = 2.5 \times 10^{-7}$ . In this low frequency region at least, the data appear to support the new formula for  $Q_u$ . At higher frequencies the experimental curve for  $Q_u$  flattens off and, above about 8 kMc,  $Q_u$  decreases with increasing frequency.

It is planned to publish a complete analysis and discussion of these and other related data in the near future.

P. S. CARTER, JR.

C. FLAMMER

Stanford Res. Inst.

Menlo Park, Calif.

<sup>6</sup> Edward L. Ginzton, "Microwave Measurements," in "Microwave Measurements," McGraw-Hill Book Co., Inc., New York, N. Y., ch. 9, pp. 391-434; 1957.

## A Note on the Derivation of the Fields in a Radial Line\*

The concept of a radial transmission line is frequently used in the description of such devices as cylindrical cavity resonators and horn radiators. An approach<sup>1-3</sup> to the problem of determining the electric and magnetic fields in the radial line has been to solve Maxwell's equations in component form with appropriate boundary conditions. While the following derivation yields nothing new, it does, however, have the advantages of being simple and of requiring a minimum of guess work as compared to other methods of solving this problem.

The technique employed here is based on the fact<sup>4</sup> that the general solution of the vector Helmholtz equation

$$\nabla^2 \bar{A}(\bar{r}) + k^2 \bar{A}(\bar{r}) = 0 \quad (1)$$

consists of a linear combination of three vector functions generated in turn from

three scalar functions:

$$\bar{L}(\bar{r}) = \nabla \phi(\bar{r})$$

$$\bar{M}(\bar{r}) = \nabla \times [\bar{u} \psi(\bar{r})]$$

$$\bar{N}(\bar{r}) = \frac{1}{k} \nabla \times \nabla \times [\bar{u} \chi(\bar{r})].$$

The vector  $\bar{u}$  is a constant vector and  $\phi$ ,  $\psi$  and  $\chi$  are each solutions of the scalar Helmholtz equation; e.g.,  $\nabla^2 \phi(\bar{r}) + k^2 \phi(\bar{r}) = 0$ .

Consider the geometry shown in Fig. 1. The region of interest is the semi-infinite space between the perfectly conducting, parallel bounding surfaces at  $z=0$  and  $z=b$ . Assume that the fields have a time dependence of the form  $e^{j\omega t}$  and that no free charge exists in the region between the bounding surfaces. Subject to these conditions, the electric and magnetic fields in the region  $0 \leq z \leq b$  must satisfy an equation of the same form as (1) with  $k^2 = -\gamma_0^2 = \omega^2 \mu \epsilon [1 - j(\sigma/\omega \epsilon)]$  where  $\sigma$ ,  $\epsilon$  and  $\mu$  are respectively the conductivity, permittivity and permeability of the medium between the surfaces and  $\omega$  is the radian frequency.

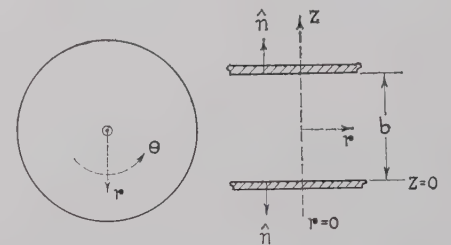


Fig. 1—A radial transmission line consisting of two parallel conducting planes.

Because of the manner in which they are defined,  $\bar{M}$  and  $\bar{N}$  are solenoidal as are  $\bar{E}$  and  $\bar{H}$  in this case, and it follows that the  $\bar{M}$  and  $\bar{N}$  solutions for (1) could correspond to either the electric or the magnetic field depending upon the choice of boundary conditions at  $z=0$  and  $z=b$ .

As an illustration let us require that  $\bar{M}$  and  $\bar{N}$  satisfy the boundary conditions for the electric field, namely,  $\hat{n} \times \bar{M} = \hat{n} \times \bar{N} = 0$ . Writing the  $\bar{M}$  solution in terms of the unit vector in the  $z$ -direction,  $\bar{M} = \nabla \times [\bar{u}_z \psi(r, \theta, z)]$ , and applying the boundary conditions after solving the scalar Helmholtz equation by the standard approach of separating variables leads to

$$\begin{aligned} \bar{E}_{m,n} = \bar{M}_{m,n} = \nabla \times \left\{ \bar{u}_z [K_1 J_m(\beta r) \right. \\ \left. + K_2 Y_m(\beta r)] e^{\pm j m \theta} \sin \left( \frac{n \pi}{b} z \right) \right\} \\ m, n = 0, 1, 2, \dots \quad (2) \end{aligned}$$

$K_1$  and  $K_2$  are arbitrary constants which specify the amplitude of the field.  $J_m$  and  $Y_m$  are the Bessel functions of the first and second kind respectively and  $\beta^2 = -\gamma_0^2 = (\omega^2 \mu \epsilon) - (n \pi / b)^2$ . In this case,  $K_2$  must be equal to zero because of the singularity of  $Y_m(\beta r)$  at  $r=0$ , but if the region of interest is that for which  $r \geq r_0 \neq 0$ , then  $K_2$  need not be zero. The corresponding magnetic field can be found from

$$\nabla \times \bar{E}_{m,n} = -j \omega \mu \bar{H}_{m,n} \quad (3)$$

\* Received by the PGM-TT, June 10, 1960. This work was supported in part by the U. S. Army Signal Engrg. Labs., Fort Monmouth, N. J., under Contract DA 36-039 sc 78254.

<sup>1</sup> S. A. Schelkunoff, "Electromagnetic Waves," D. Van Nostrand Co., Inc., New York, N. Y., pp. 260-275; 1943.

<sup>2</sup> H. R. L. Lamont, "Wave Guides," Methuen and Co. Ltd., London, Eng., pp. 19-23; 1942.

<sup>3</sup> C. G. Montgomery, R. H. Dicke, and E. M. Purcell, "Principles of Microwave Circuits," McGraw-Hill Book Co., Inc., New York, N. Y., pp. 252-254; 1948.

<sup>4</sup> P. M. Morse and H. Feshbach, "Methods of Theoretical Physics," McGraw-Hill Book Co., Inc., New York, N. Y. pp. 1764-1767; 1953.

The fields obtained from (2) and (3) are the so-called "transverse" electric fields since  $E_z(m, n)$  vanishes.

Following an identical procedure, the  $\bar{N}$  solution leads to

$$\begin{aligned} \bar{N}'_{m,n} = \bar{N}_{m,n} = & -\frac{j}{\gamma_0} \nabla \times \nabla \times \left\{ \hat{u}_z [K_3 J_m(\beta r) \right. \\ & \left. + K_4 Y_m(\beta r)] e^{\pm im\theta} \cos\left(\frac{n\pi}{b} z\right) \right\} \\ & m, n = 0, 1, 2, \dots \quad (4) \end{aligned}$$

Again the corresponding magnetic field,  $\bar{H}'_{m,n}$ , can be found using (3). These fields are the so-called "transverse" magnetic fields since  $H'_z(m, n) = 0$ .

It is also possible to derive the magnetic fields from the  $\bar{M}$  and  $\bar{N}$  solutions by requiring that  $\hat{n} \cdot \bar{M} = \hat{n} \cdot \bar{N} = 0$  at  $z=0$  and  $z=b$ , and then use (3) to determine the components of the electric fields.

JOSEPH F. DIENST  
Microwave Electronics Lab.  
College of Engrg.  
Rutgers, the State University  
New Brunswick, N. J.

### Surface Waves on Symmetrical Three-Layer Sandwiches\*

The theory of surface waves on plane dielectric slabs has been presented by Plummer and Hansen.<sup>1</sup> Additional numerical results are shown in Figs. 1 and 2 for the lowest order TM and TE modes that can exist on a grounded dielectric slab. The slab has thickness  $d_s$ , and a relative dielectric constant of 4. It is separated by an air gap of thickness  $a$  from the ground plane.  $c/v$  represents the ratio of the velocity of light in free space and the phase velocity of the surface wave. By image theory, these modes (TM<sub>0</sub> and TE<sub>1</sub>) can also exist on a symmetrical, three-layer, air-core sandwich to which the given numerical data also apply.

Figs. 3 and 4 show similar data for the TM<sub>1</sub> and TE<sub>0</sub> modes. These modes disappear if a ground plane is inserted at the center of the sandwich. For this reason, these modes are usually ignored in the literature.

The fields of a surface wave decay as  $e^{-\alpha x}$ , with distance from the surface of the plane structure. The attenuation constant  $\alpha$ , is not independent but is directly related to the phase velocity by  $(\alpha\lambda_0)^2 = 4\pi^2 [(c/v)^2 - 1]$ , as shown in Fig. 5. This may be called a universal curve of  $\alpha\lambda_0$  vs  $c/v$ , because it applies to TE and TM modes on any lossless plane structure.

The results mentioned were obtained under a project sponsored by the Air Research and Development Command, USAF.

J. H. RICHMOND  
Antenna Lab.  
The Ohio State University  
Columbus, Ohio

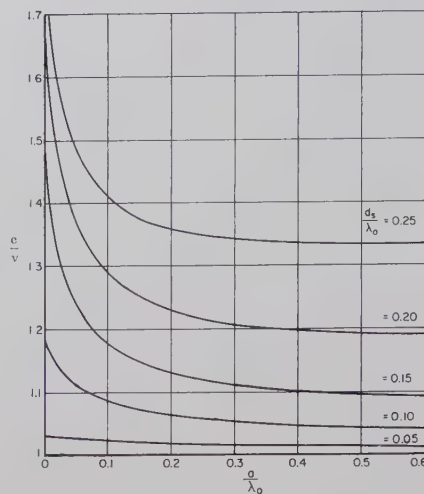


Fig. 1—Phase velocity ratio vs core thickness for the TM<sub>0</sub> mode on an air-core sandwich. (Data also apply to a single slab over a ground plane, with an air space.)

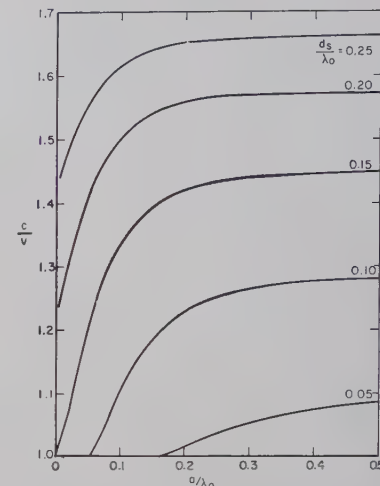


Fig. 2—Phase velocity ratio vs core thickness for the TE<sub>1</sub> mode on an air-core sandwich. (Data also apply to a single slab over a ground plane, with an air space.)

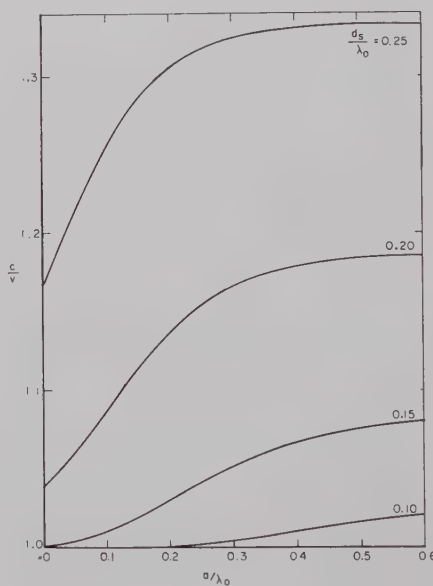


Fig. 3—Phase velocity ratio vs core thickness for the TM<sub>1</sub> mode on an air-core sandwich.

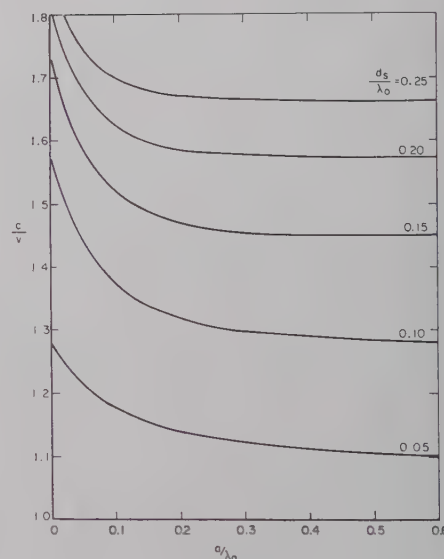


Fig. 4—Phase velocity ratio vs core thickness for the TE<sub>0</sub> mode on an air-core sandwich.

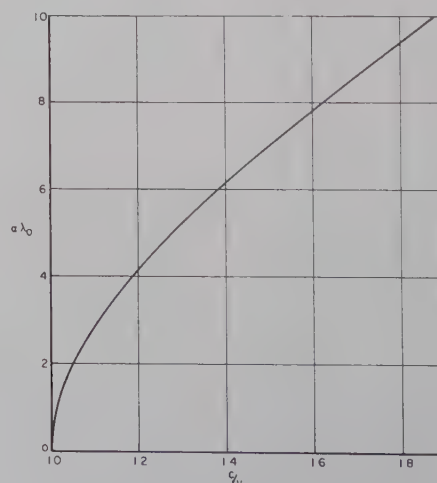


Fig. 5—Universal curve of  $\alpha\lambda_0$  vs  $c/v$ .

\* Received by the PGMTT, June 20, 1960.

<sup>1</sup> R. Plummer and R. Hansen, *Proc. IEE*, pt. C, mono. 238R, May, 1957.



## Higher-Order Evaluation of Dipole Moments of a Small Circular Disk\*

Bethe<sup>1</sup> was the first to calculate the induced electric and magnetic dipole moments if a plane wave falls upon a circular hole in an infinite plane screen. The corresponding complementary problem of a circular disk can then be solved using Babinet's principle. In some recent experimental work on circular disks in a rectangular waveguide<sup>2</sup> large discrepancies between experimental and theoretical results were found when Bethe's theory was used particularly for disks, where  $ka > 0.5$  ( $a$  = radius of the disks,  $k = 2\pi/\lambda$ ). Bouwkamp<sup>3</sup> has shown that Bethe's results can be obtained by using a first order approximation for the surface current distribution on the disk. Following the same procedures,<sup>3,4</sup> a sixth order approximation in  $(ka)$  for normal incidence and a third order approximation for oblique incidence has been found. The detailed results will be presented in a future paper. Here only the expressions for the electric and magnetic dipole moments will be given.

### NORMAL INCIDENCE

#### Electric dipole moment

$$P = \frac{16}{3} a^3 \left( 1 + \frac{8}{15} (ka)^2 - j \frac{8}{9\pi} (ka)^3 + \frac{16}{105} (ka)^4 - j \frac{176}{225\pi} (ka)^5 \right) \epsilon_0 E_{\text{tan}}^i(0, 0, 0).$$

#### Magnetic dipole moment

$$M = 0.$$

\* Received by the PGM-TT, June 20, 1960. This work has been sponsored by the Electronics Research Directorate of the Air Force Cambridge Research Center under contract no. AF 19(604)3887.

<sup>1</sup> H. A. Bethe, "Theory of diffraction by small holes," *Phys. Rev.*, vol. 66, pp. 163-182; February, 1944.

<sup>2</sup> R. A. Gardner, "Shunt Susceptance of Planar Arrays of Conducting Disks," Master's thesis, Case Inst. Tech., Cleveland, Ohio; April, 1960.

<sup>3</sup> C. J. Bouwkamp, "A Critique of Some Recent Developments in Diffraction Theory," New York University, N. Y., Res. Rept. No. EM-50, pp. 44-58; 1953.

<sup>4</sup> C. J. Bouwkamp, "On the diffraction of electromagnetic waves by small circular disks and holes," *Philips Res. Rept.*, vol. 5, pp. 401-422; December, 1950.

### OBLIQUE INCIDENCE

Electric dipole moment in plane of incidence.

$$P = \frac{16}{3} a^3 \left( 1 + \frac{8}{15} (ka)^2 - \frac{1}{10} \sin^2 \theta (ka)^2 \right) \epsilon_0 E_{\text{tan}}^i(0, 0, 0).$$

#### Magnetic dipole moment

$$M = -\frac{8}{3} a^3 \left( 1 - \frac{2}{10} (ka)^2 - \frac{1}{10} \sin^2 \theta (ka)^2 + j \frac{4}{9\pi} (ka)^3 \right) H_n^i(0, 0, 0).$$

$E_{\text{tan}}^i(0, 0, 0)$  = tangential component of electric field at the center of the disk in plane of incidence.

$H_n^i(0, 0, 0)$  = normal component of magnetic field at the center of the disk.

$a$  = radius of disk.

$\theta$  = angle between the direction of incidence of plane wave and direction of normal to the disk.

From the current distribution on the disk higher order multipole moments can easily be calculated.

WILHELM H. EGGIMANN

Elec. Engrg. Dept.

Case Inst. Tech.

Cleveland, Ohio

## Properties of Symmetric Hybrid Waveguide Junctions\*

In his letter<sup>1</sup> J. M. Smith states that in a fully symmetric lossless hybrid where all arms are matched, the amplitudes of the

waves traveling in the reverse direction in the main and auxiliary guides are equal. To allow for the existence of the reflected waves this theorem should read:

"In a slightly imperfect symmetric hybrid with matched loads on the output ports the amplitude of the reflected wave at the input port is equal to the amplitude of the wave at the isolated port."

The proof of this theorem appeared first in the appendix of the paper by H. J. Riblet describing the short slot hybrid.<sup>2</sup>

Although the phase quadrature property of the perfect symmetric hybrid is well known it is not obvious how the 90° phase division varies over a frequency band for a practical imperfect hybrid. The answer to this problem was also given by Riblet,<sup>2</sup> but the result was not well known for a number of years because the result was subsidiary to the main argument of his paper. A more recent paper<sup>3</sup> reviews all the properties of the 90° hybrid junction, and includes the proof of the theorem stated above [see Levy<sup>3</sup> (16)]. The deviation  $\Delta\theta$  of the hybrid quadrature property from the ideal 90° is given as a function of the isolation  $I$  db by means of the formula

$$\cos \Delta\theta = 2/\text{antilog}(I/10). \quad [\text{Levy}^3 (19).]$$

This formula reveals the remarkable broadband property of the quadrature phase division, which deviates by only 1.1° from the ideal 90° when the isolation has fallen to 20 db. This is in contrast to the case of 180° ring hybrids, where the phase division is a comparatively rapidly varying function of the isolation.<sup>3</sup>

R. LEVY

Mullard Research Labs.

Salfords

Surrey, England

\* Received by the PGM-TT, June 23, 1960.

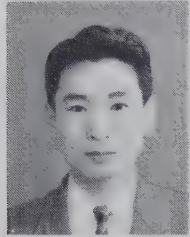
<sup>1</sup> J. M. Smith, "A property of symmetric hybrid waveguide junctions," *IRE TRANS. ON MICROWAVE THEORY AND TECHNIQUES*, vol. MTT-4, p. 251; March, 1960.

<sup>2</sup> H. J. Riblet, "The short-slot hybrid junction," *Proc. IRE*, vol. 40, pp. 180-184; February, 1952.

<sup>3</sup> R. Levy, "Hybrid junctions—frequency characteristics as phase dividers and duplexers," *Electronic Radio Eng.*, vol. 36, pp. 308-312; August, 1959

## Contributors

Saburo Adachi was born in Yamagata-Ken, Japan on September 2, 1930. He received the B.E., M.E., and D.E. degrees from the Tohoku University, Sendai, Japan in 1953, 1955 and 1958, respectively. In 1958 he was appointed as an instructor in the Electrical Communications Department of the Tohoku University.



S. ADACHI

From August, 1958 to January, 1960 he was on leave from Tohoku University and worked at The Ohio State University Antenna Laboratory, Columbus, as a Research Associate. He has been engaged in research on antennas and electromagnetic field problems.

Dr. Adachi is a member of the Institute of Electrical Engineers of Japan, the Institute of Electrical Communication Engineers of Japan, and Sigma Xi.



Donald D. Bartholomew was born in Atlanta, Ga. on August 2, 1929. He received the B.S. degree in physics from the Georgia Institute of Technology, Atlanta, Ga., and did advanced work in nuclear science at Georgia Tech until joining The Sperry Microwave Electronics Company at Clearwater, Fla. in 1958.



D. BARTHOLOMEW

While attending Georgia Tech, he participated in work being done on several research programs which were sponsored by the National Science Foundation and The Atomic Energy Commission, and worked for the Lockheed Aircraft Corporation, Nuclear Division, in the Theoretical Nuclear and Reactor Operations Groups.

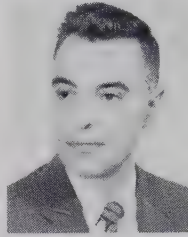
Since joining the Solid State Devices Group at the Sperry Microwave Electronics Company, he has been actively engaged in the design and development of microwave components and has more recently been working with the Sperry Microline Products Group.

Mr. Bartholomew is a member of Tau Beta Pi and Sigma Pi Sigma.



Michael Benanti (A'50) was born in New York, N. Y. on September 16, 1925. He received the Advanced Technology diploma from RCA Institute, New York, N. Y. in 1948, the B.S. degree in mathematics in 1958 from Monmouth College, West Long

Branch, N. J., and is presently undertaking graduate study at Rutgers University, New Brunswick, N. J.



M. BENANTI

N. J., working in the components field primarily on solid state devices.



Richard Benjamin was born in Spring Lake, N. J. on June 20, 1930. He received the A.A. degree from Monmouth College, West Long Branch, N. J., in June, 1958. At present, he is studying for the B.S. degree in electronic engineering at Monmouth College, where he is also employed as an electronic specialist.



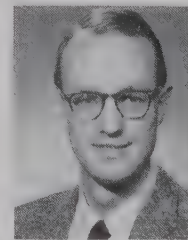
R. BENJAMIN

He is a lieutenant in the U. S. Army Reserve serving as Training Officer of a National Guard Unit. He has been employed in both government and industrial positions as an electronic specialist.

Mr. Benjamin is a member of Lambda Sigma Tau.



R. M. Bevensee (M'58) was born in Minneapolis, Minn., on May 9, 1930. He received the M.S. degree from the University of Minnesota, Minneapolis, in 1954; the E.E. degree from the Massachusetts Institute of Technology, Cambridge, in 1958; and the Ph.D. degree from Stanford University, Stanford, Calif., in 1960.



R. M. BEVENSEE

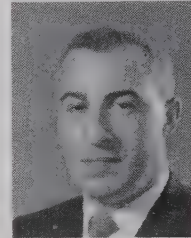
During 1954 and 1955, he worked in the Microwave Tube Division of the Sperry Gyroscope Company, Clearwater, Fla. From 1955 to 1958, he was a research assistant in the Research Laboratory of Electronics at M.I.T. He also worked in the same capacity in the Hansen Microwave Laboratory at Stanford University, until 1960. He is cur-

rently with the Research Division of Varian Associates, Palo Alto, Calif.

Dr. Bevensee is a member of Tau Beta Pi, Sigma Xi, and Eta Kappa Nu.



Frank A. Brand (M'58) was born in Brooklyn, N. Y. on June 26, 1924. He attended Hofstra College, Hempstead, N. Y., from 1946 to 1948 and the Polytechnic Institute of Brooklyn, Brooklyn, N. Y., receiving the B.S. degree in physics in 1950 and the M.S. degree in physics in 1958.

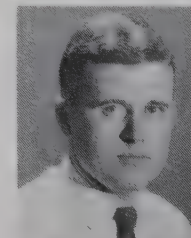


F. A. BRAND

He joined the U. S. Army Signal Research and Development Laboratory, Fort Monmouth, N. J. in 1950 as a research physicist and has since been engaged in research and development activities concerned with electron devices and semiconductor physics. He is currently Chief of the Physical Electronics Branch, U. S. Army Signal Research and Development Laboratory at Fort Monmouth. For the past three years, he has been a part-time faculty member of the Electrical Engineering Department of Monmouth College, West Long Branch, N. J.



Edward S. Cassidy, Jr. (A'52-M'57) was born in Washington, D. C., on August 19, 1927. He received the B.S. degree in electrical engineering from Union College, Schenectady, N. Y. in 1949. In 1950 he received the M.S. degree from Harvard University, Cambridge, Mass., and in 1959 the D. Eng. degree from The Johns Hopkins University, Baltimore, Md.



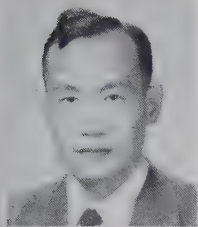
E. S. CASSEDY, JR.

In 1950 he worked for the Potomac Electric Power Company, Washington, D. C., and in 1951 he joined the U. S. Naval Ordnance Laboratory, White Oak, Md., working on telemetering problems, UHF circuit and antenna design. In 1954 he joined the Radiation Laboratory of The Johns Hopkins University, where he was engaged in research on electromagnetic scattering and microwave problems. In 1960 he joined the academic research staff at the Microwave Research Institute of the Polytechnic Institute of Brooklyn, Brooklyn, N. Y.

Dr. Cassidy is a member of Sigma Xi, the American Physical Society, and the AAAS.



Tsung-Shan Chen (A'48-M'55) was born in Hopei, China on February 2, 1913. He received the B.S. degree from Tangshan Chiao-Tung University in 1933, and the M.S. degree from Purdue University, Lafayette, Ind., in 1934. He attended the Massachusetts Institute of Technology, Cambridge, and received the M.S. degree in 1935 and the D. Sc. degree in 1938, both in electrical engineering.



T. S. CHEN

He was professor of electrical engineering at the National Central University, China, until 1947. He joined RCA in 1951, and is now with the Microwave Tube Department, Electron Tube Division, Harrison, N. J.



Marvin Cohn (S'59-A'51-M'57) was born in Chicago, Ill., on September 25, 1928. He received the B.S. degree in 1950 and the M.S. degree in electrical engineering in 1953, both from the Illinois Institute of Technology, Chicago.



M. COHN

From 1951 to 1952, he was employed by the Glenn L. Martin Company, Baltimore, Md.; he was with the Radiation Laboratory of The Johns Hopkins University, Baltimore, from 1952 until he entered the U. S. Army Signal Corps in 1953. He was stationed at White Sands Proving Grounds where he worked on the analysis of missile tracking systems.

In 1955 he returned to the Radiation Laboratory, where he has done research and development work on broad-band and super-heterodyne receivers and surface-wave transmission lines. He was head of the Millimeter Wave Techniques Group of the Radiation Laboratory.

In June of 1960 he completed the requirements for the Doctor of Engineering degree at the Johns Hopkins University. He is presently a research scientist with the research division of Electronic Communications, Inc., of Timonium, Md.

Mr. Cohn is a member of Eta Kappa Nu, Tau Beta Pi and Sigma Xi.



George A. Espersen (A'34-SM'51-F'56) was born in Jersey City, N. J., on May 17, 1906. He attended the Institute for Theoretical Physics, Copenhagen, Denmark, and received the B.S. degree in physics from New York University in 1931.

He was an electron tube development

engineer for Hygrade Sylvania Corporation from 1932 to 1939, and for National Union Radio Corporation in 1939 and 1940. From 1940 to 1942, he was project engineer engaged in research and development of klystrons at Sperry Gyroscope Company. From 1942 to 1945, he was research engineer with North American Philips Company, Inc., Irvington-on-Hudson, N. Y. Since 1945, he has been with Philips Laboratories, as section chief of the Microwave Tube and Electron Optics Sections, and, since 1959, as research physicist and staff assistant for electron tubes.

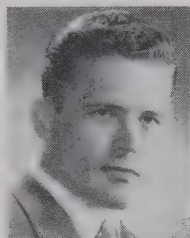


G. A. ESPERSEN

Mr. Espersen is chairman of the IRE Technical Committee on Electron Tubes, and a member of the American Physical Society and the American Rocket Society.



Nicholas George (A'51-M'56) was born in Council Bluffs, Iowa, on October 29, 1927. He received the B.S. degree in engineering physics from the University of California, Berkeley, the M.S. degree from the University of Maryland, College Park, and the Ph.D. degree from the California Institute of Technology, Pasadena, in 1949, 1956, and 1959 respectively.



NICHOLAS GEORGE

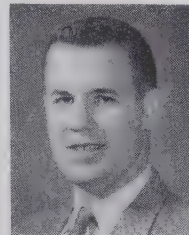
From 1949 to 1952, he was a physicist with the National Bureau of Standards, doing research on microwave receivers, and from 1952 to 1954, he was a project leader with the Diamond Ordnance Fuze Laboratories. From 1954 to 1956, he was the chief of the physics section at the Emerson Research Laboratories. In 1956, he joined the Hughes Aircraft Company Fellowship Program; and at the present time he is a senior staff physicist at Hughes, Culver City, Calif., and an associate professor at the California Institute of Technology. For the past three years, he has specialized in the fields of radar resolution, thermal radiation, and noise theory.

Dr. George is a member of Tau Beta Pi, Phi Beta Kappa, Phi Kappa Phi, and an associate member of Sigma Xi.



T. J. Goblick was born in Old Forge, Pa., on March 30, 1935. He received the B.S. degree in electrical engineering from Bucknell University, Lewisburg, Pa., in 1956, and the M.S. and Engineer's degrees from the Massachusetts Institute of Technology, Cambridge, in 1958 and 1960 respectively.

While at M.I.T. he was a research assistant in the Research Laboratory of Electronics. He was employed for two summers by the Aircraft Products Department of General Electric Co., Johnson City, N. Y., and in 1959, was a staff member at the M.I.T. Lincoln Laboratory, Lexington, Mass. He is presently continuing his studies at M.I.T.

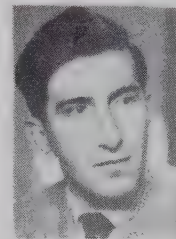


T. J. GOBLICK

Mr. Goblick is a member of Tau Beta Pi, Sigma Xi, and Pi Mu Epsilon.



Hellmut Golde was born in Berlin, Germany, on February 6, 1930. He attended the Institute of Technology in Munich, Germany, from 1948 to 1953, receiving the degree of Diplom-Ingenieur. After coming to the United States in 1953, he attended Stanford University, Stanford, Calif., where he received the M.S. degree in 1955 and the Ph.D. degree in electrical engineering in 1959.



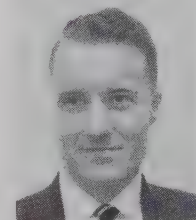
H. GOLDE

At Stanford, he was engaged in research on microwave tubes in the Microwave Laboratory. He is now an assistant professor at the University of Washington, Seattle.

Dr. Golde is a member of Sigma Xi.



E. S. Grimes, Jr. (S'53-A'55-M'58) was born on March 13, 1932 in Long Island City, N. Y. He received the B.E.E. degree from New York University, N. Y., in 1954. After graduation he joined the Sperry Gyroscope Company, Great Neck, N. Y. in the Microwave Component Group. In 1957, he moved to Clearwater, Fla., to assist in starting the newly formed Sperry Microwave Electronics



E. S. GRIMES

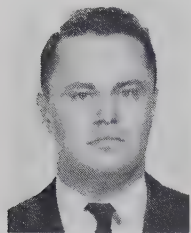
Company.

Since joining the company, he has been actively engaged in research and development work on solid state microwave components and parametric amplifiers. He is a Senior Engineer and group leader in the Applied Physics Section.



Albert Louis Holliman was born in Sandersville, Ga., on July 31, 1926. After service in the U. S. Army Paratroops from 1944 to

1946, he received the B.M.E. and M.S.M.E. degrees in 1951 and 1957, respectively, from the Georgia Institute of Technology, Atlanta. He is currently doing graduate work in electrical engineering.



A. L. HOLLIMAN

He joined the staff of the Engineering Experiment Station of the Georgia Institute of Technology in 1951, where as a member of the Radar Branch he has directed programs on the design and construction of waveguide switches, antenna pattern plotting range, antenna ground plane, and radar antennas. He is also an Assistant Professor in the School of Mechanical Engineering at Georgia Tech.

Mr. Holliman is a member of Pi Tau Sigma, Tau Beta Pi, Phi Kappa Phi, and Associate Member of Sigma Xi.



John Searcy Hollis (S'49-A'50-M'55) was born in Collier, Ga., on November 6, 1918. He was employed by Warner Robins Air Service Command from 1943 to 1944.



J. S. HOLLIS

After service in the United States Navy in 1944 and 1945, he studied at the Georgia Institute of Technology, Atlanta, receiving the B.E.E. degree in 1950 and the M.S.E.E. degree in 1956.

He joined the staff of the Engineering Experiment Station at Georgia Tech in 1948, where he was Assistant Head of the Radar Branch, and directed programs on specialized scanning techniques and radar system design. He is now Vice President—Engineering for Scientific-Atlanta, Inc., Atlanta, Ga.

Mr. Hollis is a member of Eta Kappa Nu, Tau Beta Pi, Phi Kappa Phi, and Sigma Xi.



Harold Jacobs (SM'59) was born in Port Chester, N. Y. on November 21, 1917. He received the B.A. degree from The Johns Hopkins University, Baltimore, Md., in 1938 and the M.A. and Ph.D. degrees from New York University, N. Y., in 1940 and 1945, respectively.



H. JACOBS

He was employed as a physicist at RCA, Lancaster, Pa., from 1942 to 1945, and by Sylvania Electric Products from 1945 to 1949. He joined the U. S. Army Signal Research and Development Laboratory,

Fort Monmouth, N. J. in 1949 as Chief of the Tube Techniques Section, where he performed research pertaining to electron emission, high vacua, gas discharges and semiconductor phenomena. In 1955, he was appointed Chief of the Solid State Devices Branch in the same organization and is presently Director of the Solid State Devices Division.

He has also participated in instructional activity, having been associated with the Polytechnic Institute of Brooklyn, Brooklyn, N. Y., as an instructor in electrical engineering. At present he is Chairman of the Electrical Engineering Department of Monmouth College, West Long Branch, N. J.

Dr. Jacobs is a member of the American Physical Society.



Kenneth M. Johnson was born on October 13, 1935, in Detroit, Mich. He received the B.S. degree in physics from Wayne University, Detroit, Mich., in 1957.

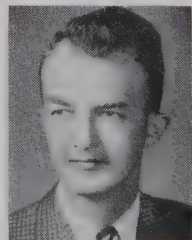


K. M. JOHNSON

During 1957 and 1958, he was engaged in plasma and back-scattering studies at Convair in San Diego, Calif. In 1958 he joined Hughes Aircraft Company, Culver City, Calif., where he has since been engaged in research and development of parametric amplifiers.



R. C. Johnson was born in Eveleth, Minn., on May 9, 1930. He received the B.S. and M.S. degrees in physics in 1953 and 1958, respectively, from the Georgia Institute of Technology, Atlanta. He is currently working toward a Ph.D. degree.



R. C. JOHNSON

In 1953 he entered the U. S. Navy where he attended the Naval Electronic Materiel School, and served as Electronics Officer aboard the U. S. S. *Moale* (DD693). Since 1956 he has been employed at the Engineering Experiment Station of the Georgia Institute of Technology, working on meteor-scatter propagation, microwave components, and microwave antennas.

Mr. Johnson is a member of Tau Beta Pi and Sigma Pi Sigma.



Edward M. Kennaugh (A'55) was born in New York, N. Y., on October 3, 1922. He received the B.S.E.E. degree in electrical

engineering from the Ohio State University, Columbus, in 1947, the M.Sc. degree in physics in 1952, and the Ph.D. degree in electrical engineering in 1959.



E. M. KENNAUGH

In 1949, he joined the staff of The Ohio State University Antenna Laboratory, Columbus, and since 1954 he has been an Associate Supervisor of that laboratory. His current field of interest is in microwave scattering and diffraction problems as well as the analysis and measurement of polarization properties of scattering objects.

Dr. Kennaugh is a member of Sigma Xi and Eta Kappa Nu.



Michael A. Kott (S'55-M'57) was born in Baltimore, Md., on February 20, 1935. He received the B.S. degree in electrical engineering from The Johns Hopkins University, Baltimore, Md., in 1956 and the M.S. degree from the same institution in 1959. In 1957 he joined the staff of the Radiation Laboratory of The Johns Hopkins University where he is presently working on microwave techniques, materials investigations and is engaged in part time graduate work.



M. A. KOTT

Mr. Kott is a member of Eta Kappa Nu, Tau Beta Pi, and Sigma Xi.



James D. Meindl (S'57-M'59) was born in Pittsburgh, Pa. on April 20, 1933. He attended Carnegie Institute of Technology, Pittsburgh, Pa., from September, 1951 to September, 1958, receiving the B.S. degree in 1955, the M.S. degree in 1956, and the Ph.D. degree in 1958 in electrical engineering.



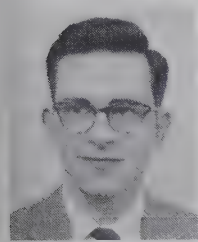
J. D. MEINDL

He is on military leave from Westinghouse Electric Corporation where he was employed as a research engineer. Since August, 1959 he has been assigned to the U. S. Army Signal Research and Development Laboratory, Fort Monmouth, N. J., where he is engaged in research work on semiconductor devices and circuits.

Dr. Meindl is a member of Tau Beta Pi, Sigma Xi, Eta Kappa Nu, Phi Kappa Phi, AIEE and the AFCEA.



Donald C. Scott (S'56-M'58) was born in Ashland, Ky. on July 17, 1930. He received the B.S.E.E. degree from the University of Kentucky, Lexington, in 1958.



D. C. SCOTT

He was an electronics technician in the U. S. Air Force from 1950 to 1954. Since 1958, he has been employed by Sperry Microwave Electronics Company, Clearwater, Fla., where he is presently engaged in the design and development of microwave solid state devices.

Mr. Scott is a member of Eta Kappa Nu.



Sandy C. Sloan, Jr. (S'56-M'58) was born on March 11, 1930, in Cordele, Ga.

He served as a Senior Operations Intelli-

gence Specialist in the Air Force Security Service from 1951 to 1955. He received the B.E.E. degree in August, 1957, from the University of Florida, Gainesville, Fla.



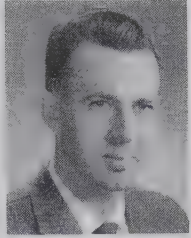
S. C. SLOAN

Since joining Sperry Microwave Electronics Company Clearwater, Fla. in 1957, Mr. Sloan has been engaged in development of microwave solid-state devices.



Rolf D. Weglein (A'52-SM'58), was born in Ichenhausen, Germany, on August 13, 1920. He received the B.S.E.E. and M.S.E.E. degrees from the California Institute of Technology, Pasadena, in 1953 and 1954, respectively.

In the years since his graduation, he has been a member of the technical staff of the Research Laboratory of the Hughes Aircraft Company, now at Malibu, Calif. Early work in research and development of backward-wave oscillators has recently resulted in his interests in solid-state devices. He now heads a group concerned with solid-state parametric amplifiers.



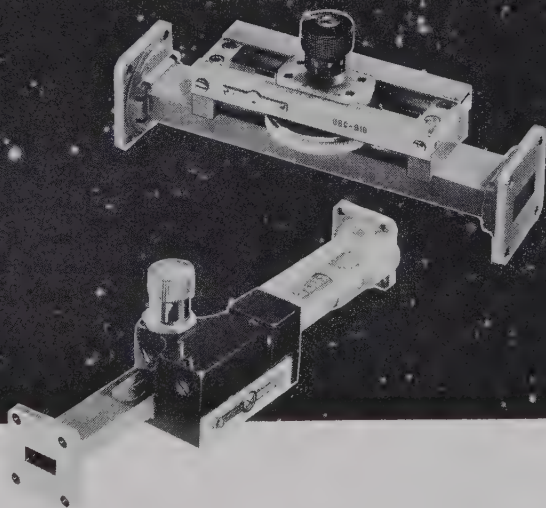
R. D. WEGLEIN

Mr. Weglein is a member of Tau Beta Pi, RESA, Sigma Xi, and the American Physical Society.



Leo Young, for a photograph and biography please see page 470 of the July, 1960, issue of these TRANSACTIONS.

what  
is the  
frequency  
standard  
for the  
U.S.A.?



**ANSWER:** By act of Congress, the U.S. Bureau of Standards determines the primary standard, based on the revolution of the earth. All DeMornay-Bonardi microwave instruments are calibrated at frequencies which are verified by our secondary standard, which, in turn, is periodically calibrated, point for point, by the U.S. Bureau of Standards.

One way to properly match a microwave transmission line is by using a D-B Stub Tuner to reduce mismatch losses and utilize the total energy available.

**D-B stub tuners** in the 2.6 to 18 KMC range have a new scale and vernier that gives precise resettability in longitudinal travel. A new micrometer scale on the probe meas-

ures penetration with very high accuracy.

Probe wobble is eliminated, and no resonances can occur under any conditions. You can correct VSWR as high as 20:1 with amazing accuracy (1.02). You can tune with precision...reset to original settings with certainty that phase and magnitude have been duplicated.

**Ditto for higher frequencies.** D-B tuners in the 18 to 90 KMC range are not simply scaled-down units—they're engineered for ultramicrowave® use. All the above features are available, plus micrometer positioning which provides readability to .0001".

*Write for data sheets—they detail all features, applications, dimensions, sizes. Bulletin DB-919.*



780 SOUTH ARROYO PARKWAY • PASADENA, CALIFORNIA









## INSTITUTIONAL LISTINGS

The IRE Professional Group on Microwave Theory and Techniques is grateful for the assistance given by the firms listed below, and invites application for Institutional Listing from other firms interested in the Microwave field.

AIRTRON, INC., A Division of Litton Industries, 200 East Hanover Ave., Morris Plains, N.J.  
Designers and Producers of Complete Line of Microwave Electronic and Aircraft Components

HUGHES AIRCRAFT CO., Florence and Teale Sts., Culver City, Calif.  
Res., Dev., Mfg.: Radar Systems and Components, Microwave Devices and Components, Antennas, Tubes

ITT LABORATORIES, 500 Washington Ave., Nutley 10, N.J.  
Line-of-Sight and Over-the-Horizon Microwave Systems; Test Equipment and Components

LITTON INDUSTRIES, Electron Tube Div., 960 Industrial Rd., San Carlos, Calif.  
Magnetron, Klystrons, Carcinotrons, TWT's, Backward Wave Oscillators, Gas Discharge Tubes, Noise Sources

MICROWAVE DEVELOPMENT LABS., INC., 92 Broad St., Babson Park 57, Mass.  
Designers, Developers and Producers of Microwave Components and Assemblies, 400 Mc to 70 kMc

WATKINS-JOHNSON COMPANY, 3333 Hillview Ave., Palo Alto, Calif.  
Res., Dev., Mfr.: Microwave Electron Devices, TWT's, BWO's, Parametric Amplifiers, Microwave Systems

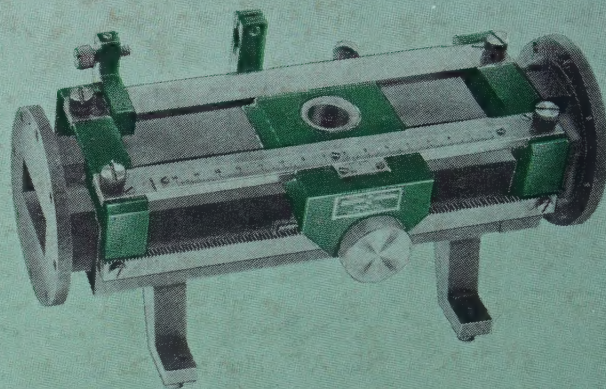
WHEELER LABORATORIES, INC., Great Neck, N.Y.; Antenna Lab., Smithtown, N.Y.  
Consulting Services, Research & Development, Microwave Antennas & Waveguide Components

The charge for an Institutional Listing is \$50.00 per issue or \$210.00 for six consecutive issues. Applications for Institutional Listings and checks (made out to the Institute of Radio Engineers) should be sent to Robert A. Rivers, PGMTT Advertising Editor, Aircom Inc., 354 Main St., Winthrop 52, Mass.



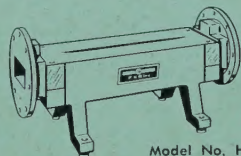
# Interchangeable SLOTTED SECTIONS

convenient and positive

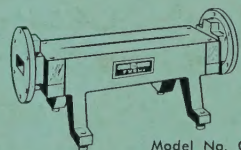


- conveniently interchangeable waveguide sections
- no slope adjustment required
- vernier position scale readable to 0.1 mm.
- dial gauge holder and movable stop
- tapered slots to minimize residual VSWR

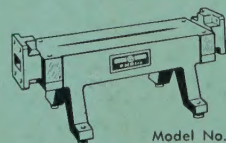
## INTERCHANGEABLE WAVEGUIDE SECTIONS



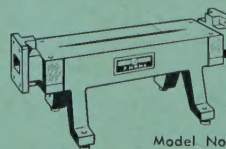
Model No. H115A



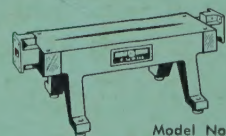
Model No. C115A



Model No. W115A

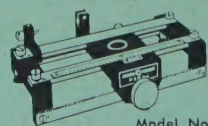


Model No. X115A



Model No. Y115A

## UNIVERSAL CARRIAGE



Model No. Z116A

Like the finest camera with a precisely fitted set of lenses, the FXR Universal Carriage and family of five Interchangeable Slotted Sections are matched to perfection. "Togetherness" with this unrivalled modular waveguide system gains new meaning . . . more rapid interchange of each section without tools or need for alignment, and more dependable performance over the entire frequency range from 3.95 kmc to 18.00 kmc. Another fine FXR "package" with quality and reliability built into it—from the first mark on the drawing board.

## SERIES 115 PRECISION SLOTTED SECTIONS

MODEL NO.	FREQUENCY RANGE (KMC)	WAVEGUIDE DIMENSIONS (Inches)	INSERTION LENGTH	WAVEGUIDE TYPE	FLANGE TYPE
H115A	3.95- 5.85	2 x 1	10 $\frac{3}{8}$ in.	RG-49/U	UG-149A/U
C115A	5.85- 8.20	1 $\frac{1}{2}$ x $\frac{3}{4}$	10 $\frac{3}{8}$ in.	RG-50/U	UG-344/U
W115A	7.05-10.00	1 $\frac{1}{4}$ x $\frac{5}{8}$	10 $\frac{3}{8}$ in.	RG-51/U	UG-51/U
X115A	8.20-12.40	1 x $\frac{1}{2}$	10 $\frac{3}{8}$ in.	RG-52/U	UG-39/U
Y115A	12.40-18.00	0.622 x 0.311 ID	10 $\frac{3}{8}$ in.	RG-91/U	UG-419/U

ACCESSORY: FXR Model No. B200A Tunable Probe.

All units when mounted in Z116A Carriage:

Slope—1.01 max. Irregularity—1.005 max.

Write for Bulletin No. SS115 or contact your local FXR representative.



## FXR, Inc.

Design • Development • Manufacture  
25-26 50th STREET RA, 1-9000  
WOODSIDE 77, N. Y. TWX: NY 43745